STRAIN MEASUREMENTS IN SILICON USING X-RAY INTERFEROMETRY

A thesis submitted to the Faculty of Science
of the University of Edinburgh, for the
degree of Doctor of Philosophy

by

C.F. Walmsley, BSc

Department of Electrical Engineering

September 1978

ABSTRACT

The aim of this work was to investigate by X-ray interferometer techniques the strain induced in silicon after thermal oxidation and boron diffusion processing. An elasticity model was developed by which the resulting strain and interferometer moiré fringe pattern could be predicted when the oxidation or diffusion took the form of a circular disc. By this means, the stress in oxide thermally grown at 950°C was measured to be 1.65×10^{9} dynes/cm^2. Double crystal techniques were used to measure the wafer bowing after oxidation, giving good agreement with the interferometer measurements. The solute lattice contraction coefficient for boron was measured by interferometry and found to be 6.0×10^{-24} cm^3/atom. Combining this result with four point probe measurements, the mobility of holes in degenerate silicon was found to be 122 cm^2/volt sec. By keeping the total dose of boron below the critical value of 3×10^{15} atoms/cm^2 in order to avoid lattice dislocation, it was found by double crystal measurements that this was insufficient to produce a significant diffraction peak from the diffused region under conditions of total Bragg reflection. The possibility of using oxidation or diffusion processing to alter the lattice parameter of silicon or germanium suitably in order to construct an X-ray monochromator or resonator capable of performing at room temperature was shown to be impracticable. Finally, the Burger's vectors of dislocations appearing in an interferometer after oxidation were successfully determined.

ACKNOWLEDGEMENTS

The author would like to express his sincere gratitude to Dr A.D. Milne, Dr A.E. Owen and Professor J.H. Collins for supervision of this work, and especially to Dr A.D. Milne for the technical advice given throughout. He would also like to thank the Wolfson Microelectronics Institute for providing the opportunity to conclude some of the experimental work.

He would also like to express his thanks to all those who have helped to make this thesis a reality, in particular to my wife for drawing the diagrams, to Mr B. Neilson for advice and assistance with processing, to Mr C.H. Matthews for photographic work and to Miss J. Clarke for typing the manuscript.

LIST OF CONTENTS

LIST OF SYMBOLS

Some symbols used in this thesis represent different parameters, depending on their context. Where this occurs, the correct symbol definition is clearly stated in the text.

a_o	Unit cell lattice parameter
$\underline{B}$	Magnetic flux density
$\underline{b}$	Burger's vector
C	Impurity concentration
C_S	Surface impurity concentration
C_B	Bulk impurity concentration
c	Polarization factor
D	Diffusion coefficient
D	Dispersion surface diameter
$D_{01}, D_{02}, D_{h1}, D_{h2}$	X-ray wave amplitudes
$\underline{D}$	Electric displacement vector
$\underline{\mathcal{D}}$	X-ray wave vector
d	Atomic plane spacing
E	Activation energy
E	Young's modulus
$\underline{E}$	Electric field vector
e	Electronic charge
F	Force
$F_h, F_{\bar{h}}$	Structure factor
f	Moiré fringe spacing
$\underline{H}$	Magnetic field intensity
$\underline{h}$	Reciprocal lattice vector
hkℓ	Miller indices

$I(\alpha)$	Intensity function
J	Flux density
K	Boltzmann's constant
$\underline{K}_{01}, \underline{K}_{02}, \underline{K}_{h1}, \underline{K}_{h2}$	Wave vector
k	Radius of Ewald sphere
ℓ, m, n	Direction cosines
m	Electron mass
N	Density of atomic sites
N	Number of extra half planes in dislocation
1-n	X-ray refractive index
n	Electron concentration
$\underline{n}$	Unit surface normal vector
$\underline{P}$	Polarization vector
$P(\alpha)$	X-ray power function
p	Hole concentration
Q	Impurity dose
q	Electronic charge
$R(\alpha)$	Reflection curve function
R	Sheet resistance
$\underline{r}$	Vector (xyz)
r_o	Oxide/diffusion disc radius
r_a	Covalent radius of impurity atom
r_b	Covalent radius of host atom
r_e	Classical electron radius
$\underline{S}$	Energy propagation vector
T	Temperature
t	Crystal thickness
t_{ox}	Oxide thickness

t_{si}	Silicon wafer thickness
u	Lattice displacement in x direction
v	Lattice displacement in y direction
v	Volume of unit cell
x_j	Junction depth
Z	Number of electrons per unit cell
z_j	Junction depth
$\underline{\alpha}_o$, $\underline{\alpha}_h$	Dispersion vectors
β	Solute lattice contraction coefficient
Δ	Extinction distance
ε	Strain
ε	Dielectric constant
ε_o	Permittivity of free space
ξ	Extinction coefficient
ξ	Ratio of wave amplitudes
η	Dispersion surface normalisation factor
θ	Bragg angle
λ	X-ray wavelength
λ,λ'	Elastic constants
μ, μ_o	X-ray absorption coefficient
μ	Elastic constant
μ_n, μ_p	Electron, hole mobility
ν	X-ray frequency
ν	Poisson's ratio
σ	Stress
ρ	Electron density
ρ	Resistivity
χ_o, χ_h	Susceptibility

ω	X-ray frequency
ω_o	Natural frequency of electron oxcillation

To my wife, Rosalind, and daughter, Rowan,
born 5th September 1978

CHAPTER 1: INTRODUCTION

In recent years, the growth of the semiconductor industry has been advancing at a considerable rate, particularly in the USA, Europe and Japan. For example, in 1965 in the US the total sale of semiconductor devices amounted to $670M, climbing to $3253M in 1977. This trend is shown in Fig 1.1 with predictions for 1981[1]. As a consequence of this, solid state physics has flourished from a mostly theoretical science into an essential applied science in order to meet the technological demands of the industry. It is interesting to note,for instance, the number of occasions when theories developed many years ago, and until recently mostly untested in practice, are now fundamental to device processing and to device diagnostics.

However, owing to the high consumer demand and the fierce competition, a significant amount of physics associated with integrated circuit processing is still not properly understood, and only empirical information is available. For instance if a certain processing technique is known to give consistent good results, it is of no interest to a semiconductor manufacturer to know why or how the process works.

It is a well established fact that stress in a silicon substrate or for example in an oxide grown on it has a significant effect on fundamental electrical parameters. This becomes apparent when it is realised that the energy levels associated with conduction and valence bands can shift independently of each other as a function of stress. In fact the valence maximum can become degenerate in some stress

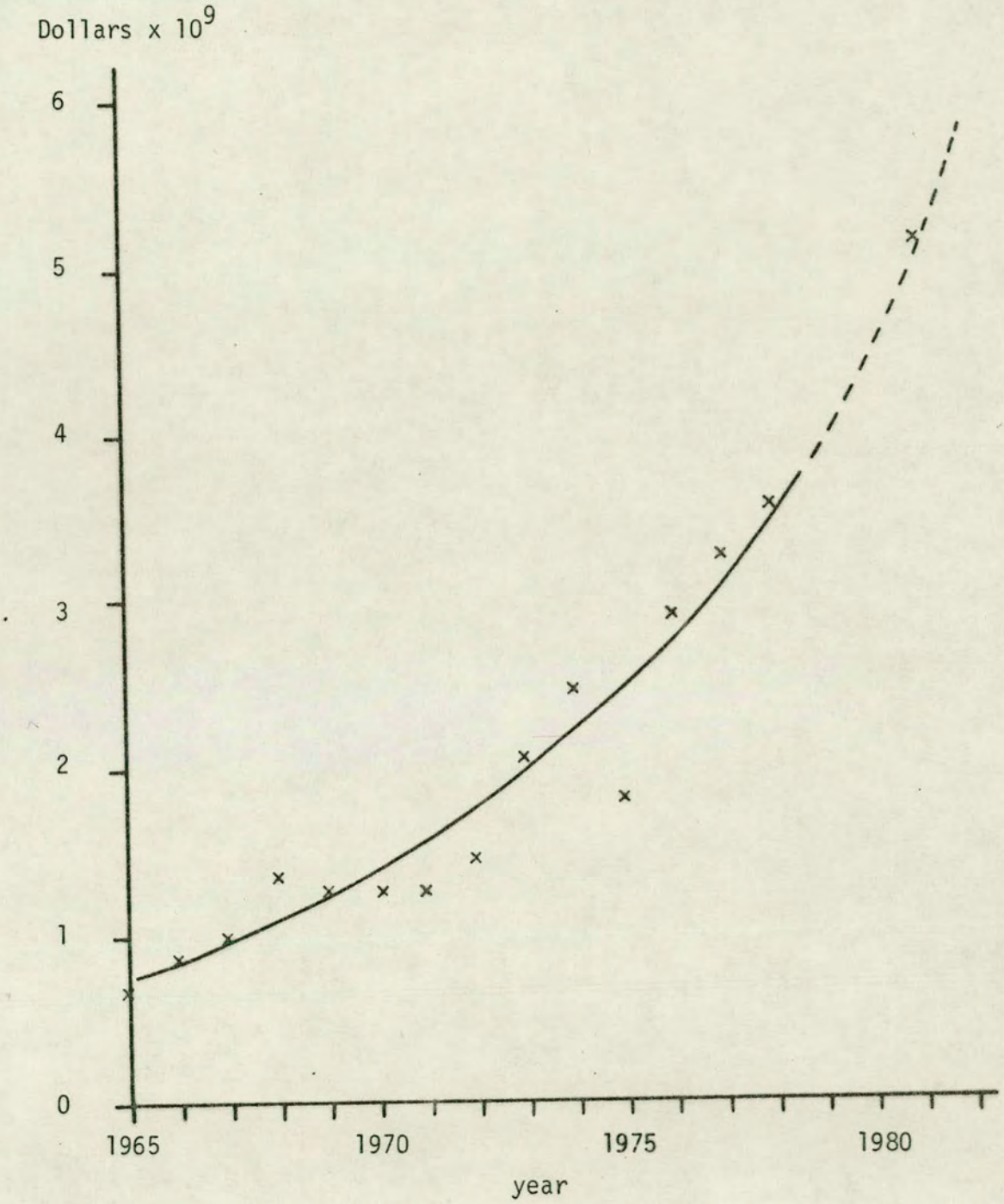

FIGURE 1.1: Growth of U.S. semiconductor industry.
Total sales of semiconductor devices between 1965 and 1977 with projection to 1981.
(Ref 1)

states. Resistivity, mobility and carrier concentration are all stress dependent. An example of the magnitude of the effect of stress may be found in Wolf[2]: a silicon crystal diffused with boron with a surface concentration equal to that of maximum solubility introduces a stress of about 10^{10} dynes/cm^2 into the silicon. The effect of this is to increase the minority carrier density by an order of magnitude!

Another serious effect of stress is to cause dislocations within the silicon which give rise to leakage paths due to impurity precipitation along the dislocation line and hence to poor device yields. Failure mechanisms of this type, because of their severity, have been studied in detail by many workers[3-11]. However, since stress *per se* is not a failure mechanism of devices but only has the effect of changing parameter values which are empirically determined anyway, there has not been the need for quite such close investigation.

The existence of stress within a crystal may be seen most easily by X-ray examination. Since the X-ray wavelengths such as CuKα, MoKα are about 1/3 and 1/7 of the lattice parameter of silicon respectively, diffraction is able to take place from the electrons associated with the atomic sites, and so any strain of this lattice may be instantly detected. Fig 1.2 illustrates this point well. The intensity variation is due entirely to strain induced within the silicon substrate by processing. Although this circuit is a digital MOS circuit, the effect on electrical parameters will be more marked for analogue circuits or those involving charge transfer such as CCDs.

Early experiments to determine the stress in an oxide involved the oxidation of one surface of the silicon and measuring the forces needed to cancel the resultant bowing of the silicon wafer[12]. Later

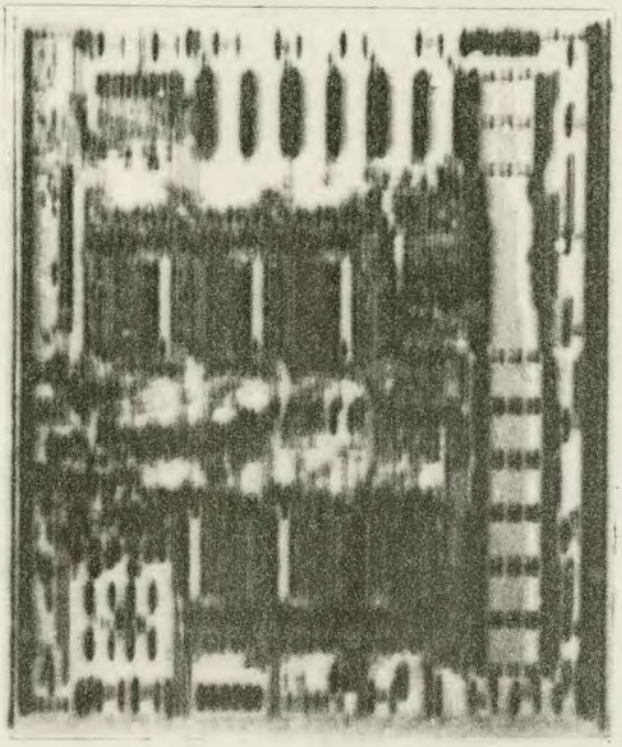

(a)

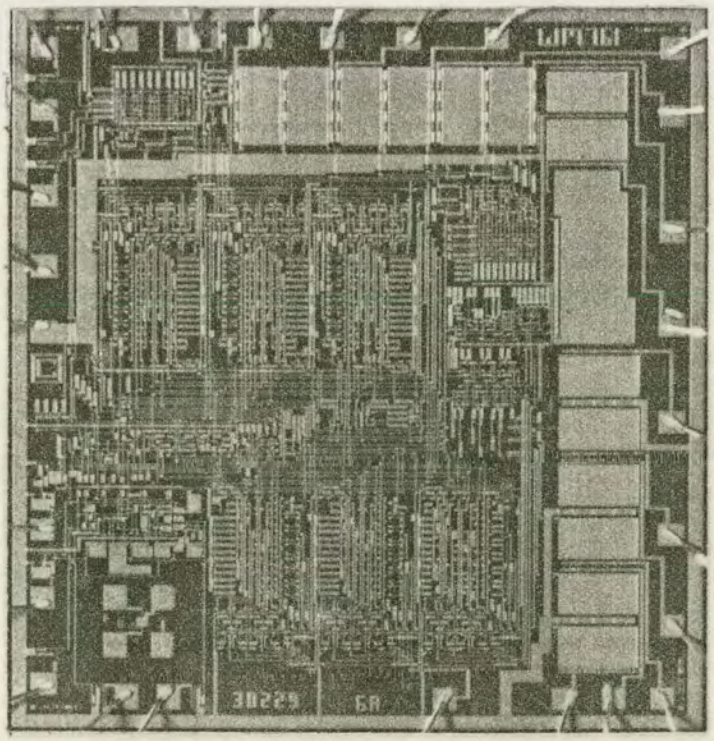

(b)

FIGURE 1.2(a): X-ray topograph of MOS chip (220 reflection, MoKα radiation)

(b): Photomicrograph of same chip

work involving the measurement of the induced radius of curvature of the silicon by X-ray methods has been carried out by Schwuttke and Howard[13], and Brotherton et al[14]. Blech and Meieran[15] measured oxide induced strain by the technique of measuring the intensity contrast of an X-ray topograph image.

Similar experiments have been performed using slices with impurity atoms such as boron or phosphorus diffused or implanted into their surfaces[16-19]. The stresses within a silicon substrate arising from effects other than oxidation or diffusion (eg metal films) have also been measured[20-24].

However, it must be stressed that by using X-ray techniques, the detailed analysis of strain within a crystal becomes extremely complex since the diffraction of X-rays is dependent on the strain itself. Much work has been done with strained crystals, not primarily to study the strain, but in order to study the effect of strain on X-ray diffraction[25-38]. Some of this work will be discussed later in order to interpret the information gained from the measuring technique used in this thesis.

One feature of all the methods discussed so far for analysing strain is that they are all indirect methods, and that up until now those using X-rays are dependent on the X-ray wavelengths used. The technique under discussion in this thesis is essentially one which is used for analysing strain in materials, by the superposition of ruled gratings, namely moiré fringe analysis[39,40]. (Of course, the strains associated with silicon processing are several orders of magnitude smaller than those analysed with the classical ruled grating). The 'ruled grating' in this application is the silicon lattice itself.

Hence the strain analysis will be seen to be directly dependent on the strained lattice, and it is this feature combined with a sensitivity an order of magnitude greater than achieved with other techniques which makes this moiré fringe technique so attractive.

By considering the silicon lattice as a 'ruled grating', some idea of the sensitivity may be obtained. The range of moiré fringe spacings which may be observed is between about 2 cms maximum to about 0.2 mm minimum. With an effective lattice spacing of 2×10^{-8} cm, the range of strains ($\Delta\ell/\ell$) which are measurable is between 10^{-8} to 10^{-6}! This is much more sensitive than a direct topographic method, such as used by Blech and Meieran[15]. In their experiment only the high strain regions close to the oxide edge could be measured.

The instrument by which moiré fringes may be obtained is the X-ray interferometer. The first interferometer was constructed by Bonse and Hart in 1965[41] and has been developed by them and other workers since[42-76]. However, it has been used mostly as a tool for X-ray diffraction analysis rather than for strain measurements. Considerable interest has been shown in recent years in using the interferometer for direct measurement of lattice parameter without resorting to measuring it in terms of the X-ray wavelength, which has been the only possible way up until now[50-52, 56-59].

Although in this thesis interest is centred on X-ray interferometry, some experiments are performed using a double crystal spectrometer. This is also a very sensitive instrument but measurements made with it do not yield 'direct' measurements of strain as is the case with the interferometer. The experiments made with the instrument are therefore either to reinforce the interferometric measurements or to be

complementary to them.

The basic aim of this thesis is to measure the strain associated with oxidation and diffusion of silicon with this new technique and to compare the results with those already published. It is also proposed to investigate the feasibility of using diffused or oxidised samples which have had their lattice parameters suitably changed as X-ray monochromators or resonators.

Chapter 2 contains a brief outline of the nature of the oxidation and diffusion of silicon in order that the origin of stress may be properly understood. The dynamical theory of X-ray diffraction is applied to the X-ray interferometer in Chapter 3 and to the double crystal spectrometer in Chapter 4. Chapter 5 describes sample preparation and experimental techniques used. Chapter 6 analyses in detail, by interferometric techniques, dislocations generated during processing. Chapter 7 analyses the strains induced by thermally grown oxides and develops an elasticity model to describe the strain in a thin slice of material induced by any shape of thin film or diffusion in one surface. Observations are made on diffused samples in Chapter 8 and the results obtained in this thesis are discussed in Chapter 9, together with suggestions for further experiments.

One interesting feature of this thesis is the inter-disciplinary nature of the work involved. A good understanding is required of integrated circuit technology, both from the processing and electrical standpoints. Also, the complexities of elasticity theory must be firmly grasped in order to attempt to compare observations with theory and, possibly most important of all, the theory of X-ray diffraction must be studied in depth in order to interpret the results.

CHAPTER 2: THE OXIDATION AND DIFFUSION PROCESSES

2.1 OXIDATION

The oxidation of silicon plays a very important part in the fabrication of integrated circuit devices. There are several quite independent roles which may be played by an oxide layer. In bipolar processes, the oxide may be used to mask off areas of the silicon substrate leaving the remaining areas to be diffused or ion-implanted with the appropriate impurity. The final stage in the process is to cover the entire chip with a pyrolytic oxide in order to protect it, and also to provide electrical passivation. More recently, a further, but fundamental, application lies in its use as the dielectric in field effect transistors which are the basis of the MOS structure. Since the electric field in these regions must be high, the oxide is made as thin as possible. In order to avoid a yield hazard on account of this, the technological development behind this aspect of the process has become very advanced. It is fortuitous that silicon oxide fulfils these functions well, since its growth on the silicon substrate is in principle a very simple task.

There are twenty two phases of silica of which the oxide of silicon, or silica glass is one[77]. Thermally grown silicon oxide, SiO_2, being a glass, is therefore amorphous rather than crystalline. Much research has been undertaken in the analysis of the structure of glass. Some theories, such as those of Zachariasen[78]. regard the structure as consisting of tetrahedra of oxygen atoms surrounding a silicon atom (as in the crystalline quartz) but with the

tetrahedra linked together by their vertices in a random fashion (Fig 2.1(b)). Other theories[79] maintain that although there is no long range order, there does exist short range order, even to the extent of the formation of small crystallites of quartz (Fig 2.1(c)).

Since the structure is irregular, the strength of the atomic bonds is not constant. Thus, different energies are required to break them. For this reason there is no sharp melting point as there is with quartz. The irregularity of structure also leads to the existence of 'holes' within the structure and to unbound oxygen atoms which are free to become attached to impurities. Thus many types of extrinsic glass exist, resulting from impurities such as boron, aluminium, phosphorus and lead, and the physical properties associated with each can be very different. Table 2.1 shows, for example, the coefficients of thermal expansion for a selection of these glasses. This is an important parameter as will be seen later when assessing the stress induced in the silicon by an oxide. In this instance, however, only oxides free from such impurities will be considered.

TABLE 2.1[80]

Corning Code No	Type of Glass	Thermal Expansion Coefficient ($X10^{-7}/^{o}C$) (0 - $300^{o}C$)
7940	Fused silica	5.6
7900	96% silica	8
7740	Heat resistant borosilicate	32.5
7070	Low loss borosilicate	32
1720	Aluminosilicate	42
0080	Soda lime	92
0010	Lead	91
	Silicon	38

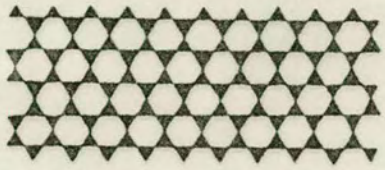

(a)

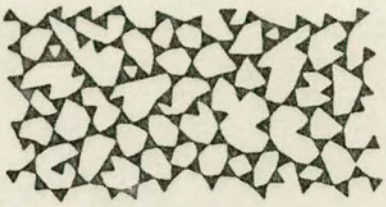

(b)

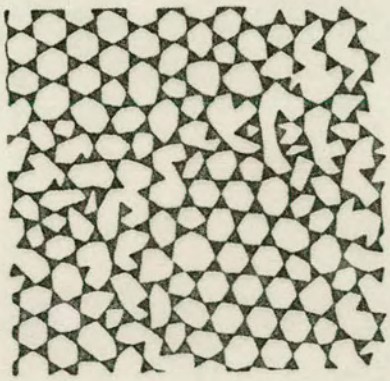

(c)

FIGURE 2.1: Two dimensional schematics of - (a) silicon crystal network, (b) silica glass network as described by Zachariasen[78] and (c) silica glass viewed as a polymer-crystalline network[79]

2.1.1 Oxide Formation

Before oxidation, the silicon substrate must be carefully prepared and cleaned by chemical or mechanical polishing. The actual oxidation process may be performed in several ways. Thermal oxidation, which is the standard method for most of the oxides grown in the IC process, involves passing oxygen or steam over the silicon in a furnace. This is the type of oxidation which will be treated in detail here. Anodic oxides are grown by applying an electric field to induce the transport of mobile ions. Oxides may also be formed by vapour deposition or sputtering techniques.

The arrangement used for steam oxidation is shown in Fig 2.2. High purity water is boiled, and the steam passed to the furnace which is heated to typically 1050^{o}C. Initially, a very thin oxide is formed on the silicon surface due to chemisorption of water until an effective barrier is set up between the oxide-silicon interface and the steam. Oxidation now proceeds by two methods. Water molecules effectively diffuse through the oxide until it becomes positioned interstitially between two silicon atoms. The following reaction now takes place.

$$H_2O + Si\text{-}Si \rightarrow Si\text{-}O\text{-}Si + H_2 \qquad (2.1)$$

Alternatively a reaction takes place at the oxide-vapour interface to produce silanol,

$$H_2O + Si\text{-}O\text{-}Si \rightarrow 2\ (Si\text{-}OH) \qquad (2.2)$$

The silanol now diffuses through the oxide until it reaches the silicon interface to build up the oxide once again,

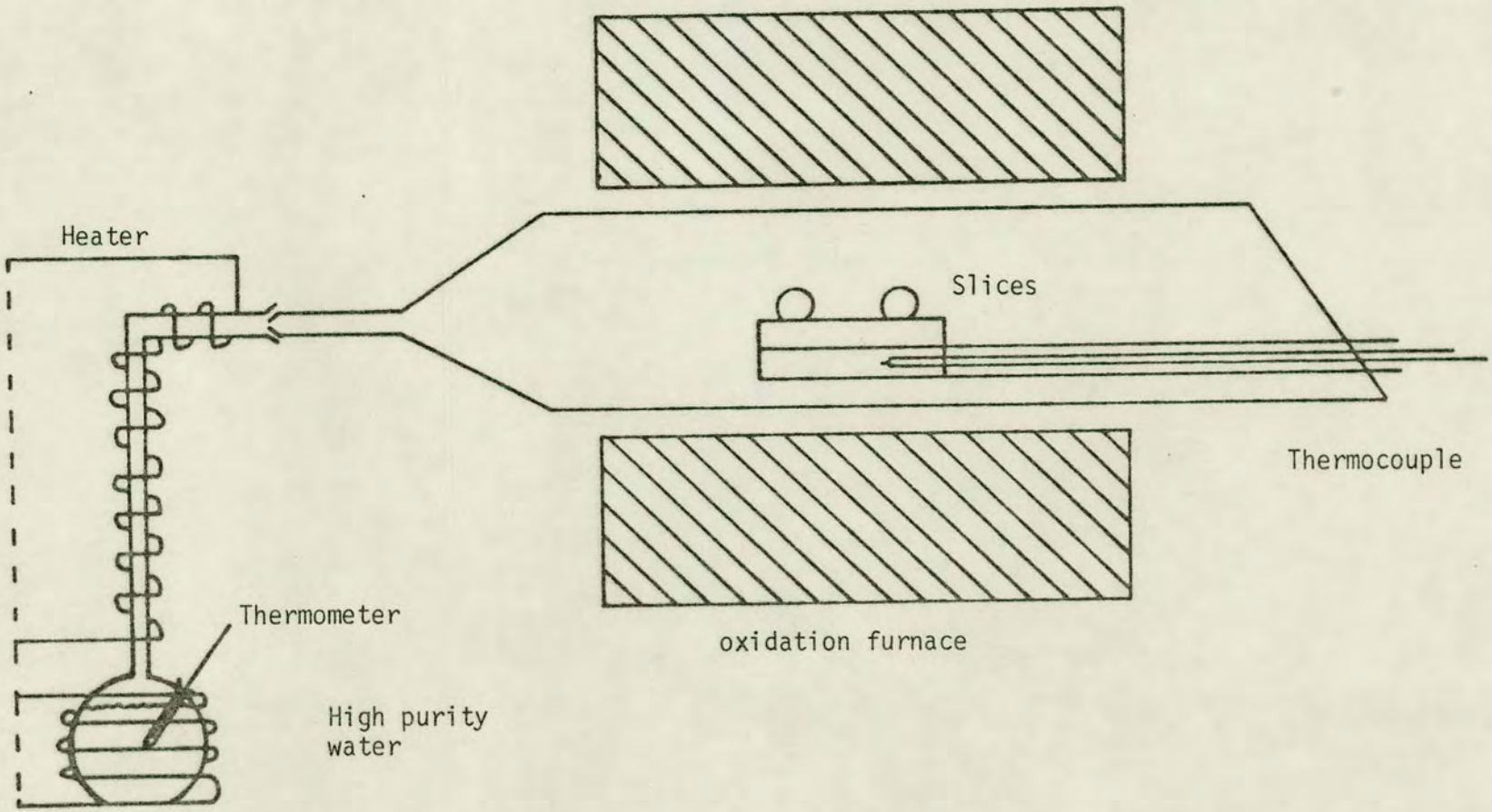

FIGURE 2.2: Open-tube steam oxidation apparatus

$$2(Si\text{-}OH) + Si\text{-}Si \rightarrow 2(Si\text{-}O\text{-}Si) + H_2 \qquad (2.3)$$

In both reactions, the hydrogen diffuses rapidly away as may be seen from the diffusion coefficients at 1050°C given in Table 2.2. However, it is possible for the hydrogen to form hydroxyl groups after reacting with other silica groups.

TABLE 2.2[80]

Diffuser	Diffusion Coefficient at 1050°C (cm^2/sec)
O_2	2.82×10^{-14}
H_2O	9.5×10^{-10}
H_2	2.2×10^{-6}

At high temperatures when the oxidation reaction is very fast, the factor limiting the speed of growth is the availability of water molecules or silanol groups at the silicon-oxide interface, and so the growth rate follows the parabolic rule,

$$x = \sqrt{ct} \qquad (2.4)$$

where x is the oxide thickness, t the oxidation time and c a constant.

When the limiting factor is not the availability of oxygen, but the speed of oxide formation as may be found at lower temperatures before the oxide has become too thick to start limiting diffusion, the growth rate becomes linear. The speed of reaction is also a function of the availability of bonds as well as temperature, so that at low temperatures the orientation of the silicon has

a significant effect. Fig 2.3 shows a graph of typical growth rates for different furnace temperatures.

Steam oxidation of silicon is therefore a relatively fast process. If a thin oxide is required with some control over its thickness, it is desirable to slow down the process. This may be conveniently done by dry oxygen oxidation. Pure oxygen is now passed through a dryer and a filter to the furnace. This is illustrated in Fig 2.4. From Table 2.2, it will be seen that the diffusion coefficient for an oxygen molecule is much smaller than that for a water molecule resulting in a slower oxidation.

Wet oxygen oxidation is probably the most common technique used. It effectively combines steam oxidation with dry oxygen oxidation by passing pure oxygen through a water bath. The temperature of the water bath may be controlled such that at room temperature, the gas present in the tube is almost entirely oxygen with only a small trace of water vapour. As the temperature is raised, the water vapour content increases until at boiling point the oxidation is effectively steam oxidation. For controlling the thickness of very thin oxides an inert gas is passed through the water bath so that only a very small amount of water vapour enters the tube.

After oxidation, photoresist methods are used to define areas to remain as oxide. The remaining oxide is etched in hydrofluoric acid which is capable of breaking the loose bonds in the amorphous material but not the stronger crystalline structure of the silicon substrate.In this way, islands of oxide remain.

If the oxide is removed from only one side of a silicon slice, then quite a pronounced warpage results. The strain in the silicon

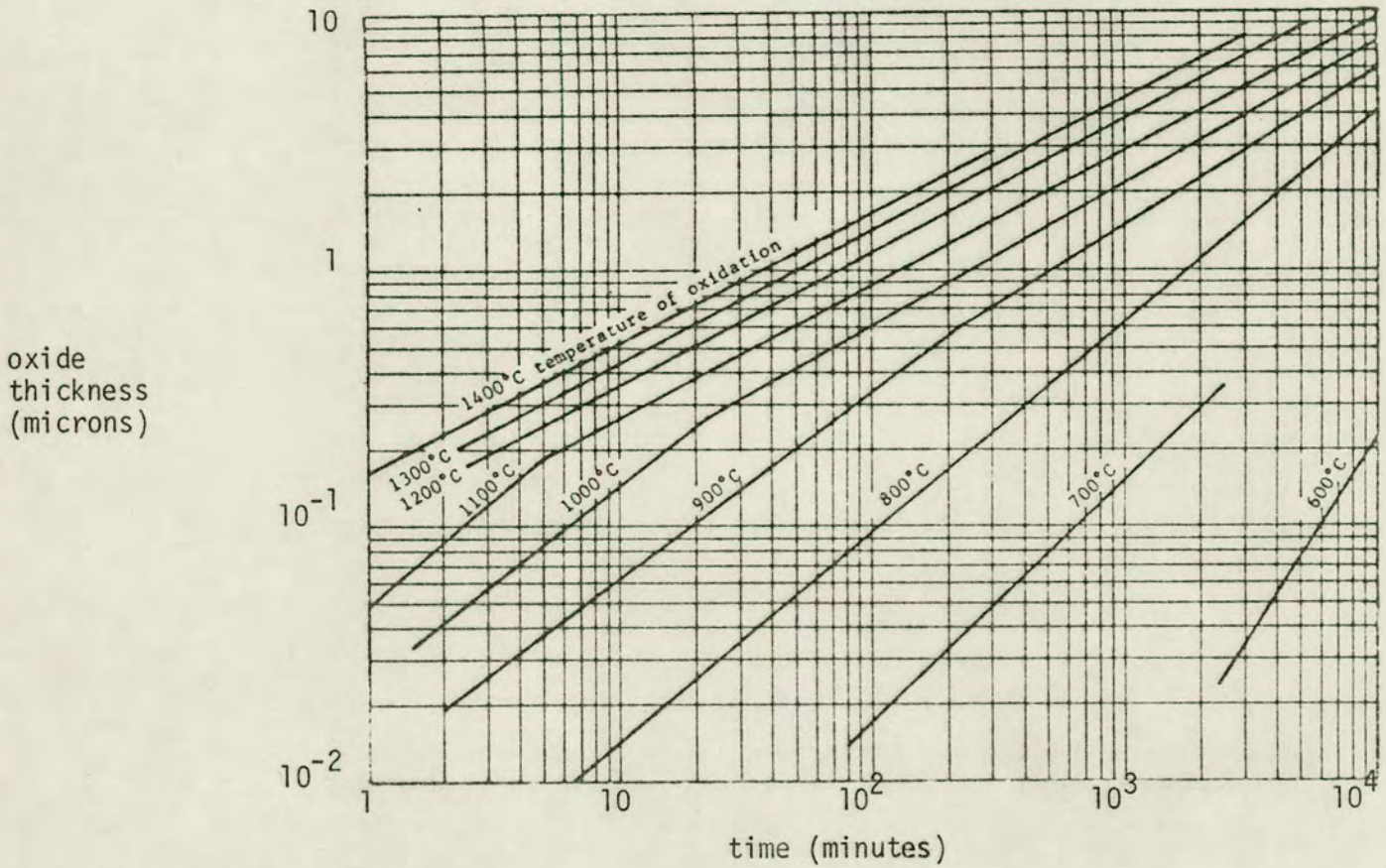

FIGURE 2.3: Oxide growth in atmospheric steam

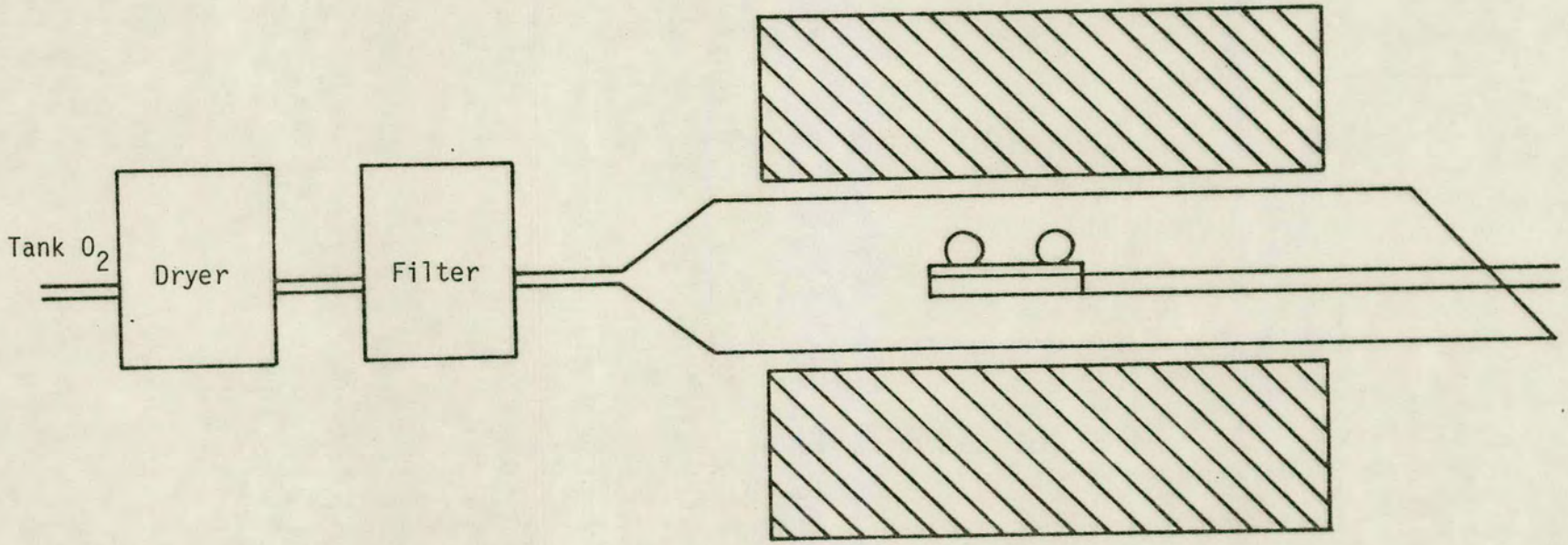

FIGURE 2.4: Open tube oxidation in dry oxygen

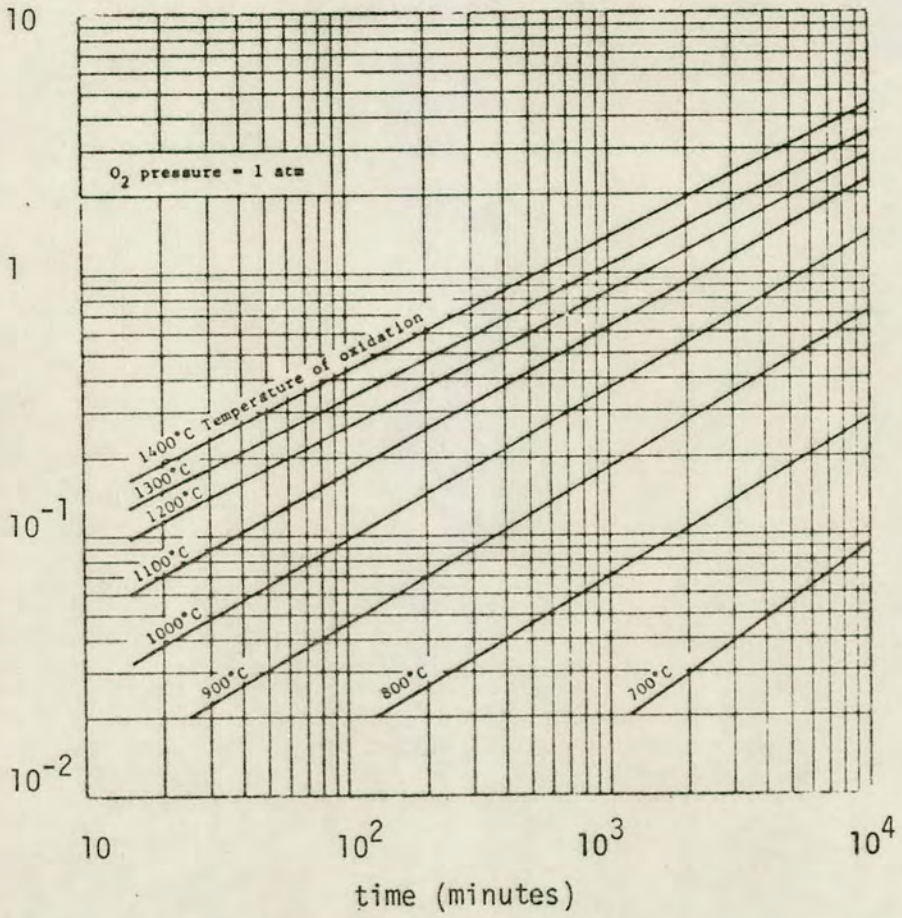

FIGURE 2.5: Oxide growth in dry oxygen

can be shown to be purely elastic with no plastic deformation by removing the remaining oxide, when the slice becomes perfectly flat again. This effect is entirely due to the discrepancy in the thermal coefficients of silicon and its oxide as will be seen in Table 2.1. As the silicon wafer cools, so conflict results between the two layers. It would be expected therefore that the warpage would be a direct function of the oxidation temperature. It will be seen at once by studying the coefficients of thermal expansion that the silicon contracts more than the oxide so that at room temperature the silicon underneath an oxide is in tension and the oxide and silicon surrounding the oxide in compression. A full analysis of these phenomena will be given in Chapter 7.

2.2 DIFFUSION

The diffusion process is an essential part of the fabrication of integrated circuits by which many electrical characteristics may be realised such as conducting paths, junction diodes and channel stops with suitable choice of p or n type dopants. However, a high degree of control is required in order to achieve desired junction depths to a small fraction of a micron and surface concentration to close tolerances. It is from a knowledge of diffusion constants and surface impurity concentration, together with precision of time and temperature control, that these requirements may be met.

The observed diffusion results compare favourably in general with those predicted by theory except in the case of shallow diffusions or high surface concentrations (greater than about 10^{19} atoms/cm^3). Reasons for deviations under these conditions are

understood qualitatively to be due to factors such as a dependence of the diffusion constant on impurity concentration and structural imperfections. Other causes of error are due to interactions taking place between impurity atoms and the fact that boundary conditions applying to the theory may not apply rigourously in practice. These causes of error, rather than being understood quantitatively, tend to be treated empirically. Even when quantitative analysis is undertaken - for functions such as the temperature dependence of the diffusion coefficient on temperature - the results tend to be applicable only to the experimental environment under which they were measured and are far removed from the real life world of the diffusion furnace.

The technology of diffusion as applied to silicon integrated circuits is centred on the open-tube diffusion method. Initially, solid sources (such as P_2O_5 and B_2O_3 for phosphorus and boron diffusion) were used until it was found that better reproducibility could be achieved with liquid and gaseous sources. Of course, the best controllability of impurities (of both concentration and profile) may be realised with ion-implantation, thus rendering standard diffusion techniques obsolete for a majority of uses.

2.2.1 Introduction to Diffusion Theory

It is interesting to note that the theory of diffusion was developed long before the advent of semiconductor device technology, so that only recently has the theory been tested experimentally. Fortunately, many simplifications may be made in the theory when applied to integrated circuitry. For example, the single crystal

nature of the solid in which diffusion takes place allows the effects of grain boundaries to be ignored. Also, since the ratio of concentrations of impurity atoms to silicon atoms is very small, dimensional changes may be ignored. Finally, the planar nature of the devices results in a considerable simplification in the mathematics.

The process of diffusion is concerned with the movement of atoms within a crystal lattice. The primary concern, required here, is limited to the movement of impurity atoms which are introduced on the crystal surface in order to alter the electrical properties of the substrate. This movement of atoms takes the form of random jumps in all three dimensions, their net flow being the statistical average over a period of time. Although there are many mechanisms by which diffusion takes place, only the two primary ones - interstitial and substitutional diffusion - need be considered here.

Interstitial diffusion is that in which atoms jump from one interstitial site to the next (Fig 2.6(a)). Substitutional diffusion, on the other hand,occurs when impurity atoms move between lattice sites of the host material (Fig 2.6(b)). However, it is necessary for an adjacent site to be vacant. In other words, vacancies must exist for substitutional diffusion to take place. These vacancies are provided by thermal fluctuations within the lattice. Since the concentration of vacancies tends to be quite low, the rate of substitutional diffusion is much slower than that for interstitial diffusion.

In general, diffusion through a crystal is anisotropic and the diffusion coefficient D_{ij} is a second order tensor[81],

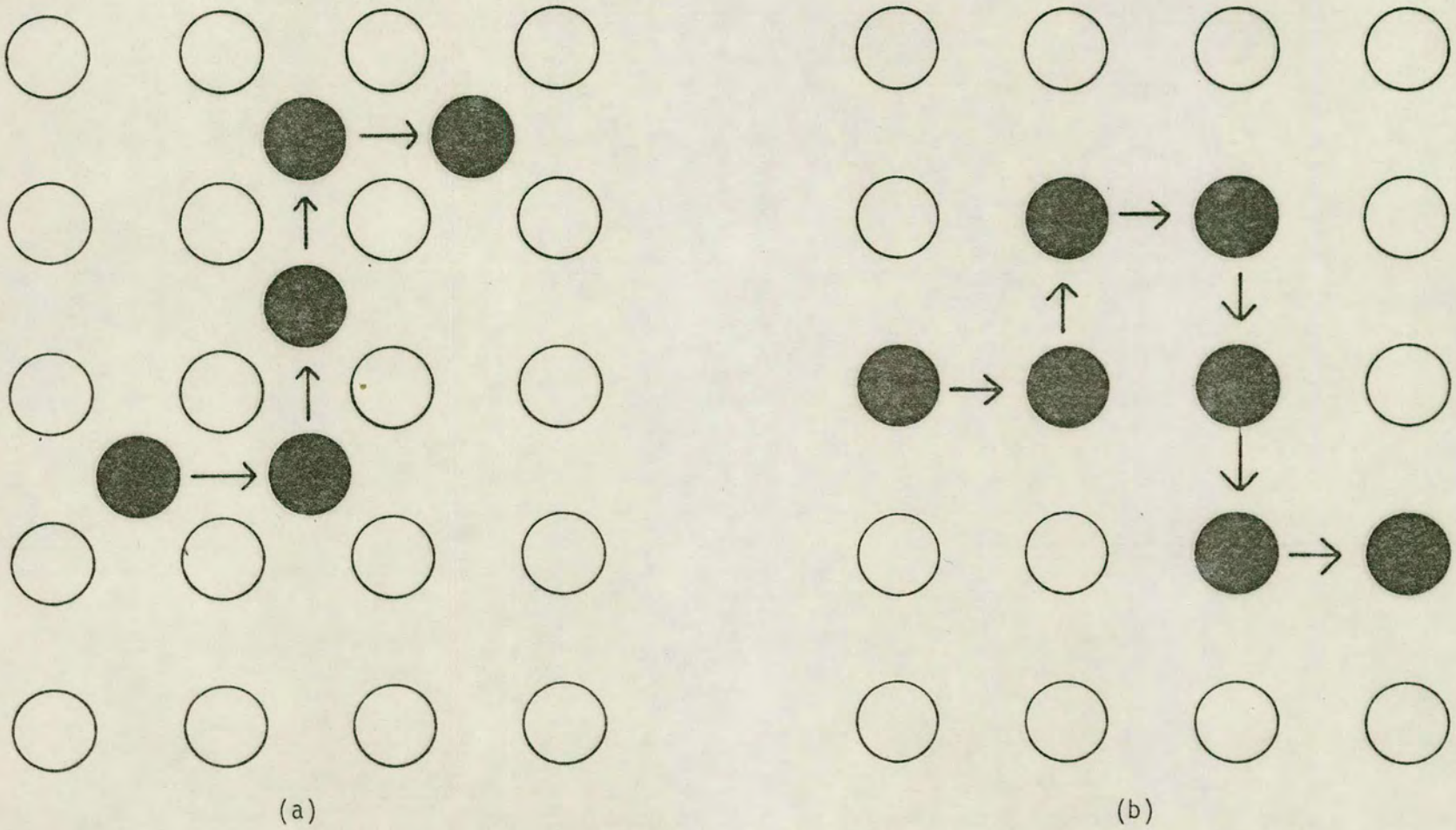

FIGURE 2.6: Interstitial Diffusion (a) and Substitutional Diffusion (b)

$$J_i = \sum_j D_{ij} \frac{\partial C}{\partial x^j} \qquad (2.5)$$

where J_i is the flux density of impurity atoms, C the concentration of diffusing atoms. However, it can be shown[80] that for a cubic lattice, the diffusion is isotropic. Since diffusion takes place from a planar boundary, the diffusion is essentially one dimensional (ie depth into the crystal). Equation 2.5 may therefore be considerably simplified,

$$J = -D \frac{\partial C}{\partial x} \qquad (2.6)$$

This is the fundamental law of diffusion and is known as Fick's Law. The negative sign in Equation 2.6 indicates that the diffusion occurs in the direction of decreasing concentration.

The change in dopant concentration as a function of time can be given by the equation,

$$\frac{\partial C}{\partial t} = \frac{dJ}{dx} \qquad (2.7)$$

If the diffusion coefficient D is not a function of dopant concentration, then it will be constant for all x, ie $\partial D/\partial x = 0$ so that by comining Equations 2.6 and 2.7,

$$\frac{\partial C}{\partial t} = D\frac{\partial^2 C}{\partial x^2} \qquad (2.8)$$

This is Fick's second law of diffusion and by application of boundary

conditions is fundamental to the study of the diffusion process. Since typical diffusion depths are of the order of microns and slice thicknesses are of the order of hundreds of microns, the silicon is assumed to be a semi-infinite solid with diffusion taking place from one surface (x = 0).

2.2.2 Diffusion from a Constant Surface Concentration

The boundary conditions for a fixed concentration C_S at the surface x = 0 are,

$$C_{x>0,\ t=0} = 0.$$

$$C_{x=0,\ t \geq 0} = C_S \tag{2.9}$$

Solving Equation 2.6 with these boundary conditions gives

$$C(x,t) = C_S \operatorname{erfc} \frac{x}{2\sqrt{Dt}} \tag{2.10}$$

If there exists a non-diffusing bulk impurity of opposite type (p or n), then

$$C(x,t) = C_S \operatorname{erfc} \frac{x}{2\sqrt{Dt}} - C_B \tag{2.11}$$

The junction depth is defined as that point where the effective impurity concentration is zero and so may be calculated from Equation 2.6, ie

$$x_j = 2\sqrt{Dt}\ \operatorname{erfc}^{-1} \left(\frac{C_B}{C_S}\right) \tag{2.12}$$

Fig 2.7 shows typical impurity concentrations calculated from Equation 2.9 as functions of depth (x) and time (t).

The rate of impurity flow through the surface (x = 0) is given by

$$J(t) = -D\frac{\partial C}{\partial x}\Big|_{x=0} = \frac{DC_S}{\sqrt{\pi Dt}} \exp\left(\frac{-x}{2\sqrt{Dt}}\right)^2\Big|_{x=0} \qquad (2.13)$$

so that the total amount of material to have entered the solid after time t may be calculated to be

$$Q = \int_0^t J(t)dt = 2C_S\sqrt{Dt/\pi} \qquad (2.14)$$

Experiments involving the diffusion of boron into silicon have been undertaken by many workers[82-87] in order to measure its diffusion coefficient and associated activation energy. Table 2.3 shows some of these results for D_o and E in the equation

$$D = D_o \exp\left(\frac{-E}{KT}\right) \text{ cm}^2/\text{sec} \qquad (2.15)$$

TABLE 2.3

Date	Worker	D_o	E	D at 1100°C
1954	Dunlop et al[82]	~7.0	3.5	$\sim 10\times10^{-13}$
1956	Fuller and Ditzenberger[83]	.001	2.52	$\sim 6\times10^{-13}$
1956	Fuller and Ditzenberger[83]	10.5	3.69	3.0×10^{-13}
1960	Yamaguchi et al[84]	17.1	3.68	5.3×10^{-13}
1960	Kurtz and Yee[85]	2.5	3.51	3.3×10^{-13}
1961	Williams[86]	16.0	3.69	4.6×10^{-13}
1972	Ghoshtagore[87]	2.46	3.59	1.6×10^{-13}

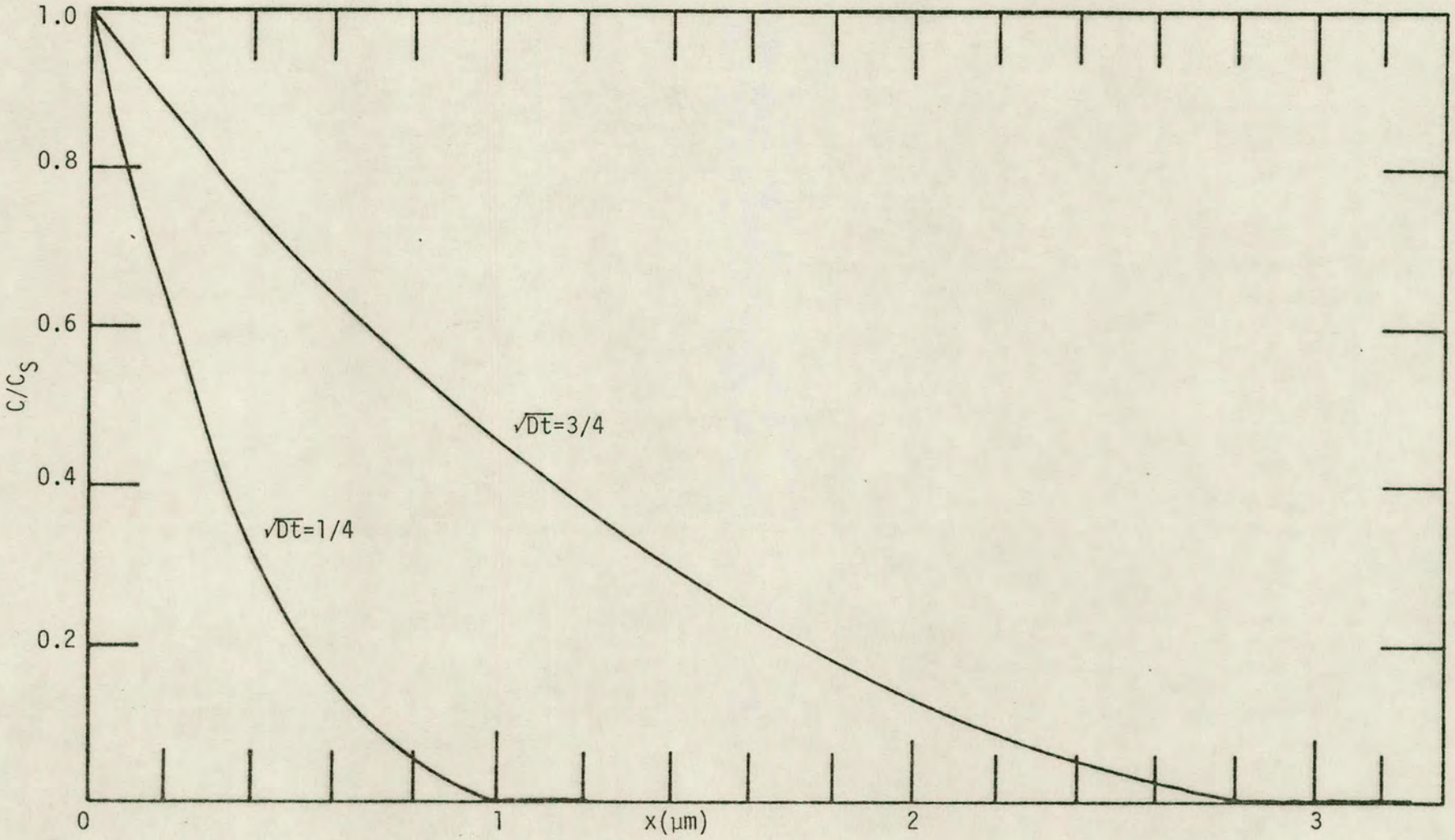

FIGURE 2.7: Diffusion from a constant surface concentration

It will at once be apparent that the diffusion coefficient, when experimentally determined as in Table 2.3, has a wide range of experimental variation associated with it. Fig 2.8 shows a typical graph of diffusion coefficient vs temperature (Kurtz and Yee[85]).

2.2.3 Diffusion Techniques

The most common form of diffusion furnace is that which employs an open ended tube. The impurity source may be either a solid, liquid or a gas, the liquid and the gaseous sources providing the better controllability and reliability. For the experiments described in Chapter 8, the diffusion was carried out using a liquid source and this is the diffusion technique to be described here.

Boron tribromide ($B\ Br_3$) is the liquid source used in this case. Since the liquid is maintained at room temperature, only one furnace zone is required. A typical apparatus is illustrated in Fig 2.9. A large flow (2 litres/min) of inert gas such as nitrogen flows down the tube and when diffusion is required to take place another flow of nitrogen (~30 cc/min) passes over the source in order to transport impurity atoms into the furnace tube.

A major advantage of this system is that the silicon slice may be loaded into the furnace tube and allowed to reach thermal equilibrium before the impurity is admitted to the tube.

The process of diffusion is now performed by growing a Boron glass B_2O_3 from the $B\ Br_3$ on the silicon to act as a local impurity source. This is achieved by introducing oxygen gas as shown in Fig 2.9 at a rate of about 200 cc/min. Diffusion without the oxygen

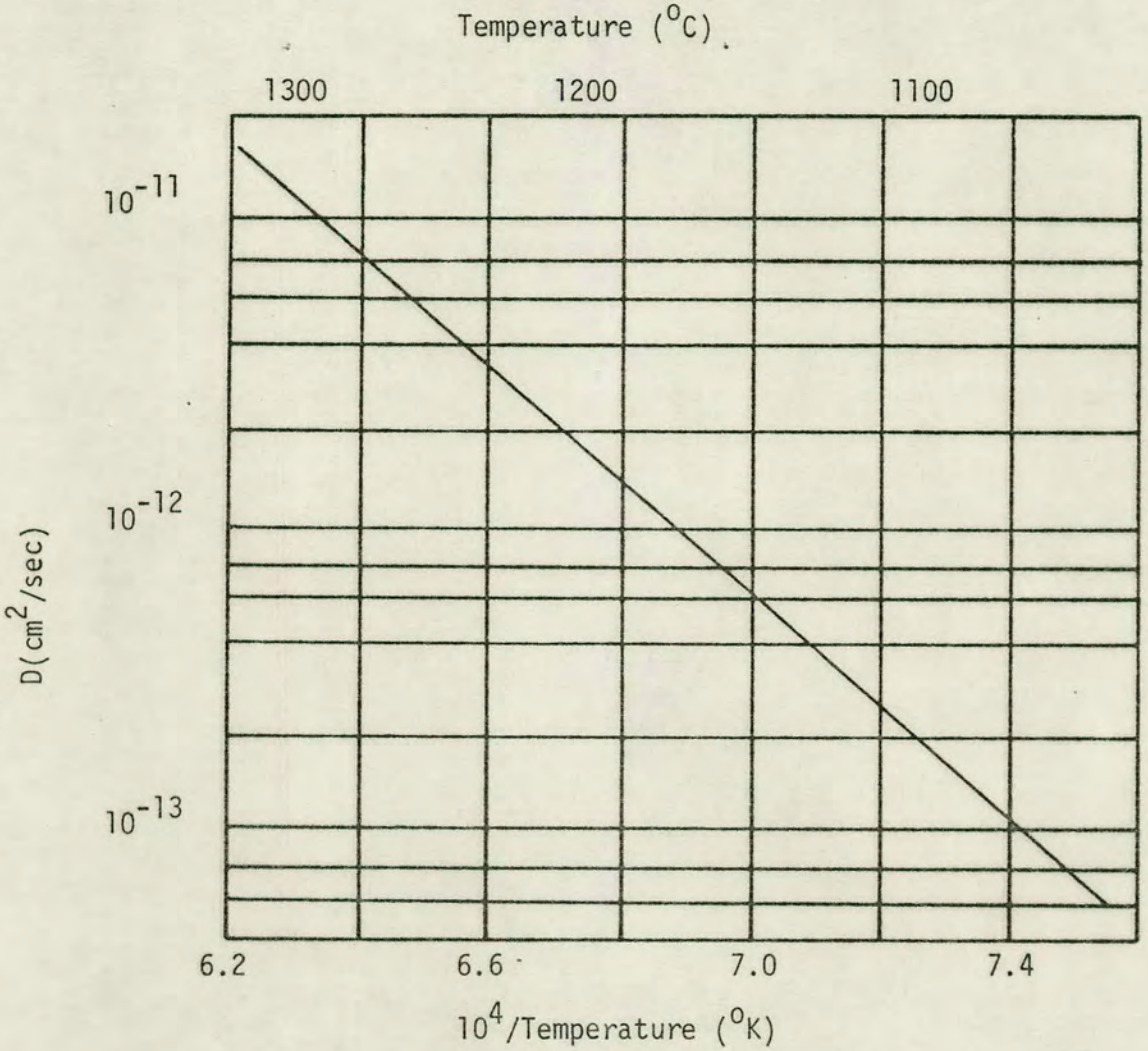

FIGURE 2.8: Diffusion coefficient of boron in silicon

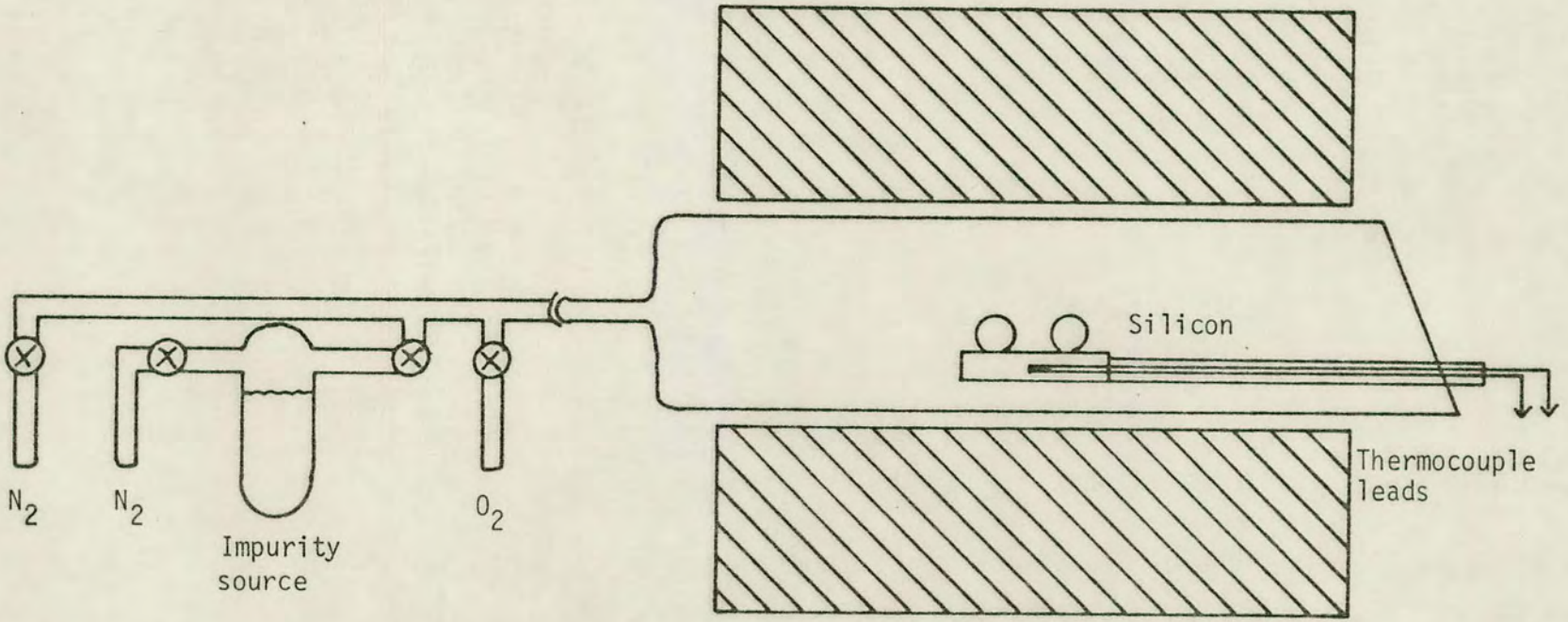

FIGURE 2.9: Open-tube diffusion arrangement employing a liquid source

may result in insoluble black deposits on the silicon surface. This oxidation has the advantage that the underlying silicon surface becomes protected from evaporation or chemical reaction. Also, it is found that the oxide layer facilitates the production of a diffused layer that is uniform and reproducible as well as showing little surface damage or pitting. Oxides so formed may be easily removed by etching in hydrofluoric acid.

Methyl borate (a mixture of methyl alcohol with boric acid) may also be used as a liquid diffusion source. In this case, however, the carrier gas (N_2) is actually bubbled through the liquid before passing into the diffusion furnace. A result of this is that the surface concentration tends to be the maximum possible (the solid solubility which is ~5 x 10^{20} cm^{-3} for boron in silicon).

In general, the surface concentration of impurity may be controlled by adjusting the nitrogen flow rate or the furnace temperature. It is found that better control may be achieved by leaving the nitrogen flow fixed and adjusting the temperature.

CHAPTER 3: INTERFEROMETER THEORY

It is only in the last ten to fifteen years that X-ray interferometry has established itself in the repertoire of techniques available for crystal analysis. This may seem surprising since interferometry has been used extensively in optics, and X-ray theory has been worked out in detail for many years. However, the reason becomes apparent when it is realised that the refractive index for X-rays is close to unity by an amount of the order of 10^{-5} to 10^{-6}. In other words, standard lens techniques relying on refraction for beam recombination are out of the question (although early work on these lines has been achieved[88]). From X-ray theory of diffraction, however, it is seen that the beam division and recombination (essential in interferometry) may be achieved by diffraction from a crystal lattice, but this leads to another severe problem - the perfection of the crystal lattice. It is only with the advent of solid state electronics and the need for highly perfect single crystals of silicon,quartz and germanium that the concept of an X-ray interferometer becomes realisable. With suitable crystal costing in the region of $1/gm, single crystal interferometers may be made extremely cheaply.

Before considering the use of such an interferometer, it is necessary to review some of the theory relating the propagation of an X-ray wavefield and its interaction with a regular crystalline structure. This theory is the dynamical theory of X-ray diffraction and extensive work has been done developing it[89-98]. A brief outline of the theory, showing how Maxwell's equations are solved in the

periodic dielectric medium of the perfect crystal lattice, is given in Appendix 1. It is shown how the wave vectors with significant intensity within the crystal may be calculated, by finding the intersection of the incoming wave vector and the dispersion surfaces (tiepoints).

The application of the dynamical wave theory which is required here predicts results for the interferometer in the case of both 'thick' and 'thin' wafers (as defined later) and also indicates the constraints on its construction - eg the maximum wafer roughness which may be tolerated.

3.1 APPLICATION OF DYNAMICAL THEORY

The dynamical theory shows how an incoming wave can excite no fewer than eight separate waves within the crystal if both states of polarization are taken into account. Since X-ray interferometry involves the eventual recombination of these waves, the resulting wave pattern can become extremely complex. For an initial analysis of interferometry, it is desirable therefore to simplify matters as far as possible. Fortunately, the dynamical theory shows how this may be done by utilising the phenomenon known as the Borrmann effect associated with 'thick' crystals[97].

The symmetric Laue geometry occurs when the 'Bragg' diffracting planes (with reciprocal lattice vector $\underline{h}$) are normal to the crystal surface. The Bragg condition is met when the incident beam strikes the diffracting planes at such an angle that the difference in wave vectors within the crystal ($\underline{K}_0$ and $\underline{K}_h$ in the forward and diffracted directions respectively) equal the reciprocal lattice vector $\underline{h}$. These

conditions may be expressed as

$$|\underline{K}_o| = |\underline{K}_h| \tag{3.1}$$

and $\underline{K}_h - \underline{K}_o = \underline{h}$

When these conditions are met the absorption in the direction of energy propagation $\underline{S}$ is given by[98]

$$\mu(\underline{S}) = \frac{\mu_o}{\cos\theta}\left(1 \pm c\frac{\chi_h''}{\chi_o''}\right) \tag{3.2}$$

where θ is the 'Bragg' angle, c the polarization factor which has the value 1 or cos 2θ for the σ polarization state ($\underline{E}$ perpendicular to the plane of incidence) and the π polarization state ($\underline{E}$ in the plane of incidence) respectively. χ'' is the imaginary part of the susceptibility χ. The choice of $\pm$ in the expression depends on whether the wave has tie point on branch 1(+) (that nearest to the origin of the reciprocal lattice) or branch 2(-) of the dispersion surface.

Hence it will be seen that $\mu(\underline{S})$ is a minimum for waves associated with tie point on branch 2 of the dispersion surface under conditions of σ polarization. Batterman and Cole[98] calculate values for $\mu(\underline{S})$ for the various branches of the dispersion surface for a 1 mm slab of germanium with reflection of CuKα radiation from 220 planes. Table 3.1 gives these results.

TABLE 3.1[98]

Dispersion Surface	$\mu(S)t$
σ Polarization, branch 1	1.9
π Polarization, branch 2	12.5
σ Polarization, branch 2	63.5
π Polarization, branch 1	74
Normal photoelectric absorption ($\mu_o t$)	38

For any material which may be considered to be thick (ie $\mu_o t > 5$), only waves with tie points on the 2σ dispersion surface need be considered since all others will suffer photoelectric absorption. This is the anomalous transmission or Borrmann effect[97], and only these waves will be considered in the ensuing discussion (Fig 3.1).

3.1.1 The 'Thick' Crystal Case

The two waves generated from the 2σ dispersion surface may be expressed as

$$\underline{\mathcal{D}}_{o2} = D_{o2} \exp 2\pi i \, (\nu\tau - \underline{K}_{o2} \cdot \underline{r}) \qquad (3.3a)$$

$$\underline{\mathcal{D}}_{h2} = D_{h2} \exp 2\pi i \, (\nu\tau - \underline{K}_{h2} \cdot \underline{r}) \qquad (3.3b)$$

The wave amplitudes are connected by (see Appendix, Equation A19),

$$\xi_2 = \frac{D_{h2}}{D_{o2}} \qquad (3.4)$$

and their wavevectors are connected by the Laue equation,

$$\underline{h} = \underline{K}_{h2} - \underline{K}_{o2} \qquad (3.5)$$

The total standing wave field within the crystal therefore becomes

$$|\underline{\mathcal{D}}_2|^2 = |\underline{\mathcal{D}}_{h2} + \underline{\mathcal{D}}_{o2}|^2 \; \alpha[1 + \xi_2^2 + 2\,\xi_2 \cos(2\pi \underline{h}.\underline{r})] \qquad (3.6)$$

Since by convention ξ_2 is negative for branch 2 of the dispersion surface, the electric field is at a minimum when $\underline{h}.\underline{r}$ is an integer or

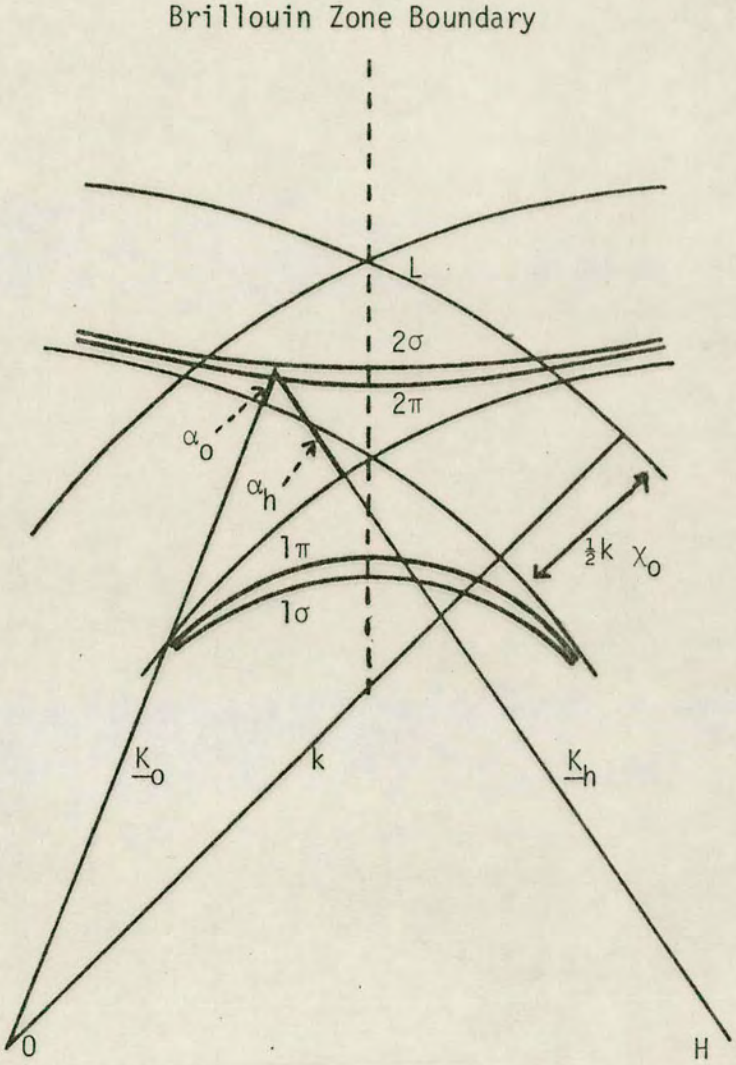

FIGURE 3.1: Locus of tie points (such as A) defining the dispersion sheets

zero. In other words, the field intensity minima occur in the planes of the diffracting atoms. The effect of anomolous absorption may now be given a physical interpretation - there is a minimum of interaction between the electric field and the electrons localised close to the atomic sites (Fig 3.2).

By the same token, the increased absorption of the waves emanating from the branch 1 dispersion surface may be explained from the fact that with ξ positive, the electric field intensity maxima now coincide with the atomic sites. Hence absorption is stronger due to the greater interaction between them.

3.1.2 Laue Case with 'Thin' Crystals

In the case of diffraction involving thin crystals ($\mu t < 1$), the standing wave pattern within the crystal becomes more complex since eight waves make a significant contribution to the exit waves instead of two as found in the 'thick' crystal case. With the crystal 'thin' and weakly absorbing, the crystal waves for each polarization state are

$$\underline{\mathcal{D}}_{h1} = D_{h1} \exp 2\pi i \, (\nu\tau - \underline{K}_{h1} \cdot \underline{r}) \qquad (3.7a)$$

$$\underline{\mathcal{D}}_{o1} = D_{o1} \exp 2\pi i \, (\nu\tau - \underline{K}_{o1} \cdot \underline{r}) \qquad (3.7b)$$

$$\underline{\mathcal{D}}_{h2} = D_{h2} \exp 2\pi i \, (\nu\tau - \underline{K}_{h2} \cdot \underline{r}) \qquad (3.7c)$$

$$\underline{\mathcal{D}}_{o2} = D_{o2} \exp 2\pi i \, (\nu\tau - \underline{K}_{o2} \cdot \underline{r}) \qquad (3.7d)$$

As before, the amplitude ratios between pairs of waves generated from the same dispersion surface are connected by

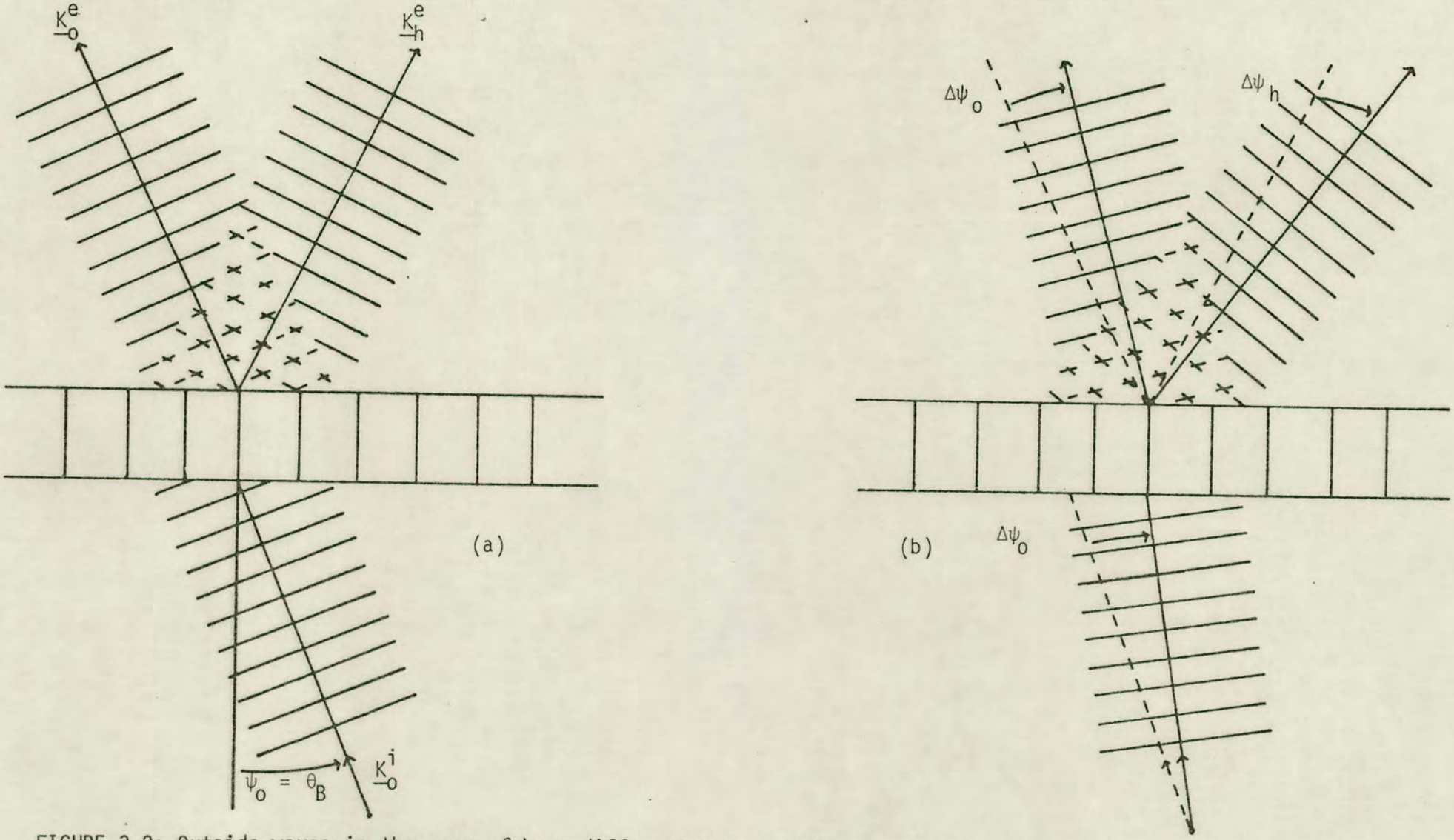

FIGURE 3.2: Outside waves in the case of Laue diffraction by a thick crystal. Note position of standing wave pattern - (a) exact Bragg position; (b) slightly off Bragg position.

$$\xi_2 = D_{h2}/D_{o2} \tag{3.8a}$$

$$\xi_1 = D_{h1}/D_{o1} \tag{3.8b}$$

Also, two Laue equations give

$$\underline{K}_{h1} - \underline{K}_{o1} = \underline{K}_{h2} - \underline{K}_{o2} = \underline{h} \tag{3.9}$$

In addition, it is possible to relate the waves belonging to the two dispersion surfaces by Snell's Law,

$$\underline{K}_{h2} - \underline{K}_{h1} = \underline{K}_{o2} - \underline{K}_{o1} = \Delta^{-1}\,\underline{n} \tag{3.10}$$

where $\underline{n}$ is the unit vector normal to the crystal surface, Δ^{-1} is the distance in reciprocal space between tie points on the branches of the dispersion surface as illustrated in Fig 3.3. The simultaneous solution to these equations can be greatly simplified by restricting the incoming wave to the exact Bragg angle such that $\xi_1 = -\xi_2$. Since the waves are all phase coherent (they are all generated from the same incident beam) the resulting intensity may be written as,

$$|\underline{D}|^2 = |\,\underline{D}_{h1} + \underline{D}_{o1} + \underline{D}_{h2} + \underline{D}_{o2}|^2 \propto 1 + \sin(2\pi\underline{h}.\underline{r})\,\sin(2\pi\Delta^{-1}t) \tag{3.11}$$

If this result is compared with Equation 3.6, some very interesting deductions can be made. The intensity maxima/minima now occur not half way between the atomic planes (a distance d/2 away) but d/4 away (Fig 3.4). This standing wave pattern is now modulated with depth into the crystal by the term $\sin 2\pi\Delta^{-1}t$. This can be thought

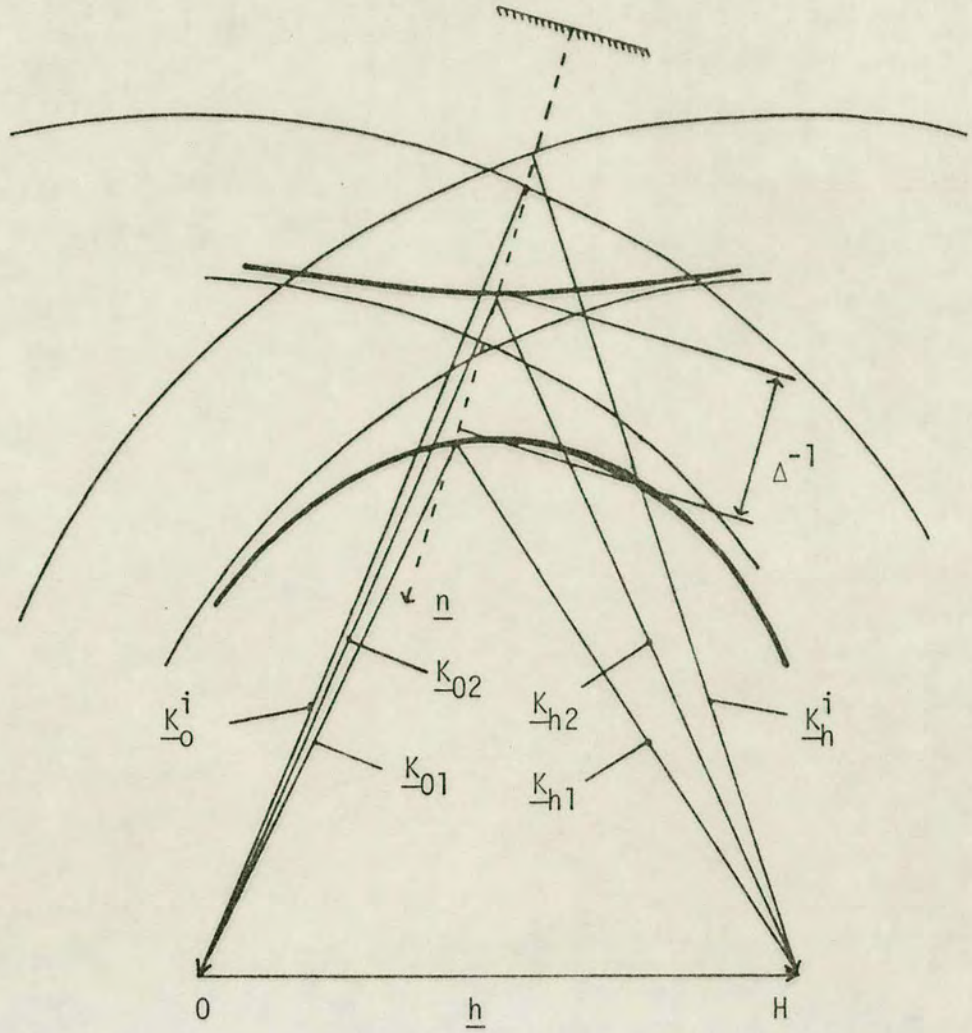

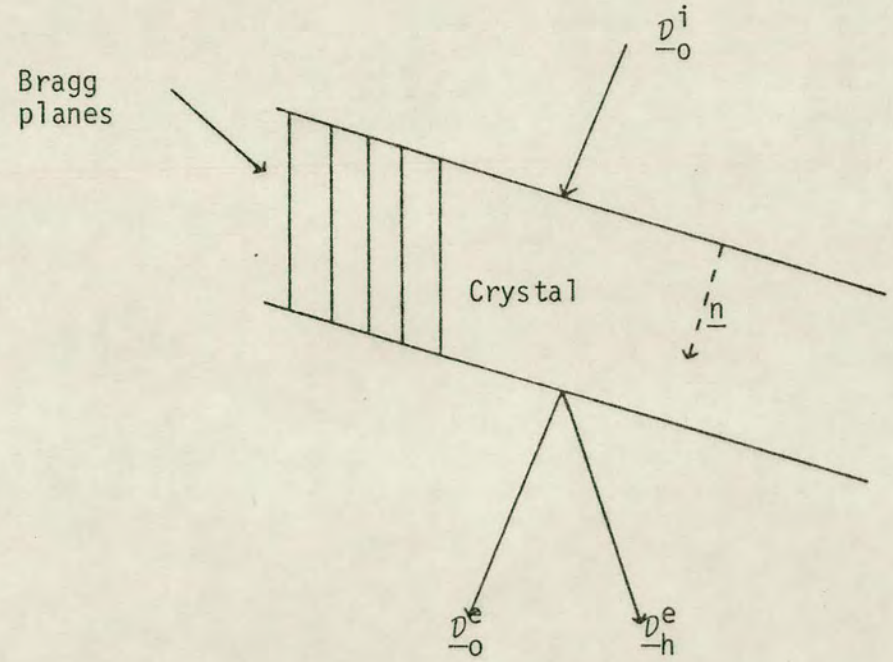

FIGURE 3.3: Geometrical relationships between allowed wavevectors in the Laue case, shown for just one state of polarisation of the incident wave

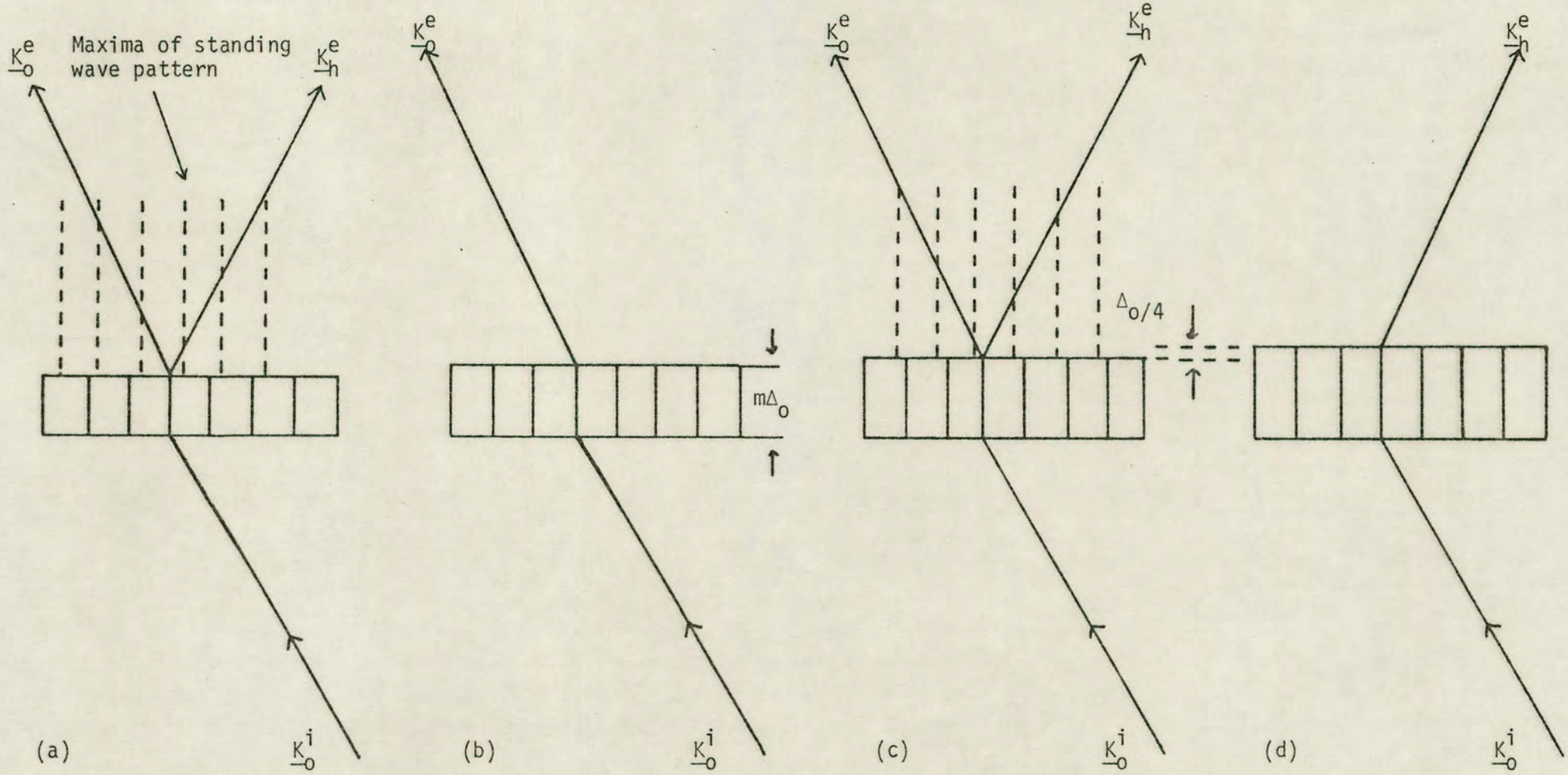

FIGURE 3.4: Outside waves in the case of Laue diffraction by a thin crystal. Crystal thickness varies in steps of the extinction distance Δ. Incidence at exact Bragg angle θ_B. Note the position of standing wave pattern which is different for (a) and (c). m is an integer 0,1,2,3 .....

of as beating taking place between waves generated from the points on the two branches of the dispersion surface. A further modulation may be observed from beating taking place between waves in the two polarization states but this is at a much lower frequency. For $\Delta^{-1}t = p/2$ (p is zero or an integer) the intensity is constant. In other words there does not appear to be an interference pattern set up by the two waves $\underline{K}_o$ and $\underline{K}_h$. This can be explained by considering the intensity functions in each wavefield separately,

$$|\underline{D}_h|^2 = |\underline{D}_{h1} + \underline{D}_{h2}|^2 \propto \sin^2(\pi\Delta^{-1}t) \tag{3.12a}$$

$$|\underline{D}_o|^2 = |\underline{D}_{o1} + \underline{D}_{o2}|^2 \propto \cos^2(\pi\Delta^{-1}t) \tag{3.12b}$$

It can now be seen that for $\Delta^{-1}t = p/2$ the intensity will be totally within one beam or the other, hence the absence of a standing wave pattern.

By applying the necessary boundary conditions for the existing beams, it can be seen that the X-ray intensity will swap back and forth between the forward and diffracted beams with varying crystal thickness (t). This is known as the Pendellösung effect. It should be noted, however, that in general the incoming wave will have spherical and not planar wavefronts since the origin of the X-rays will be a point source at a finite distance from the crystal. This has the effect that the standing wavefield within the crystal is made up of the superposition of plane waves, but with a range of incident angles (the range which is considered to be significant is that subtended by the diameter of the dispersion surface at the origin of the reciprocal lattice - ie ~2"). Hence, Δ will not be a constant and

so the swapping of intensities will not be total[99].

3.2 L-L-L INTERFEROMETER

The construction of an interferometer with three wafers giving Laue-type diffraction is shown in Fig 3.5. Three crystal wafers are required. The first, the beam splitter, generates two coherent waves. The second acts as a mirror to divert the two beams together and the third, the analyser, interprets the resulting standing wave-form. As became apparent in Section 3.1, the standing wavefield at the recombination of the beams is a spatial function of the atomic lattice within the different parts of the interferometer. Obviously, if the standing wavefield is to be periodic over a wide area, then a high degree of matching, both in lattice parameter, rotation and translation as well as lattice perfection is required between all three wafers. The variation in thickness of the wafers (the roughness) must also be controlled, otherwise there will be an associated phase variation resulting in a distorted wavefield. In the case of 'thin' crystals, this roughness will result in intensity variation due to the Pendellösung effect and hence variation in contrast. Bonse and Te Kaat[62] have considered the degree of defocussing as a function of positional stability and phase coherence which may be tolerated for interference still to occur.

Fortunately all these problems can be overcome without too much difficulty. Dislocation free single crystals of silicon are readily available and so an interferometer can be easily made out of a monolithic block with the unwanted crystal regions between the wafers either sawn away or milled out.

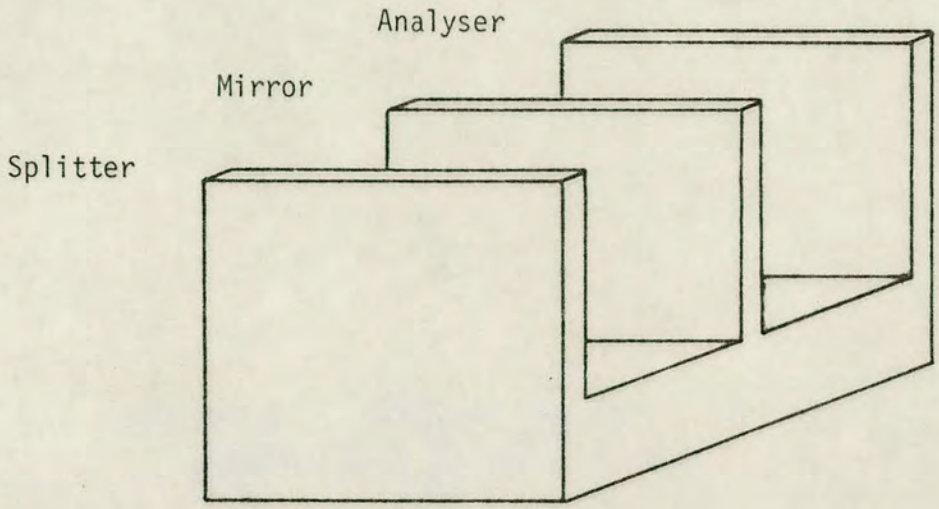

FIGURE 3.5: Definition of interferometer wafers. The splitter wafer is nearest the X-ray source

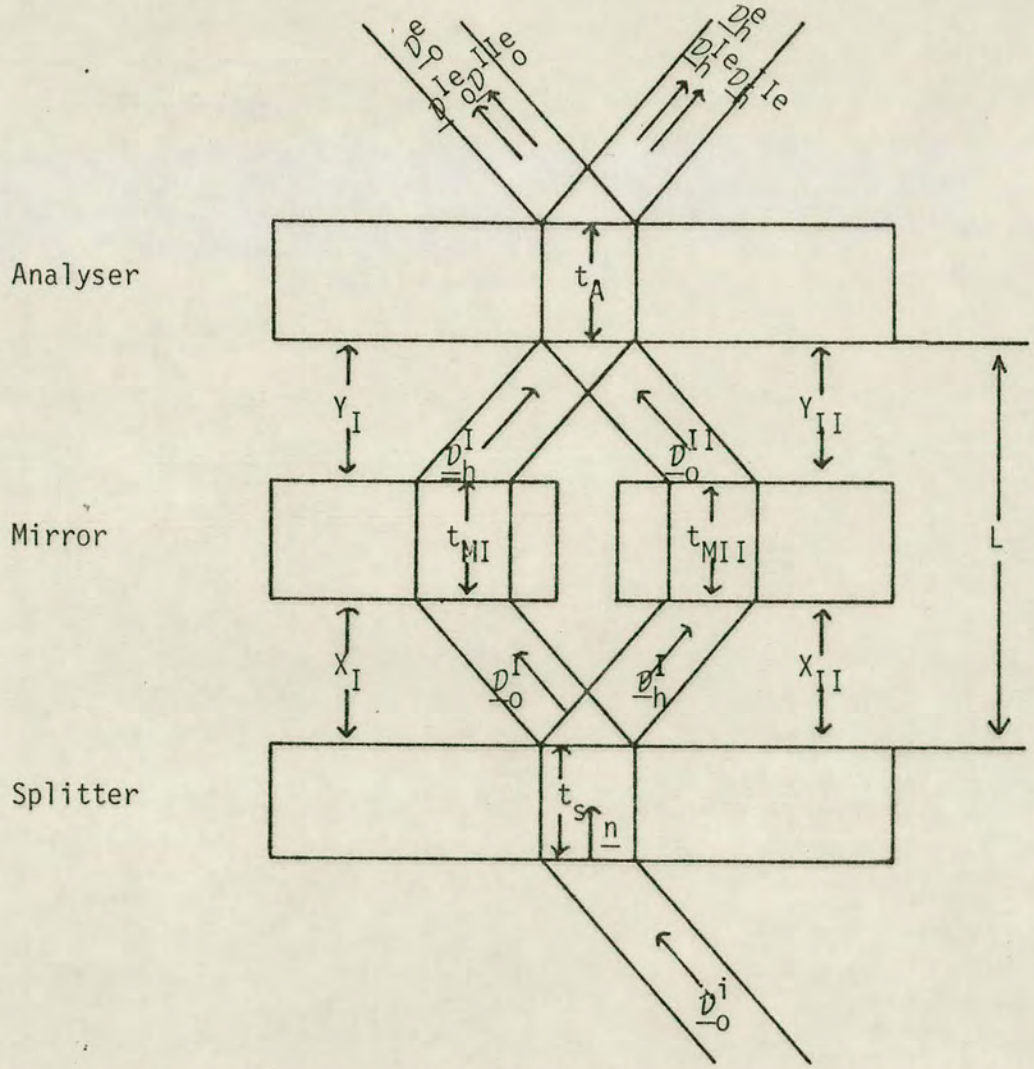

FIGURE 3.6: Arrangement of interferometer wafers with arbitrary separation and thickness

Fig 3.6 shows an interferometer with arbitrary wafer separation and thickness.(In this analysis the wafer separations must not be considered equal since even by accurate cutting they will not be equal on the X-ray scale). At the first entrance surface the wave amplitudes can be matched giving

$$D_o^i = D_{o1} + D_{o2} \tag{3.13a}$$

$$0 = D_{h1} + D_{h2} \tag{3.13b}$$

The waves themselves may be obtained by multiplying the amplitudes by factors of the form $\exp(2\pi i(\nu\tau - \underline{K}.\underline{r}))$.

Since $D_{h1}/D_{o1} = \xi_1$ and $D_{h2}/D_{o2} = \xi_2$, the wave amplitudes within the crystal surface may be expressed by the relations

$$D_{o2} = \xi_1 (\xi_1 - \xi_2)^{-1} D_o^i \tag{3.14a}$$

$$D_{h2} = \xi_1 \xi_2 (\xi_1 - \xi_2)^{-1} D_o^i \tag{3.14b}$$

This process may be repeated for each wafer (Bonse and Hart[43]) to obtain the wave amplitudes at the exit face of the analyser wafer. If the origin is taken to be the entrance surface of the splitter wafer then the phases of the two waves (considering only the weakly absorbed waves - a valid assumption for the 'thick' crystal case) may be calculated by considering the dot product $\underline{r}.\underline{n}$ where $\underline{n}$ is the surface normal vector. At the entrance surface of the analyser wafer,

$$\underline{r}.\underline{n} = t_s + x_I + t_{HI} + y_1 = t_s + x_{II} + t_{MII} + y_{II} \tag{3.15}$$

The amplitude ratio of the two beams combining to give $\underline{D}_o^e$ and

the two giving $\mathcal{L}_h^e$ may be expressed as

$$D_o^{Ie}/D_o^{IIe} = D_h^{Ie}/D_h^{IIe} = \exp\{-2\pi i\, k\, [\delta_2'(y_I - y_{II}) + \delta_2(x_I - y_{II})]\} \tag{3.16}$$

where

$$\delta_2 k = \underline{K}_o^i - \underline{K}_{o2} \tag{3.17a}$$

$$\delta_2' k = \underline{K}_h^i - \underline{K}_{h2} \tag{3.17b}$$

Hence it can be seen at once that the two beams are in phase over the whole interferometer width provided that $y_I = y_{II}$ and $x_I = x_{II}$, and hence from Equation 3.15 $t_{MI} = t_{MII}$. The results of work by Bonse and Te Kaat[62] show that the wafers must be cut accurately to within a few microns if high contrast fringes are to be observed.

It will also be seen from Equation 3.16 that if a π phase shift is introduced into one of the beams, then destructive interference will occur and nothing will be observed in the exit beam.

The wafer roughness can also have a significant effect, since a phase change will be introduced due to the refractive index of the material from which the interferometer is made. For a maximum allowable phase change of, say, $2\pi/10$ to occur, then it is possible to calculate the optical path length necessary to give this phase change. For silicon, this length works out at 4.5 μm for MoKα radiation and 2.1 μm for CuKα radiation. Hence optical smoothness is perfectly acceptable and the required polish may be easily achieved with readily available chemical etches. A point that should be noted is that the roughness is more critical when CuKα radiation

is used rather than MoKα.

It can now be seen that if perfect mirrors are assumed, then the standing wave pattern at the exit face of the splitter is transferred to the entrance face of the analyser crystal. Any lattice variation or rotation in the splitter will be present in this wavefield. These standing wavefields are represented in Fig 3.7. The interaction between the standing wavefield and the analyser crystal is now an exact optical equivalent of the superposition of two sets of finely ruled gratings to give moiré fringes. For example, in the case of a 'thick' crystal interferometer, when the intensity maxima of the standing wavefield are positioned midway between the diffracting planes of the analyser crystal, an X-ray beam will be transmitted, but when the maxima occur on the atomic planes, the analyser crystal will see this as a beam generated from branch 1 of the dispersion surface. High attenuation will take place so that no intensity will be present at the exit surface. Lattice mismatches in any part of the crystal (splitter, mirror or analyser) will therefore show up as moiré contrast.

The mechanism of interference in the 'thin' crystal case, however, is completely different. Whereas in the 'thick' crystal case no intensity is observed in the exit beam when the electric field maxima coincide with the atomic sites due to absorption,so in the 'thin' crystal case it is the relative position of the electric field maxima and atomic sites which determines the ratio of intensities in forward and diffracted directions due to the Pendellösung effect. Ie zero intensity in the 'thin' crystal case is a result of all the energy being diverted out of the observed beam rather than being due to

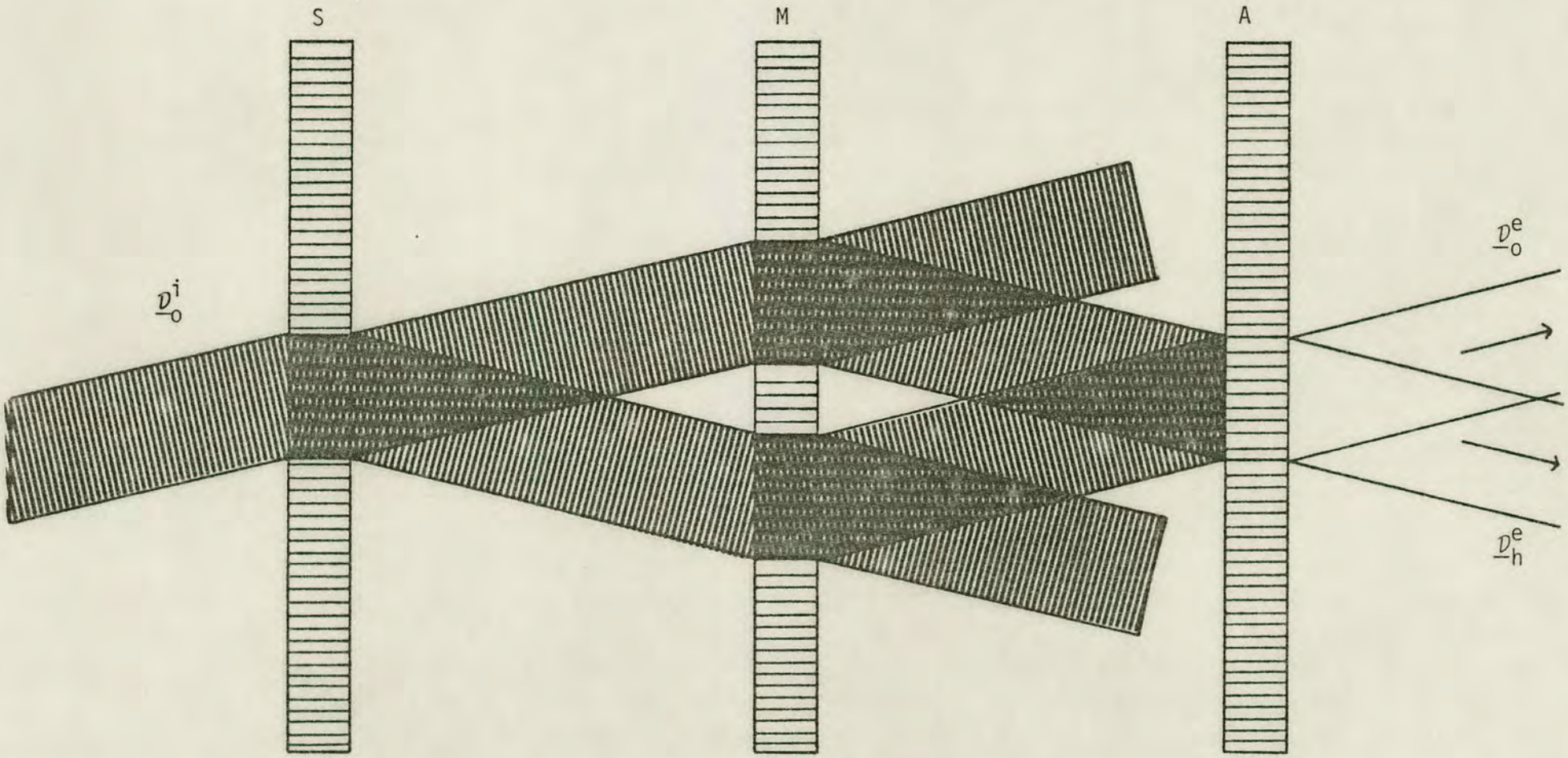

FIGURE 3.7: Schematic diagram of standing wavefields in an ideally perfect Laue case interferometer ('Thick' crystal case)

absorption. It is for this reason that, in the thin crystal case, fringes observed in forward and diffracted directions are complementary.

The sensitivity of the instrument is now obvious. Not only will minute variations in lattice parameter ($\Delta\ell/\ell \simeq 10^{-8}$) and rotation ($\sim 10^{-8}$ radians) be observable, but also single dislocations. Much work has been done involving the translation of the analyser crystal resulting in the exit beam alternating between maxima and minima of intensity[52]. In this way an Angstrom scale may be realised. One point which must be stressed, however, is that the standing wavefield immediately outside the analyser crystal is constant in relative position (there will be a small (d/4) translational effect when moving from 'thick' to 'thin' crystal cases) for all X-ray wavelengths. Thus, results obtained by interferometric techniques are wavelength independent.

3.2.1 Fringe Contrast

A rigorous treatment of the wavefield intensities as a function of wafer thickness taking into account the fact that the incoming wave is really spherical (ie illuminating the whole dispersion surface as the integral of a range of plane waves) rather than a plane wave, is extremely complex. However, an initial simplification may be made by considering the 'thick' crystal case - ie $\mu t > 10$.

If the transmitted beam is denoted by T and the reflected beam by R, then the exit beam in the forward direction will consist of the superposition of the two beams $T_S R_M R_A$ and $R_S R_M T_A$ (Fig 3.8). If the splitter and analyser wafers are made the same thickness,

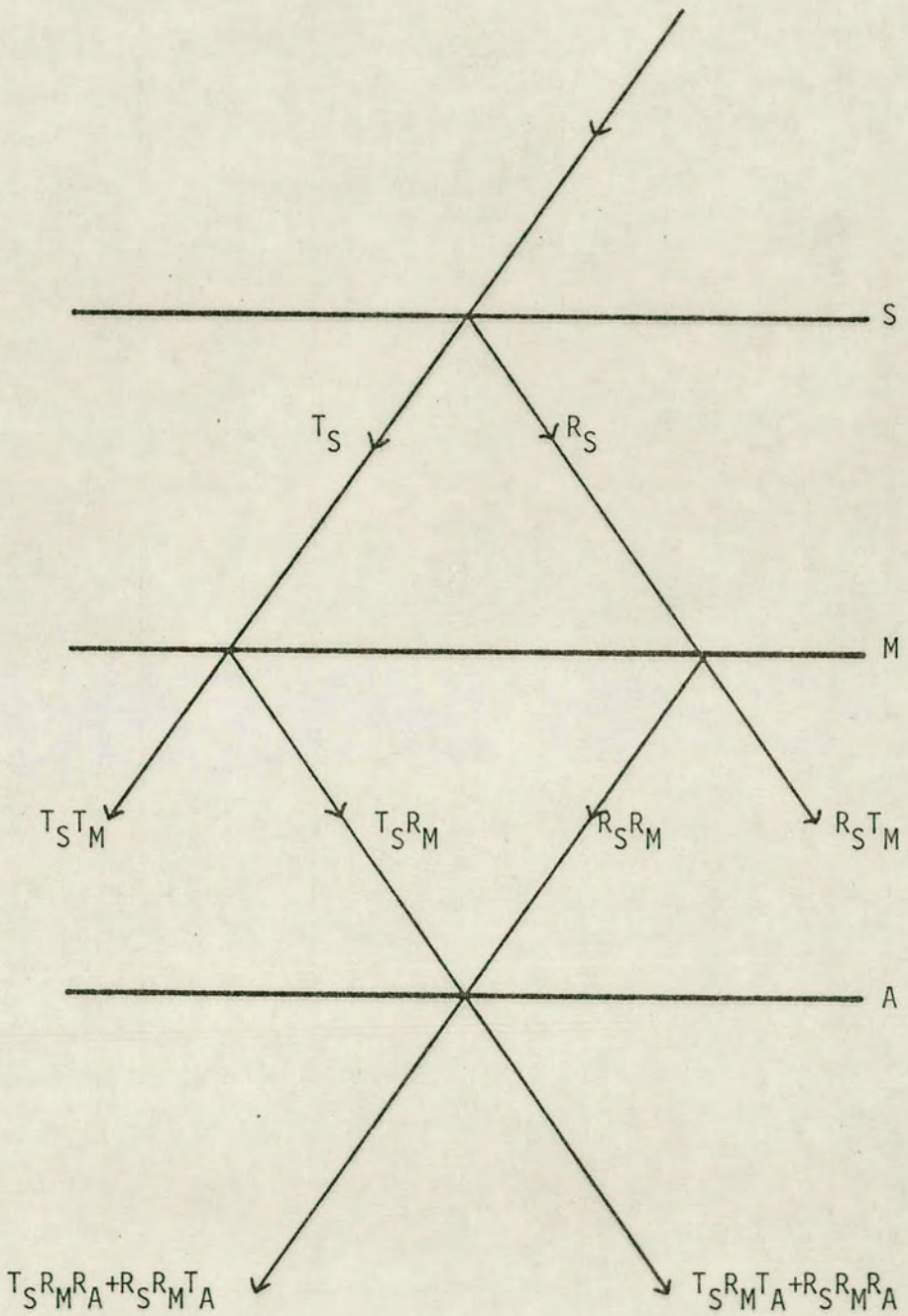

FIGURE 3.8

then $R_A = R_S$ and $T_A = T_S$ so that the two beams will have the same maximum intensity allowing 100% contrast to occur in the 'thick' crystal case. The exit beam in the reflected direction will be composed of the beams $T_S\ R_M\ T_A$ and $R_S\ R_M\ R_A$ and so will not necessarily be matched in intensity with the result that poorer contrast is obtained.

Kato[100] has calculated the intensity profiles expected from a section topograph in both the forward and diffracted directions for different values of μt. These profiles (after spatial averaging of the Pendellösung effect) are shown in Fig 3.9. For large μt (>10) only one beam (2σ) is transmitted through the crystal and its intensity is essentially the same in both transmitted and reflected beams. Thus, in the thick crystal case, fringe contrast in the forward direction may approach 100% (as deduced from the simple approach outlined above).

However, in the thin crystal case (μt <5) it will be seen from Fig 3.9 that the intensities in the forward and diffracted directions do not match each other - the intensity being symmetric over the width of the reflected beam, but not the transmitted beam. The result of this is that the contrast between the nodes and anti-nodes of the standing wave pattern, and hence the contrast of moiré fringes, gets progressively worse with decreasing μt.

From a practical point of view, however, the crystal thickness and X-ray wavelength must be chosen such that the fringe contrast is acceptable (μt >~1) but also such that the X-ray intensity is acceptable (μt <~10).

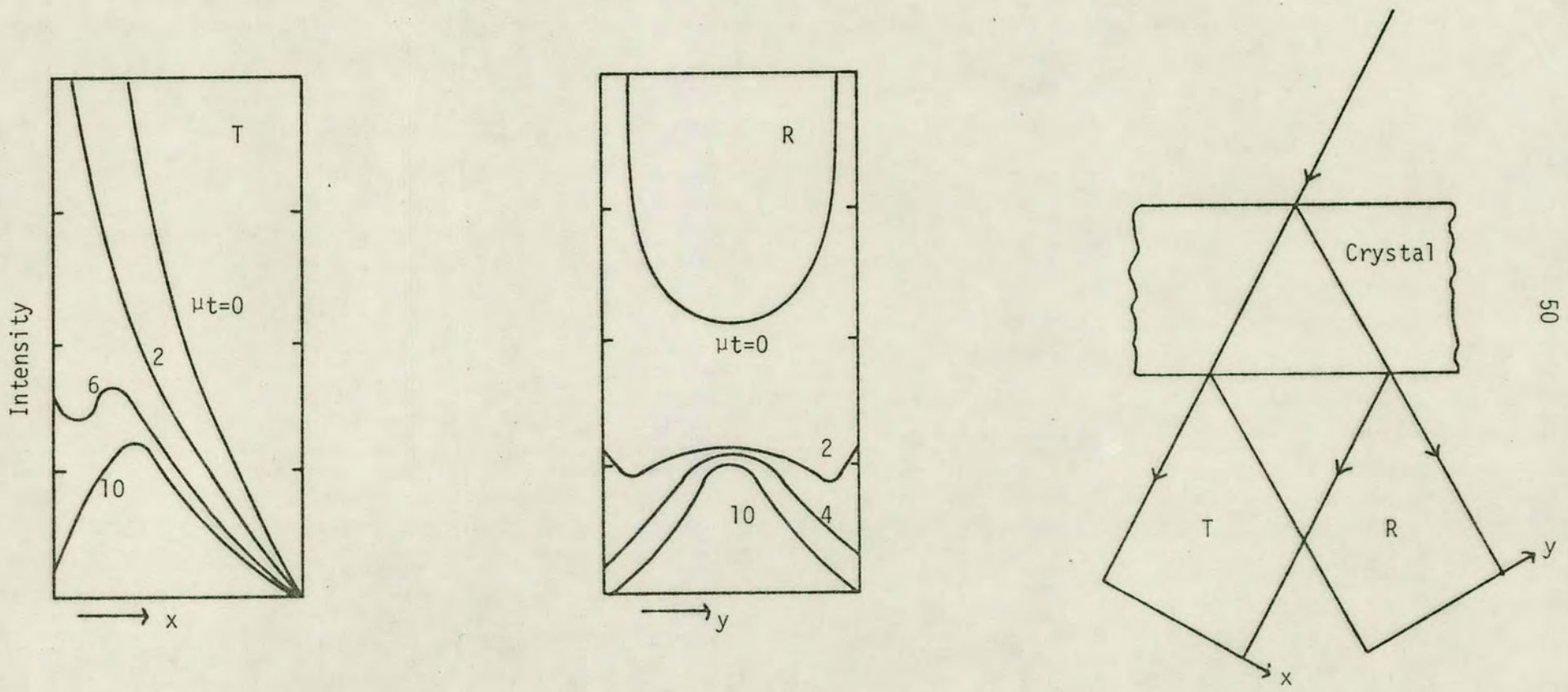

FIGURE 3.9: Intensity profiles of section patterns according to Kato[100]

3.2.2 Diffraction from Strained Crystals

The theory which has been developed so far has assumed a perfect crystalline structure. Naturally, if an interferometer is to be used for measuring the effects of strain, then the X-ray wavefield will be propagating through an imperfect medium. It is therefore relevant to assess the validity of the theory under these conditions.

The adaption of the dynamical theory to the strained crystal case has been performed by Penning and Polder[25], Bonse[28] and Takagi[33], and experimental work testing the theory by observation of Pendellösung fringes has been undertaken by Kato[26,27], Kuriyama[31,32] and Hart[29,30]. Since the theory is long and complex and since interferometry is not dependent on the details of the theory, such as the precise trajectory of wave paths, only a brief summary will be given here.

The interferometer is only sensitive to small strains (ie 10^{-8} - 10^{-6}) so that the strains within the crystal must be very small and slowly varying if they are to be observed. When this is the case, then a local dispersion surface will always be definable at every point in the crystal and will itself only vary slowly in space. Hence, a dynamical wavefield will always be present with a variable reciprocal lattice vector $\underline{h}$.

In optics, it is well known that the variation in the wave vector of some particular wave in a medium of varying refractive index is proportional to, and lying in the same direction as, the gradient of the refractive index.

$$\underline{\Delta K} \propto \underline{\nabla n} \qquad (3.18)$$

By analogy, in the X-ray case (Penning and Polder[25]),

$$\underline{\Delta K} \propto \nabla(\underline{h}.\underline{K_h}) \qquad (3.19)$$

Fig 3.10(a) shows how the variation in the wave vector $\underline{\Delta K}$ and reciprocal lattice vector $\underline{\Delta h}$ affect the excitation of tie points on the dispersion surface. A ray entering the crystal excites the appropriate tie points dependent on the surface normal and deviation from the Bragg angle as shown in Appendix 1. As the ray progresses through the crystal with slowly varying strain, so the tie points effectively migrate about the dispersion surface. Since the direction of energy flow lies in a direction normal to the dispersion surface at the selected tie point, it also will vary as the tie points sweep across the dispersion surface. Thus there will exist two X-ray paths (ignoring polarization) through the crystal, one for each branch of the dispersion surface as shown in Fig 3.10(b). It was shown earlier (Section 3.1.2) how beating takes place between waves associated with the two branches of the dispersion surface to produce Pendellösung fringes. Now that the ray paths associated with these two branches follow independent trajections strongly dependent on the strain within the crystal, the Pendellösung fringe pattern will also be dependent on the strain. It is by analysing this pattern that the theories of ray trajectories through strained crystals may be checked[26,27,29,30].

When the strain gradient is large, as would be found in the

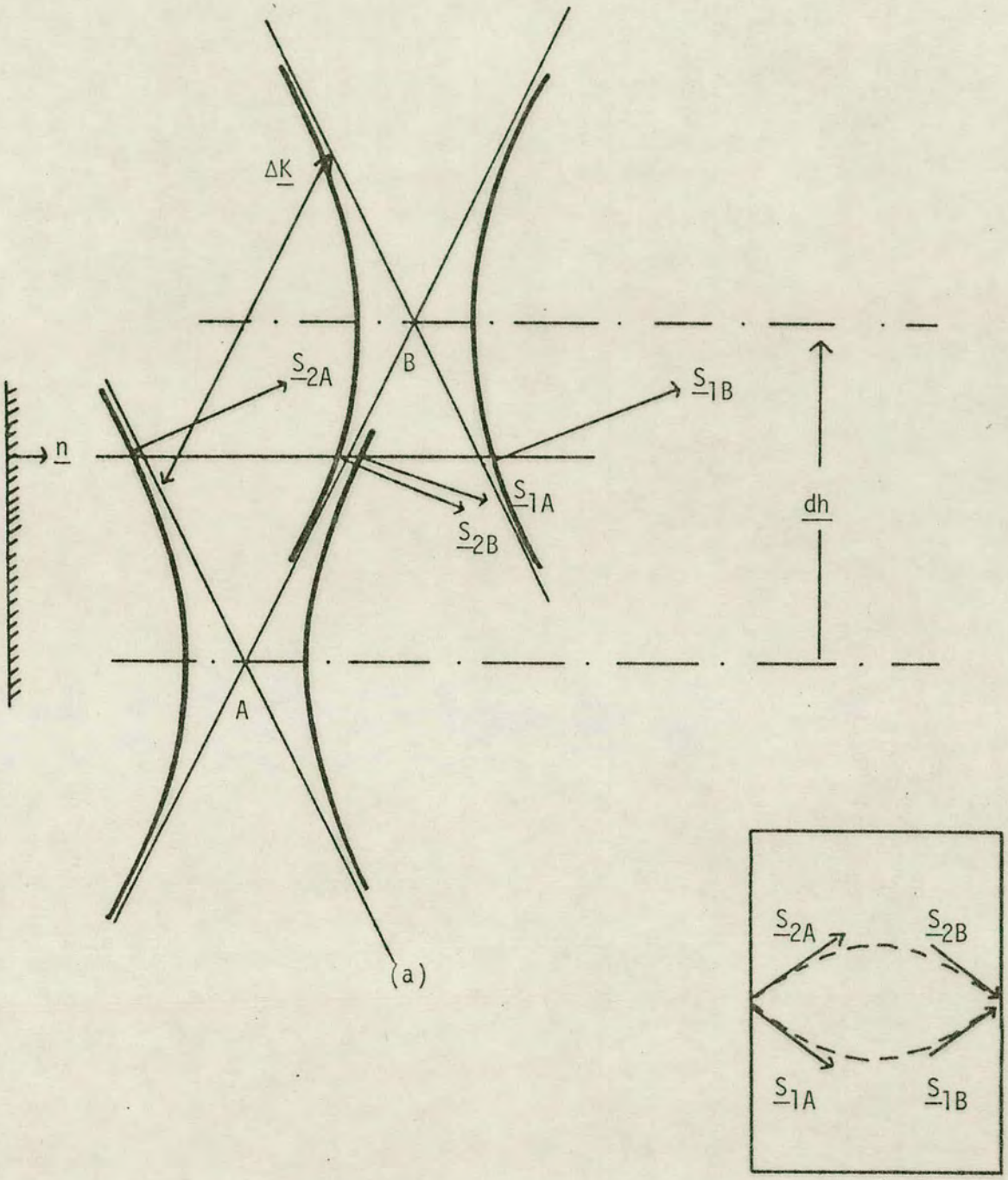

FIGURE 3.10: Showing migration of tie points in a region of slowly varying refractive index

vicinity of an imperfection such as a dislocation, the crystal is unable to support the dynamical wavefield. A boundary is effectively set up and the boundary conditions applicable to an exiting beam apply. This beam then propagates through the high strain area until the crystal is able to support a dynamical wavefield again when entrance boundary conditions are applicable.

However, in this analysis it is only necessary to observe that near the exit surface of a slightly strained crystal there exists a dynamical wavefield which is independent of the strain in the rest of the crystal. If the angular width of the incident beam (Ω) is much greater than any angle of curvature of the crystal (α), (this is certainly true for an interferometer application - $\Omega \simeq 3'$ and $\alpha \simeq 10''$ typically) then the wavefield near the exit surface will exist only as a function of the local dispersion surface.

In Section 3.2 it was shown that the moiré fringe pattern observed with an interferometer arises from the interaction between the standing wave pattern at the inside surface of the splitter wafer and the lattice of the analyser wafer (assuming a perfect mirror wafer). In thick crystals λ It has just been shown that the standing wave pattern at the inside surface of the splitter wafer is dependent only upon the strain *at* the exit surface (assuming that the strain is small enough to allow a dynamical wavefield to exist) and not upon strains elsewhere in the wafer. Fig 3.11 illustrates the maxima of the standing wavefield on the inside of the strained wafer. This standing wavefield is a result of the interaction between the forward and diffracted beams determined by application of exit boundary conditions to the dynamical wavefield within the crystal.

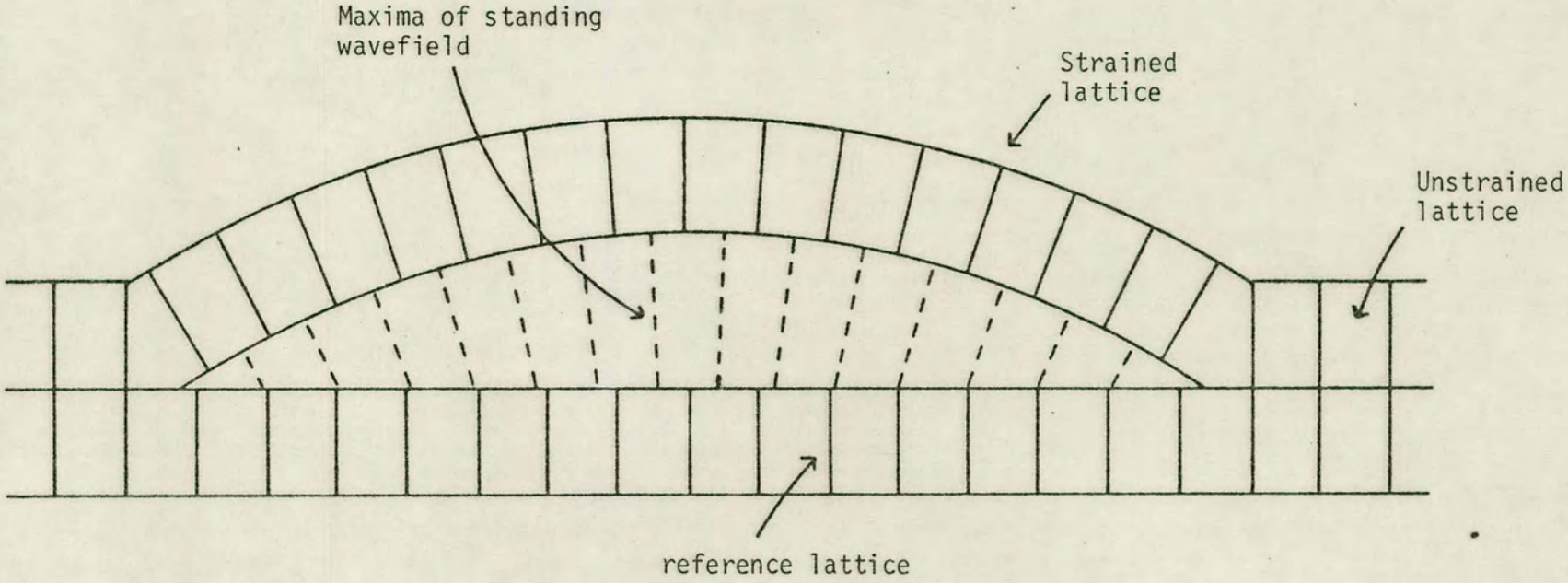

FIGURE 3.11: Maxima of standing wavefield for a strained crystal

The effective position of the analyser wafer is also shown (again assuming a perfect mirror crystal). The 'focussing' effect of the distorted crystal should be noted. It is shown quantitatively in Chapter 7 that the error introduced into the moiré fringe pattern by the 'bowing in' of the electric field maxima is negligible.

3.3 INTERPRETATION OF MOIRÉ FRINGES

It has been shown in Section 3.2 that the moiré fringe contrast arises due to the interaction between the standing wave pattern set up in front of the analyser crystal and the crystal lattice of the analyser wafer itself. This section uses the analogy of superposed linear gratings to analyse the moiré fringes themselves.

The phenomenon and underlying theory of moiré fringes has been studied for more than 100 years, notably by Focault[101], Lord Rayleigh[102] and others. The widest application for moiré fringe analysis is in mechanical engineering where finely ruled gratings are employed to detect strains in materials whilst undergoing load tests. The first observation of moiré fringes resulting from atomic planes was by Pashley, Menter and Basset[103] using an electron microscope to view appropriately oriented thin lamellae. In their experiment it was possible to observe individual dislocations appearing as extra half fringes.

In this analysis, only straight line regular pitch gratings will be considered. These ruled gratings consist of alternate light and dark bars of equal width. When two such gratings are superposed with slightly different pitch and angle, there will occur areas where the

dark bar of one grating exactly coincides with the light bar of the other. These continuously dark areas link up to form the moiré fringes. Figs 3.12(a) and (b) illustrate purely rotational and dilatational moiré images respectively. Figs 3.12(c) and (d) illustrate the effect of translation of two identical gratings directly superposed upon each other. These are typical of the kinds of pattern presented by the X-ray interferometer. The first task towards analysing these fringes is to establish equations which yield the rotation and dilatation parameters from the observed moiré data.

Let the reference gratings be defined by the family of curves $R(x,y) = k$ where k may represent any integer from $-\infty$ to $+\infty$. The scale is represented by the pitch p. Similarly, let the sample grating be defined by the family $S(x,y) = \ell$. In this case, however, the grating is distorted in the sense that its pitch is $p\,(1+\lambda)$ where $|\lambda| \ll 1$, (ie λ may be positive or negative). A system of cartesian coordinates is referred to both gratings with its y axis coinciding with line $k = 0$ and with origin occurring at the coincidence of line $k = 0$ and $\ell = 0$ (Fig 3.13).

The equation of the family of lines in the reference grating is given by

$$x = pk \tag{3.20}$$

If the sample grating is rotated through a small angle θ, then the equation of the family of lines in the sample is given by

$$y = (x \cot \theta - \frac{\ell\, p(1+\lambda)}{\sin \theta}) \tag{3.21}$$

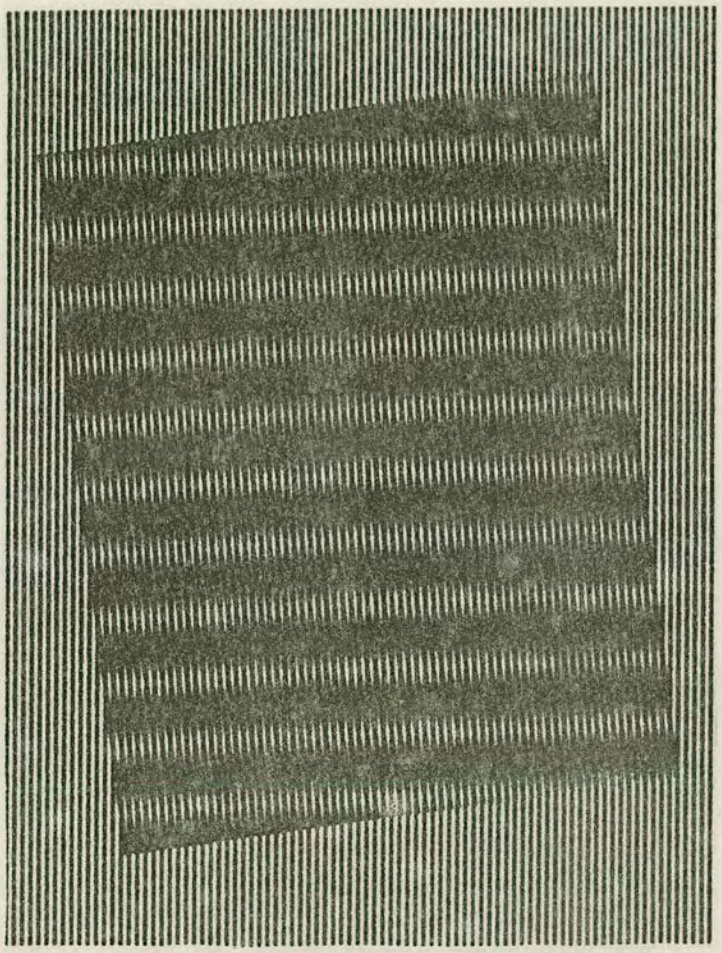

FIGURE 3.12(a): Moiré pattern by two identical gratings angularly displaced by a small angle θ

(b)

(c)

(d)

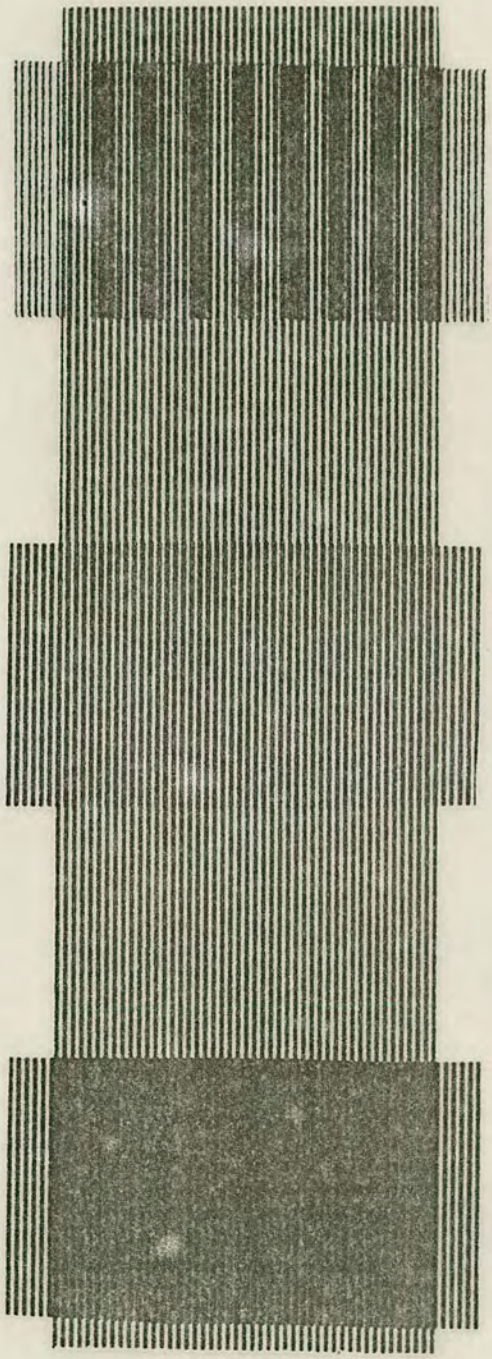

FIGURE 3.12(b): Moiré pattern by two gratings of different pitch but no angular displacement
(c): Two identical gratings superposed exactly
(d): Two identical gratings but displaced by half their pitch

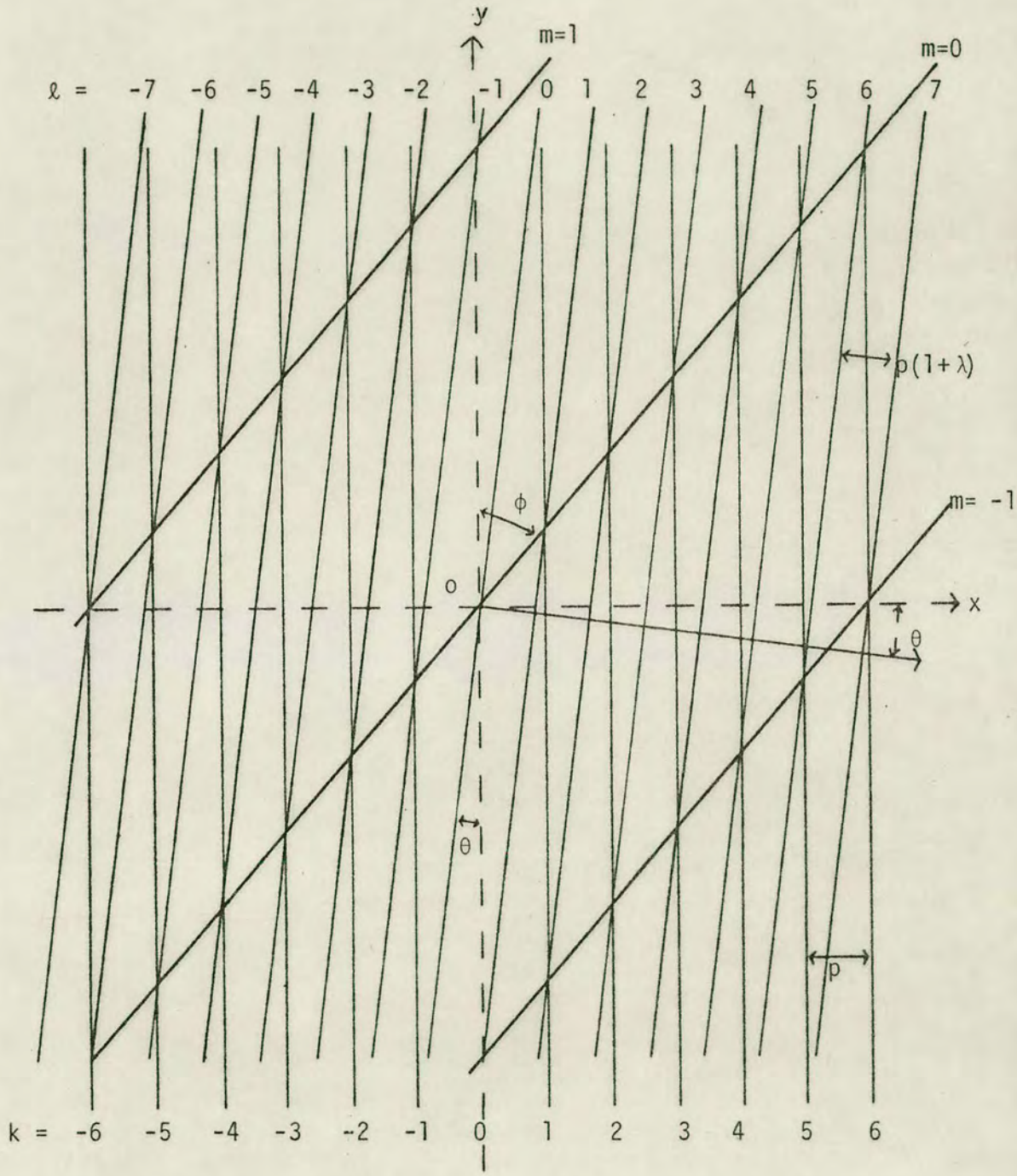

FIGURE 3.13: Schematic representation of formation of a moiré pattern by two gratings of different pitch angularly displaced through angle θ

This may be rewritten

$$(y \cos \theta - x \sin \theta) = \ell p(1 + \lambda) \tag{3.22}$$

The effective moiré fringes run along the shortest diagonals of the parallelograms formed by the intersections of the rulings. Let the angle between the moiré fringes and the y axis be ϕ and let their pitch be f. The equation representing the family of moiré fringes may be written

$$y = (x \cot \phi + \frac{mf}{\sin \phi}) \tag{3.23}$$

where m is an integer between $-\infty$ and $+\infty$. This index may be related back to the indices k and ℓ of the reference and sample gratings by the simple expression

$$m = k - \ell \tag{3.24}$$

This is obvious from Fig 3.12.

Eliminating the indices k and ℓ from equations 3.20, 3.22 and 3.24 yields the following equation for the moiré fringes

$$y = x[\frac{\cos \theta - (1+\lambda)}{\sin \theta}] + \frac{mp(1+\lambda)}{\sin \theta} \tag{3.25}$$

Equations 3.23 and 3.25 are identical. Therefore, by equating coefficients, it is deduced that

$$f = p(1+\lambda)[\lambda^2 \cos^2 \theta/2 + (2+\lambda)^2 \sin^2 \theta/2]^{-\frac{1}{2}} \qquad (3.26)$$

$$\sin \phi = \sin \phi \ [\lambda^2 \cos^2 \theta/2 + (2+\lambda)^2 \sin^2 \theta/2]^{-\frac{1}{2}} \qquad (3.27)$$

If θ and λ are very small - as the case would be with X-ray interferometry, then Equations 3.26 and 3.27 reduce to

$$f = \frac{p}{\sqrt{\lambda^2 + \theta^2}} \qquad (3.28)$$

and

$$\sin \phi = \frac{\theta}{\sqrt{\lambda^2 + \theta^2}} \qquad (3.29)$$

These equations may now be expressed as

$$\text{rotation:} \quad = \frac{p \sin\phi}{f} \qquad (3.30)$$

$$\text{dilatation:} \quad = \frac{p \cos \phi}{f} \qquad (3.31)$$

Now it can be seen that the dilatation and rotation parameters are inversely proportional to the components of the moiré fringe spacing in the x and y directions respectively, and therefore may be measured very easily. One important point which may be deduced immediately from Equations 3.30 and 3.31 is that if the moiré fringes are vertical ($\phi = 0$) then the distortion in the sample grating is

purely dilatational with no rotation. Conversely, if the fringes are horizontal ($\phi = 90^{o}$) then the distortion is purely rotational.

It is now possible to calculate the degree of performance which may be expected from the X-ray interferometer. The 220 atomic plane spacing in silicon is ~2 Å. Suppose that an interferometer is cut from a 2" diameter boule of silicon, then the fringe spacing could be as great as 2 cm. This represents a dilatation of one part in 10^{8} or a rotation of 10^{-8} radians (~2 x 10^{-3} seconds of arc) depending on whether the fringes are vertical or horizontal. On the other hand, the smallest readily measurable fringe spacing is about five fringes per mm implying that the maximum dilatation and rotation which may be observed is one part in 10^{6} or 10^{-6} radians.

3.3.1 Dislocation Patterns

As indicated earlier, moiré fringes may be used to interpret atomic dislocations. Again, an optical analogue may be used (Pashley, Menter and Bassett[103]). The number of extra half fringes N observed from a dislocation with Burger's vector $\underline{b}$ using diffraction from Bragg planes $\underline{h}$ is given by

$$N = |\underline{h}.\underline{b}| \qquad (3.32)$$

Since the dislocation length is an integral number of Bragg planes, then N will always be an integer. It can be seen from Equation 3.32 that if the dislocation Burgess vector lies within the diffracting Bragg planes then $\underline{h}.\underline{b} = 0$ resulting in the dislocation being invisible. If $\underline{b}$ is written as the vector [UVW] then its solution obviously

requires three independent equations. These may be realised by choosing three sets of non-coplanar diffracting Bragg planes $\underline{h}$. Typical dislocation images are shown in Fig 3.14.

(a)

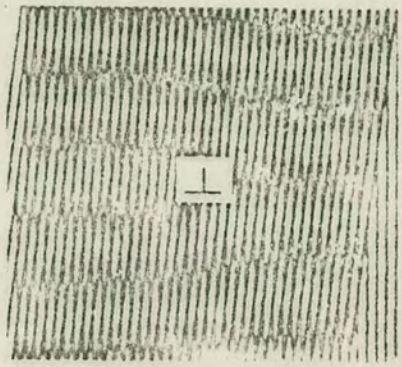

(b)

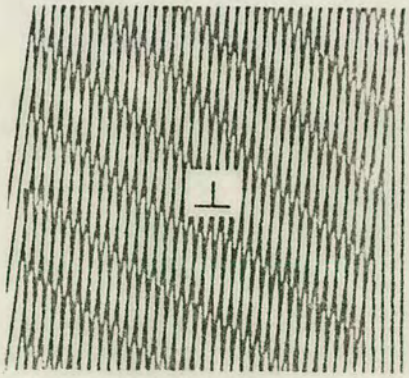

(c)

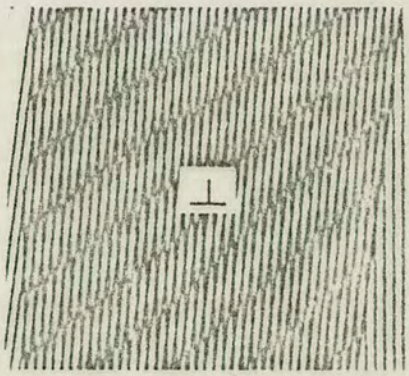

(d)

FIGURE 3.14: Typical moiré dislocation images. The symbol ⊥ represents the extra half plane.

CHAPTER 4: DOUBLE CRYSTAL SPECTROMETER THEORY

The double crystal spectrometer consists essentially of two crystals which are Bragg reflecting, ie the diffracted beam exits from the same face that the incident beam enters. Uncollimated X-rays are diffracted first of all from a 'perfect' reference crystal and then from the crystal under study. By this means, far better resolution is obtained than with the conventional single crystal methods employing a well-collimated beam of X-rays,as will be shown later.

This principle of using a preliminary crystal to select the X-ray beam has been in use for many years, among the early experimenters being Compton[104], Bragg, James and Bosanquet[105] and Davis and Stempel[106]. These early experiments were aimed at determining the reflection coefficients and widths of the reflection curves from crystals such as calcite. Later, the instrument became very popular when it was realised how high its resolving power could be. The first attempts at a theoretical understanding were made by Davis and Parks[107] and also (independently) by Ehrenberg and Mark[108].

Before analysing the particular benefits of the Double Crystal geometry, it is important, first, to study the nature of the Bragg reflection. A brief outline of the development of the dynamical theory and the solution of the waves propagating within the crystal is given in Appendix 1. Darwin[89] was the first to develop a theoretical approach to the scattering of X-rays from a perfect crystal. Ewald[90,91] and Von Laue[92] later developed the dynamical theory predicting the energy flow within the crystal and also by

taking absorption into account.

In Fig 4.1(a) and (b) it will be seen how the surface normal selects the incident and diffracted exit beams from its intersection with the Ewald spheres about O and H respectively. In Fig 4.1(a) the diffracted beam lies in the direction away from the surface normal and giving, by definition, the 'Laue' geometry. However, in Fig 4.1(b) the diffracted beam lies in a direction back towards the entrance surface and so is defined as 'Bragg' geometry where entrance and exit beams enter and leave the same face. It can now be seen that the limiting condition occurs when $\underline{n}$ is perpendicular to $\underline{K}_H$. When the surface normal becomes perpendicular to LO the symmetric Bragg case results, and this is the condition which will primarily be considered here.

4.1 THE BRAGG CASE REFLECTION CURVE

Fig 4.2 represents a crystal in the symmetric Bragg condition with two possible cases of incident wave, $\underline{K}_o^i$ (ψ_1) and $\underline{K}_o^i$ (ψ_2) where ψ_1, ψ_2 are the angles of incidence. At ψ_1, it will be seen that two tie points are selected on the same dispersion surface with their Poynting vectors directed into and out of the crystal respectively. However, it has been shown by Kohler[109] and Authier[110] that only one of the tie points gives a physically meaningful solution and that is the one where the energy flow is directed into the crystal (in this case, Al). At ψ_2, however, no tie points are selected indicating that there no longer exists a solution for the propagating wavefield within the crystal. In this case the incident X-ray beam is totally reflected away from the crystal; the angular range over which this

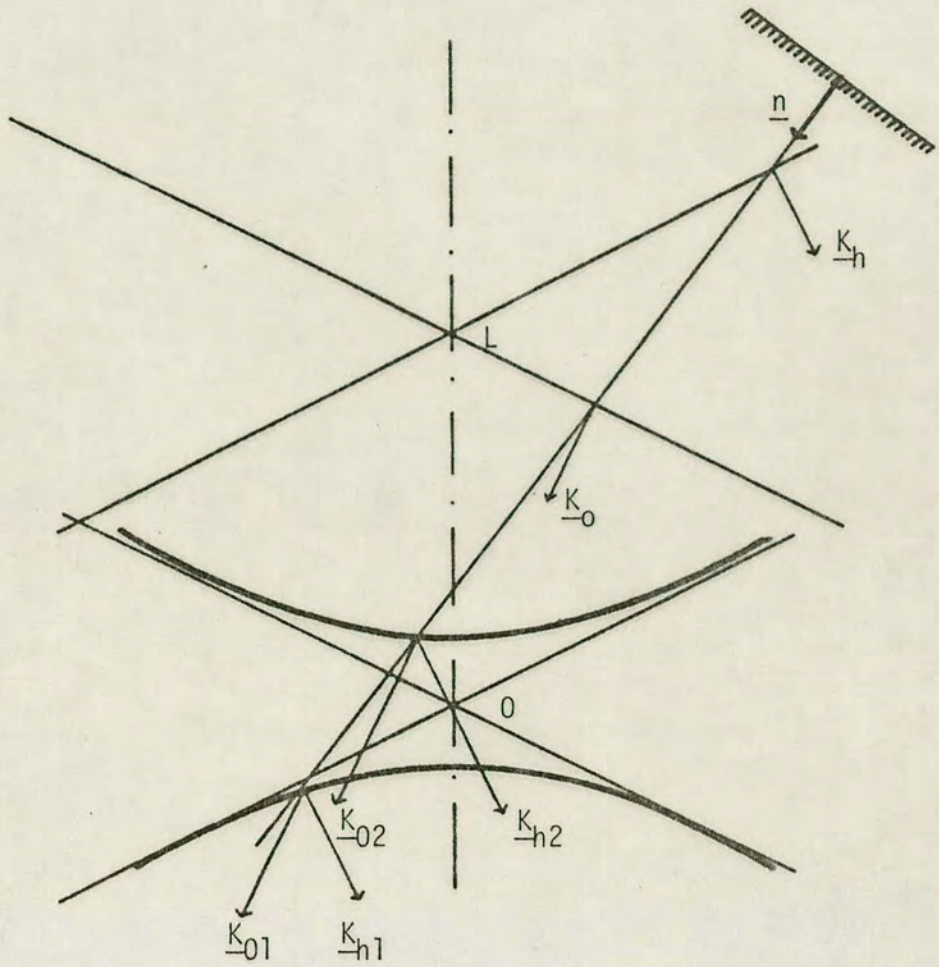

FIGURE 4.1(a): Laue case geometry

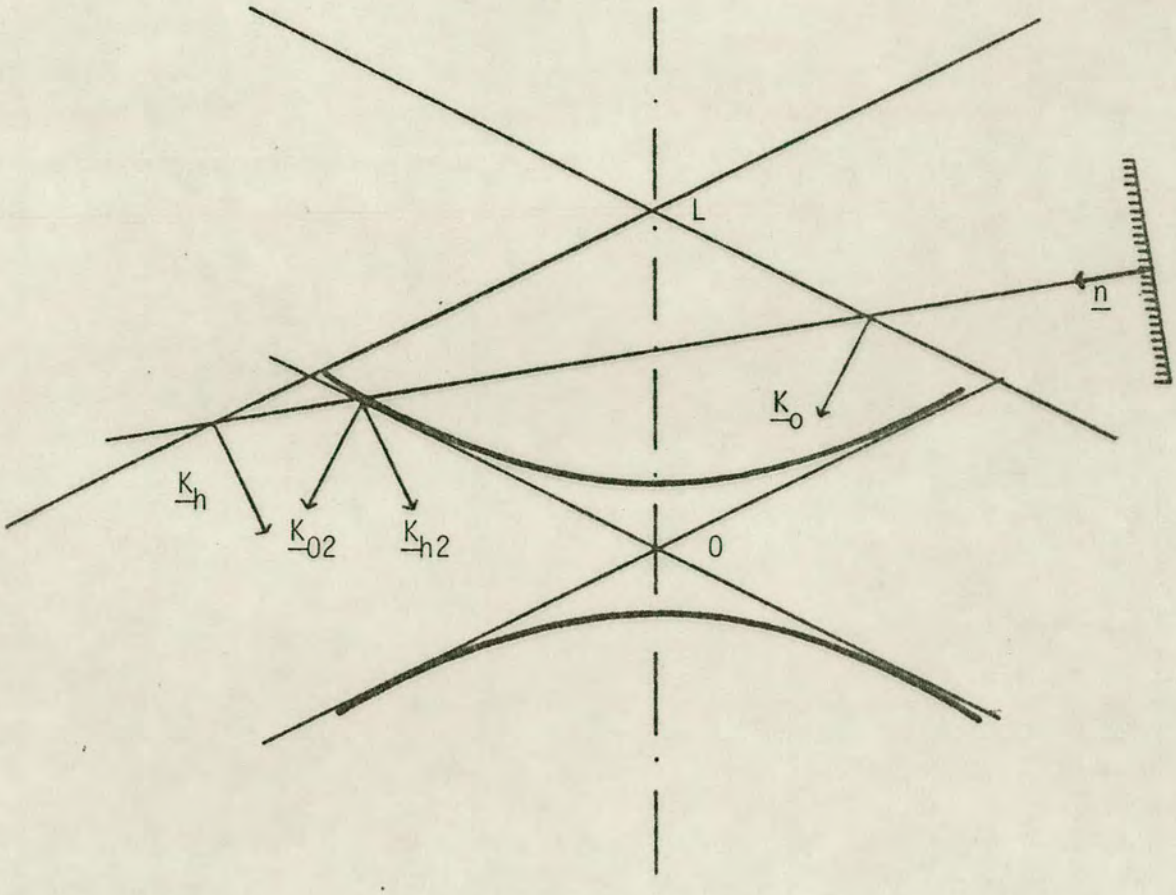

FIGURE 4.1(b): Bragg case geometry

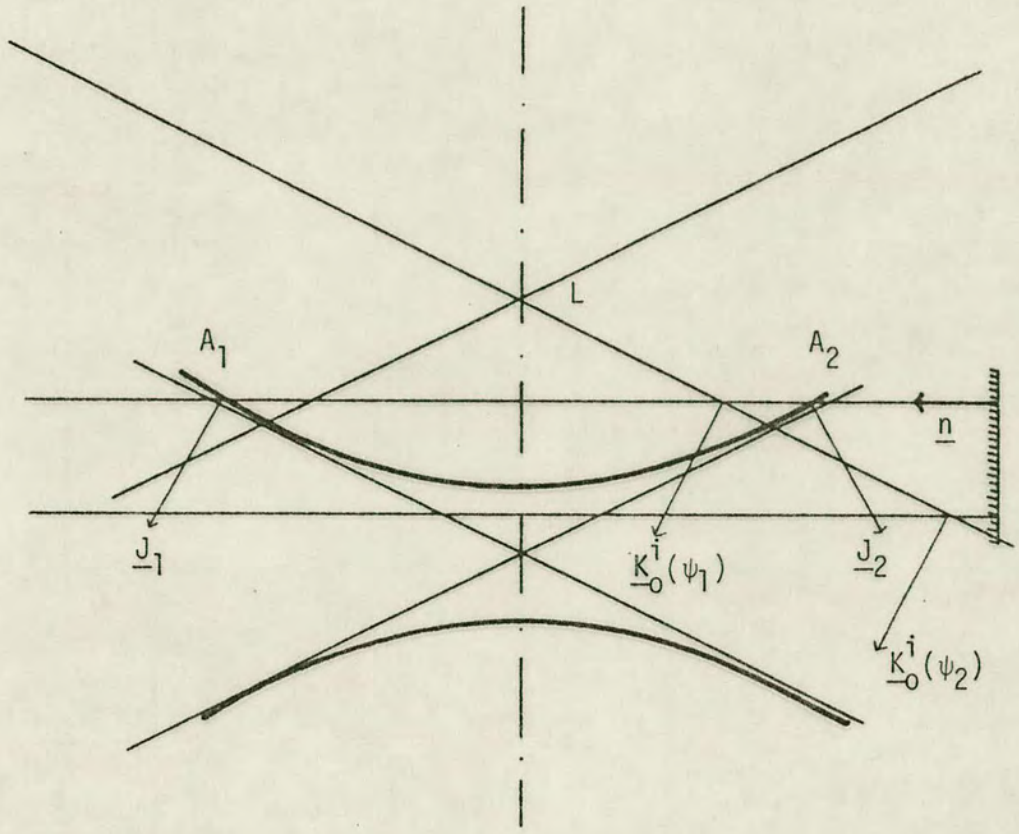

(a)

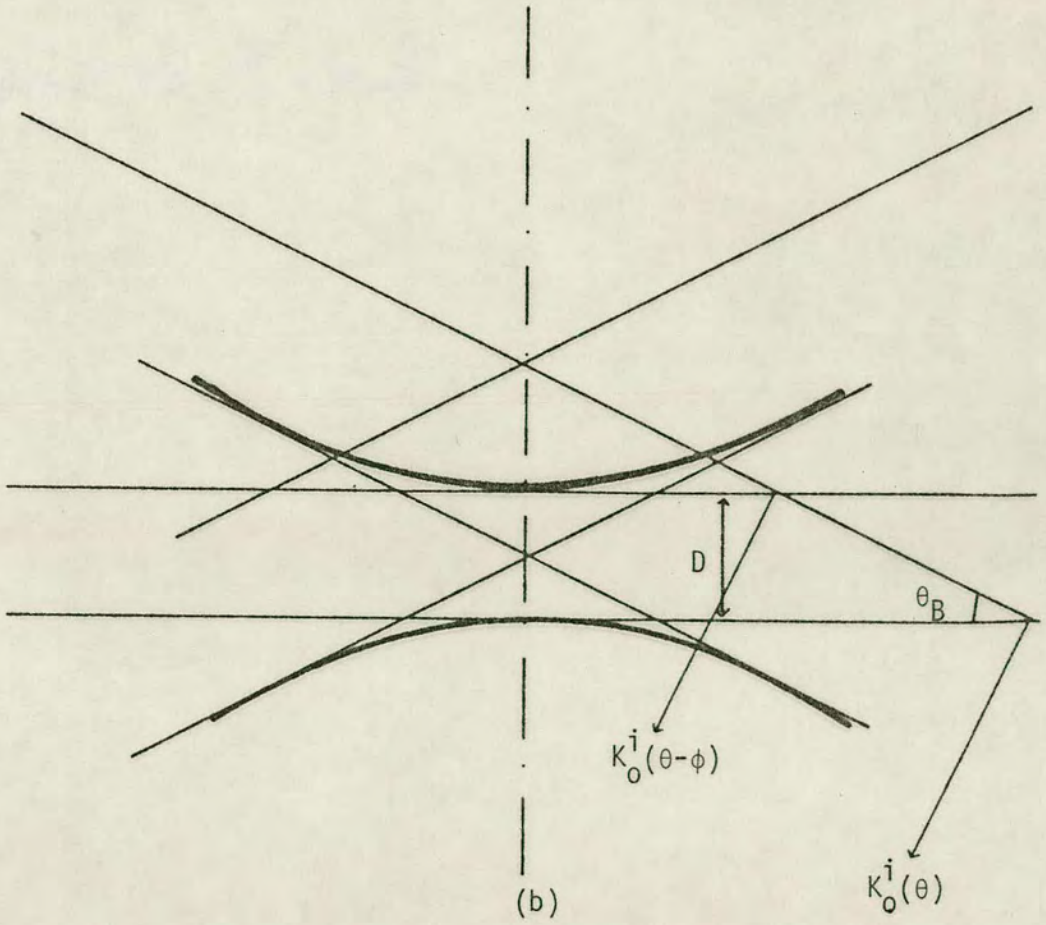

(b)

FIGURE 4.2: Bragg reflecting geometries

occurs may be found geometrically (as in Fig 4.2(b)), being a direct function of the diameter of the dispersion surface.

$$\phi = \frac{D \csc\theta_B}{k} \tag{4.1}$$

where θ_B is the Bragg angle, $k = 1/\lambda$ and D the diameter of the dispersion surface which is given by

$$D = k|c|(\chi_h \chi_{\bar{h}})^{\frac{1}{2}} \sec \theta_B \tag{4.2}$$

where $c = 1$ or $\cos 2\theta$ for σ and π polarization respectively, and χ_h is the Fourier coefficient of order h in the expansion of the susceptibility (see Appendix Equation A10).

In Table 4.1 the angular widths over which total reflection occurs in the symmetric Bragg reflecting case are calculated from Equations 4.1 and 4.2 for a range of reflections and wavelengths.

TABLE 4.1 Angular widths (seconds of arc) for selection of reflections and wavelengths

hkℓ	CuKα	MoKα	AgKα
111	6.40	2.87	2.26
333	1.96	0.65	0.50
440	2.69	0.80	0.61
422	2.89	0.89	0.78

It is now convenient to normalise the parameters relating to the dispersion surface. The difference in radius of the Ewald spheres before and after correction for the average refractive index is

$\frac{1}{2} k\chi_o$. From purely geometrical consideration of the dispersion surfaces, it will be seen at once that the angular divergence (ψ) between the symmetric Laue and symmetric Bragg case reflections is $\chi_o/\sin 2\theta$ radians. The parameter η is now defined as a function of the deviation from the symmetric Laue case reflection $\Delta\theta$ such that η is zero when $\Delta\theta$ gives the symmetric Bragg condition ($\Delta\theta = -\psi$) and $\eta = \pm 1$ at the two limits of total reflection. It then follows quite naturally that

$$\eta = \frac{\psi + \Delta\theta}{\phi/2} \tag{4.3}$$

Hence

$$\eta = \frac{\chi_o + \Delta\theta \sin 2\theta}{|C| \chi_h} \tag{4.4}$$

It is shown in Appendix 1 (Equation A19) that the ratio of the field amplitudes D_h/D_o may be expressed by

$$\frac{D_h}{D_o} = \xi = \frac{2\alpha o}{C\chi_{\bar{h}} k} = \frac{C\chi_h k}{2\alpha_h} \tag{4.5}$$

Hence

$$\left(\frac{D_h}{D_o}\right) = \frac{|\alpha_o| \chi_h}{|\alpha_h| \chi_{\bar{h}}} \tag{4.6}$$

Now that the dispersion surfaces have been normalised by the parameter η the ratio $\frac{|\alpha_o|}{|\alpha_h|}$ may be calculated from geometrical considerations of Fig 4.3 to yield,

$$\left(\frac{D_h}{D_o}\right)^2 = \left(\eta \pm \sqrt{\eta^2 - 1}\right)^2 \frac{\chi_h}{\chi_{\bar{h}}} \tag{4.7}$$

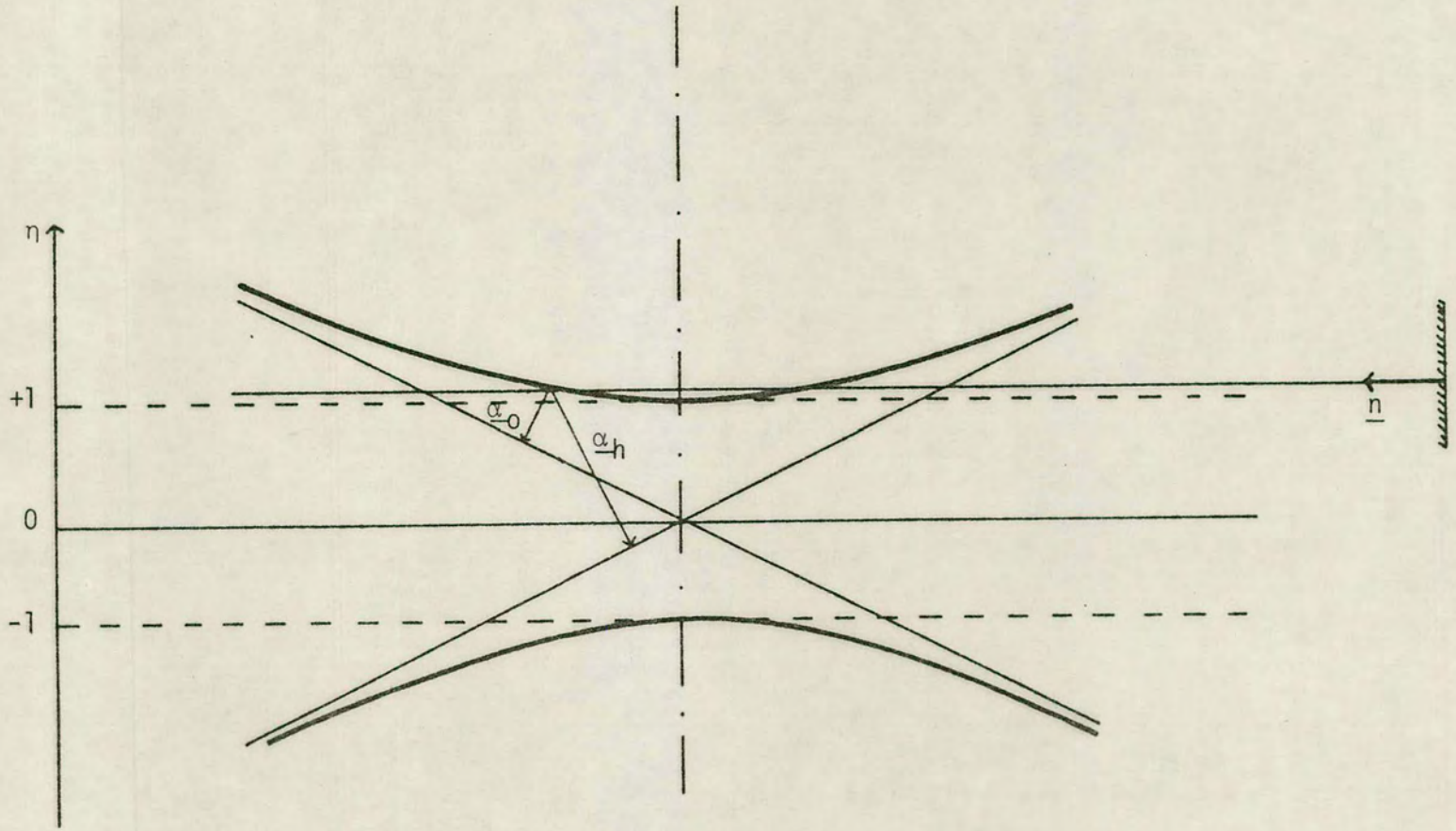

FIGURE 4.3: Normalised dispersion surface

For a centrosymmetric crystal $\chi_h = \chi_{\bar{h}}$. Since χ_o and χ_h have real and imaginary components associated with them when absorption is taken into account, so η is complex (from Equation 4.4). An analysis of Equation 4.7 now shows that for complex η, $(D_h/D_o)^2$ is always less than it would be for η wholly real. In particular, there is now no longer total reflection in the range $-1 < \eta < +1$. This may be understood in physical terms by considering energy conservation. In the zero absorption case the direction of energy flow, as determined from the Poynting vector being perpendicular to the dispersion surface, lie along the crystal surface in the region of total reflection. When absorption is taken into consideration, there exists a component of energy flow directed into the crystal resulting in the reflection now being less than total. Fig 4.4 shows the ratio of beam intensities as a function of $Re(\eta)$ with and without absorption calculated from Equation 4.7. This is known as the Darwin-Prins reflection curve. It will be seen that in the absorbing case, the reflection curve is no longer symmetric. This is due to the fact that the linear absorption coefficient varies significantly over the range of 'total' reflection in a manner somewhat akin to that associated with the Borrmann effect.

4.2 THE DOUBLE CRYSTAL ROCKING CURVE

Having established the shape of the Bragg reflection curve, this section is now devoted to the geometry of the double-crystal arrangement and hence to the shape of the rocking curve which may be obtained from it.

Fig 4.5 shows the parallel arrangement of the two crystals where

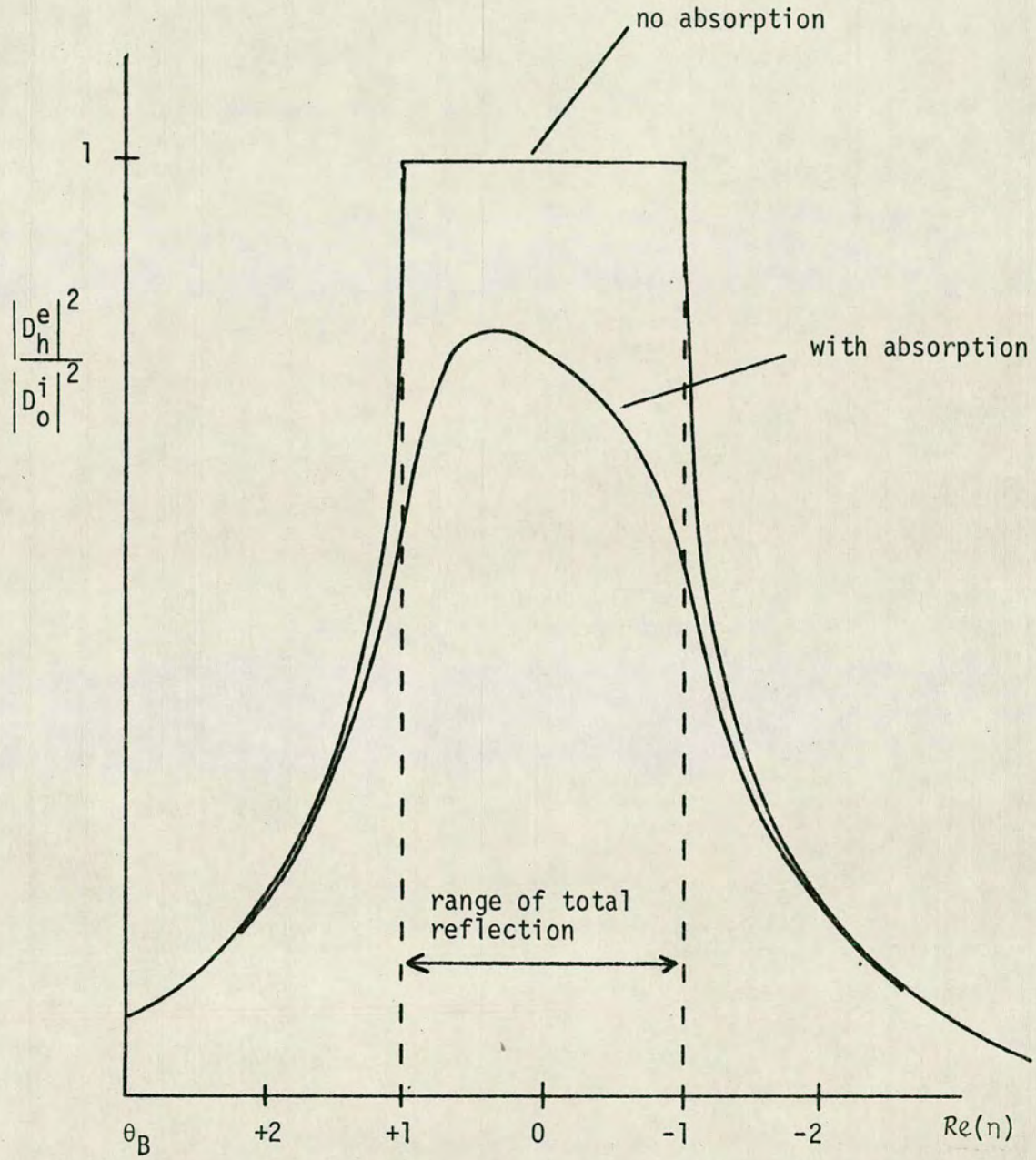

FIGURE 4.4: Reflection curve from Bragg reflecting crystal with and without absorption

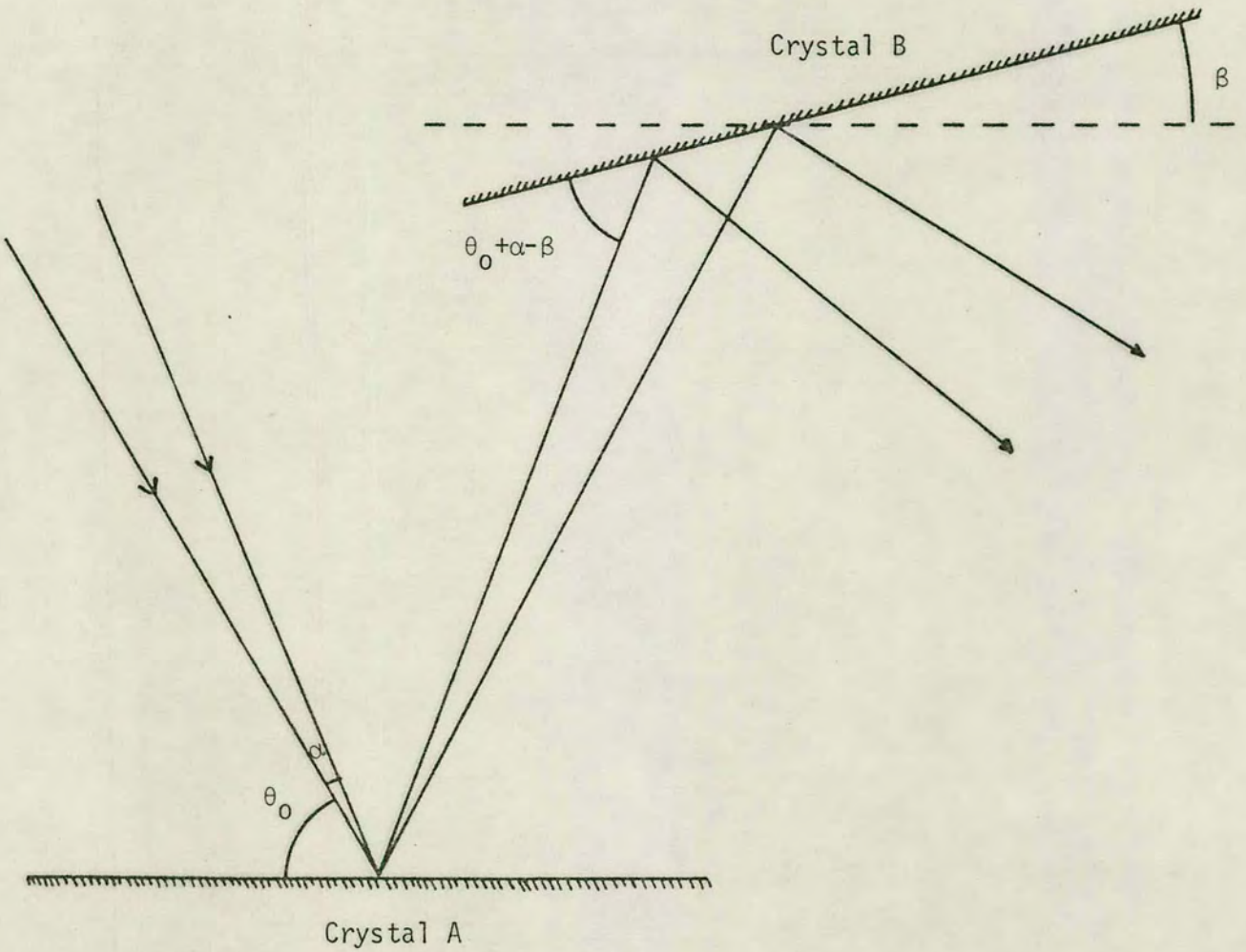

FIGURE 4.5: Showing geometrical arrangement of double crystal

the two sets of diffracting planes are the same and parallel to each other. In this analysis, crystal A is fixed and the intensity diffracted from crystal B is calculated as a function of its angular deviation from the parallel condition. The X-ray source has a finite divergence of both beam angle and wavelength and both these points must be considered. For simplicity, they will be considered separately so that in the first instance, the wavelength will be assumed to be homogeneous.

Let the incident beam contain rays with a range of incident angles such that one ray makes an angle which is diffracted in the centre of the reflection curve and let this angle be θ_o. It was seen in the last section that the angular range over which significant diffraction takes place is only of the order of seconds of arc. On the other hand, the range of incident angles will be many times greater than this. For the present, only rays in the horizontal plane will be considered. Let a ray with angular deviation from θ_o of α strike crystal A. If the incident beam has an intensity function of $I(\alpha)$, then its diffracted ray will have intensity $I(\alpha)\ R_A(\alpha)$ where $R_A(\alpha)$ is the reflection curve of crystal A. If crystal B is rotated anticlockwise from the parallel position by β, then this ray will make an angle of $(\theta_o + \alpha-\beta)$ with its diffracting planes, and so its intensity will become multiplied by $R_B(\alpha-\beta)$ where $R_B(\phi)$ is the reflection curve of crystal B. Hence its intensity will become

$$I = I(\alpha)\ R_A(\alpha)\ R_B(\alpha-\beta) \qquad (4.8)$$

In order to obtain the total power which will be detected in the

diffracted beam, it is necessary to integrate over the whole angular range of the incident beam.

$$\text{ie} \quad P(\beta) = \int_{\alpha_1}^{\alpha_2} I(\alpha)\, R_A(\alpha)\, R_B(\alpha-\beta)\, d\alpha \qquad (4.9)$$

Since $R(\alpha)$ only has a significant value for α close to zero, and since $I(\alpha)$ is (relatively) a very slowly varying function of α, the term $I(\alpha)$ $(= I(\theta_o))$ may be taken outside the integral. By the same token, since the contribution of $R(\alpha)$ for large $|\alpha|$ is negligible the limits of integration may be extended to $\pm\infty$ (for small β). Thus

$$P(\beta) = I(\theta_o) \int_{-\infty}^{\infty} R_A(\alpha)\, R_B(\alpha-\beta)\, d\alpha \qquad (4.10)$$

This equation will at once be recognised as the correlation function. In other words, the measured rocking curve will be the correlation of the reflection curve from crystal A with that of crystal B. If the two reflection curves are equal, then the autocorrelation function will be obtained. In this case

$$P(\beta) = I(\theta_o) \int_{-\infty}^{\infty} R(\alpha)\, R(\alpha-\beta)\, d\alpha \qquad (4.11)$$

If the substitution $\phi = (\alpha+\beta)$ is made, then

$$P(-\beta) = I(\theta_o) \int_{-\infty}^{\infty} R(\phi-\beta)\, R(\phi)\, d\phi$$

$$= P(\beta) \qquad (4.12)$$

This implies that the function $P(\beta)$ is always symmetric about $\beta=0$ even if $R(\alpha)$ is non-symmetric, which was shown to be the case for an

absorbing perfect crystal in the last section. Laue[111] has shown that a knowledge of the shape of the rocking curve $P(\beta)$ is not sufficient to enable calculation of the original reflection curve.

It will now be shown that the rocking curve obtained with parallel geometry is independent of the small range of wavelengths associated with a characteristic line. The assumption which has to be made is that the reflection curve is not a function of the wavelength. This is valid for the small range of wavelengths involved here although in general it would not be. Consider two wavelengths present in the incident beam λ_o and $\lambda_o + \Delta\lambda$. The centres of the reflection curves will occur at θ_o and $\theta_o + \Delta\theta$ respectively. A ray with wavelength $\lambda_o + \Delta\lambda$ making an angle $\theta_o + \Delta\theta + \alpha$ with crystal A will cause a diffracted ray to strike crystal B at an angle $\theta_o + \Delta\theta + \alpha - \beta$. Hence, the expression for the rocking curve $P^{\lambda+\Delta\lambda}(\beta)$ is

$$P^{\lambda+\Delta\lambda}(\beta) = I^{\lambda+\Delta\lambda}(\theta+\Delta\theta) \int_{-\infty}^{\infty} R(\alpha)\ R(\alpha-\beta)\ d\alpha \qquad (4.13)$$

which is identical with the expression given in Equation 4.10. In other words, the contributions from rays with different wavelengths exactly superimpose. This result is particularly important when it is realised that the width of a spectral line is greater than the angular range over which total reflection occurs. This is particularly marked in the case of the $K\alpha_1$ and $K\alpha_2$ lines whose spectra are very close together.

It will now be seen that the width at half height of the double crystal rocking curve is a direct function of the width of the Darwin-

Prins reflection curve. For example, by calculating the auto-correlation of the zero absorption Darwin curve it is found that its width at half height is 1.40 times the width of the total reflection region. By referring to Table 4.1, it will be seen that very narrow rocking curves may be obtained, indicating the high resolution which may be obtained with the instrument. The width of the rocking curve may be further reduced by using non-symmetric Bragg geometry. The effect of this is to reduce the angular range of incident beams which do not excite a tie point on either branch of the dispersion surface. Hence the width of the total reflection region of the reflection curve is correspondingly reduced.

CHAPTER 5: SAMPLE PREPARATION AND EXPERIMENTAL TECHNIQUES

5.1 INTERFEROMETER PREPARATION

All the interferometers used in these experiments were cut monolithically from the same 2" diameter boule of Monsanto float-zoned intrinsic silicon (resistivity >1000 Ωcm) grown in the <111> direction. A slice coaxial with the silicon boule (ie <111>),12mm thick, was first cut from the boule and then oriented on an orienting rig so that it could be cut across a diameter forming a <211> flat. These two pieces were then in turn oriented and halved again, this time forming a <110> flat. The four blocks of silicon thus formed made up the embryos of four identical interferometers. All that now remained was to cut out the three wafers. This was achieved with a Capco precision diamond saw by using a thick blade to saw away the silicon between and on the outside of the wafers, so that the required wafers were left standing. The blade could be positioned to an accuracy of about 10 μm and so was well within the tolerance calculated in Section 3.2 which is required to achieve good focussing and hence good image contrast. The wafers were cut with separation of 3 mm and thickness 0.5 mm. This thickness was chosen so that with appropriate X-ray wavelength, the interferometer could present thin, intermediate or thick crystal characteristics as shown in Table 5.1 (shown overleaf).

Here t is taken as 1.5 mm although after etching it reduces slightly. Fig 5.1(a) shows the interferometer dimensions together with the axial conventions assigned to each.

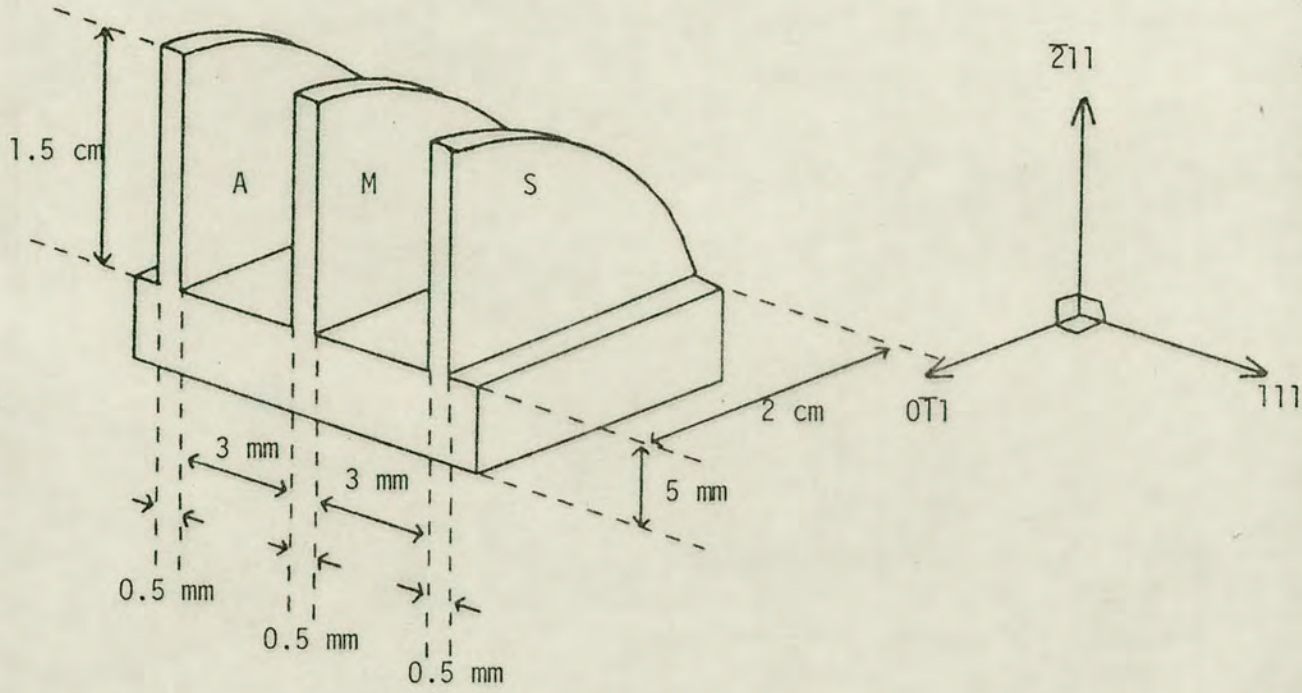

FIGURE 5.1(a): Dimensions and orientation of interferometer

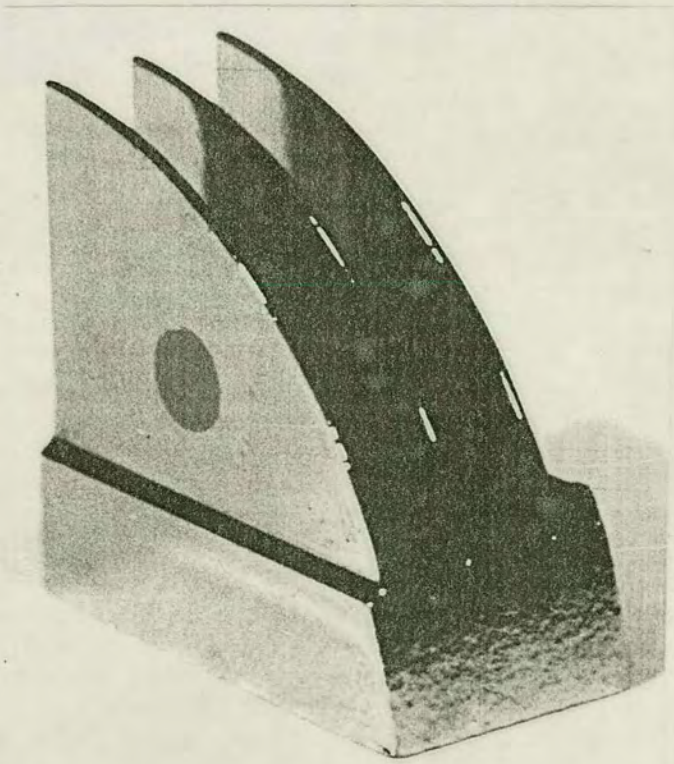

FIGURE 5.1(b): Interferometer (with 3.5 mm diameter oxide disc on splitter wafer)

TABLE 5.1

Wavelength	μt	
AgKα	1.1	thin
MoKα	2.2	intermediate
CuKα	21.2	thick

After cutting, the interferometers were cleaned thoroughly to remove silicon grit and grease, and then etched chemically in 19 parts HNO_3 to 1 part 48% HF for about half an hour. This etching not only polishes the saw damage (which is only a few tens of microns deep) but also renders the silicon very strong (after cutting, it is fragile). During etching, the silicon must always be kept in the etch, otherwise a bloom forms on the surface. Also, the silicon must be continuously agitated to give an even etch. Figs 5.2(a) and (b) show the effect of an uneven etch on the interferometer image in which the varying wafer thickness causes a built-in phase pattern.

5.2 INTERFEROMETER OXIDATION AND DIFFUSION

The experiments which were performed in order to study the strain field in the silicon required only one wafer to have a thermal oxide grown on it, the others to be oxide free and thus unstrained in order that moiré fringes should be observable. In all instances it was the splitter wafer which was chosen to be oxidised, although as seen in the theory presented in Chapter 3, no difference in image is to be expected by turning the interferometer round such that the

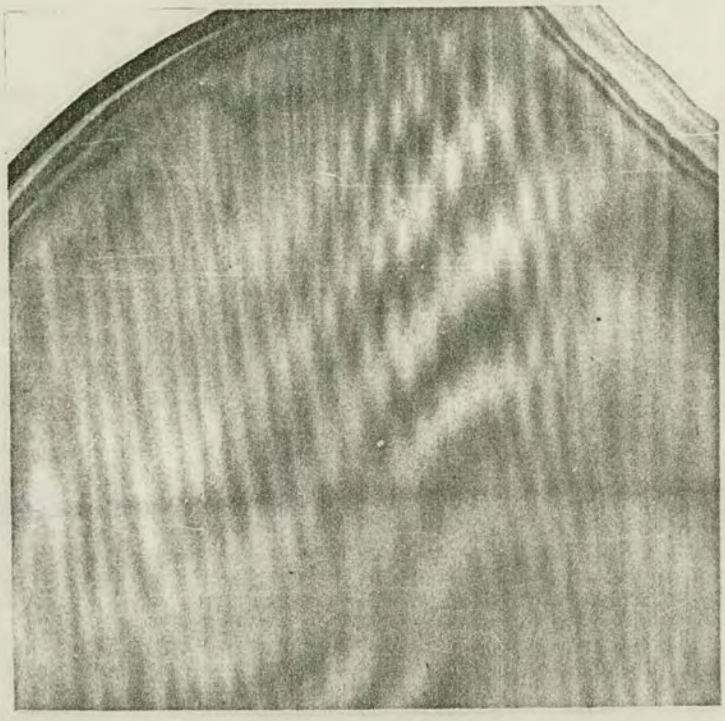

(a)

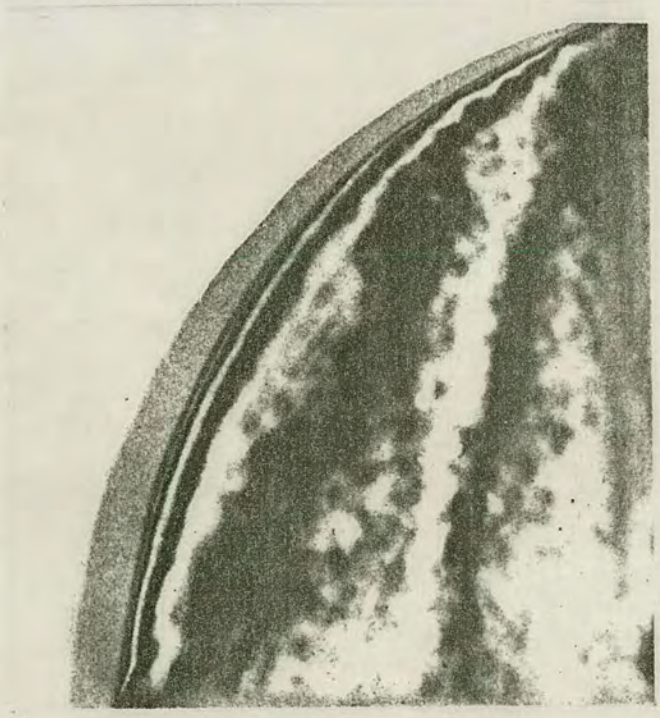

(b)

FIGURE 5.2: Effects of poor etching of interferometers
(a): Vertical grooves ($02\bar{2}$ reflection, MoKα radiation)
(b): 'Orange peel' pits ($02\bar{2}$ reflection, CuKα radiation)

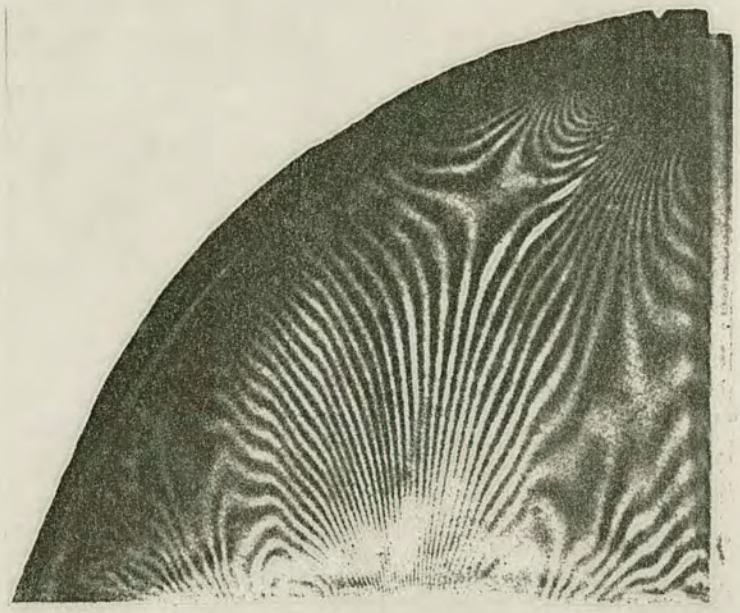

(a)

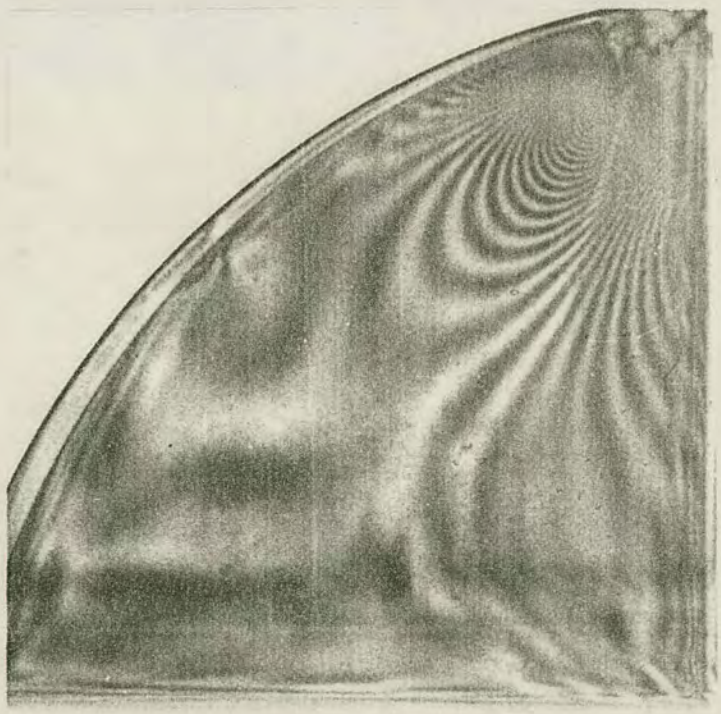

(b)

FIGURE 5.3: The relief of strain by etching, (a) before etching, (b) after etching. The strain remaining in (b) is due to an optically visible crystal fault in the splitter wafer. ($02\bar{2}$ reflection, MoKα radiation)

oxidised face becomes the analyser wafer. In any case, the first step involved the complete oxidation of the interferometer.

The theory behind the growth of thermal oxides has been presented in Chapter 2, together with a brief outline of the oxidation furnace. In this section, details of the experimental procedure are given.

The initial step in any semiconductor processing is to clean and degrease the samples thoroughly. In device manufacture this is possibly one of the most critical steps of all since any dust will immediately render the best of processing useless. Hence the need for a dust-free environment for all sample handling and preparation at this stage. The standard cleaning procedure is outlined below:

1. Slice clean

(a) 20 minutes at $85^{o}C$ in 6 parts H_2O, + 2 parts H_2O_2, + 1 part NH_4OH.

(b) 5 minutes wash in 'Super Q' water

(c) 10 seconds dip in 5% HF

(d) 5 minutes wash in 'Super Q' water

(e) 15 minutes at $110^{o}C$ in HNO_3

Quartz beakers to be used throughout to prevent sodium contamination.

2. Oxidation

(a) 15 minutes dry O_2

(b) Appropriate length of time for required oxide thickness, wet O_2 (ie, O_2 bubbled through 'Super Q' at $95^{o}C$).

(c) 10 minutes dry O_2

(d) 10 minutes pull-out in N_2

The oxidation experiments involved the removal of all oxide except for a disc (3.5mm in diameter on the splitter wafer) so that photo-resist techniques were now required.

3. Photo-resist (Positive)

(a) Shipley AZ1350H applied with small artist's brush

(b) Dry for 30 minutes at $85^{o}C$

(c) Black circle (Bishop Graphics symbol) applied to photo resist to act as mask

(d) 10 minutes exposure to UV

(e) 3 minutes develop

(f) Wash in DI water

(g) 30 minutes post bake at $110^{o}C$

(h) 18 minute etch in 5% HF

(i) 5 minute wash in 'Super Q' water

(j) 10 minutes in fuming nitric acid to remove photo-resist

(k) 5 minute wash in 'Super Q' water

Since it was not possible to spin the interferometers, it was necessary to bake the resist for longer than would be normal. The oxide was measured initially with a talisurf using control slice in order to determine the approximate thickness (to about 20%) and then colour charts[80] were used to give a more accurate measurement (to

about $\pm$0.01 μm).

The diffusion experiments involved selective boron diffusion (see Section 2.2)and so a SiO_2 masking procedure was required following the same techniques as outlined above except that negative photoresist was used (this was so that oxide was removed only where the diffusion was to take place). The masking oxide was ~.7 μm. This is quite sufficient to prevent any boron diffusion through it.

4. Diffusion

(a) Load devices and leave to heat for 10 minutes in N_2

(b) Diffuse for appropriate length of time at 1100°C with the following gas rates: N_2 (main) - 2.0 litres/min
O_2 - 200 cc/min
N_2 over BBr_3 - 30 cc/min

(c) 10 minutes pull-out in N_2

(d) 10 minutes dip in 5% HF to remove both masking oxide and boron glass

This kind of diffusion is known as predeposition diffusion. Since only a total dose of impurity atoms was required, it was unnecessary to perform a drive-in diffusion. A standard four point probe was used to measure the sheet resistivity of a control slice in order to determine the total impurity dose (see Chapter 8).

5.3 INTERFEROMETER EQUIPMENT

Since the X-ray interferometer is a very sensitive instrument,

as shown in Chapter 3, it is necessary to mount it on an antivibrational platform. For this reason the standard Lang traversing technique cannot be used. Instead, it is the X-ray source which traverses past the stationary crystal, as shown in Fig 5.4. In these experiments, the source makes just one pass across the crystal driven by a stepper motor linked via a gear box to a precision micrometer. The pulse rate to the stepper motor could be controlled by dividing 100 Hz by powers of 2 up to 2^9. The overall gearing was such that the traverse was caused to move 1 μm by 5 pulses to the stepper motor. The X-rays were generated in a Philips vacuum tube by an ultra stable Enraf Nonius HT supply (40 KV, 20 mA) and were then collimated to form a ribbon beam 0.4 mm wide and up to 40 mm in height. The collimator length was 43 cm, resulting in an angular divergence of X-rays at the crystal of 3.2 minutes of arc. Since this is very much larger than the diameters of the dispersion surfaces pertaining to the wavelengths used here (~2 seconds of arc), the incident beam was treated as being spherical rather than planar.

It will be seen from Fig 5.4 that six beams leave the interferometer - three in the forward direction and three in the diffracted direction. Of the three beams, only the central one contains the moiré image. It was shown in Chapter 3 that the better fringe contrast is to be found in the beam in the forward diffracted direction. Slits were constructed out of tantalum sheet and arranged such that the central beam in the forward direction could be selected as shown in Fig 5.4. When MoKα is chosen for a $\{220\}$ reflection (as used for most experiments) the three beams are only separated by 1.7 mm. Hence the need for both narrow slits and a well collimated

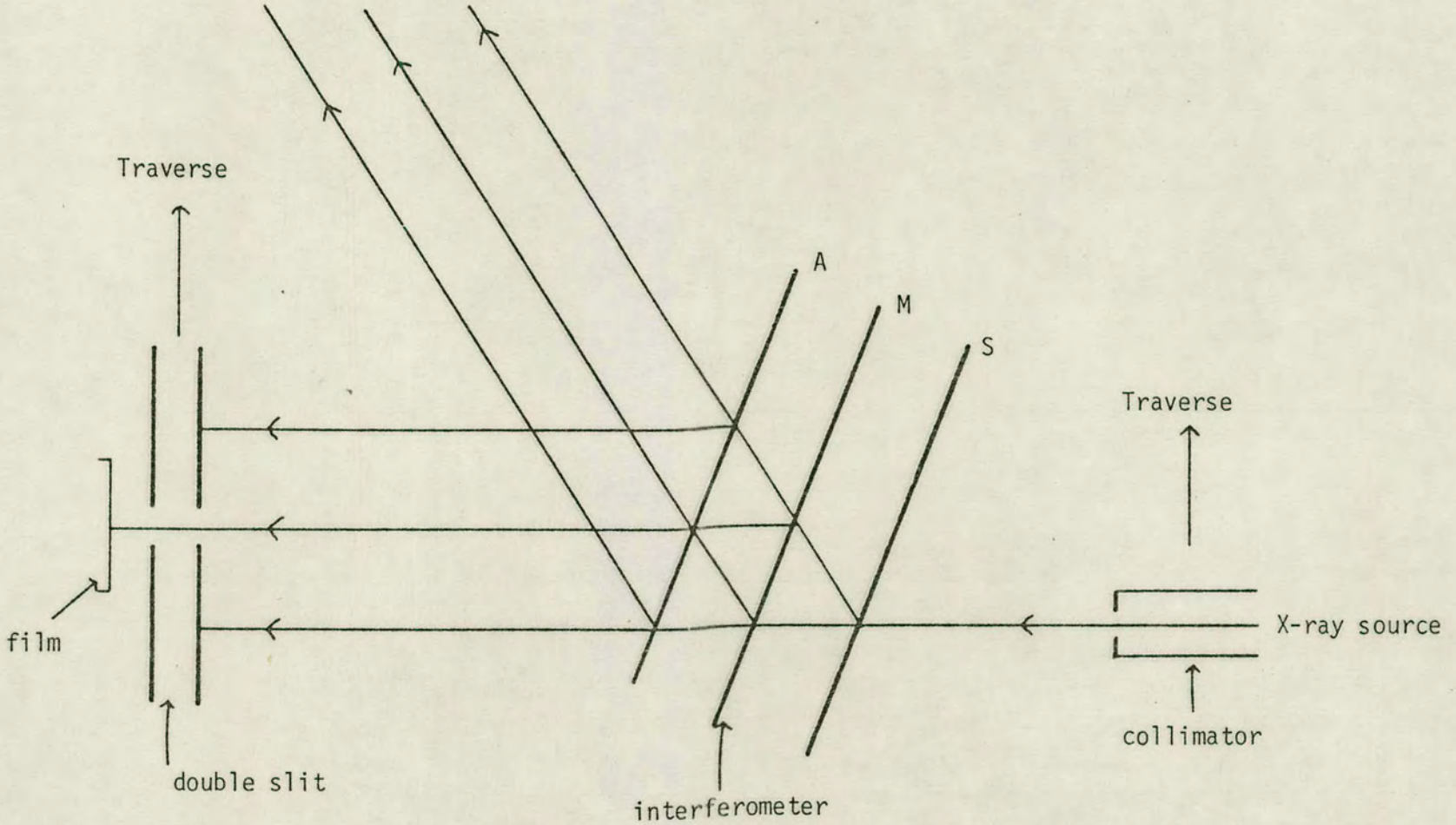

FIGURE 5.4: Lang travelling source

beam. It was found that background radiation could be improved by using a double slit arrangement as illustrated.

A scintillation counter was used in conjunction with pulse counting equipment for setting the crystal on the chosen Bragg peak. For topographs requiring high resolution (ie those with closely spaced moiré fringes) Ilford nuclear emulsion plates were used. However, with this film an exposure of six days was required to obtain a 2 cm scan of the crystal so that topographs requiring low resolution were taken with Kodak dental X-ray film (4S-150 ESTAR). This film, although very grainy (grain size ~10 μm) was found to be about eight times faster than the nuclear emulsion film.

The overall experimental set-up is shown in Fig 5.5.

5.4 INITIAL INTERFEROMETER EXPERIMENTS

5.4.1 Refractive Index

A standard test which can be made to verify that interference is taking place within an interferometer is to insert a wedge of some absorbing material into one of the beam paths. This will introduce a phase advance with the other beam which will vary linearly over the beam height. The standing wavefield in front of the analyser wafer is effectively rotated by this phase advance resulting in equally spaced horizontal moiré fringes. This is indeed the observed result, shown in Fig 5.6.

This technique has been used by Bonse and Hellkötter[54] to measure the refractive index of various materials using CuKα

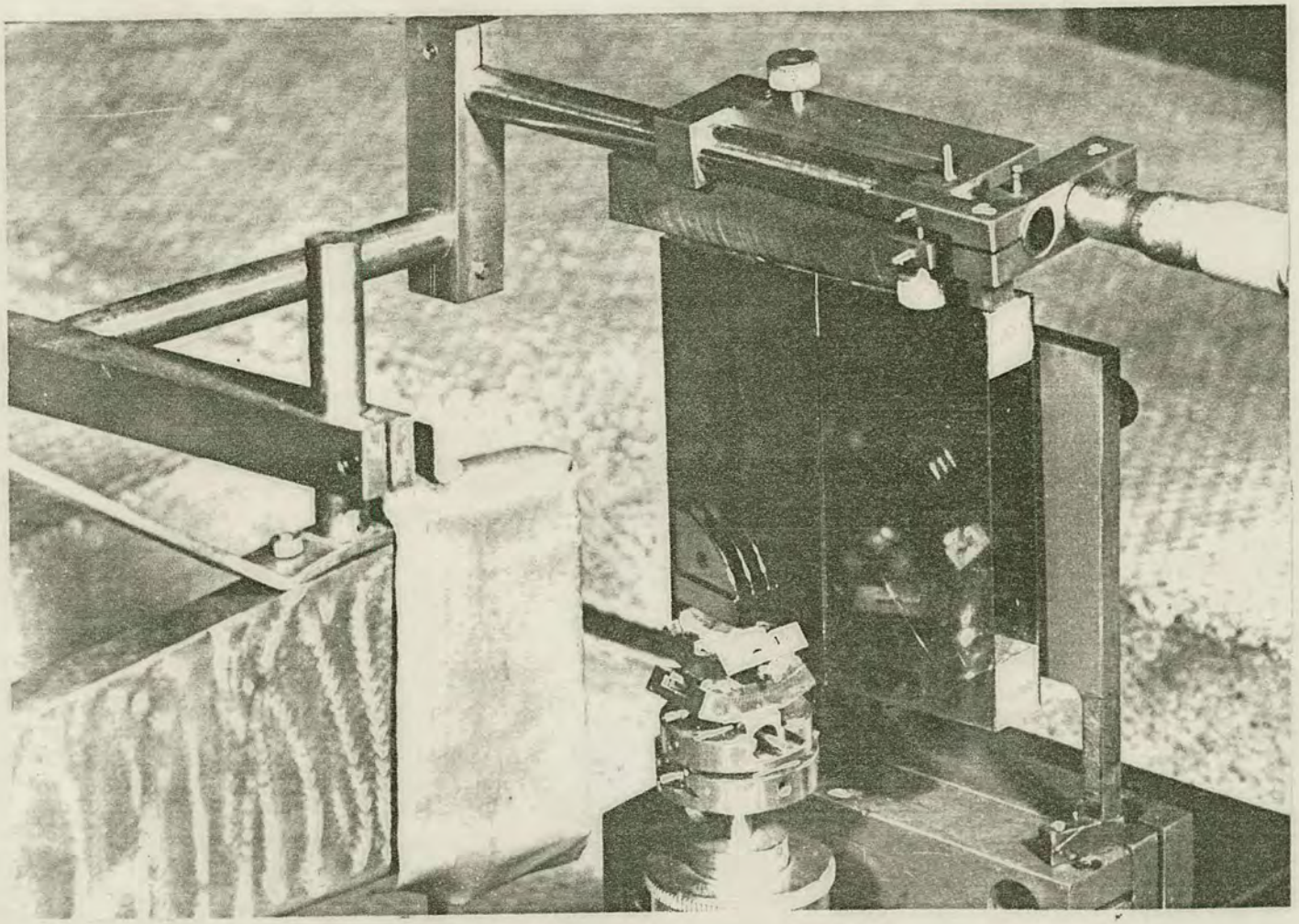

FIGURE 5.5: Lang travelling source with interferometer mounted on anti-vibrational mount.

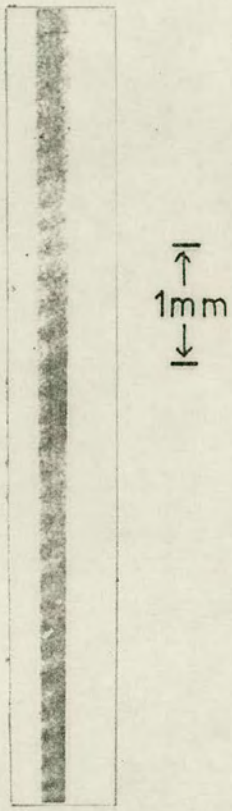

FIGURE 5.6: Interference fringes as a result of a silicon wedge being introduced into the path of one X-ray beam

($02\bar{2}$ reflection, MoKα radiation)

radiation and also by Creagh and Hart[61] to measure the refractive index of lithium fluoride with various wavelengths. In this experiment an interferometer with negligible built-in phase contrast was chosen and a collimated ribbon beam of MoKα radiation was used. The wedge was cut from silicon and its angle was measured to be $\tan^{-1}$ (0.195 $\pm$ .004) Kodak dental film was used because of its high speed - the large grain size and resultant relatively low definition was deemed unimportant in this application.

If f is the fringe spacing then it can easily be seen from Fig 5.7 that the path length (ℓ) over which there is a phase change of 2π radians, is given by

$$\ell = f \tan \theta \qquad (5.1)$$

where f is the fringe spacing.

Since the refractive index is simply a correction factor by which the X-ray wavelength in some material may be calculated, then

$$\ell = \frac{\lambda}{1-n} \qquad (5.2)$$

where n is the refractive index. The concept that the refractive index is less than unity for X-rays (ie the phase velocity of X-rays in materials is greater than the velocity of electromagnetic waves in free space) has been known since Darwin[89] originally postulated the theory. Hence

$$f \tan \theta = \frac{\lambda}{(1-n)} \qquad (5.3)$$

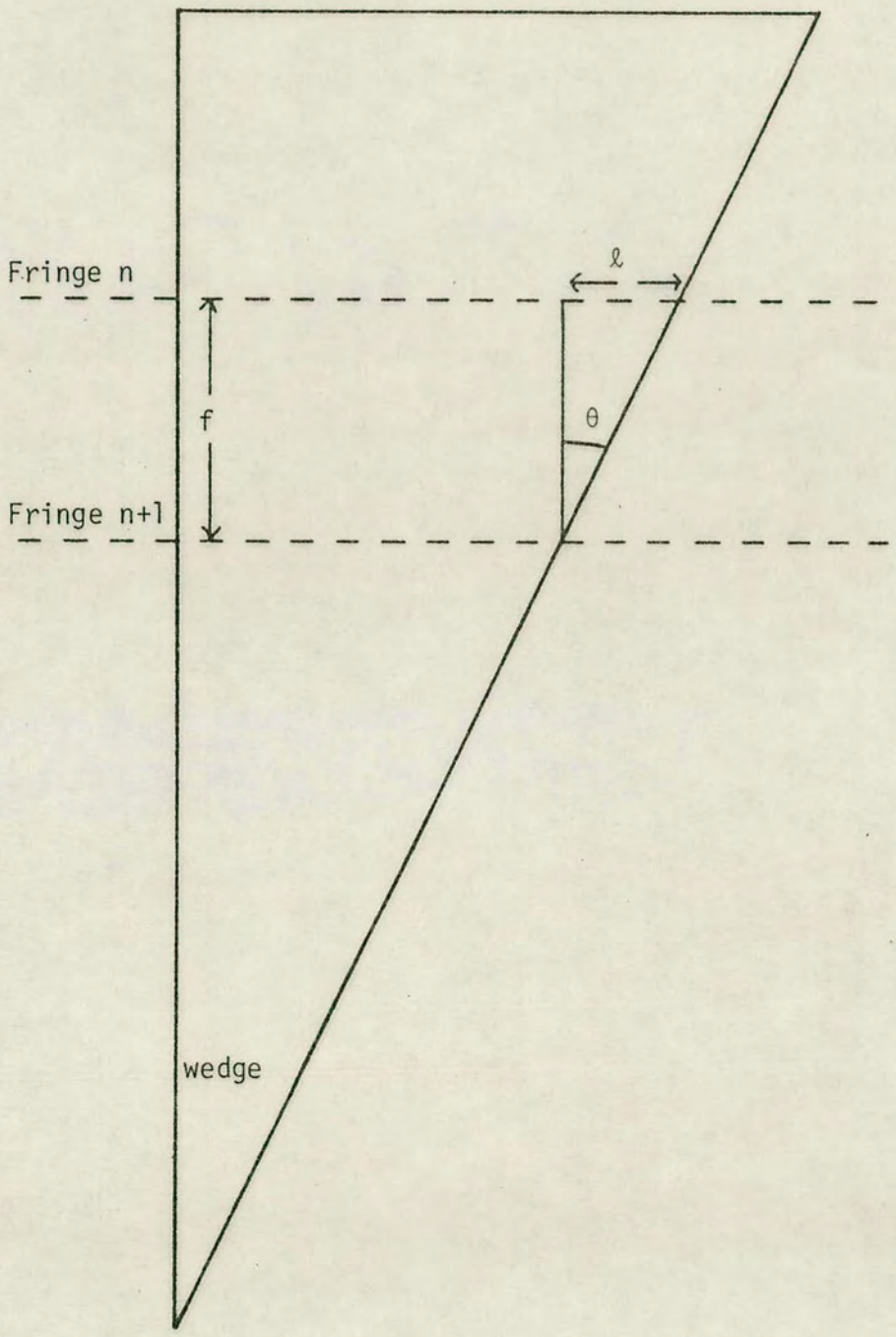

FIGURE 5.7

36 fringes were counted in 8.40 $\pm$0.05 mm by using a travelling microscope. This yields an average fringe spacing (f) of 0.233 $\pm$ .001 mm. With λ (for MoKα) = 0.709 Å, (1-n) was calculated to be $1.56 \pm .04 \times 10^{-6}$. James[94] shows that (1-n) may be calculated for a crystal with cubic symmetry from the expression

$$(1-n) = \frac{1}{2\pi} \frac{e^2}{mc^2} \lambda^2 \rho \qquad (5.4)$$

where e^2/mc^2 is the classical electron radius (2.82×10^{-15} m) and ρ is the electron density.

The measured result would be accurate if the experiment had been carried out in a vacuum. Before it can be deemed valid, the refractive index of air at STP must be calculated using Equation 5.4. In fact (1-n) is found to be 8.7×10^{-10} for MoKα, and so has negligible effect.

The refractive index for silicon with MoKα radiation may also be calculated from Equation 5.4, $\rho = \sum Z/a_o^3$ where Z is the number of electrons per unit cell (112). This expression yields (1-n) to be 1.58×10^{-6} which gives excellent agreement with the observed value.

5.4.2 Pendellösung Effect

It was shown in Chapter 3 how the ratio of beam intensities in the forward and diffracted directions during Laue geometry diffraction varied with crystal thickness, when the crystal was 'thin' enough for waves associated with all four dispersion surfaces only to be weakly absorbed. This is known as the Pendellösung effect.

With MoKα radiation ($\mu t = 2.2$) this phenomenon has a significant effect on the X-ray intensity from the interferometer. (Pendellösung fringes may be seen round the edge of the interferometer topographs due to the rounding of the wafers after etching). The distance between Pendellösung maxima, Δ, is related to the diameter of the dispersion surface and may be calculated from

$$\Delta = \frac{\pi a_o^3 \cos\theta}{r_e \lambda \sqrt{F_h F_{\bar{h}}}\, c} \qquad (5.5)$$

where $c = 1$ or $\cos 2\theta$ depending on σ or π polarization.
For $\lambda = 0.709 \times 10^{-10}$ m (MoKα radiation) $\Delta = 36.5$ μm (σ polarization)

In order to vary the effective wafer thickness, the interferometer was tilted about $\underline{h}$, the vector normal to the diffracting Bragg planes. The intensities were compared for five different angles of rotation and are shown in Fig 5.8. The angles of rotation and corresponding increased wafer thickness are given in Table 5.2 for a wafer thickness t_o of 350 $\pm$5 μm.

TABLE 5.2

ϕ	Δt (μm)
0^o	0
4^o	0.9
8^o	3.4
12^o	7.8
16^o	14.1

where $\Delta t = t_o (\sec\phi - 1)$. By using a microdensitometer it appeared

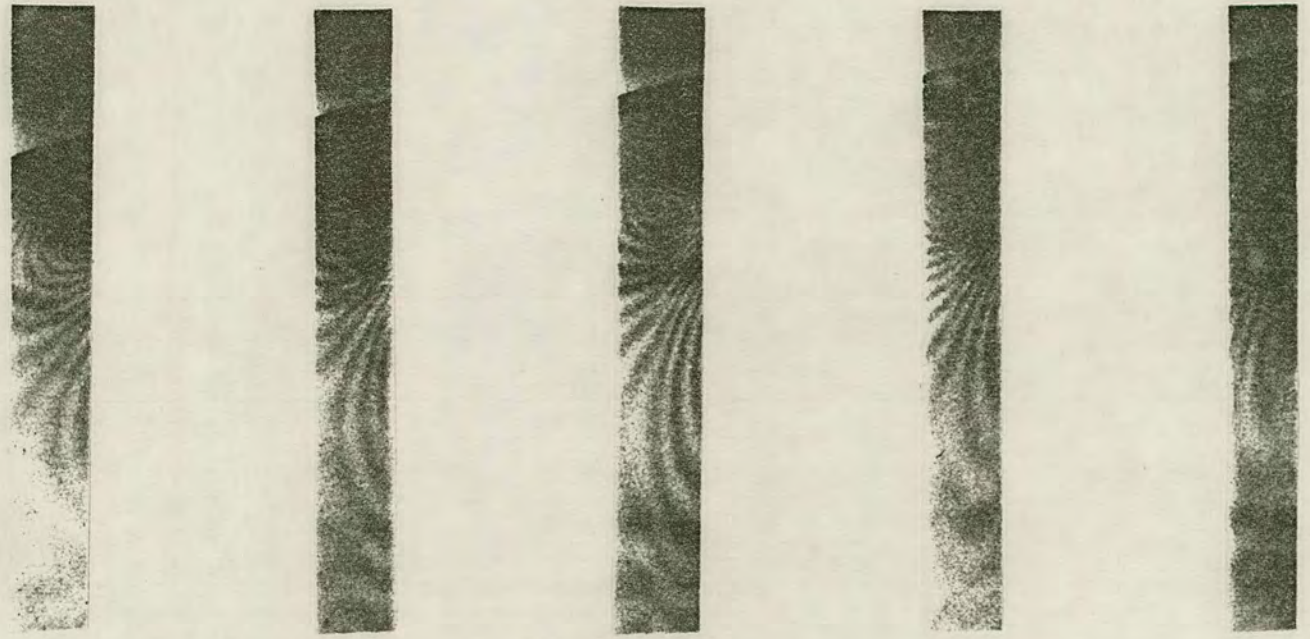

(a) $\phi = 0^{o}$ (b) $\phi = 4^{o}$ (c) $\phi = 8^{o}$ (d) $\phi = 12^{o}$ (e) $\phi = 16^{o}$

FIGURE 5.8: Contrast variation as a function of rotation of interferometer about the normal to the Bragg planes
(02$\bar{2}$ reflection, MoKα radiation)

that there was a significant variation - the intensity appeared to be a maximum for $\phi = 8^{o}$. As a result of this experiment, all interferometry topographs involving MoKα were optimised for maximum intensity. Theoretically this occurs for wafer thicknesses $(m \pm \frac{1}{4})\Delta$ where m is an integer and Δ = 36.5 μm. From these results, it would imply that the present wafer thickness is 352 μm (with m = 9).

5.5 DOUBLE CRYSTAL EXPERIMENTAL TECHNIQUE

The geometrical arrangement of the double crystal spectrometer has been described in Chapter 4. Although the instrument may be used most effectively for topographical work, in these experiments it was used in order to gain information about the shape of the rocking curve. As shown in Chapter 4, the width of the rocking curve for perfect sample and reference crystals is of the order of 1-2 seconds of arc. For accurate measurements of these curves, it is essential to have a very stable system. As with the travelling source arrangement of Fig 5.4, the crystal rotation is controlled by a pulse stepper motor connected to a micrometer via a gear box. The micrometer then rotates the axis on which the crystal is mounted,by a lever arm. With this arrangement, the crystal is caused to rotate by 1/20 second of arc for every pulse to the stepper motor.

Since this system is so sensitive, it is necessary to enclose the whole double crystal spectrometer in a water jacket in order to maintain a constant temperature. Despite this, it was found that the angular position of the rocking curve would drift during the course of its measurement. It was also found that the measurement of many rocking curves by manual methods became tedious.

For these reasons a system was designed to automate the process completely, with rocking curve data being outputted on paper tape

so that computer analysis could be immediately available (Fig 5.9).

A Racal pulse counter was linked via a pulse-height analyser to an X-ray scintillation counter monitoring the intensity of the diffracted beam from the crystal. The counting period could be chosen (10, 1, 0.1 seconds, etc), and the number of counts stored for a length of time (variable up to 10 seconds) when a new count cycle would be automatically initiated. During the holding period, a predetermined number of pulses would be passed to the stepper motor in order to rotate the crystal such that a new reading could be taken. The circuitry for this was built using TTL components and is illustrated in Fig 5.10.

The Racal pulse counter had a parallel BCD output which required an interface to the teletype. This was essentially a parallel to serial converter and is shown in Fig 5.11. A typical output from the teletype is given in Fig 5.12, and after computer processing, in Fig 5.13.

An added refinement was a shutter arrangement to select alternately two points on the sample crystal for analysis. The distance between these two points could be varied between 2 mm to 3 cm. Thus, for example, diffused and undiffused regions of crystal could be analysed simultaneously. Also, the variation of angular position of the rocking curve across the crystal (due either to angular variation or spacing of the Bragg planes) could be measured by keeping one point on the crystal fixed as a reference, and scanning across with the other.

The shutter was controlled by a solenoid which changed state with every burst of pulses to the stepper motor. The shutter and

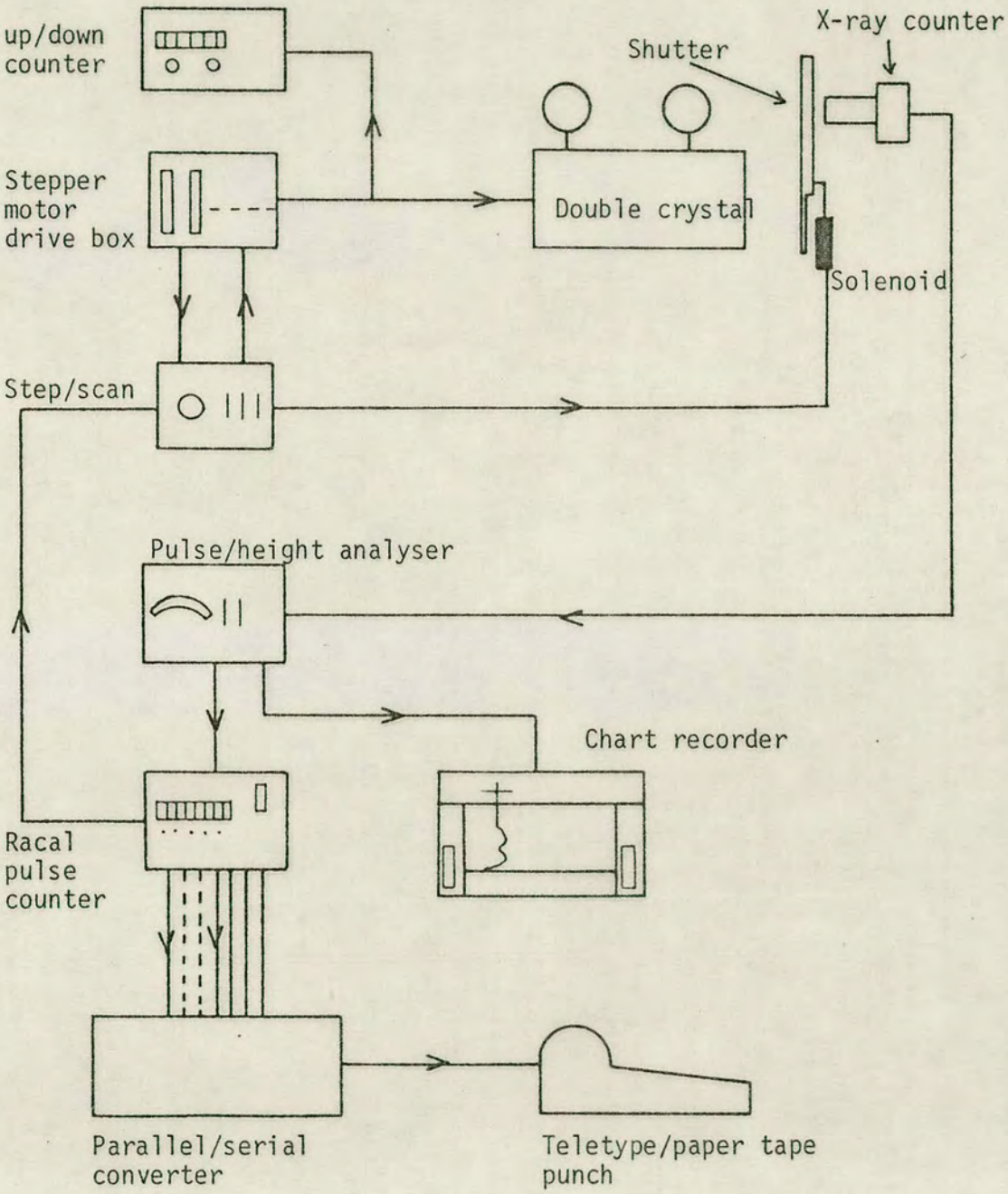

FIGURE 5.9: System for automatic rocking curve measurements

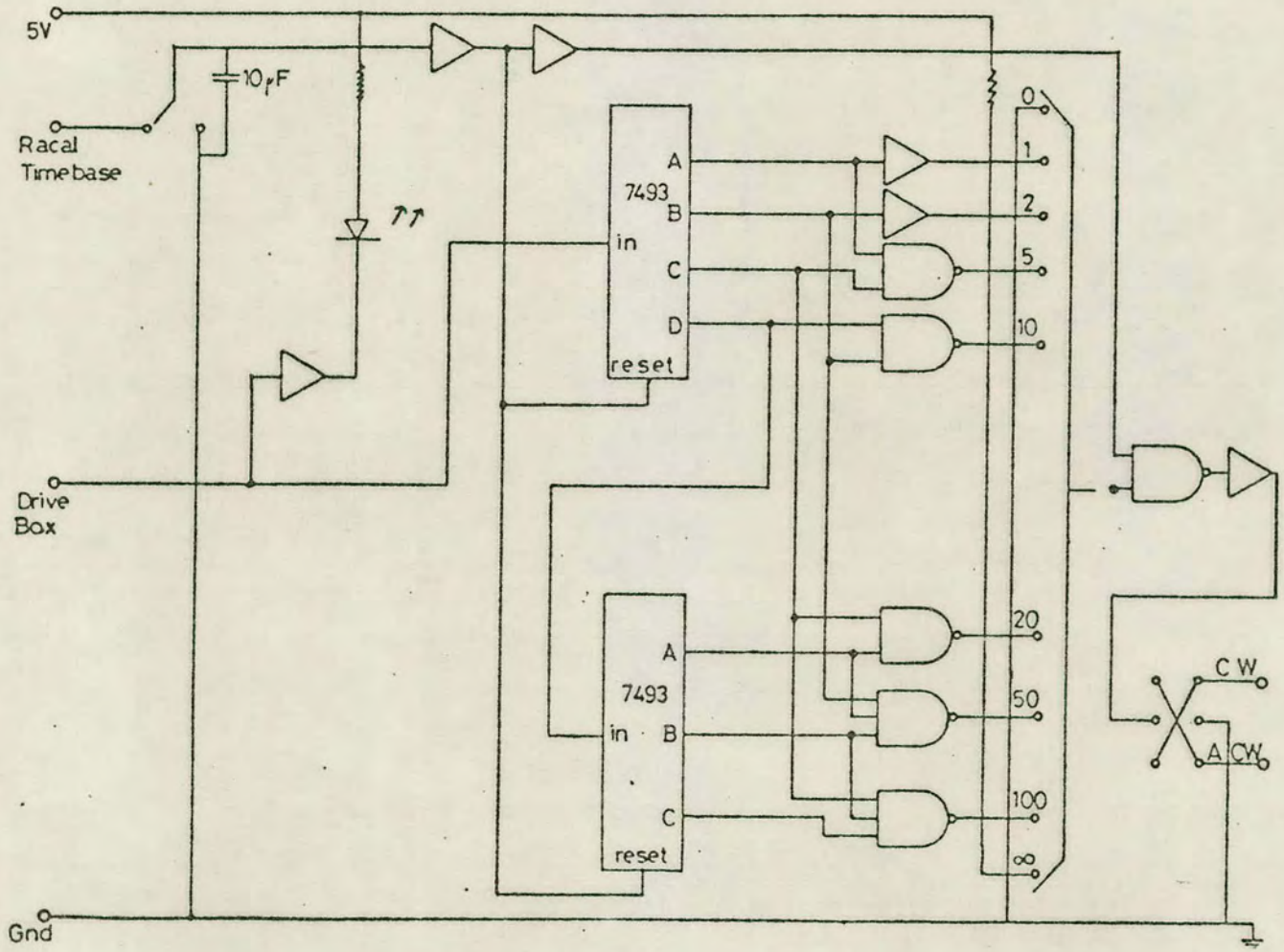

FIGURE 5.10: Step/scan electronic circuitry

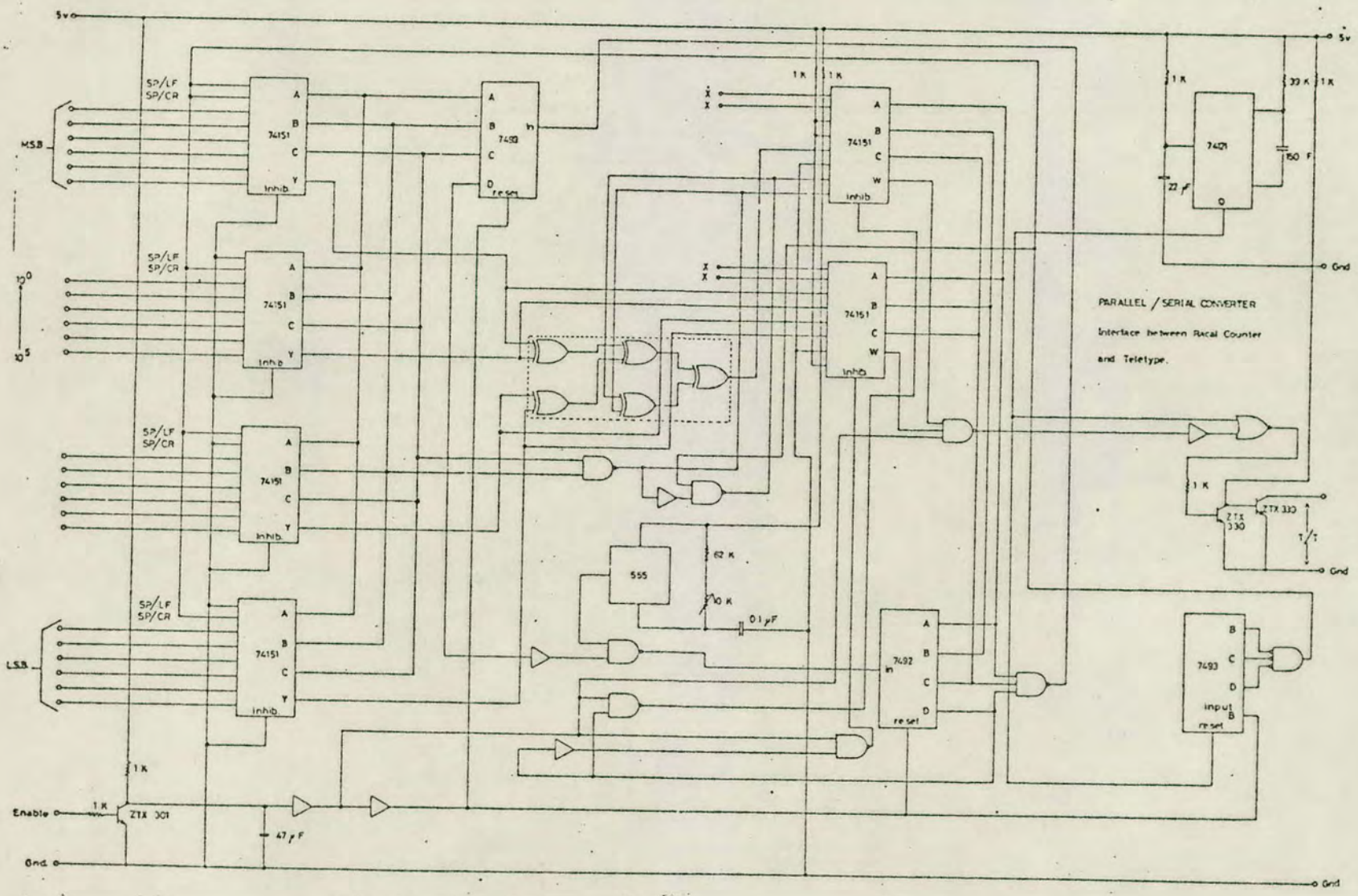

FIGURE 5.11: Parallel/serial teletype interface

000669	000656	000691	000685	000693	000688	000689	000669
000631	000680	000669	000668	000665	000662	003087	000652
000676	000642	000661	000656	000637	000648	000635	000684
000648	000658	000661	000639	000657	000647	000663	000673
000662	000697	000668	000693	000690	000743	000683	000720
000706	000745	000723	000702	000705	000719	000703	000739
000674	000757	000688	000803	000718	000891	000732	001081
000779	001394	000848	001718	000903	001979	001068	001937
001422	001593	001777	001328	002049	001011	002375	000812
002215	000784	002002	000752	001519	000712	001121	000695
000932	000668	000842	000656	000775	000655	000760	000658
000711	000660	000679	000662	000679	000629	000673	000647
000691	000622	000683	000641	000675	000659	000662	000647
000641	000641	000651	000641	000668	000637	000656	000615
000649	000643	000660	000632	000610	000644	000654	000659

FIGURE 5.12: Teletype output giving rocking curve data.

FIGURE 5.13: Data of Figure 5.12 after computer processing.

slits were constructed out of tantalum sheet and the main body of brass. The experimental arrangement for the double crystal is shown in Fig 5.14 together with the automatic shutter described above.

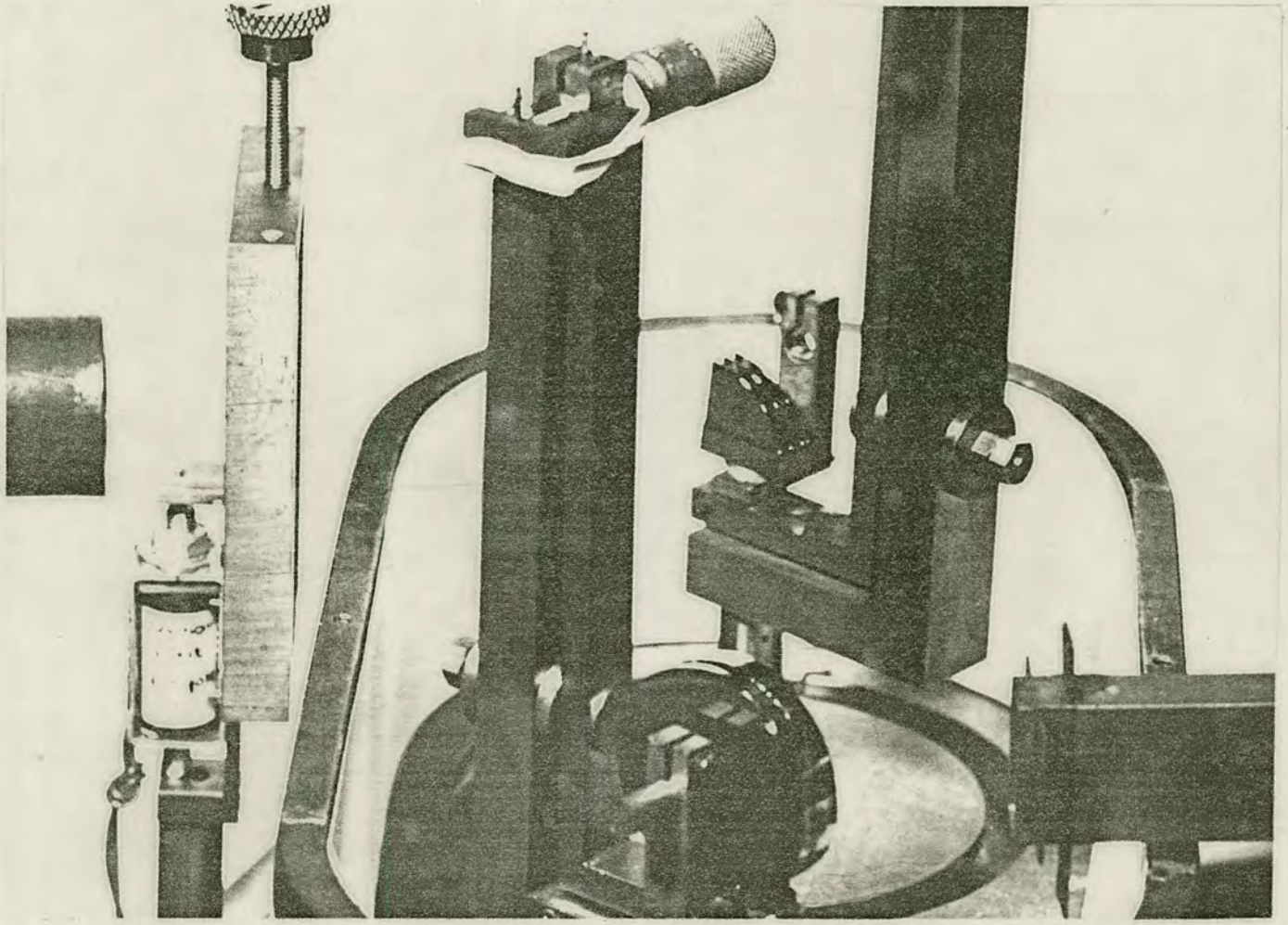

FIGURE 5.14: Double crystal experimental arrangement showing automatic shutter. An interferometer is acting as sample crystal.

CHAPTER 6: ANALYSIS OF DISLOCATION IMAGES

After two preliminary attempts at selective oxidation of an interferometer, some dislocation images were noticed and analysed (after removal of the oxide). Hart[66] performed similar work, but since the dislocations which he observed lay in different wafers of the interferometer, their images superposed in some instances resulting in complex and sometimes ambiguous interpretation. As it will be shown later, all the dislocations observed in these experiments were to be found in the same wafer, namely the splitter. Hence, all the dislocations could be unambiguously identified in each topograph.

Dislocations are imperfections which are invariably found in great numbers in all naturally grown crystals. It is only with the requirement for dislocation free crystals such as silicon, germanium and quartz in the semiconductor industry that the technology for growing such crystals has been developed. The appearance of just a few dislocations in originally dislocation free material is therefore particularly interesting.

There are many different forms of dislocation (Cottrell[112]), but the two basic types are known as edge-type and screw-type dislocations. An edge-type dislocation is shown in Fig 6.1(a). This type of dislocation can be considered to arise as a result of partial internal slip in the plane ABCD along the direction BC. The vector in the direction BC is called the Burger's vector, $\underline{b}$, and has magnitude equal to the slip distance, which in the figure is one interplanar spacing. Obviously the magnitude may be any multiple of this

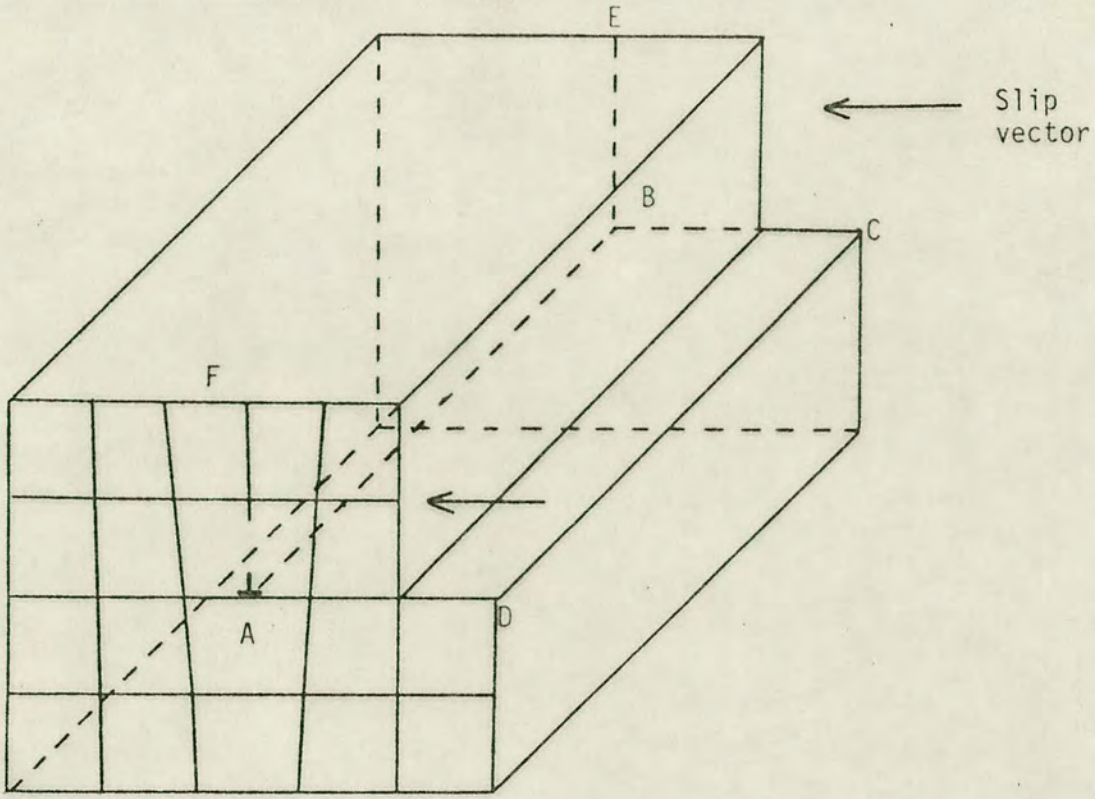

(a)

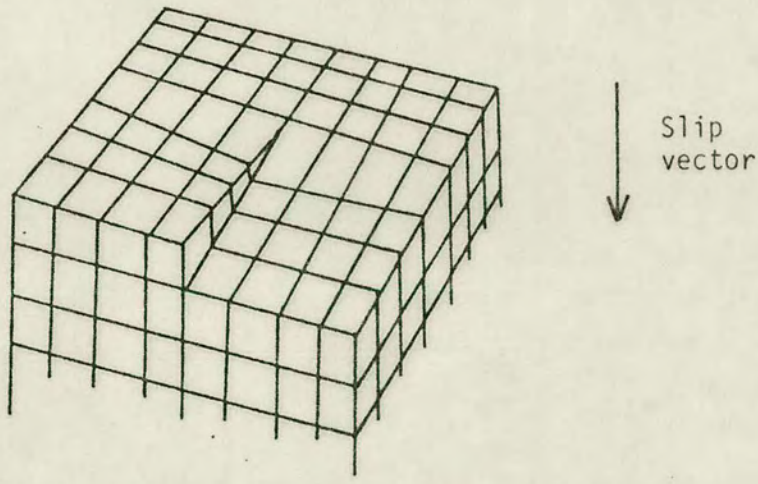

(b)

FIGURE 6.1: Schematic diagram of (a) an edge-type dislocation and (b) a screw-type dislocation

depending on the number of extra half planes (such as ABEF) which are caused by the dislocation. From energy considerations, it can be shown that for crystals with the diamond structure (eg germanium and silicon) the most likely edge-type dislocation has slip plane {111} with Burger's vector in the direction <110>. It will be seen from Fig 6.1(a) that the crystal lattice is in a state of mechanical strain around the dislocation edge AB such that the material is in tension below and in compression above the edge. Since the presence of an impurity atom will tend to ease this strain and thereby lower the energy state, impurity precipitation will occur along the dislocation edge. Since electrical conduction paths are formed as a result of this precipitation dislocations may be a serious yield hazard and are to be avoided in semiconductor fabrication.

Fig 6.1(b) is a schematic illustration of a screw-type dislocation. In this structure the slip takes place parallel to the line of the dislocation rather than perpendicular to it as is the case with an edge-type dislocation.

It will be seen from Fig 6.1 that atomic planes with their normals perpendicular to the Burger's vector $\underline{b}$ will be unstrained by the dislocation, and so the dislocation will be invisible when diffraction takes place from these planes. This condition alternatively may be written

$$|\underline{h}.\underline{b}| = 0 \qquad (6.1)$$

By similar arguments, it can be shown that the number of extra half fringes N observed in a moiré topograph can be expressed as

$$N = \pm |\underline{h}.\underline{b}| \qquad (6.2)$$

In Burger's vector determination three unknowns must be solved, (u, v, w). Hence three independent equations must be obtained. By algebraic manipulation it can be shown that for this to be the case, the three chosen values of $\underline{h}$ must not be coplanar.

The reflections used in this experiment are indicated in the stereographic projection of Fig 6.2, together with an illustration of an interferometer to show its orientation. In order to show up the dislocation in a moiré topograph it is necessary to introduce a small twist to one of the wafers. This has the effect of producing horizontal rotation fringes by which the dislocation image may be defined, and even dislocations lying close together may be resolved. A comparison between Figs 6.3(a) and 6.3(b) will illustrate this. Table 6.1 lists the conditions under which the topographs of Fig 6.3 were taken.

TABLE 6.1

Fig 6.3	radiation	$\underline{h}$	moment (about 111)
a	MoKα	$0\bar{2}2$	-
b	MoKα	$0\bar{2}2$	ACW
c	CuKα	$0\bar{2}2$	ACW
d	CuKα	$0\bar{2}2$	ACW (15^{o} rotation about $\underline{h}$)
e	CuKα	$\bar{2}20$	CW
f	CuKα	$20\bar{2}$	CW
g	MoKα	$\bar{1}3\bar{1}$	ACW

Fig 6.4 defines the positions of the dislocations (A-M).

The first task is to establish in which wafer the various dislocations lie. This was achieved by taking two topographs using the

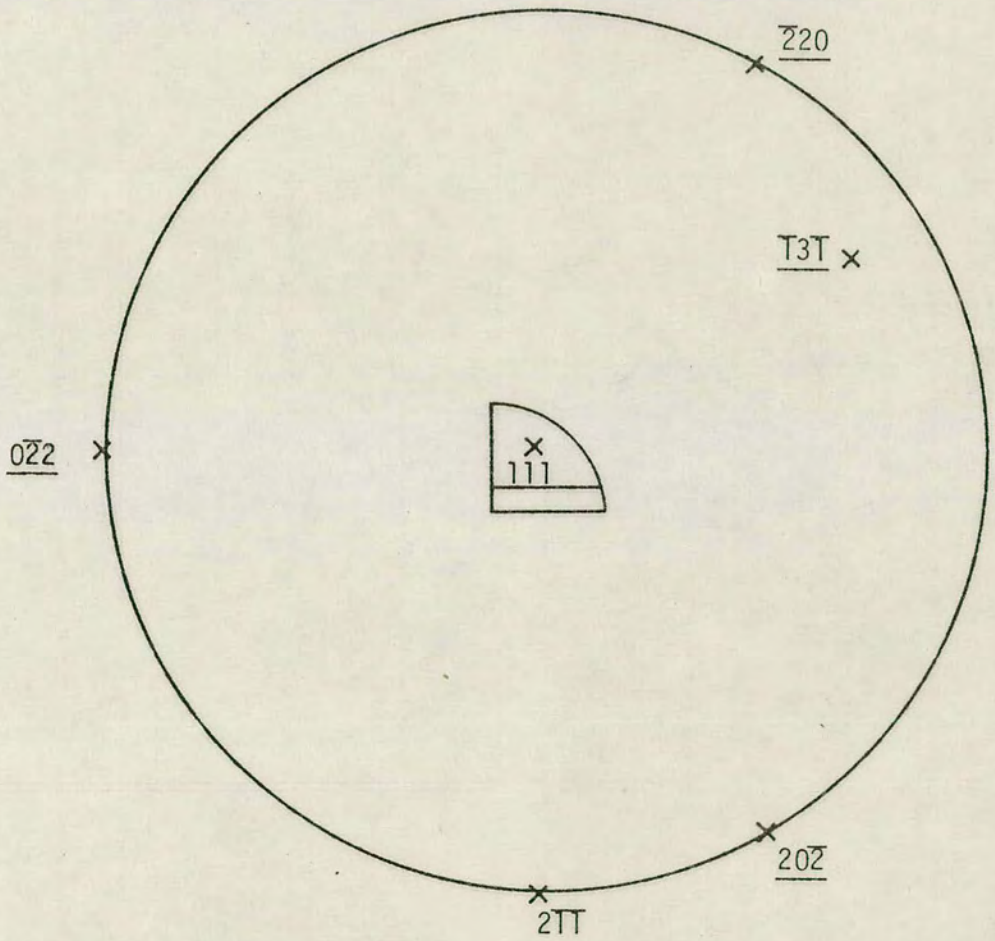

FIGURE 6.2: Stereographic projection showing reflections (underlined) used for Burger's vector determination

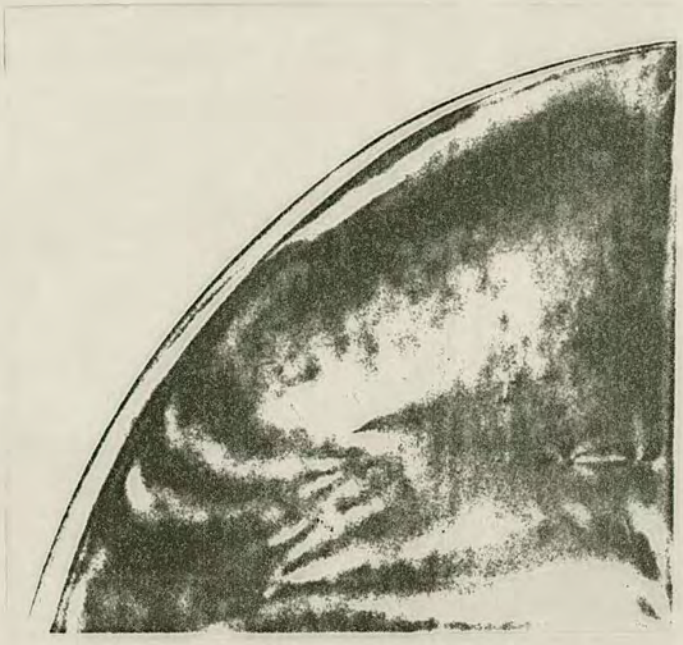

(a)

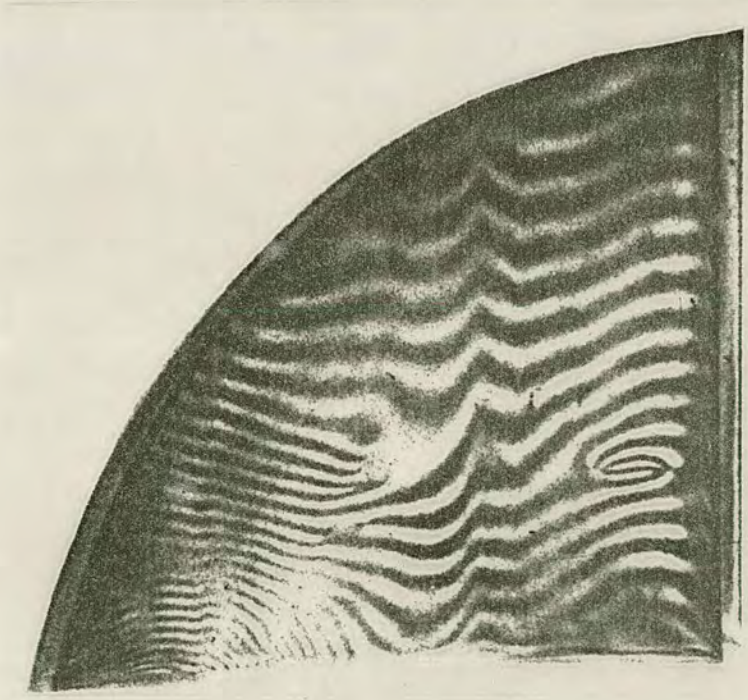

(b)

FIGURE 6.3(a): Dislocation images
(b): Same as (a) but with a small torque applied to introduce rotation moiré fringes
$0\bar{2}2$ reflection; MoKα radiation

(c)

FIGURE 6.3: Dislocation images - $0\bar{2}2$ reflection, CuKα radiation

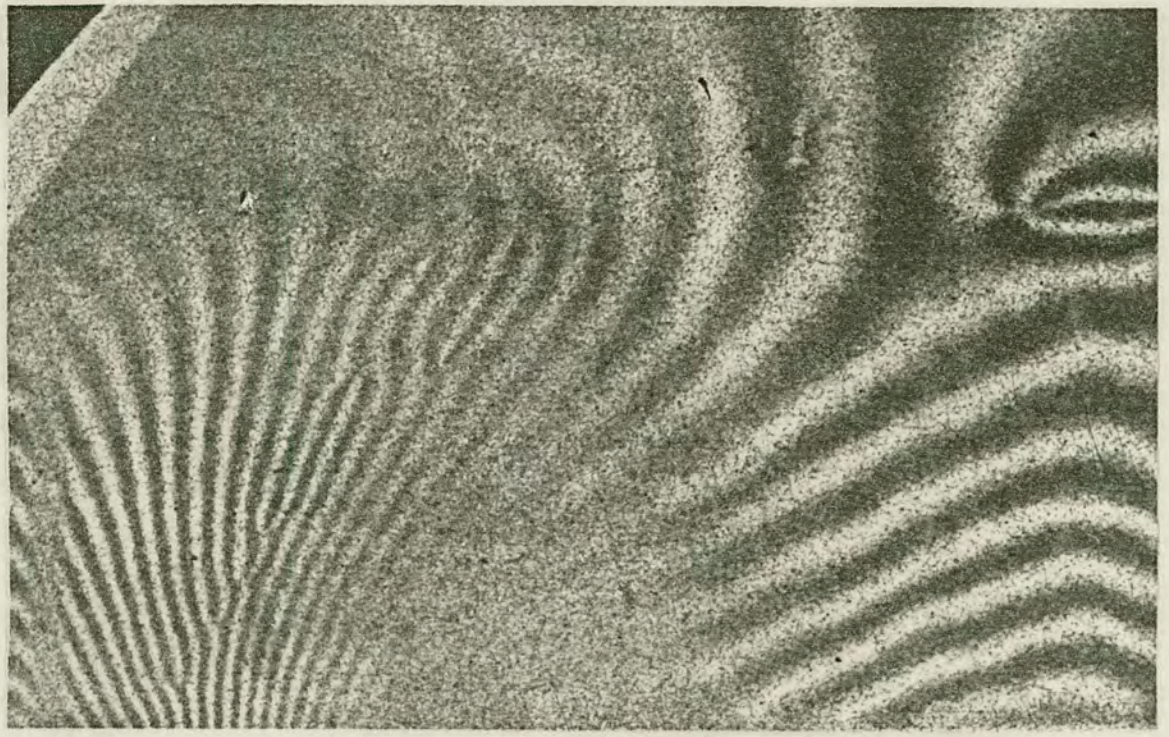

(d)

FIGURE 6.3: Dislocation images - $0\bar{2}2$ reflection; CuKα radiation

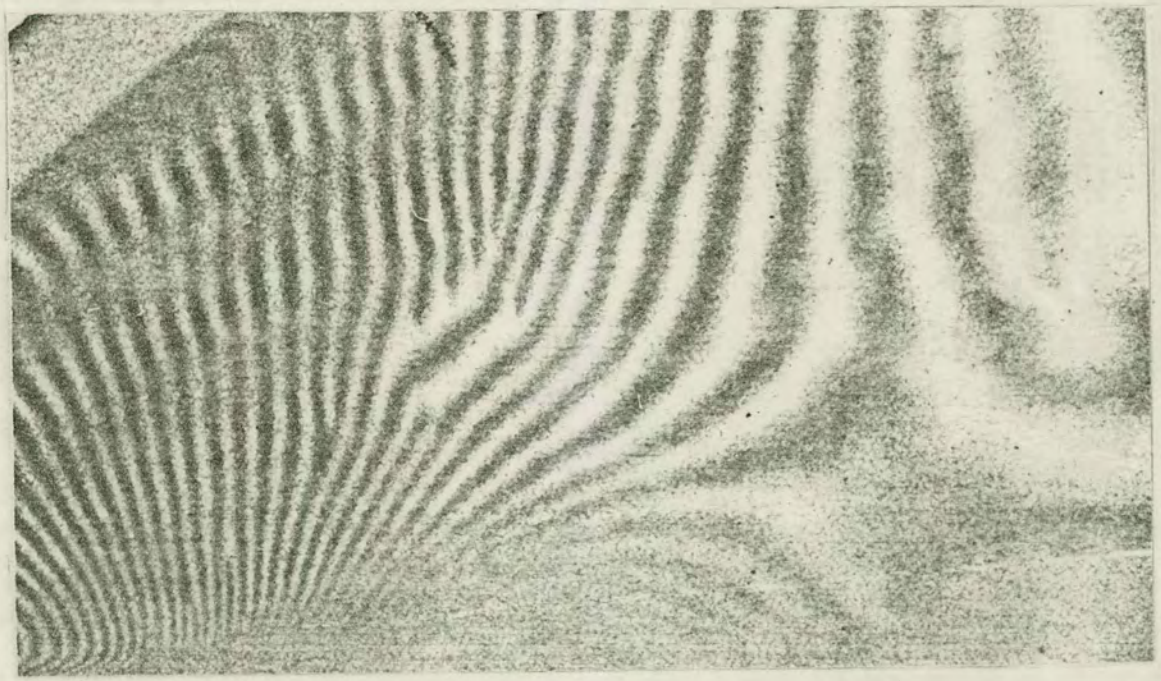

(e)

FIGURE 6.3: Dislocation images; $\bar{2}20$ reflection, CuKα radiation

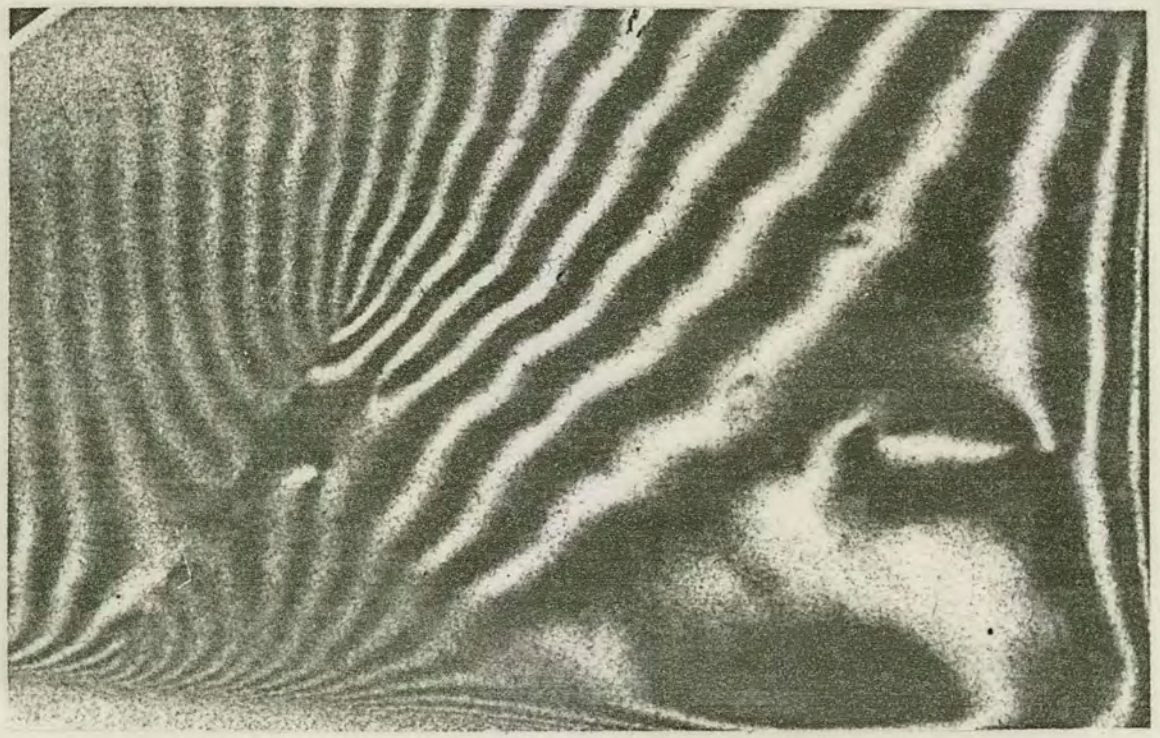

(f)

FIGURE 6.3: Dislocation images - $20\bar{2}$ reflection, CuKα radiation

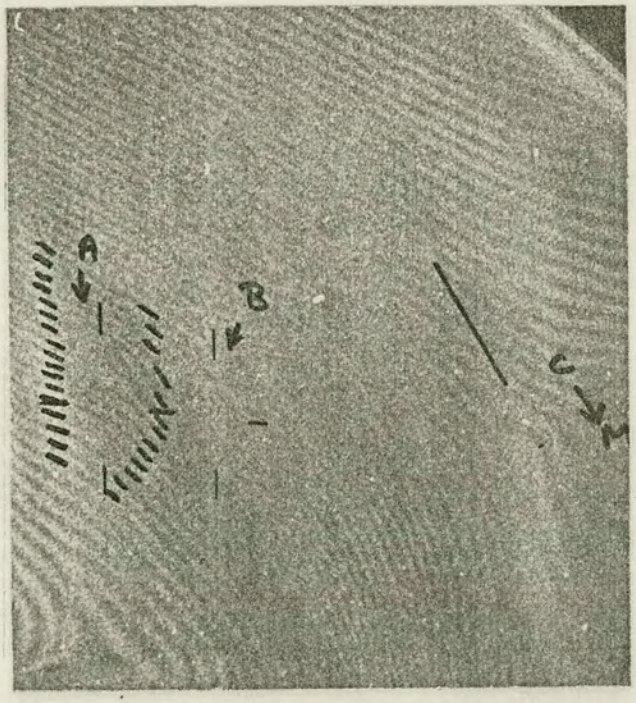

(g)

FIGURE 6.3: Dislocation images. Dislocations C-M are too indistinct to be seen in this topograph.

T3T reflection, MoKα radiation

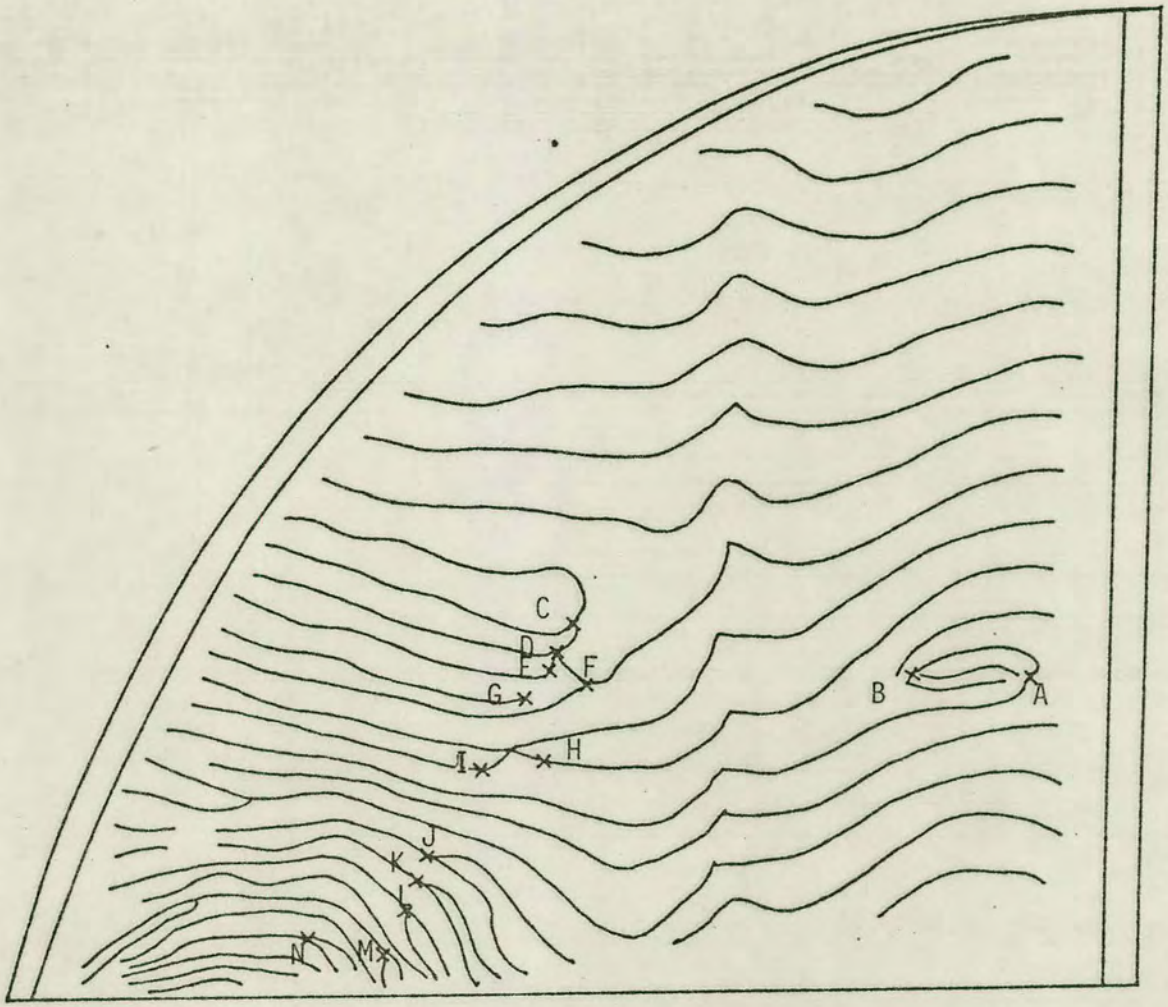

(a)

FIGURE 6.4: Dislocation images labelled A-M (see Figure 6.3(b))

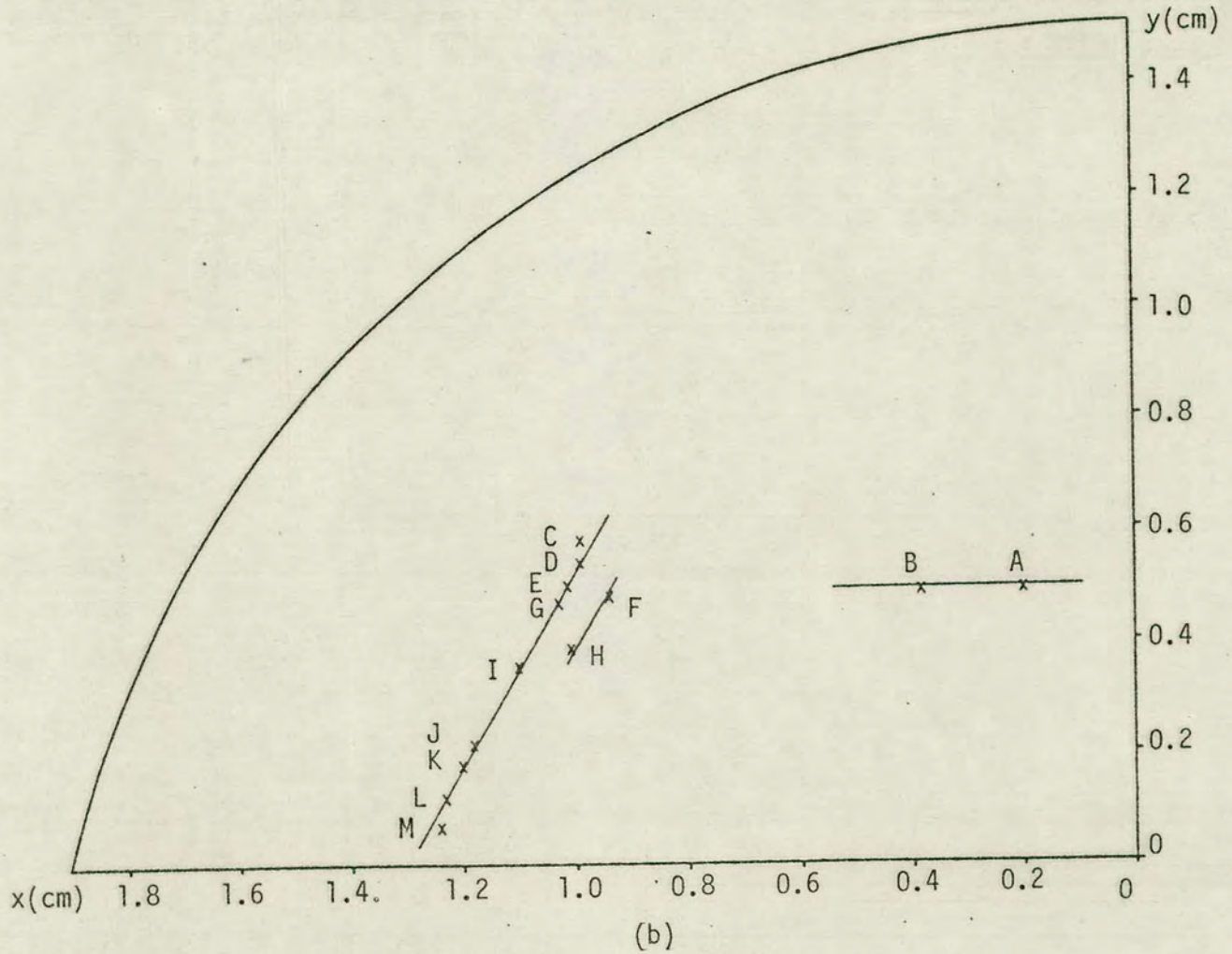

(b)

FIGURE 6.4: Plotting of dislocation co-ordinates

same reflection, but rotating the interferometer through 15° about $\underline{h}$ for the second topograph. In this way, the relative displacements of the dislocation images yield their positions (Fig 6.5). Table 6.2 lists the dislocations under study and gives the mean coordinates (mm) of the projected dislocation images in Figs 6.3(b) and 6.3(c) (correcting for the image projection) compared with the coordinates measured in Fig 6.3(d) (ie after 15° rotation about $\underline{h}$)

TABLE 6.2

Dislocation	(b)	(c)	$\bar{x}$	$\bar{y}$	(d)
A	1.9,4.8	1.9,5.0	1.9	4.9	2.1,4.8
B	3.9,4.8	3.9,5.0	3.9	4.9	2.1,4.8
C	9.7,5.9	9.7,5.9	9.7	5.9	10.0,5.7
D	10.0,5.3	9.3,5.6	9.9	5.5	9.7,5.4
E	10.1,5.0	10.1,5.2	10.1	5.1	9.8,5.0
F	9.6,4.7	9.3,5.0	9.5	4.9	9.2,4.8
G	10.4,4.5	10.1,4.8	10.3	4.7	10.0,4.5
H	10.1,3.8	10.0,3.8	10.1	3.8	9.9,3.5
I	11.2,3.5	10.9,3.7	11.1	3.6	10.8,3.4
J	11.7,2.3	11.8,2.1	11.8	2.2	11.6,2.0
K	11.9,1.7	12.1,1.8	12.0	1.8	11.7,1.6
L	12.2,1.2	12.2,1.4	12.2	1.3	12.1,1.2
M	12.4,0.7	12.3,0.9	12.4	0.8	12.4,0.6

If a dislocation is in the splitter wafer, its projected y coordinate remains unchanged. If it is in the mirror wafer the projected y coordinate will decrease by 0.9 mm. In this case one dislocation will produce two images- originally, it was thought that images A and B were such a dislocation, but their positions remained constant irrespective of reflection. If the dislocation is in the analyser, its projected y coordinate will decrease by 1.8 mm (Fig 6.5).

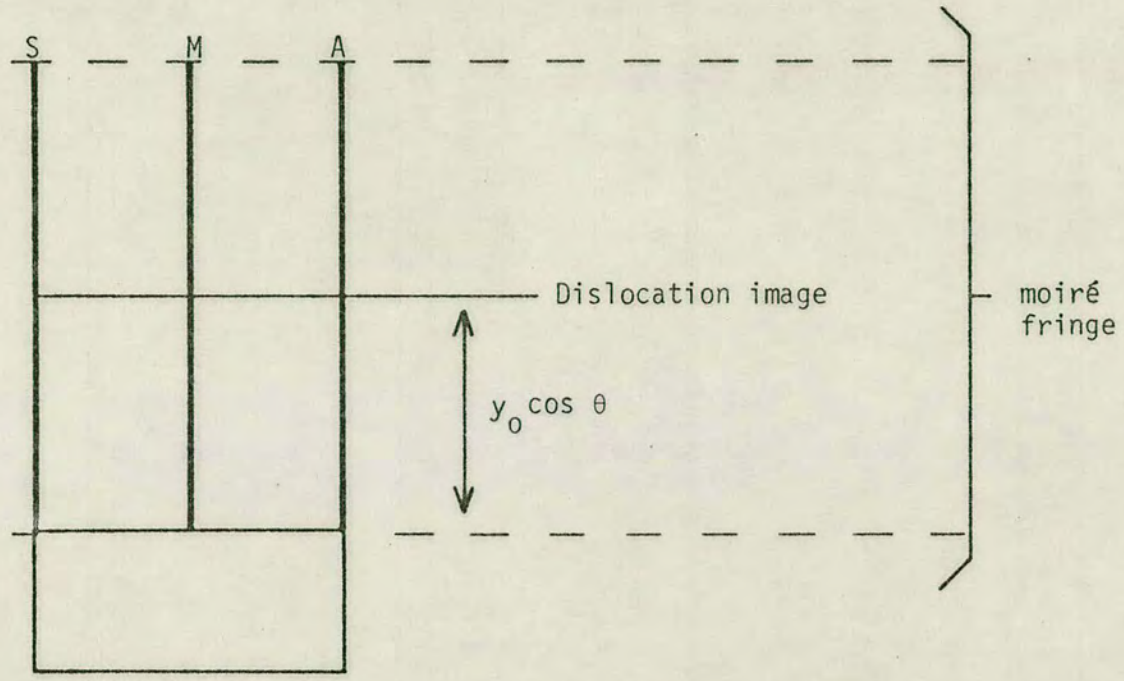

(a)

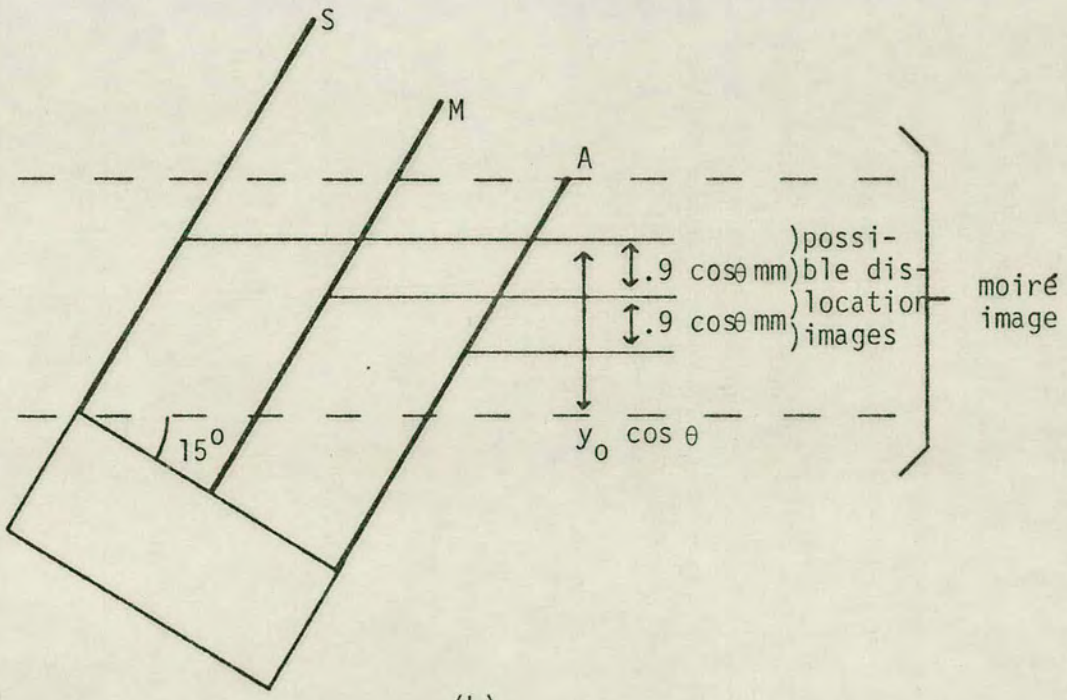

(b)

FIGURE 6.5: Effect of rotation about h on moiré images

It can be seen at once, however, that in each case the y coordinate remains unchanged implying that all the dislocations are in the splitter wafer.

By studying all the topographs it may be seen that dislocations A and B are a complementary pair since the extra half fringes are always in opposite directions, ie $\underline{b}_A = -\underline{b}_B$. Each reflection yields an equation, by which $|\underline{h}.\underline{b}| = \pm N$ may be solved. For $\underline{b}$ = [uvw]

$$-2v \quad +2w \quad = \pm 4 \quad \text{(Figs 6.3(b),6.3(c),6.3(d))} \qquad (6.3a)$$

$$-2u \quad +2v \quad = \overline{+}2 \quad \text{(Fig 6.3(e))} \qquad (6.3b)$$

$$2u \quad -2w \quad = \overline{+}2 \quad \text{(Fig 6.3(f))} \qquad (6.3c)$$

$$-u \quad +3v \quad -w \quad = \overline{+}4 \quad \text{(Fig 6.3(g))} \qquad (6.3d)$$

It can be seen that the first three equations are not independent - eg Equation 6.3c = -(Equation 6.3a + Equation 6.3b). This is to be expected since the three reflections used are in the same zone. Solving these four equations yields $\underline{b}_A = \pm a_o[01\bar{1}]$ and hence $\underline{b}_B = a_o[01\bar{1}]$. This result is not surprising since <110> type dislocations are by far the most common.

Unfortunately, it is impossible to count the extra half fringes corresponding to dislocations C-M in Fig 6.3(g) and so a little more ingenuity is required to solve their Burger's vectors. If their coordinates of Table 6.2 are plotted (Fig 6.4(b)), it will be seen that dislocations CDEGIJKLM all lie on a straight line at exactly 60^o from the horizontal $(2\bar{1}\bar{1})$. This line has vector direction $10\bar{1}$. It is reasonable to suppose that this line lies in the dislocation slip plane $\underline{S}$ [abc]. Hence for dislocations CDEFGI

$$\underline{S}.[10\bar{1}] = 0 \rightarrow a - c = 0 \qquad (6.4a)$$

$$\underline{S}.\underline{b} = 0 \rightarrow au + bv + cw = 0 \qquad (6.4b)$$

$$-2v \quad +2w = \pm 1 \quad \text{(Figs 6.3(b), 6.3(c), 6.3(d))} \qquad (6.4c)$$

$$-2u \quad +2v \quad = \pm 1 \quad \text{(Fig 6.3(e))} \qquad (6.4d)$$

$$2u \quad -2w = \mp 2 \quad \text{(Fig 6.3(f))} \qquad (6.4e)$$

The solution of these equations gives

$$\underline{S} = 1\bar{1}1 \text{ and } \underline{b} = \pm\tfrac{1}{2}\, a_o[10\bar{1}]$$

or $\underline{S} = 1\bar{2}1$ and $\underline{b} = \pm\tfrac{1}{2}\, a_o[10\bar{1}]$ or $\mp\tfrac{1}{2}\, a_o[123]$ or $\pm\tfrac{1}{2}\, a_o[321]$

Since <110> type dislocations with <111> type slip planes are most common, the dislocation Burger's vector may be classed as follows:

Dislocation	Burger's vector
A	$\pm a_o[01\bar{1}]$
B	$\mp a_o[01\bar{1}]$
CDEFGI	$\pm a_o/2\,[10\bar{1}]$
HJKLM	$\mp a_o/2\,[10\bar{1}]$

CHAPTER 7: OXIDE INDUCED STRAIN

It is a well known phenomenon that an oxide grown on a silicon wafer induces strain in the substrate. In fact, strain will always be present when one material is grown, vapour-deposited or plated on another. One of the first studies of electrodeposited layers was carried out by Stoney[113] who showed how the stress may be calculated from measurements of the radius of curvature arising from mechanical warpage. When SiO_2 is thermally grown on a silicon wafer, this warpage may even be observed with the naked eye for thick oxides (>1 μm) grown on thin substrates (~150 μm), after the oxide has been stripped from one face.

The origin of the stress has been attributed to several causes, in particular physical mismatch between the oxide and the substrate and also to the different coefficients of thermal expansion of Si and SiO_2 when the oxide is thermally grown in an oxidation furnace. Experiments[12-15] conclusively show that for thermal oxides, this latter cause is by far the dominant effect.

The thermal expansion coefficients for both silicon and SiO_2 are very dependent on temperature, so that care must be taken in calculating the contraction which takes place from, say, 950°C to room temperature. For example, $\alpha_{si} = 2.5 \times 10^{-6}$ at 293°K and 4.3×10^{-6} at 1000°K. The American Institute of Physics handbook[114] quotes the expansion $\Delta\ell/\ell$ at various temperatures. For a cooling from 950°C to room temperature, silicon contracts by an amount $\Delta\ell/\ell = 3.63 \times 10^{-3}$ and SiO_2 by $\Delta\ell/\ell = 4.95 \times 10^{-4}$. Hence the oxide will be in a state of compression and the substrate in tension under the oxide and in compression

elsewhere. This stress is relieved by mechanical warpage resulting in a convex bowing (Fig 7.1).

Using the above figures the net strain in the oxide is therefore calculated to be 3.14×10^{-3}. Jaccodine and Schlegel[12] measured Young's modulus in such an oxide as 6.6×10^{11} dynes/cm^2 and Poisson's ratio as 0.18. In any stress system, the extensions in the directions of the axes (ε) and the normal stresses across planes at right-angles to the axes (σ) are connected by the equations (Love[115])

$$\varepsilon_x = \frac{1}{E}\{\sigma_x - \nu(\sigma_y + \sigma_z)\}$$

$$\varepsilon_y = \frac{1}{E}\{\sigma_y - \nu(\sigma_z + \sigma_x)\} \qquad (7.1)$$

$$\varepsilon_z = \frac{1}{E}\{\sigma_z - \nu(\sigma_x + \sigma_y)\}$$

where E is Young's modulus and ν, Poisson's ratio.

For an oxide grown on a silicon substrate, the strain occurs only in the plane of the slice and not in the direction normal to it since it is not constrained in this direction. Hence, assuming isotropy in the plane of the slice (this will be shown later) $\varepsilon_x = \varepsilon_y$ and $\varepsilon_z = 0$. Also $\sigma_x = \sigma_y$ and $\sigma_z = 0$. This leads to the stress-strain relationship,

$$\sigma = \frac{E\varepsilon}{1-\nu} \qquad (7.2)$$

Using these figures for an oxide grown at 950^{o}C, the stress in the oxide may be calculated to be 2.5×10^9 dynes/cm^2.

Jaccodine and Schlegel[12] oxidised slices at temperatures ranging from 855^{o}C to 1200^{o}C and determined the stress by measuring the bowing caused by an oxide grown on one side and also by using an unsupported SiO_2 window as a balloon and measuring the strain as a function of air pressure inflating the balloon. The stress was found to range from

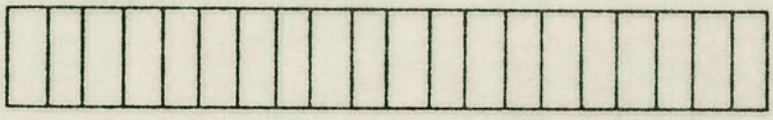

(a)

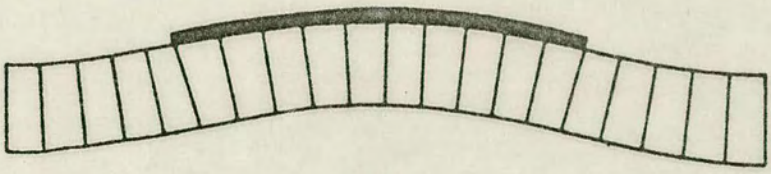

(b)

FIGURE 7.1: Silicon wafer before (a) and after oxidation, (b) showing mechanical warpage

2.1×10^9 dynes/cm^2 at 900^{o}C to 3.2×10^9 dynes/cm^2 at 1100^{o}C.

Blech and Meieran[15] measured the lattice distortion underneath an oxide film by observing the anomolously enhanced intensity of X-rays diffracted by the substrate. In so doing, they developed a model from elasticity theory to predict the strain as a function of position within the substrate. This model is developed by Love[115] for a semi-infinite isotropic body. As such, it is only applicable to the region of substrate in the immediate vicinity of the oxide (ie to a depth much less than the slice thickness). The model is therefore able to explain the relatively high strain field at the oxide edge which Blech and Meieran observed, but does not predict the strain fields which may be found through the depth of the slice. Hashizume[34] uses this model to predict strain within the whole slice but is unable to correlate theory with experimental measurements. Blech and Meieran measured a compressive stress of 3×10^9 dynes/cm^2 for an oxide grown at 1200^{o}C.

Brotherton et al[14] investigated the relationship between oxide stress and the density of interface surface charges. The model that they developed was based on bimetallic strip theory, and by making lattice parameter measurements found the stress in an oxide grown at 1200^{o}C to be 2.5×10^9 dynes/cm^2.

Kato and Patel[35-37], by observing the trajectories of X-ray beams through a strained wafer and adopting the model for a semi-infinite body proposed by Blech and Meieran[15], obtain the high value of 4×10^9 dynes/cm^2 for oxides grown at 950^{o}C.

7.1 ELASTICITY MODEL

The use of an interferometer for measuring oxide induced strain is therefore the first 'direct' method in which the strain may be

immediately 'seen' as moiré fringes. The bimetallic strip model of Brotherton et al[14] was ruled out since it does not predict the strain-field surrounding an oxide region. It was not possible to use the theory for a semi-infinite body used by Blech and Meieran[15] since a 300 μm wafer with a 3.5 diameter disc grown on it should be considered as a thin plate.

Love[115] develops an expression relating the displacements u and v in the directions x and y respectively as a function of position in a two-dimensional elastic system when a force is applied at the origin. He then applies a correction factor such that the theory may be extended to a thin plate.

If an element of area within an oxide film is under stress, then it will exert forces in all directions on its elemental neighbours. Within the oxide shape, therefore, all these forces will cancel out (provided that the oxide is uniform) but there will be resultant forces acting at and perpendicular to the oxide edge (Fig 7.2), so that only these forces need be considered.

If a force of $-2A\pi$ dynes/cm acts in the positive direction of the x axis, then provided that the body is isotropic, the displacements u, v at the point x, y are given by (Love[115])

$$u = \frac{\lambda+3\mu}{2\mu(\lambda+2\mu)} \; A \; \ell n \; r + \frac{\lambda+\mu}{2\mu(\lambda+2\mu)} \; A \frac{y^2}{r^2}$$

$$v = - \frac{\lambda+\mu}{2\mu(\lambda+2\mu)} \; A \frac{xy}{r^2} \qquad (7.3)$$

where $r = \sqrt{x^2 + y^2}$

and where $\lambda = \frac{E\nu}{(1+\nu)\,(1-2\nu)}$, $\mu = \frac{E}{2(1+\nu)}$

where E is Young's modulus of elasticity and ν Poisson's ratio.

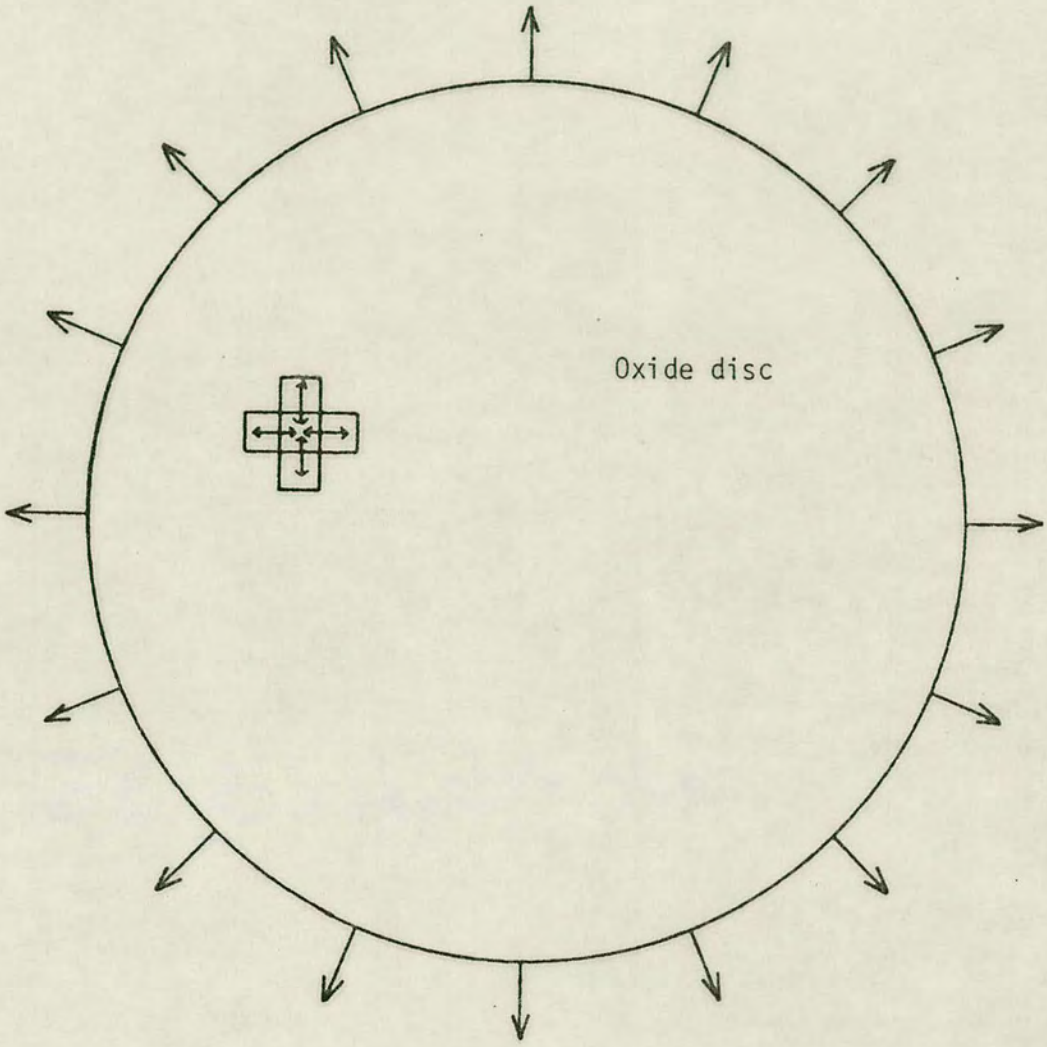

FIGURE 7.2: Elemental forces within oxide disc cancel. Forces acting on substrate effectively act around and normal to the oxide edge

These equations are valid for a two-dimensional elastic system. When the theory is extended to cover the displacements in a thin plate, λ must be substituted by λ' where $\lambda' = 2\lambda\mu/(\lambda+2\mu)$.

It is reasonable to assume that the silicon wafer undergoes mechanical warpage such that it is uniformly curved through its thickness. For the wafer to be in equilibrium the net force must be zero and the total moment must also be zero.

Let the stress in the oxide be σ. If the thickness of the oxide is very much less than the thickness of the wafer, the force acting on an element dydz of the oxide edge can be considered constant throughout. The magnitude of this force is $F_{ox} = (\sigma dy)dz$ (see Fig 7.3). Since the wafer is assumed to bend uniformly, the forces acting in the substrate will be linear with depth (z) and so may be written

$$F(z) = cz + F_{int} \tag{7.4}$$

where c is a constant and F_{int} the force acting in the substrate at the Si-SiO_2 interface.

By resolving moments about y,

$$\int_0^{t_{si}} F(z)\, z\, dz + F_{ox} \int_0^{t_{ox}} z\, dz = 0 \tag{7.5}$$

ie

$$\frac{ct_{si}^3}{3} + F_{int}\frac{t_{si}^2}{2} = -\frac{F_{ox}\, t_{ox}^2}{2} \tag{7.6}$$

By resolving forces in x

$$\int_0^{t_{si}} F dz + F_{ox} \int_0^{t_{ox}} dz = 0 \qquad (7.7)$$

ie,

$$\frac{ct_{si}^2}{2} + F_{int}\, t_{si} = -\, F_{ox}\, t_{ox} \qquad (7.8)$$

By solving Equations 7.6 and 7.8,

$$\frac{F(z)}{F_{ox}} = \left[\frac{6z}{t_{si}} - 4\right] \frac{t_{ox}}{t_{si}} \qquad (7.9)$$

This force diagram is illustrated in Fig 7.3. It will be seen at once that the force in the substrate immediately underneath the oxide edge is opposite in sign to the force in the oxide. This means that whereas the oxide is in compression, the substrate is in tension. However, on the opposite side of the wafer the silicon is in compression with a neutral plane two-thirds of the wafer width from the oxide. This is due to the warpage of the wafer. As seen in Section 3.2.2 the interferometer is sensitive to strain on the inside of its splitter or analyser wafers, so that it is this compressive force that is of consequence here. From Equation 7.9, this force will be seen to be

$$F(t_{si}) = 2\frac{t_{ox}}{t_{si}} F_{ox} = 2\,(\sigma dy)\, dz\, \frac{t_{ox}}{t_{si}} \text{ dynes} \qquad (7.10)$$

This force may now be substituted in Equation 7.3 in order to calculate the resultant displacements at any point (x, y, t_{si}). An alternative way of arriving at the same solution is to constrain the wafer from bending such that the force acting in the substrate is

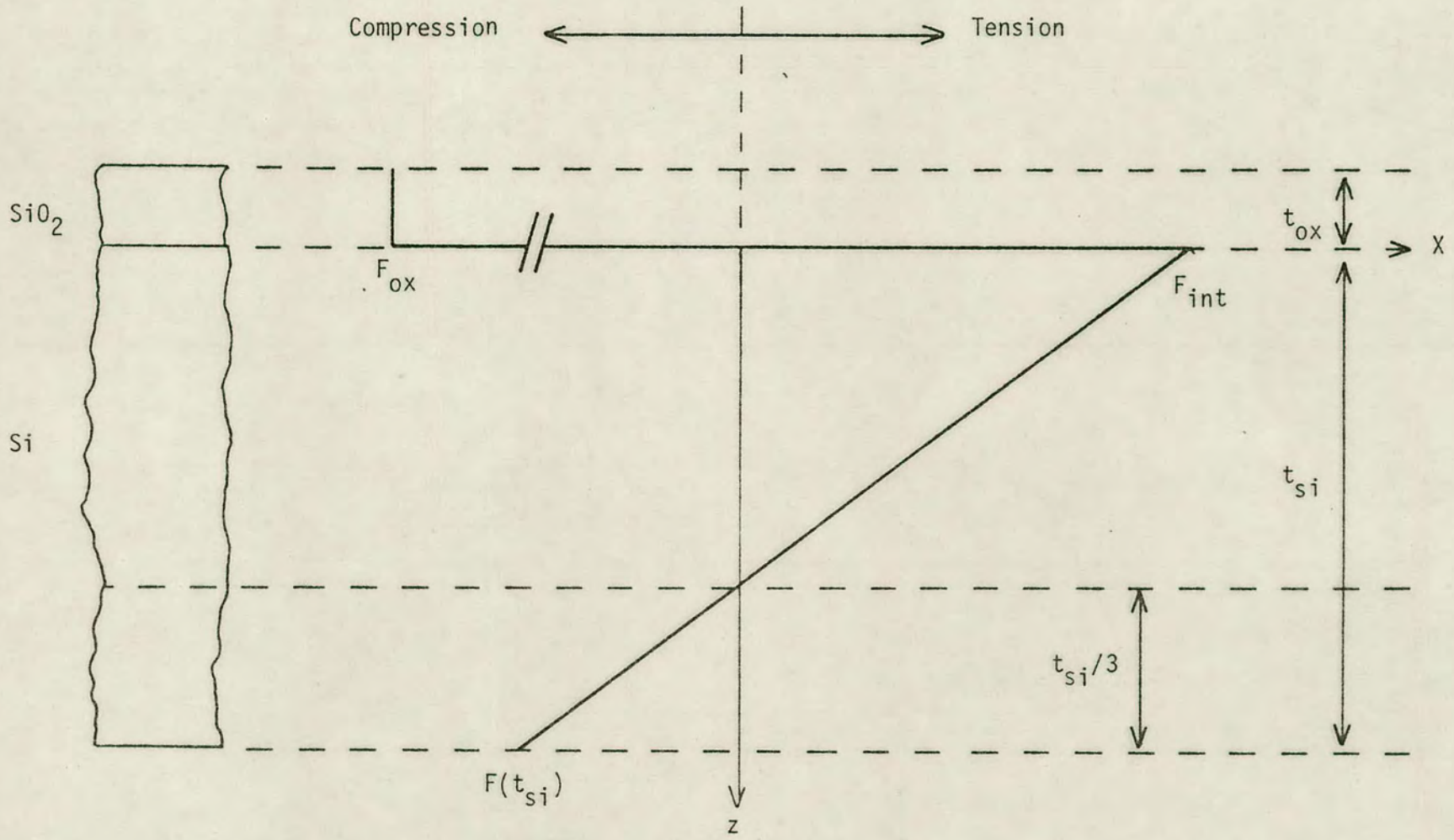

FIGURE 7.3: Schematic illustration of forces acting in an oxidised silicon slice

constant throughout its depth and is determined simply by resolving forces in y. The strain at the inside surface is then calculated by resolving the moments of stress at every point in the wafer as before.

By either method, the displacement du in the direction of x at a point $(x, o, -t_{si})$ resulting from a force $(\sigma d\ell)dz$ acting at a point r_o, ϕ on an element $d\ell$ on the edge of an oxide disc, is given by (see Fig 7.4),

$$\frac{du}{d\ell} = -\frac{\sigma t_{ox}}{\pi t_{si}} \left[\left\{\frac{\lambda+3\mu}{2\mu(\lambda+2\mu)} \ell n\, r + \frac{\lambda+\mu}{2\mu(\lambda+2\mu)} \left(\frac{r_o \sin\phi}{r}\right)^2\right\} \cos\phi + \left\{\frac{\lambda+\mu}{2\mu(\lambda+2\mu)} \frac{(x-r_o\cos\phi) r_o \sin\phi}{r^2}\right\} \sin\phi\right] \quad (7.11)$$

where $r^2 = (x - r_o \cos\phi)^2 + (r_o \sin\phi)^2 = x^2 + r_o^2 - 2xr_o \cos\phi$

This simplifies algebraically to

$$\frac{du}{d\ell} = \frac{-\sigma\, t_{ox}}{2\pi\mu(\lambda+2\mu)\, t_{si}} \left[(\lambda+3\mu)\, \ell n\, (r) \quad \cos\phi + \frac{(\lambda+\mu) x r_o \sin^2\phi}{r^2}\right] \quad (7.12)$$

In order to calculate the total displacement at a point (x,o) it is therefore necessary to integrate this expression around the border of the oxide shape by putting $d\ell = r_o\, d\phi$, ie

$$u(x,o) = \frac{\sigma}{2\pi\mu(\lambda+2\mu)} \frac{t_{ox}}{t_{si}} r_o \int_{-\pi}^{\pi} \left[(\lambda+3\mu)\ell n(r) \cos\phi + \frac{(\lambda+\mu) x r_o \sin^2\phi}{r^2}\right] d\phi \quad (7.13)$$

If the oxide disc is circular and the material isotropic, it is only necessary to calculate u(x,o) in order to determine the displacement

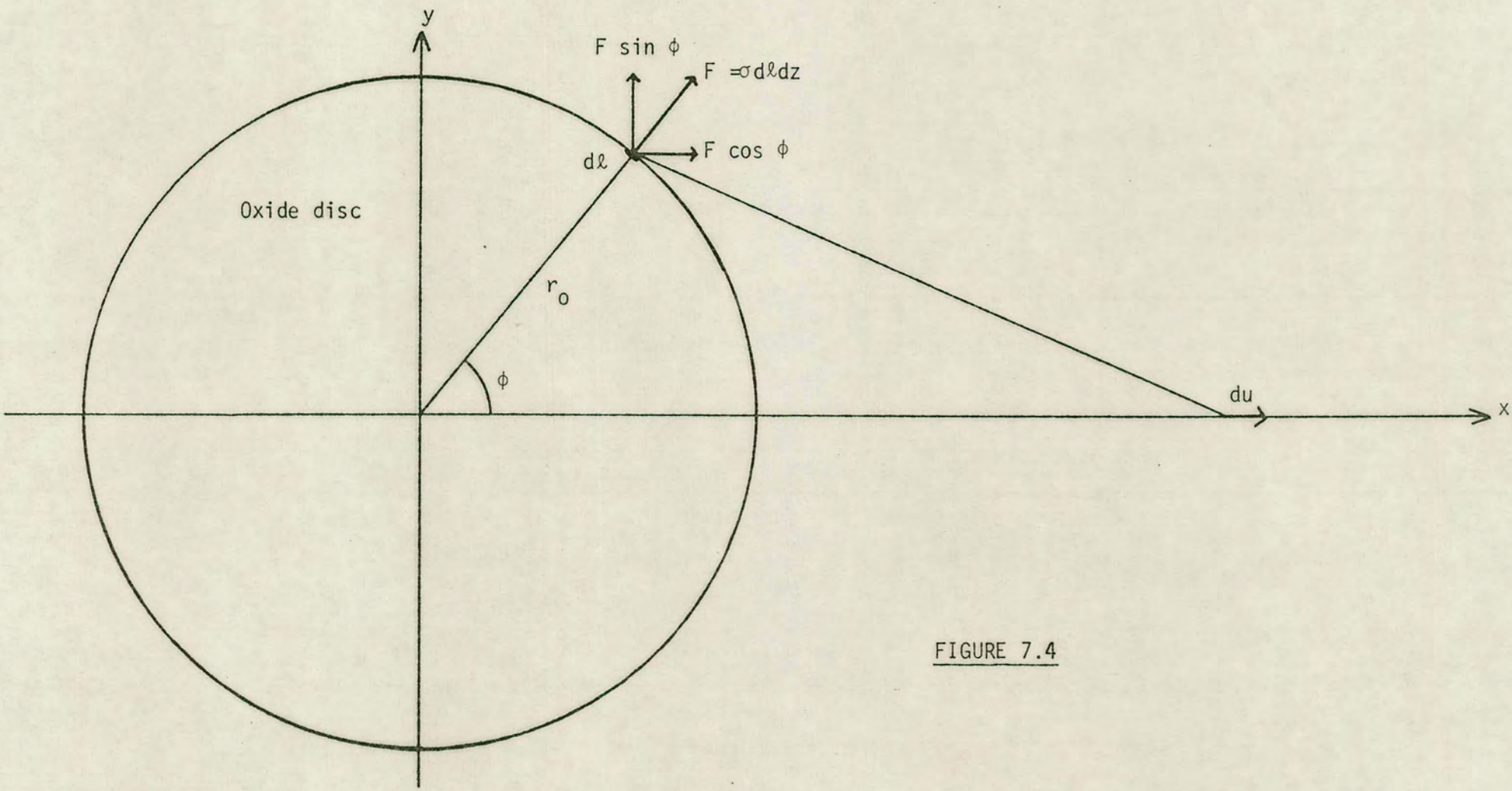

FIGURE 7.4

u(x,y). If X-ray diffraction takes place from Bragg planes normal to the direction of x, then the resultant moire fringes in the interferometer are insensitive to v(x,y).

This technique may be used for calculating the strainfield resulting from any shape of oxide (provided that the oxide dimensions are much greater than the wafer thickness), simply by integrating the effects of the forces acting round the oxide.

It would appear, at first, that the ℓn function in Equation 7.13 causes the displacement to increase with distance from the origin of the force. However, for a pair of opposing forces at a distance r_1 and r_2 from (x,o) the function is in reality $\ell n(r_1/r_2)$ which tends to zero as the distance increases ($r_1/r_2 \rightarrow 1$). The theory of plane strain as a function of a force acting at a point by Love[115] assumes that the force acts in a cavity within the body. Therefore, when $x = r_o$, the integral of Equation 7.13 must not include the condition when $\phi = 0$, ie

$$u(r_o,0) = \frac{\sigma}{2\pi\mu(\lambda+\mu)} \frac{t_{ox}}{t_{si}} r_o \int_{\delta}^{2\pi-\delta} [(\lambda+3\mu)\, \ell n\, (2r_o^2(1-\cos\phi)) \cos\phi + \frac{(\lambda+\mu)\, r_o^2 \sin^2\phi}{r^2}]\, d\phi \qquad (7.14)$$

where $\delta \rightarrow 0$.

The theory developed so far assumes that the substrate material is isotropic. In general, however, all crystalline materials are anisotropic and silicon is no exception to this rule. However, elasticity theory (Love[115]) shows that Young's modulus is a minimum in the directions of the principal axes (ie <100>) and a maximum in the directions equally inclined to the principal axes (ie <111>). However, it is constant in directions whose directions cosines ℓ, m and n are given by the expression $\ell \pm m \pm n = 0$. This means that all directions lying within the {111} plane have the same elastic parameters, and so the theory developed above is valid after all.

Wolf[2] quotes the following values for Young's modulus (E):

TABLE 7.1

Direction	E (dynes/cm^2)
<100>	1.301×10^{12}
<111>	1.878×10^{12}
<110>	1.690×10^{12}
<211>	1.690×10^{12}

A computer programme was written to perform the integral of Equation 7.11, and this is given in Appendix II. Young's modulus, $E = 1.69 \times 10^{12}$ dynes/cm^2, and Poisson's ratio, $\sigma = 0.262$ were used. The oxide disc radius and thickness and substrate thickness were read into the programme. The measured fringe spacing was also read and the oxide stress required to give this fringe spacing calculated. The fringe pattern was then produced as line printer output.

7.2 RESULTS

Five interferometers were used, having been constructed in the way described in Section 5.1. These were labelled I1-I5. Initially they were examined with the Lang traversing source arrangement (Fig 5.4) in order to check for built in strainfields and dislocations (Fig7.5(a) to (e)) and then submitted for cleaning and oxidation (as described in Section 5.2). By using photoresist techniques, all the oxide was etched off the interferometers except for a disc 3.5 mm in diameter on the splitter wafer. Table 7.2 gives details relating to each interferometer.

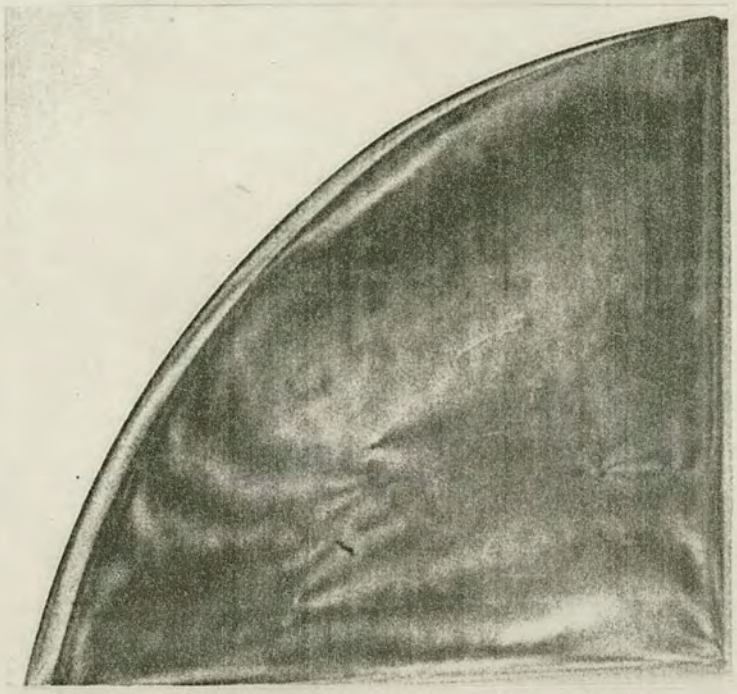

(a) Interferometer I1
Note dislocations resulting from previous oxidation

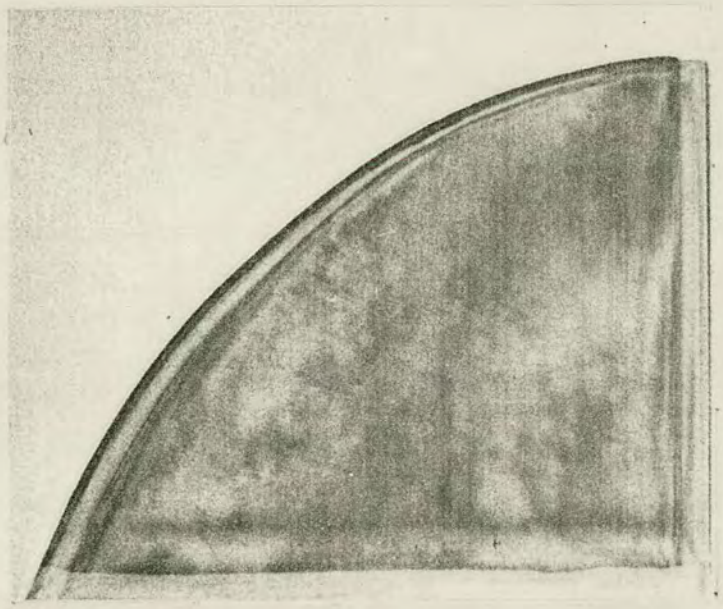

(b) Interferometer I2

FIGURE 7.5: Interferometers after cutting and etching ($02\bar{2}$ reflection, MoKα radiation)

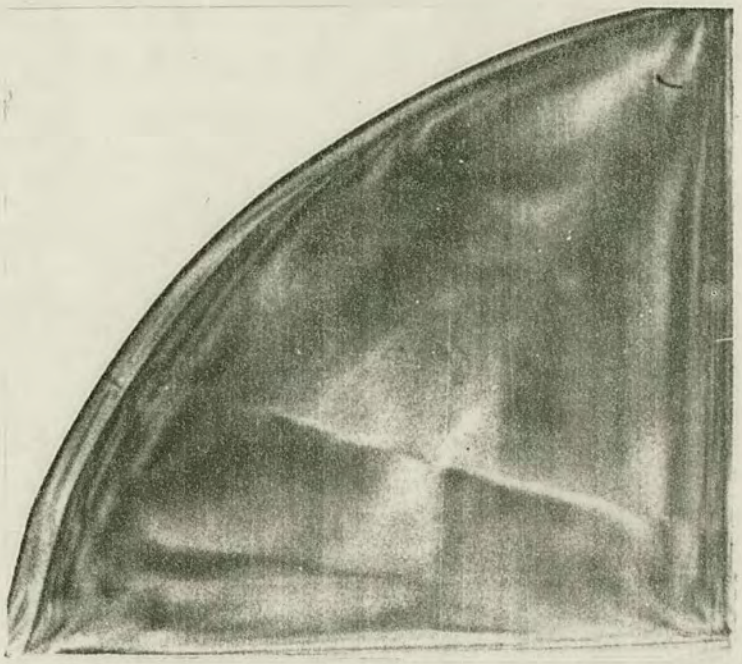

(c) Interferometer I3

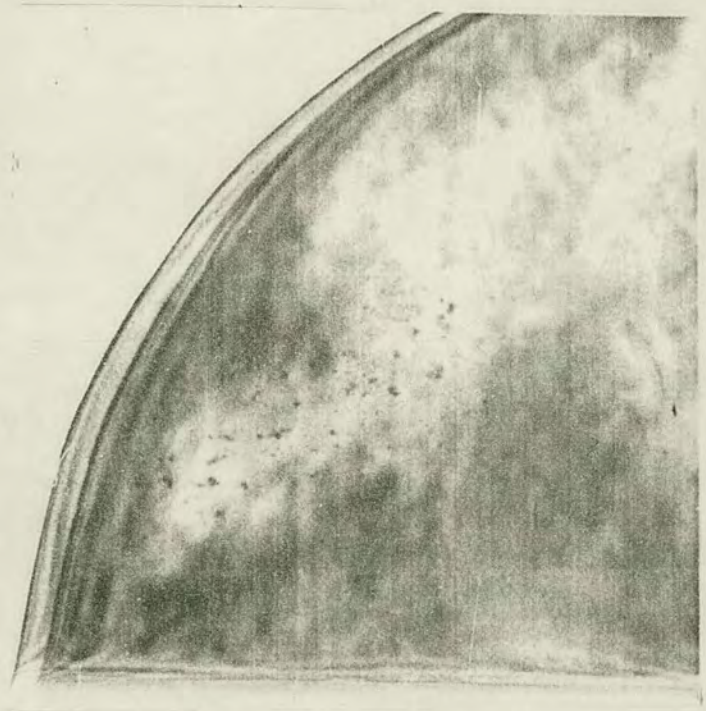

(d) Interferometer I4

FIGURE 7.5: Interferometers after cutting and etching
($02\bar{2}$ reflection, MoKα radiation)

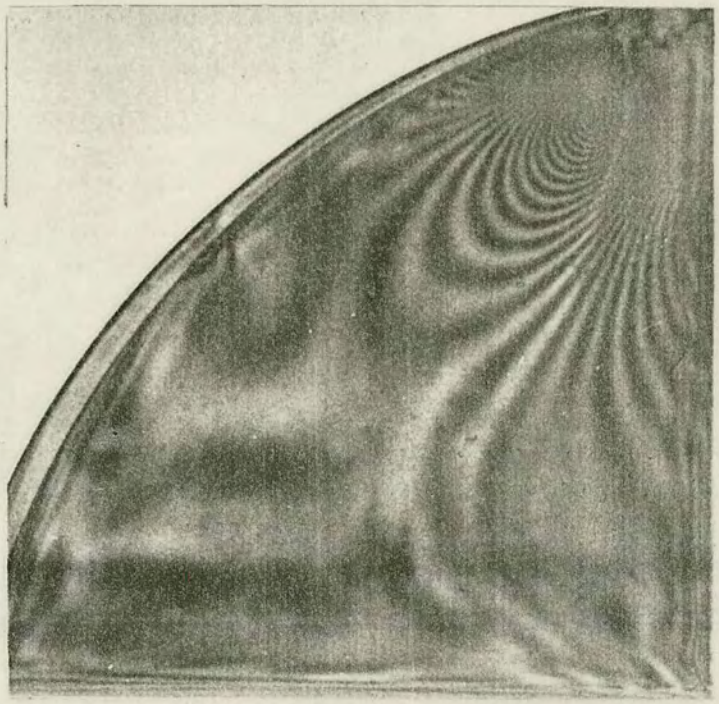

(e)

FIGURE 7.5: Interferometer I5 after cutting and etching. Note high strain region in upper corner. The opposite corner, however, is relatively strain free and is therefore usable.
($02\bar{2}$ reflection, MoKα radiation)

TABLE 7.2

Interferometer	Oxide thickness (μm)	Wafer thickness (μm)	Oxide disc diameter (mm)	Typical IC Application
I1	.12	315	3.5	Gate oxide
I2	1.18	378	3.5	Field oxide
I3	.19	302	3.5	-
I4	.37	337	3.5	Masking oxide
I5	.72	346	3.5	Masking oxide

The oxide thickness was determined using colour charts[80] giving an accuracy of $\pm$.01 μm. The wafer thicknesses and oxide disc diameters were measured using a travelling microscope.

The strain patterns were observed as moiré fringes and are shown in Figs7.6(a) -7.10(a) together with those predicted by the theory developed above (Figs7.6(b) -7.10(b)). Topographs relating to the interferometers I1 and I3 were taken using Kodak dental film and those relating to interferometers I2, I4 and I5 on Ilford nuclear emulsion film in order to resolve fringes close together. Since the X-ray intensity was relatively low, nuclear emulsion films required an exposure of about three days/cm of traverse.

It must be noted that there are two effects which cause the topograph image to become distorted. The first is that the interferometer must be rotated through the Bragg angle (10.6^{o} for 220 reflection with MoKα radiation) and the second is that the X-ray beam which originates from essentially a point source has angular divergence. The effect of this is to enlarge the vertical scale by a

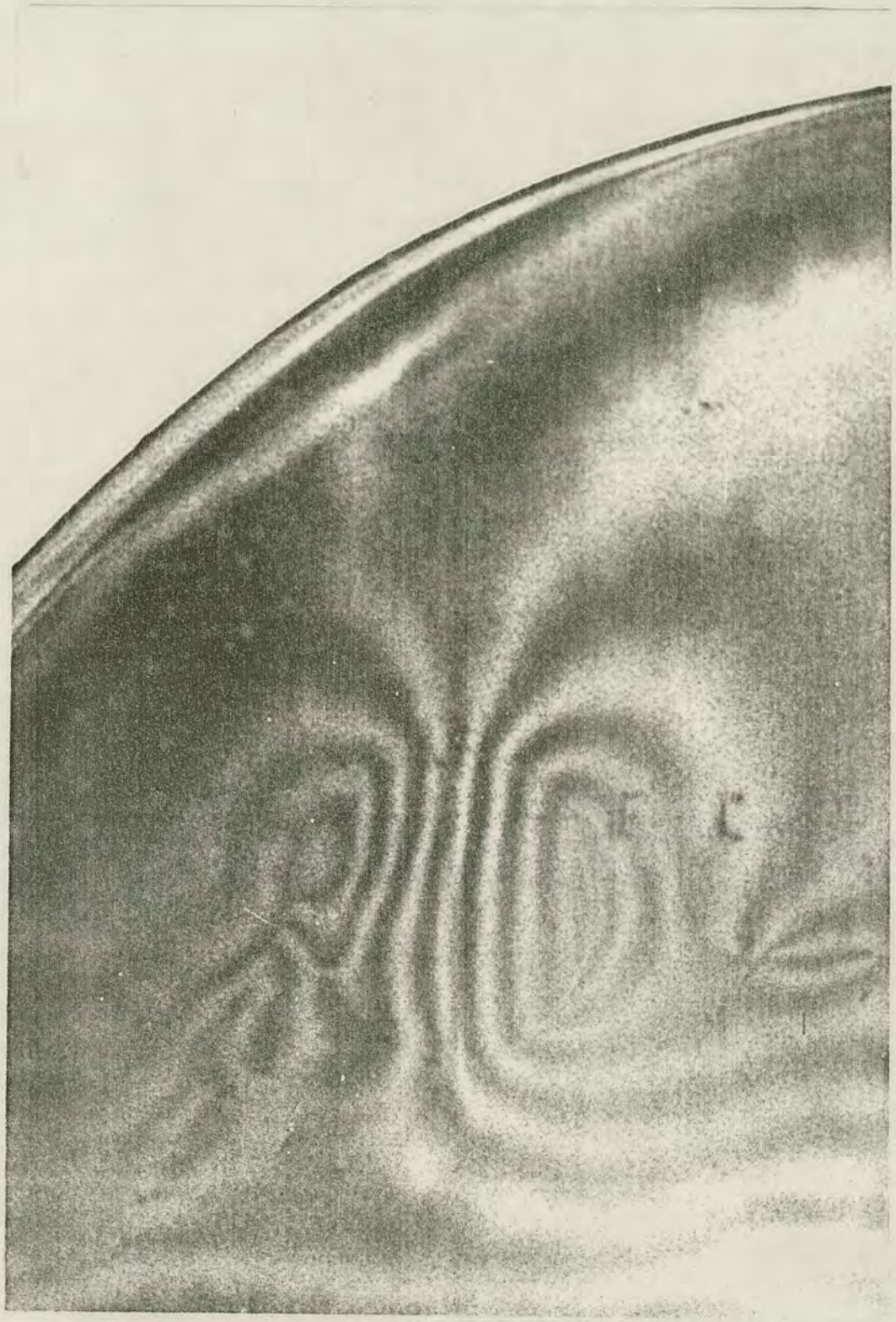

(a)

FIGURE 7.6(a): Observed moiré fringe pattern (I1) - note dislocations analysed in Chapter 6.
t_{ox} = .12 μm, t_{si} = 315 μm.
(02$\bar{2}$ reflection, MoKα radiation)

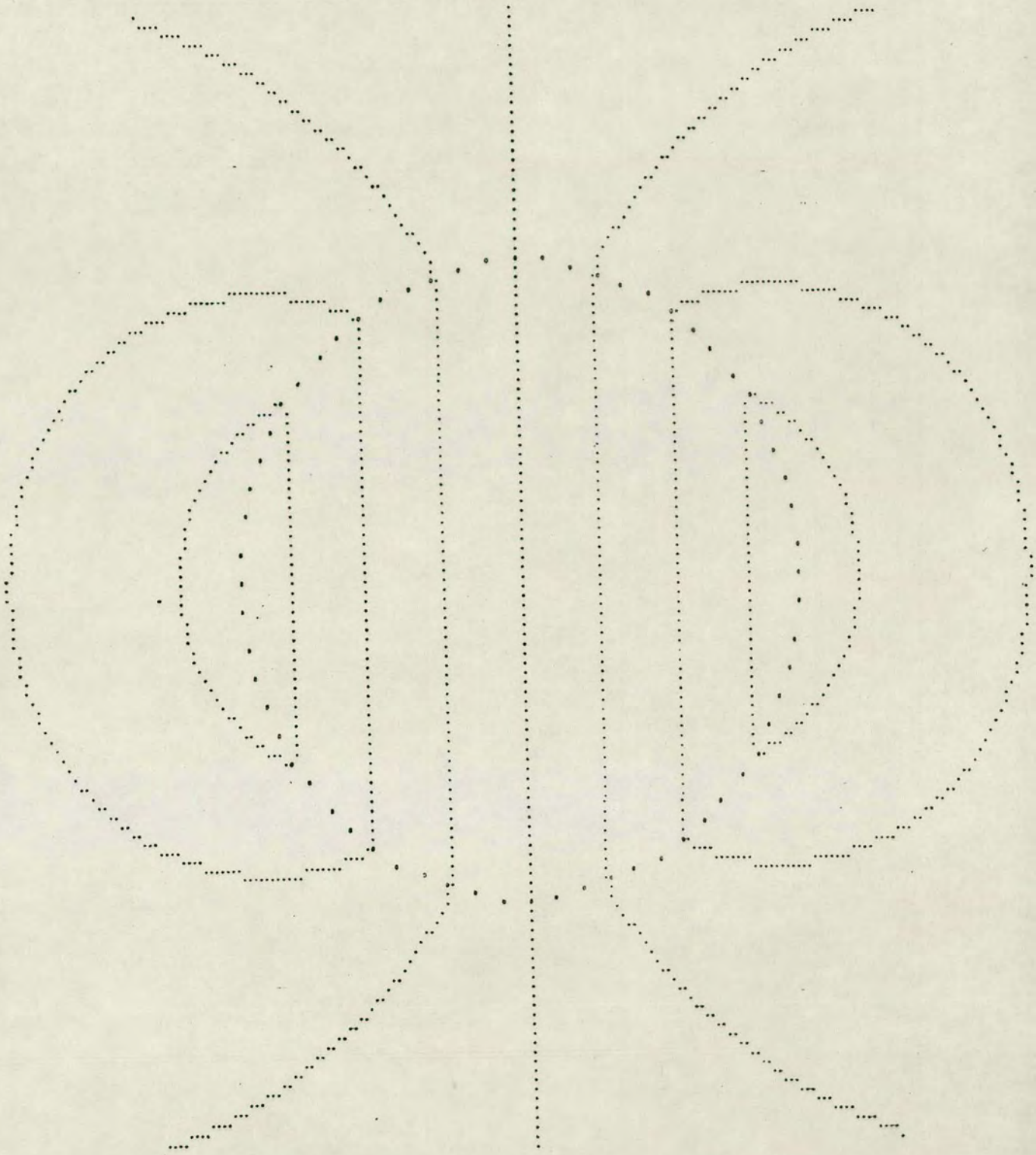

FIGURE 7.6(b): Calculated fringe pattern
t_{ox} = .12 μm, t_{si} = 315 μm
σ_{ox} = 1.92 x 10^9 dynes/cm^2

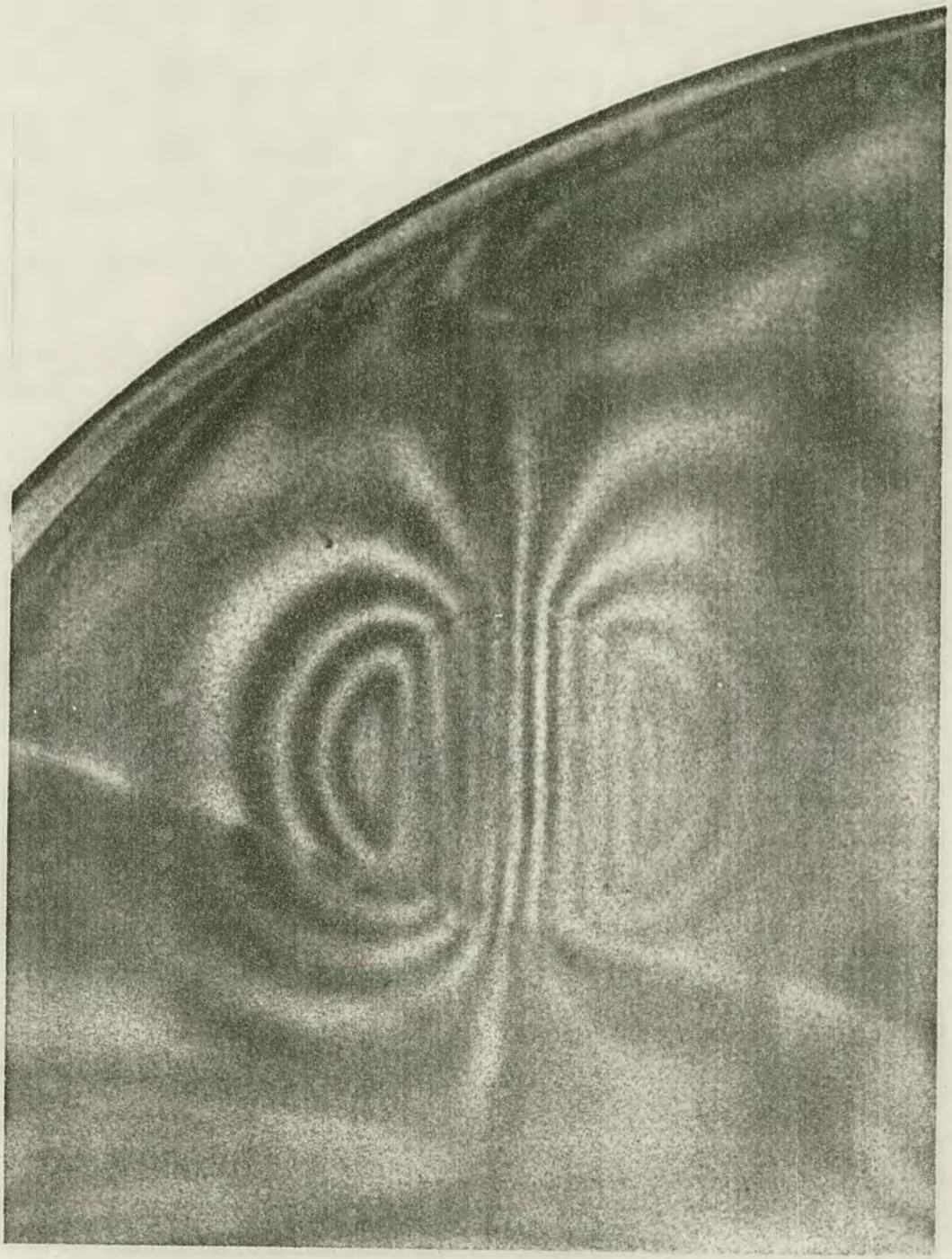

(a)

FIGURE 7.7(a): Observed moiré fringe pattern (I3)
t_{ox} = .19 μm, t_{si} = 302 μm
($02\bar{2}$ reflection, MoKα radiation)

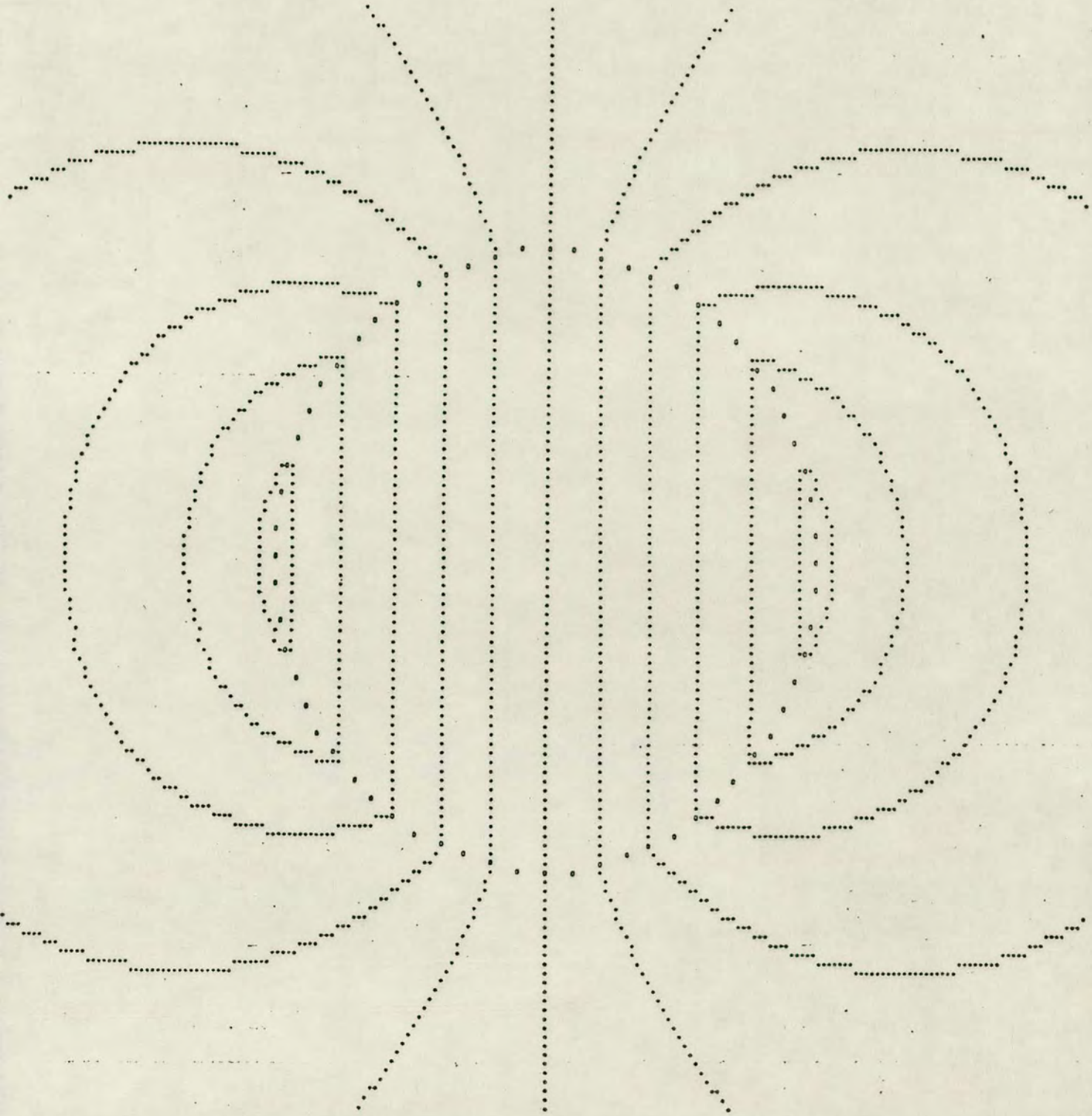

FIGURE 7.7(b): Calculated fringe patterns
t_{ox} = .19 μm, t_{si} = 302μ m
σ_{ox} = 1.69 x 10^9 dynes/cm^2

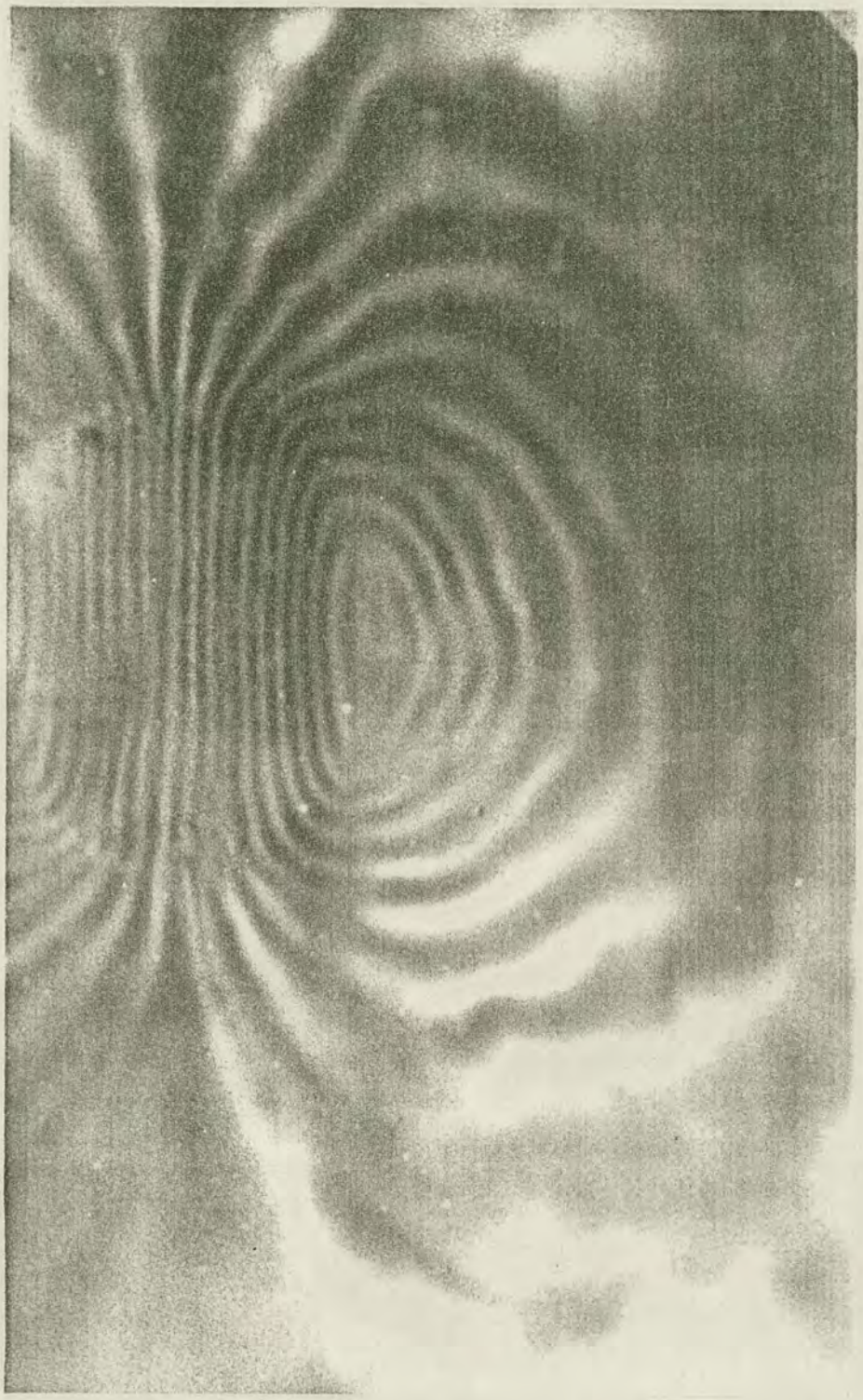

(a)

FIGURE 7.8(a): Observed moiré fringe pattern (I4)
t_{ox} = .37 μm, t_{si} = 337 μm
($02\bar{2}$ reflection, MoKα radiation)

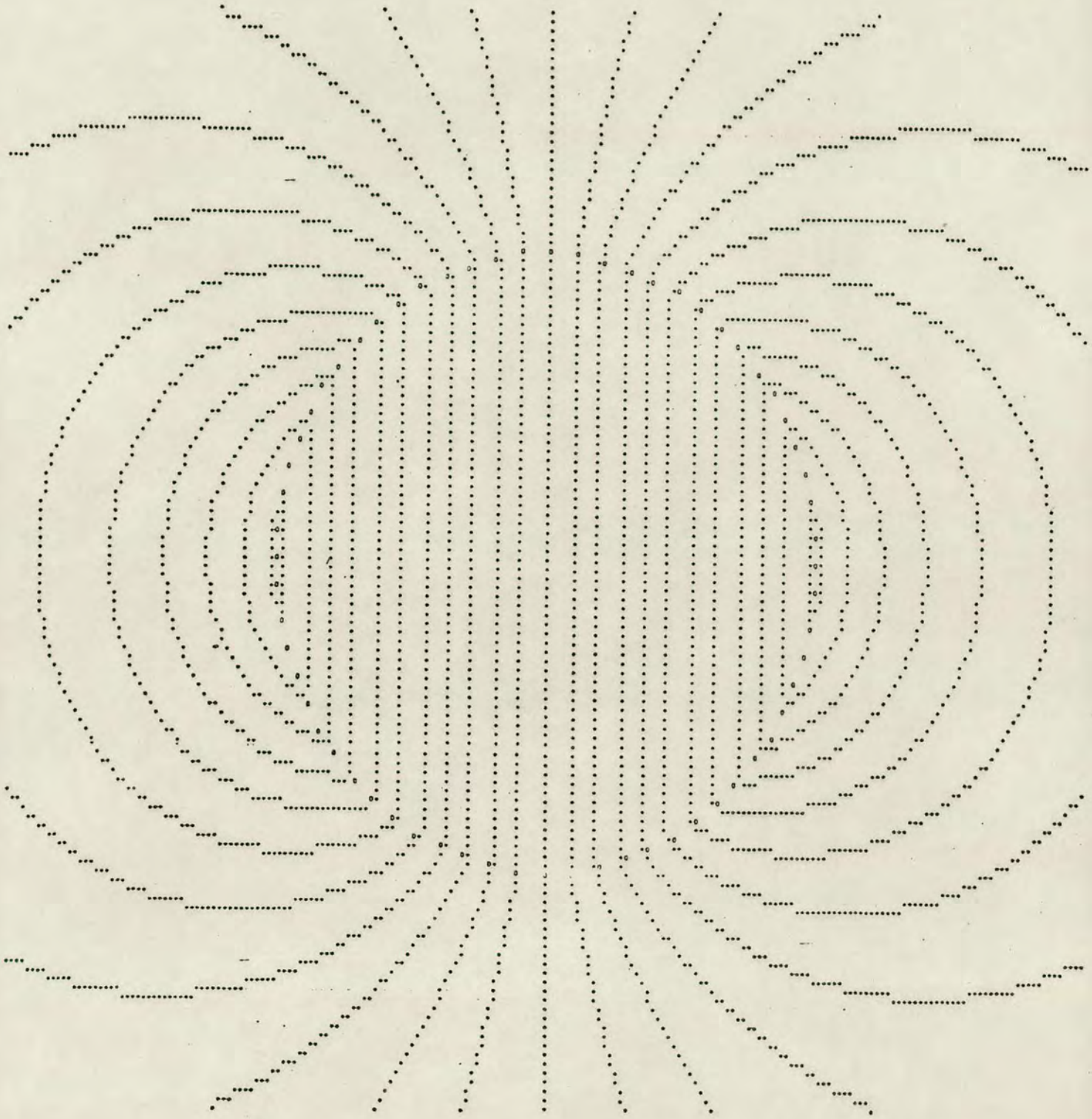

FIGURE 7.8(b): Calculated fringe pattern
t_{ox} = .37 μm, t_{si} = 337 μm
σ_{ox} = 2.06 x 10^9 dynes/cm

(a)

FIGURE 7.9(a): Observed moiré fringe pattern (I5)
t_{ox} = .72 μm, t_{si} = 346 μm
($02\bar{2}$ reflection, MoKα radiation)

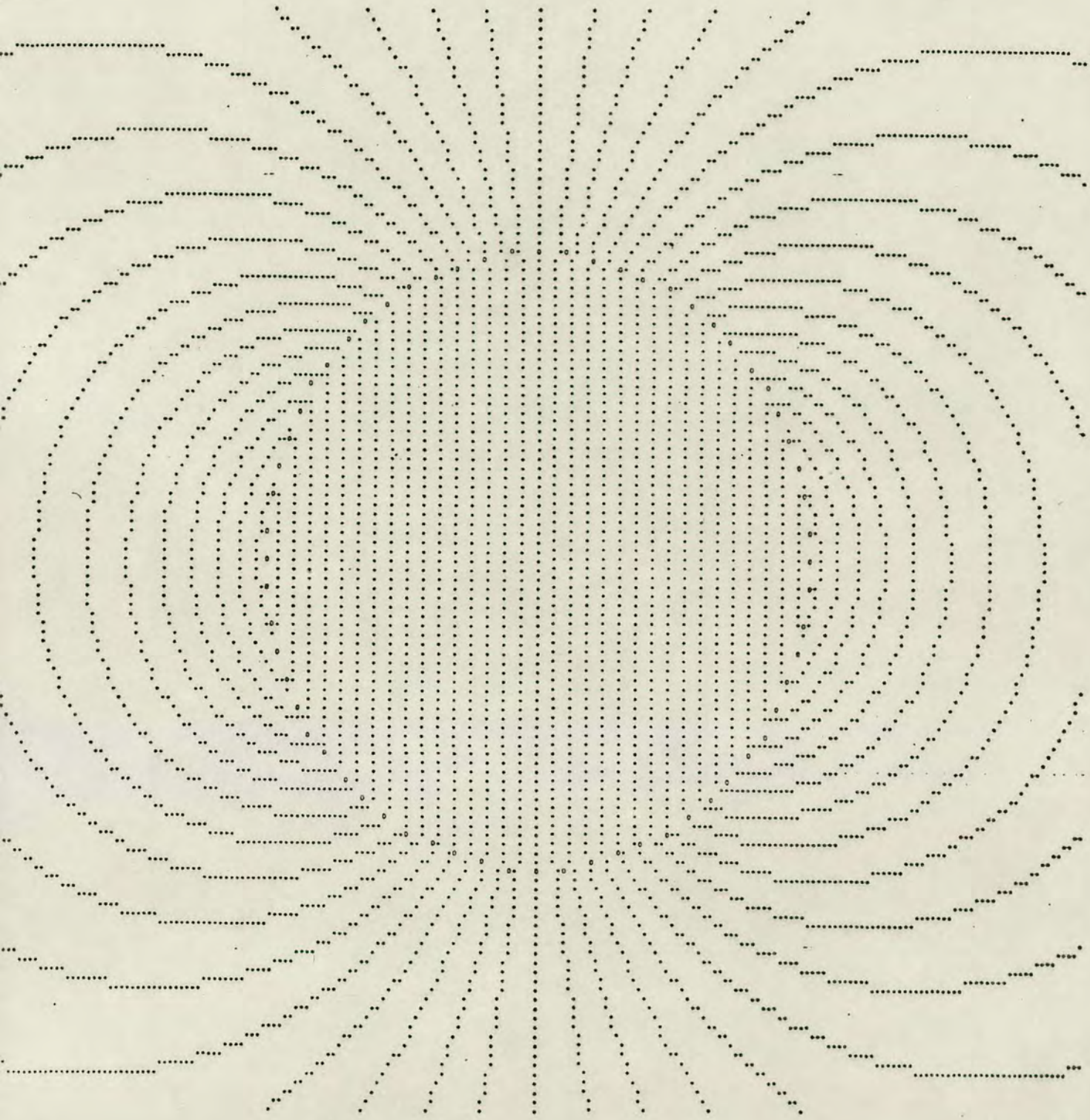

FIGURE 7.9(b): Calculated fringe pattern
t_{ox} = .72 μm, t_{si} = 346μ m
σ_{ox} = 1.60 x 10^9 dynes/cm^2

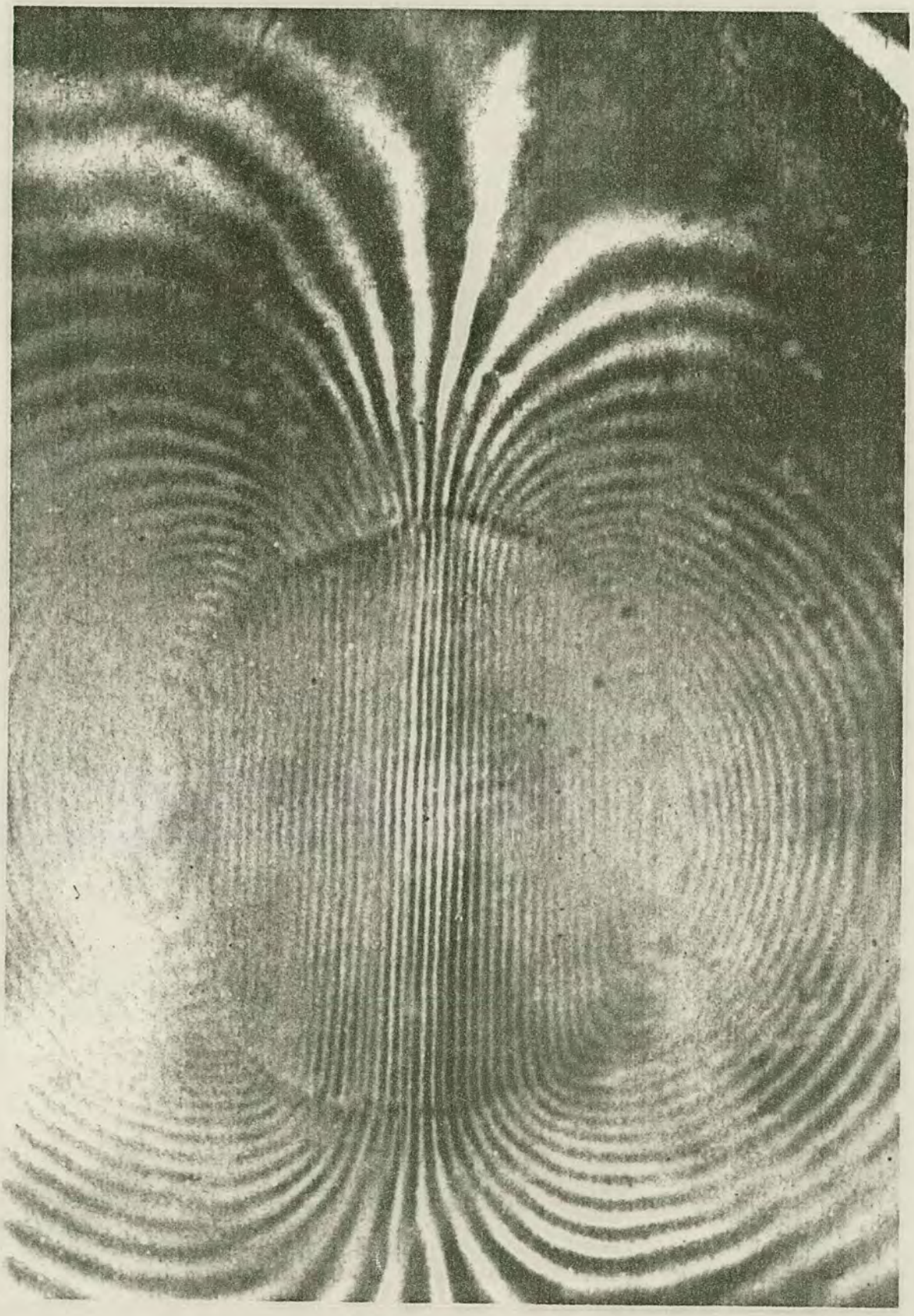

(a)

FIGURE 7.10(a): Observed moiré fringe pattern (I2)
t_{ox} = 1.18 μm, t_{si} = 378 μm
($02\bar{2}$ reflection, MoKα radiation)

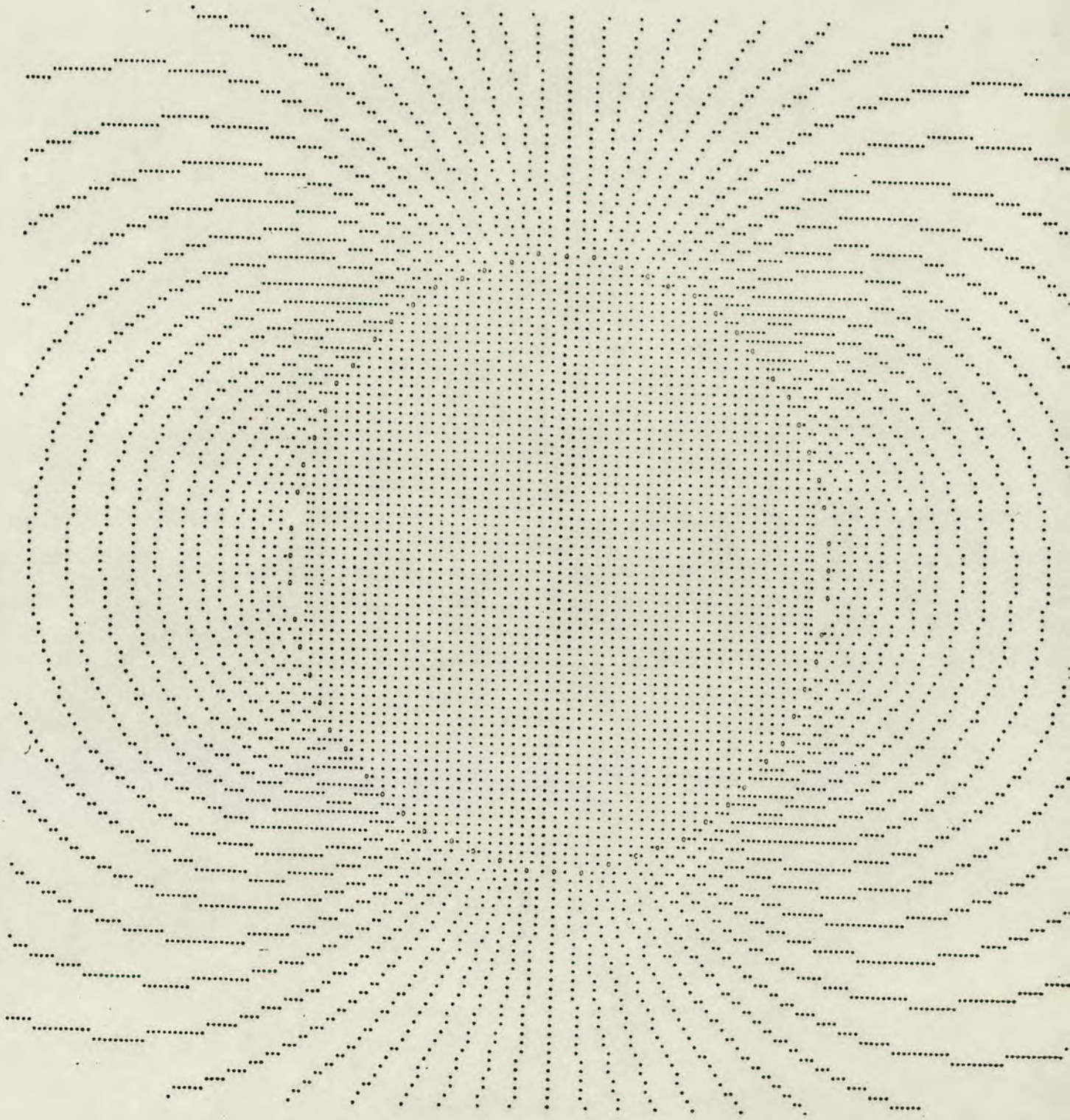

FIGURE 7.10(b): Calculated fringe pattern
t_{ox} = 1.18 μm, t_{si} = 378 μm
σ_{ox} = 1.62 x 10^9 dynes/cm^2

factor of about 1.1. The calculated fringe spacings are distorted in similar fashion to give exact correlations.

The results obtained from the moiré topographs are presented in Table 7.3, and in graphical form in Fig 7.11. A least squares

TABLE 7.3

Interferometer	σ(dynes/cm^2)	σt_{ox} dynes/cm
I1	1.92×10^9	2.30×10^4
I2	1.62×10^9	1.91×10^5
I3	1.69×10^9	3.22×10^4
I4	2.06×10^9	7.62×10^4
I5	1.60×10^9	1.15×10^5

analysis gives $\sigma = 1.65 \times 10^9$ dynes/cm^2. This value is significantly lower than that predicted by thermal contraction considerations (2.5×10^9 dynes/cm^2). This may be due to the fact that the oxide was grown on a chemically etched surface rather than a mechanically polished one resulting in a rougher surface. This would allow some of the compressive stress in the oxide to resolve itself. However, a comparison between Figs 7.6(a) - 7.10(a) with 7.6(b) - 7.10(b) shows that the elasticity model predicts the moire fringe pattern with good accuracy.

It should therefore be possible to calculate the relative strain (if not the actual strain) in a silicon substrate for any shape of oxide pattern grown on it (provided of course that the oxide lies well within the boundary of the substrate since the model is valid only for a thin plate infinite in extent).

By using the elasticity model for calculating relative strain,

contours of equirotation (Fig 7.12) and equidilatation (Fig 7.13) were calculated for the results obtained with interferometer I3 (t_{ox} = .19 μm, t_{si} = 302 μm).

An idea of the lattice distortion may be gained from Figs 7.14 and 7.15 which were also calculated using the elasticity model. Fig 7.14 represents the distortion of the lattice immediately beneath the oxide disc where the lattice is in a state of tension. Fig 7.14 on the other hand, represents the opposite side of the wafer which, due to warpage, is in a state of compression. These figures can not relate to any particular moiré topograph since the distortion is obviously greatly exaggerated.

7.3 DOUBLE CRYSTAL MEASUREMENTS

The interferometer topographs give information about the strain within the plane of the wafer but the warpage or curvature predicted by elasticity theory may only be inferred from these results. It is important to establish the curvature in order to find out if it has any significant effect on the X-ray standing wave pattern within the interferometer by the focussing effect described in Section 3.2.2 and Fig 3.11. A more direct method of measuring the curvature may be achieved by using a double crystal spectrometer. The theory behind this instrument has been outlined in Chapter 4.

The X-ray incident beam was diffracted initially from a perfect reference crystal and then from the splitter wafer of interferometer I2 (t_{ox} = 1.18 μm). Both crystals were diffracting from $\{333\}$ Bragg planes under conditions of symmetric Bragg reflection. With CuKα radiation, this represents a Bragg angle (θ) of 47.48^{o}.

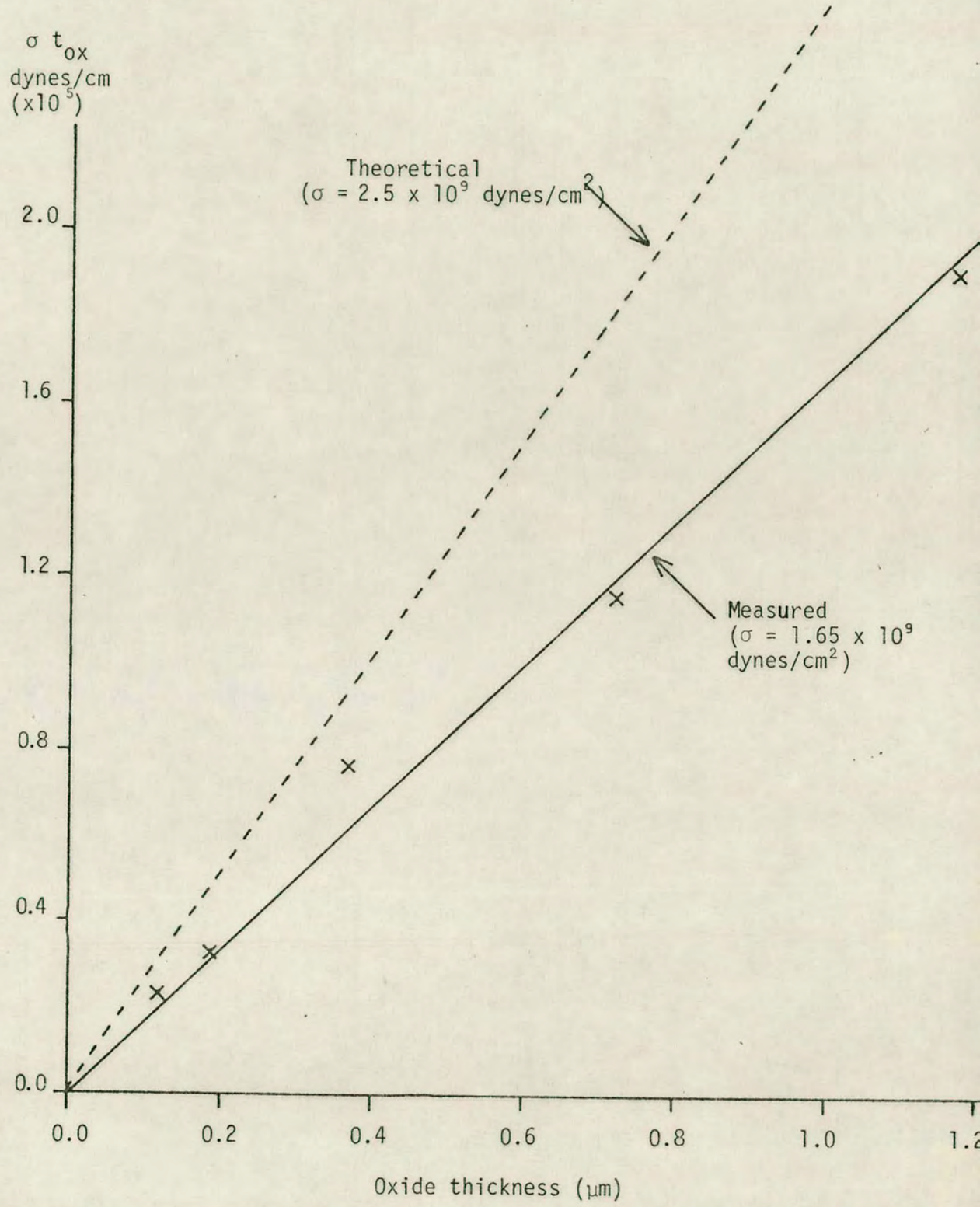

FIGURE 7.11: Theoretical and observed force/cm of oxide length vs oxide thickness.

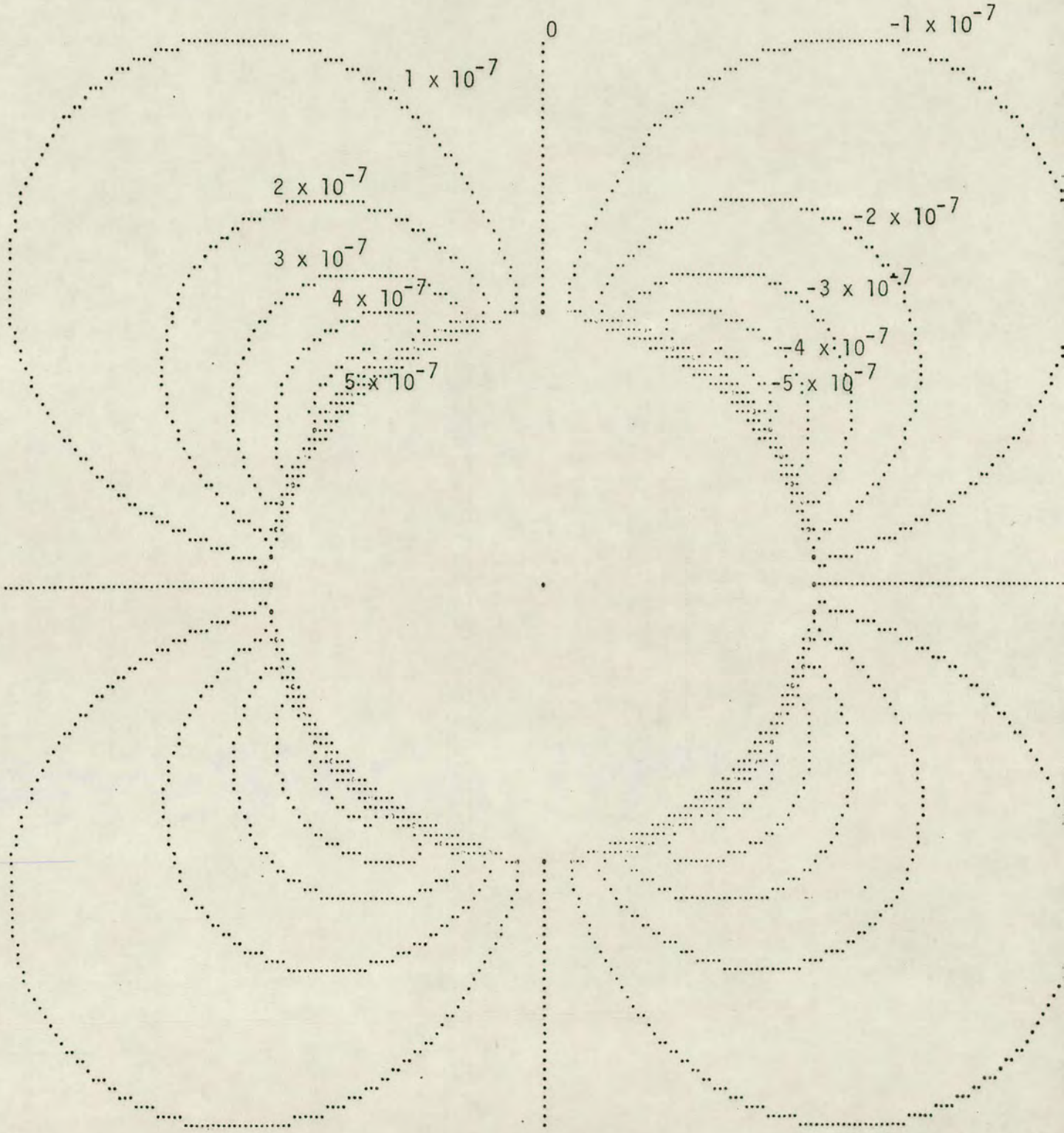

FIGURE 7.12: Calculated contours of equi-rotation (radians)
(non-oxidised side of wafer)
t_{ox} = .19 μm, t_{si} = 302 μm

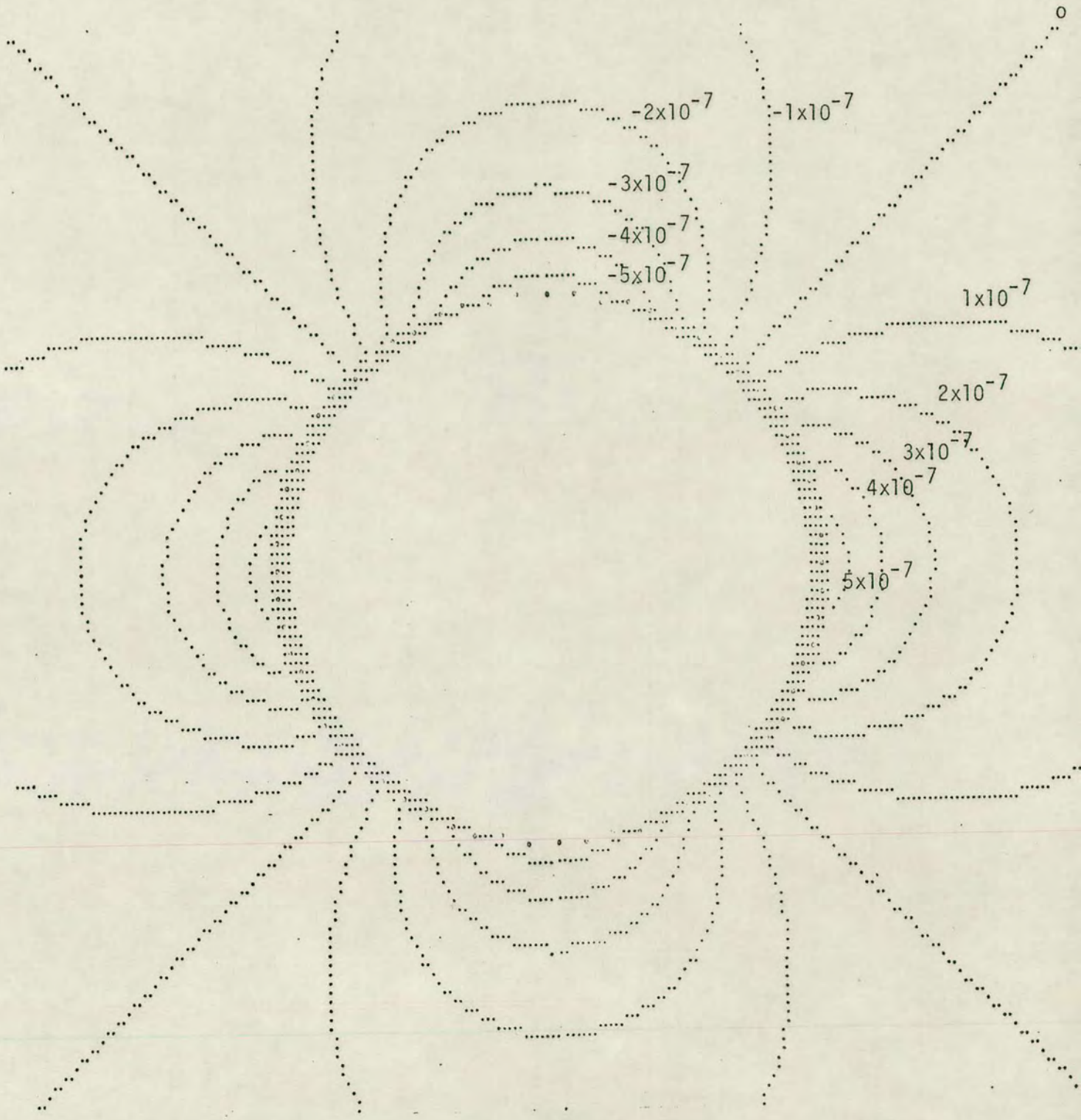

FIGURE 7.13: Calculated contours of equi-dilatation ($\Delta\ell/\ell$)
(non-oxidised side of wafer)
t_{ox} = .19 μm, t_{Si} = 302 μm

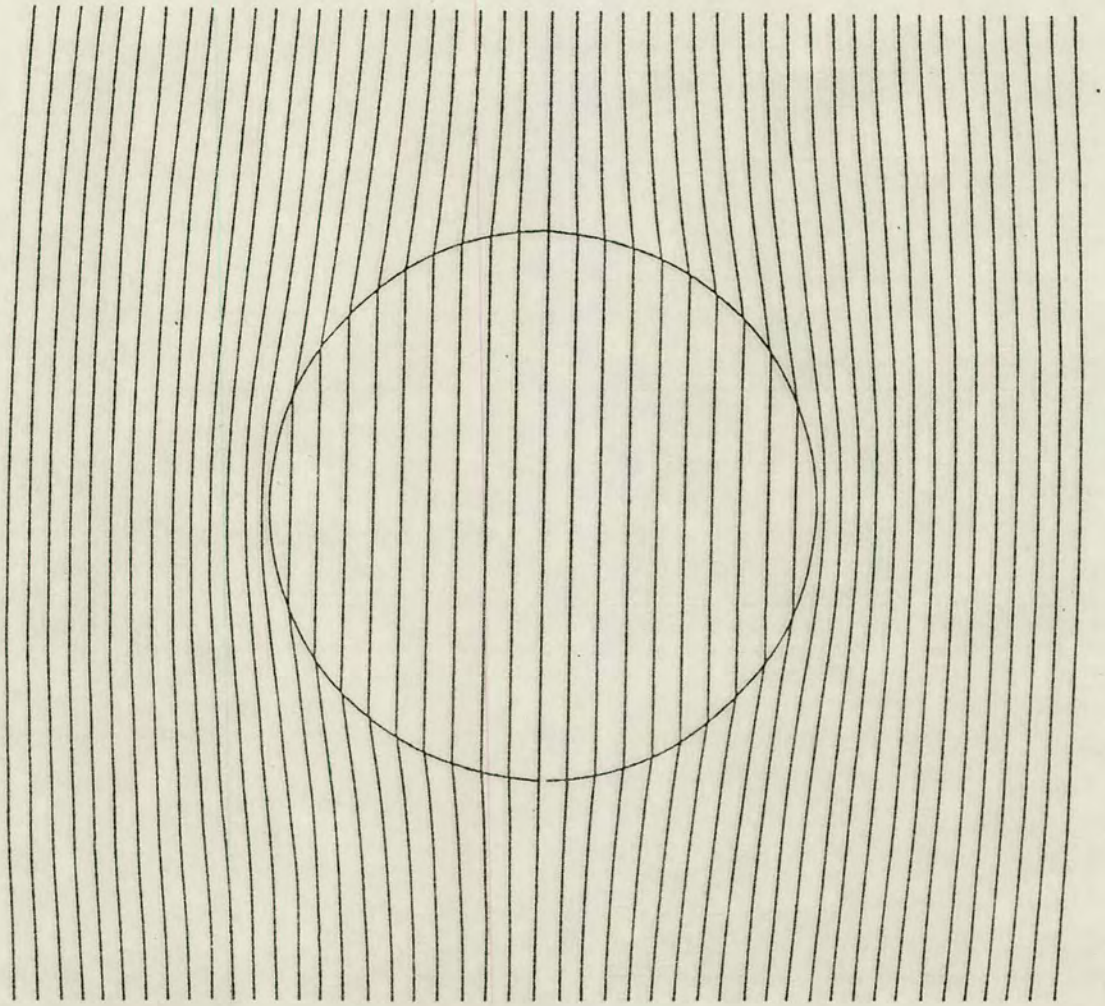

FIGURE 7.14: Lattice distortion immediately beneath oxide disc

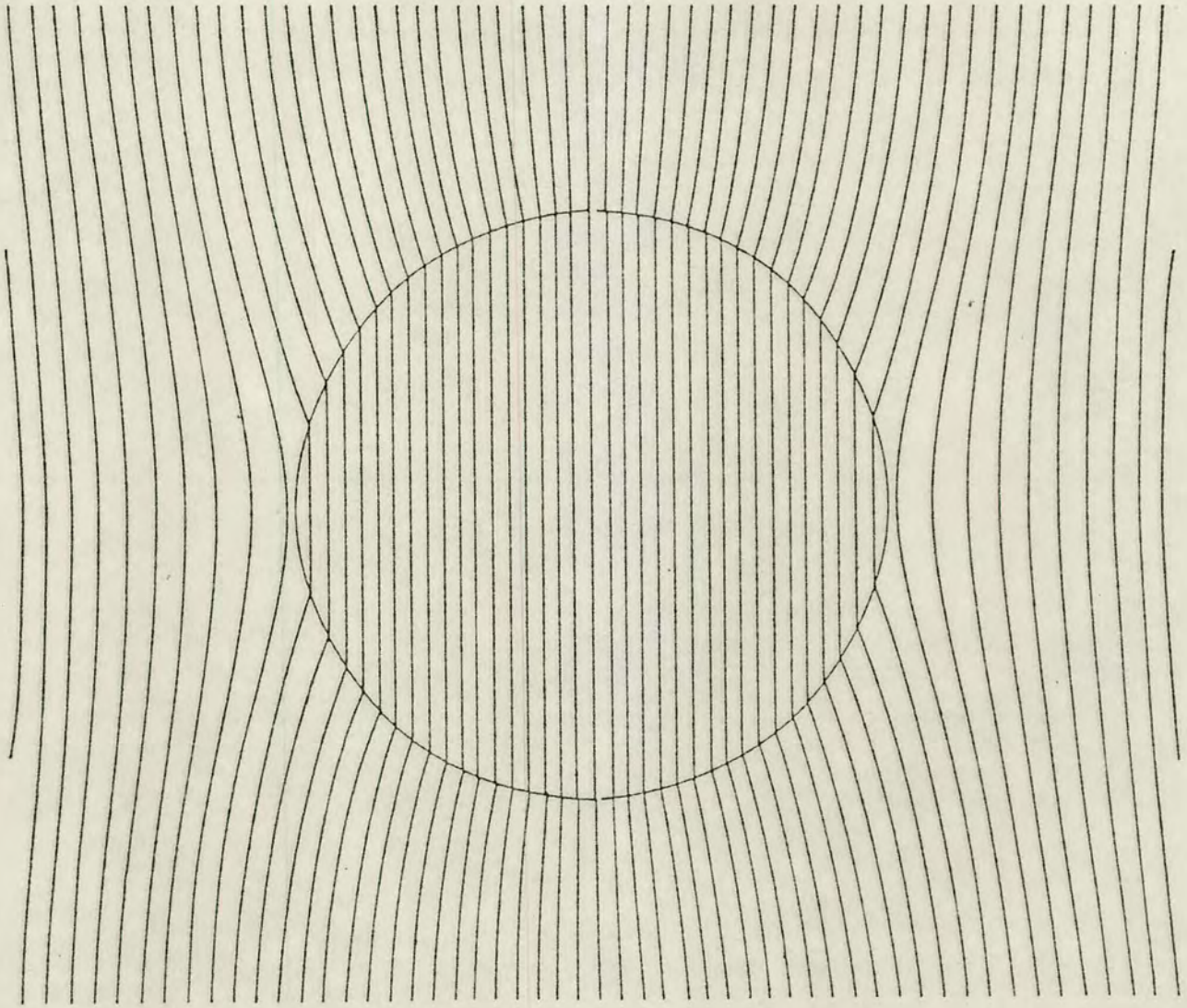

FIGURE 7.15: Lattice distortion on non-oxidised side of wafer

The shutter system described in Section 5.5 was used. Two small holes (.25 mm x .25 mm) in the shutter were arranged such that one allowed a beam, diffracting from a point ~5 mm from the centre of the oxide disc, to pass to the counter to act as reference while the position of the other could vary horizontally, scanning across the crystal. By rotating the crystal through the Bragg peaks of the two beams and alternately recording the X-ray count in each beam using the automatic measuring technique described in Section 5.5, the angular displacements between the two peaks could be determined. The effects of crystal drift were thus minimised. Two effects can cause angular displacement of the Bragg peak. The first is variation in tilt of the lattic planes, and the second is variation in the spacing between the Bragg planes normal to the surface. In this application, it is the lattice tilt which is the dominant effect. Under the oxide disc, the spacing of the Bragg planes is constant since the stress is constant (as shown by the interferometer topographs) but elsewhere a second order effect will be introduced. Although the forces are acting in the plane of the surface, variation of Bragg plane spacing normal to the surface will occur by an amount determined by the value of Poisson's ratio.

Table 7.4 shows the angular variation (α) between the centre of the diffraction peak of the reference and sample beams as a function of distance between them, after correcting for projection of diffracted X-ray beam.

TABLE 7.4

Δx (mm)	α (secs)	Δx (mm)	α (secs)
0.0	0.63	4.15	1.01
0.35	1.72	4.50	-0.58
0.69	1.36	4.84	-2.32
1.04	2.47	5.19	-3.83
1.38	3.60	5.54	-3.39
1.73	4.31	5.88	-4.79
2.08	4.32	6.23	-5.81
2.42	4.44	6.57	-5.92
2.77	4.31	6.92	-4.48
3.11	3.17	7.27	-6.13
3.46	4.85	7.61	-3.94
3.81	1.77		

By assuming uniform bending of the wafer with a neutral plane two-thirds of the wafer thickness from the oxide the variation of angle across the wafer was calculated and the results are presented in Table 7.5 with α as a function of distance from centre of the disc.

The measured results are only relative to one another and not related to absolute position with respect to the oxide disc. However, this may be deduced from symmetry considerations. It must also be noted that the measured results are in fact the convolution of the actual angle function with a square pulse of unity area and width equal to the slit width.

Figure 7.16 compares measured and calculated angle of tilt across the oxidised wafer. The important point to notice is that the radius of curvature of the disc is close to that predicted from the interferometer experiments (~46 metres). Some variation, however, does occur towards

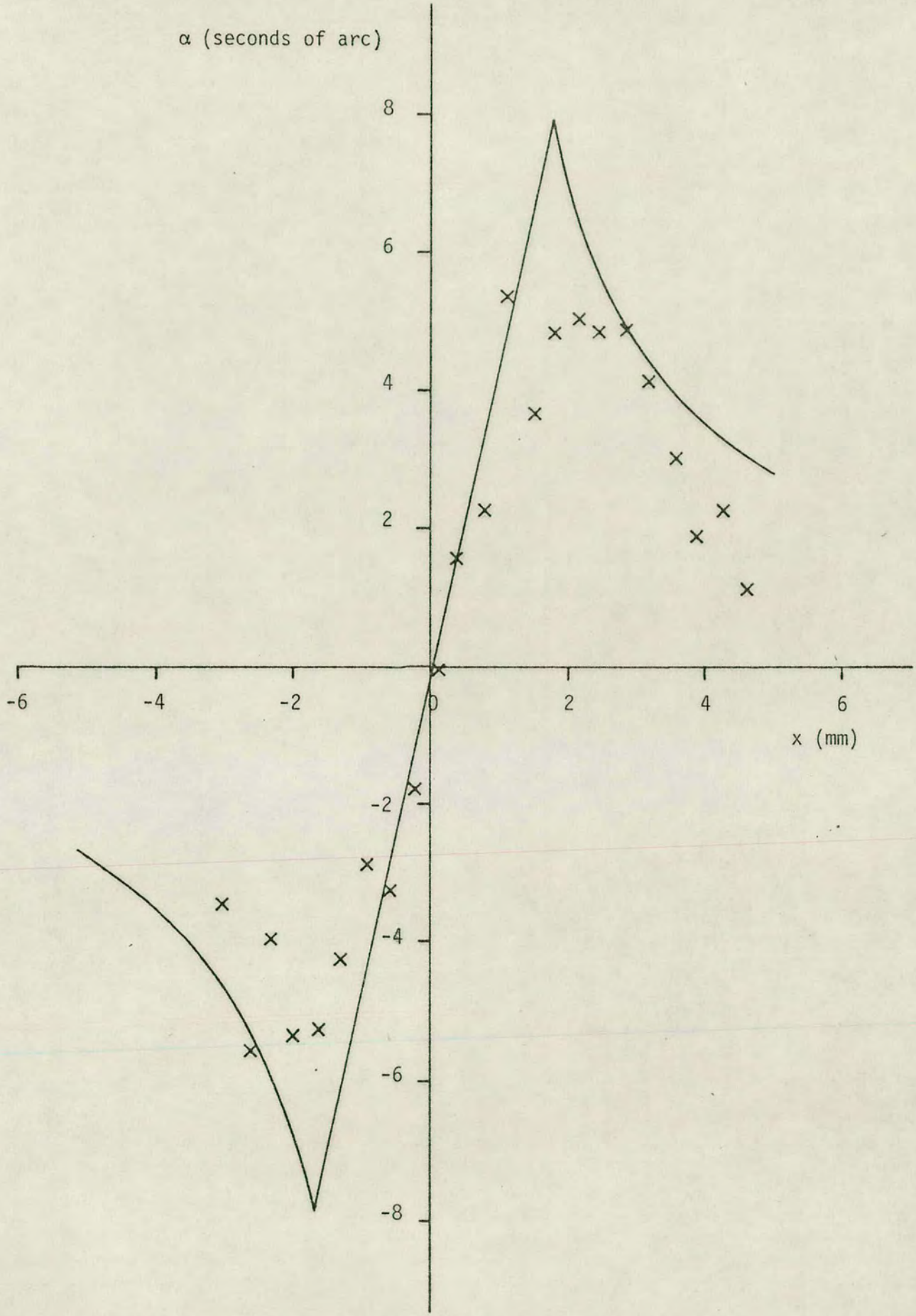

FIGURE 7.16: Angle of tilt across slice with 3.5 mm oxide disc (t_{ox} = 1.18 μm, t_{si} = 378 μm)
- calculated from moiré fringe topographs
x measured with double crystal spectrometer

TABLE 7.5

Δx (mm)	α (secs)	Δx (mm)	α (secs)
0.0	0.0	2.80	5.02
0.17	0.80	2.97	4.72
0.35	1.61	3.15	4.46
0.52	2.41	3.32	4.23
0.70	3.21	3.50	4.02
0.87	4.02	3.67	3.82
1.05	4.82	3.85	3.65
1.22	5.62	4.02	3.49
1.40	6.42	4.20	3.35
1.57	7.23	4.37	3.21
1.75	7.90	4.55	3.09
1.92	7.30	4.72	2.97
2.10	6.69	4.90	2.87
2.27	6.18	5.07	2.77
2.45	5.74	5.25	2.68
2.62	5.35		

the edge of the disc, but this may be due to the traverse being displaced by a small amount vertically. Fig 7.17 shows the wafer curvature predicted by the calculated values of lattice tilt - obviously in the figure this is grossly distorted.

These results obtained so far relate to the largest measured distortion - ie the distortion in interferometer I2 with an oxide thickness 1.18 μm - and enable the determination of the error introduced into the interferometer moiré fringe pattern by 'focussing' of the X-ray standing wave pattern and the curvature of the wafer. The maximum error occurs at the edge of the oxide disc where the displacement of the wafer in the direction normal to the unstrained crystal surface (z) is estimated to be ~0.2 μm (from Fig 7.17). With a lattice tilt (α)

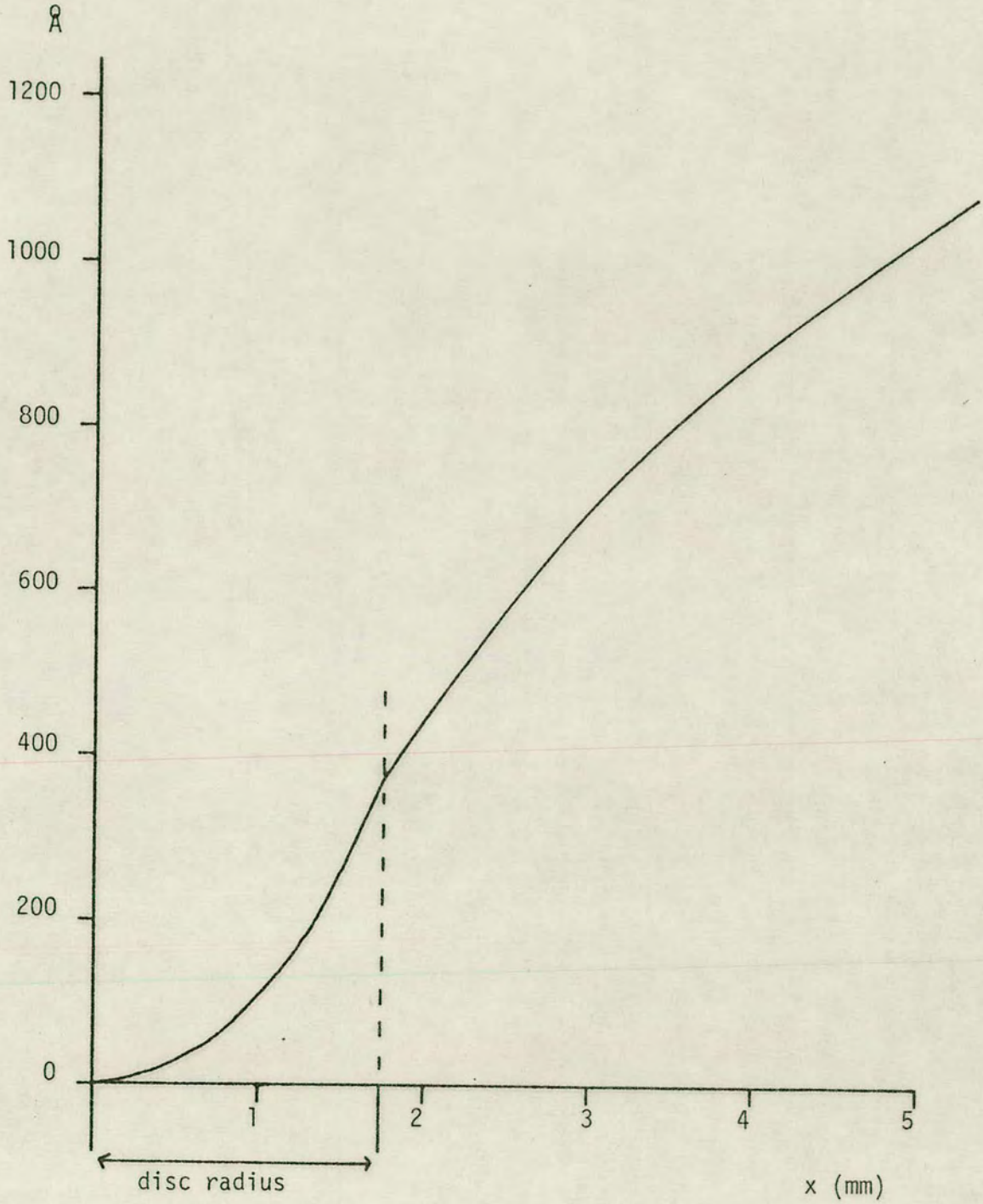

FIGURE 7.17: Distortion of wafer (warpage) vs distance from oxide disc centre (calculated)

of 7.9", this represents an error (Δ) of 0.2 tan (7.9") μm = .077 Å. The curvature of the wafer causes an error equivalent to the difference between the arc and chord of a circle (ℓ-w) in Fig 7.18). This may be calculated to be .004 Å, resulting in a total error of .081 Å. Interferometer topographs (Fig 7.10(a)) show that the displacement at the disc edge due to strain is 25 x 1.98 Å. Hence the error is only ~.16% and so the effects of curvature on the moiré fringe pattern may be neglected.

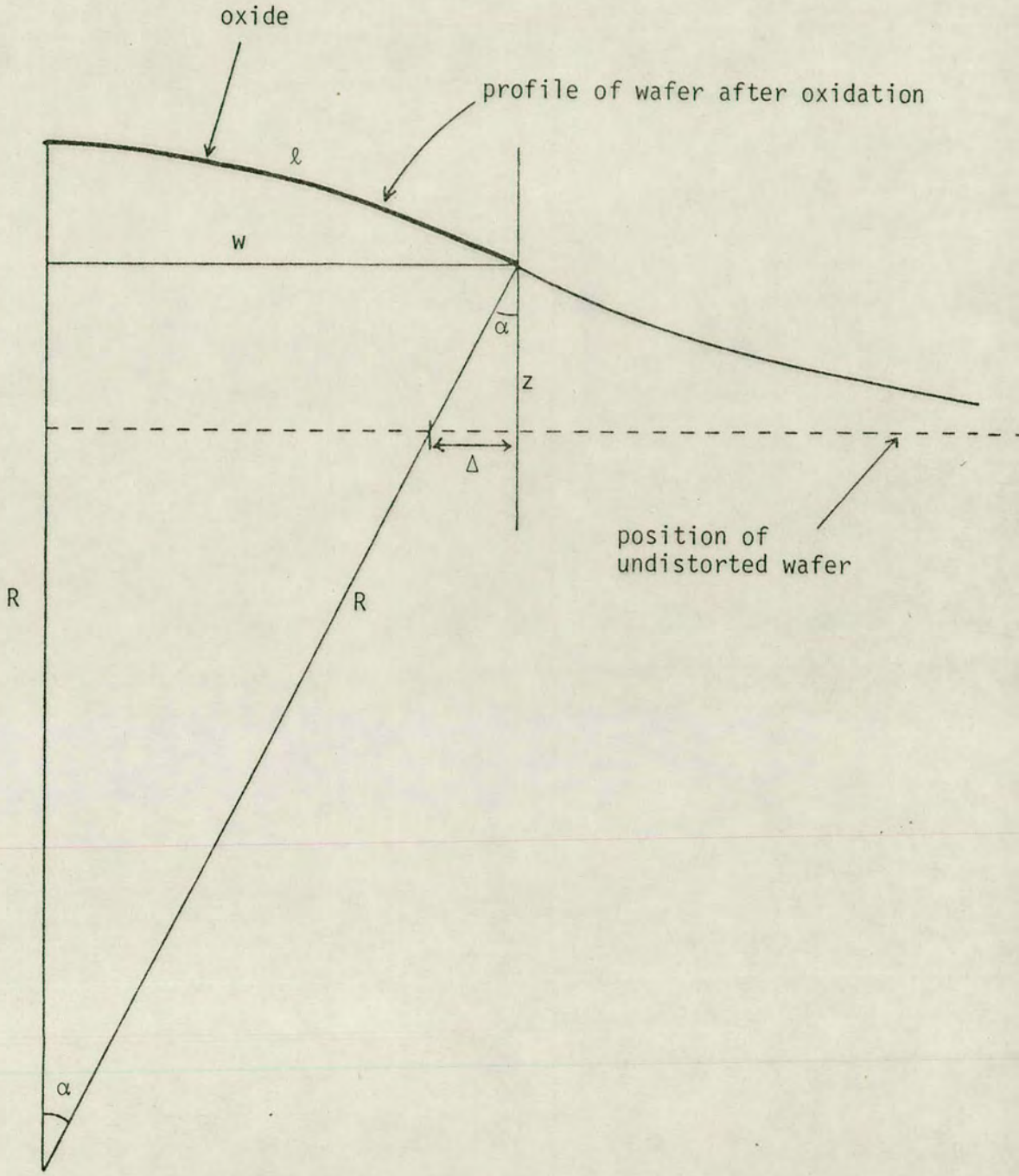

FIGURE 7.18: Error introduced in moiré fringe topograph image by 'focussing' of the X-ray standing wave pattern.

CHAPTER 8: DIFFUSION INDUCED STRAIN

When diffusion of impurity atoms takes place in a crystalline material the material becomes strained due to the resultant distortion of the lattice. In Chapter 2, the two basic mechanisms of impurity diffusion, interstitial and substitutional diffusion, were described. The strain resulting from substitutional diffusion may be calculated simply by considering the atomic lattice as the packing together of spheres (Vegard's Law) and is expressed as

$$\varepsilon = \frac{C}{N} \left[1 - \frac{r_a}{r_b}\right] \qquad (8.1)$$

where r_a is the covalent radius of the impurity atom, r_b that of the host material atom; C the concentration of impurity atoms and N the density of atomic sites of the host material. The solute lattice concentration coefficient, β, is expressed by

$$\beta = \frac{1}{N} \left[1 - \frac{r_a}{r_b}\right] = \frac{1}{N} \left[\frac{\Delta r}{r_b}\right] \qquad (8.2)$$

In the experiments performed in this chapter, boron diffusion was used on account of the large discrepancy in atomic radius between the boron and silicon atom (0.88 Å and 1.17 Å respectively) in order to maximise the strain for a given dose of impurity. Boron diffusion being substitutional, Equations 8.1 and 8.2 may be applied in order to calculate the expected strain in the silicon substrate. The density of silicon atomic sites, N, is 5.00×10^{22} cm^{-3} (Wolf[2]). Using these values for atomic radii, β may be calculated to be 5.0×10^{-24} cm^3. Many workers have performed experiments in order to measure the value of β.

Early work (eg Pearson and Bardsen[116], Horn[117]) was concerned with observing the effects on the silicon lattice of impurity diffusion among which the variation in lattice parameter was measured by X-ray techniques. McQuhae and Brown[17] have derived values for β from their results. Cohen[16] used double crystal X-ray techniques to observe diffraction peaks simultaneously from the thin diffused region in the surface of a silicon wafer and from the undiffused region beneath. By measuring the angular displacement between peaks he was able to calculate the relative change in lattice parameter. Table 8.1 gives the results quoted by McQuhae and Brown[17].

TABLE 8.1

	β (cm^3)
Calculated	5.0×10^{24}
Pearson and Bardsen[116]	2.5×10^{24}
Horn[117]	5.6×10^{24}
Cohen[16]	2.3×10^{24}
McQuhae and Brown[17]	5.2×10^{24}

The stresses and forces acting in a silicon wafer may be calculated in exactly the same fashion as in Chapter 7 for an oxide grown on its surface. However, in this case, since the boron atom is smaller than the silicon atom, the diffused region is in a state of tension, as will be the region of silicon surrounding the diffused area. Conversely the silicon immediately beneath the diffusion but too far from the surface for any significant diffusion to have taken place will be in a state of compression. The effect of this will be to cause the wafer

to bow, but this time the bowing will be concave rather than convex as in the oxidation case (Fig 8.1). As in the oxide case, the forces acting into the substrate lie round the periphery of the diffused area.

The stress at the diffusion edge σ is given by

$$\sigma = \frac{E\varepsilon}{1-\nu} \qquad (8.3)$$

where ε is the strain, E Young's modulus (= 1.692×10^{12} dynes/cm^2) and ν Poisson's ratio (= 0.262). Combining Equations 8.1,8.2 and 8.3

$$\sigma = \frac{\beta CE}{1-\nu} \qquad (8.4)$$

As shown in Chapter 2, the impurity concentration after a pre-deposition diffusion has a complementary error function profile with depth into the silicon. The total force acting at the diffusion edge may be found by integrating the stress with depth, ie

$$F = \int \sigma dz = \int \frac{\beta C(z) E dz}{1-\nu} \qquad (8.5)$$

where z is directed normal to the crystal surface. β, E and ν are independent of z, ie

$$F = \frac{\beta E}{1-\nu} \int C(z) dz \qquad (8.6)$$

It will now be realised that C(z)dz represents the total *dose* of impurity diffused into the silicon. In other words, the force is independent of the diffusion profile. Let the force now be represented

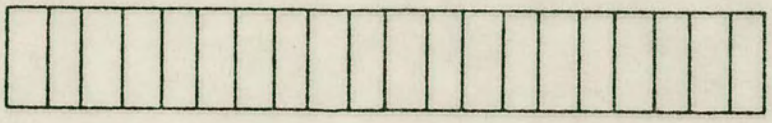

(a)

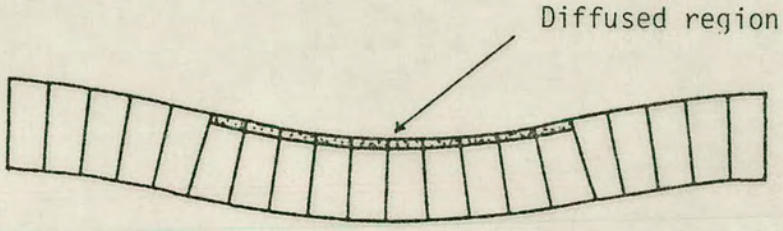

(b)

FIGURE 8.1: Silicon wafer before (a) and after boron diffusion (b) showing mechanical warpage.

as a function of the dose Q,

$$F = \frac{\beta EQ}{1-\nu} \text{ dynes/cm} \qquad (8.7)$$

The stresses in the silicon at the diffusion edge are represented in Fig 8.2.

8.1 LATTICE CONTRACTION COEFFICIENT MEASUREMENTS

The experimental procedure for the diffusion experiments was very similar to that for the oxidation experiments and is outlined in Chapter 7. Masking oxides were grown on the interferometers, this time using photoresist techniques of the opposite sense such that the interferometers were covered in oxide (~0.7 μm thick) except for a 3.5 mm disc on the outside surface of the splitter wafer. After diffusion, the masking oxide and boron glass were removed by techniques described in Chapter 5, leaving a circular diffused area in the centre of the splitter wafer.

The diffusions were carried out at 950°C for times ranging from 15 minutes to 135 minutes. The gas flows were arranged such that there was an excess of boron atoms at the silicon surface giving the maximum surface concentration (Wolf[2] gives $C_{Bmax} = 4.0 \times 10^{20}$ cm^{-3} at 950°C).

The moiré topographs arising from the diffusions are given in Figs 8.3 - 8.6. Using the elasticity model derived in Chapter 7, the total force acting at the diffusion edge may be calculated. Assuming a complementary error function profile (see Chapter 2) the dose may be calculated from knowledge of the diffusion constant D, diffusion time

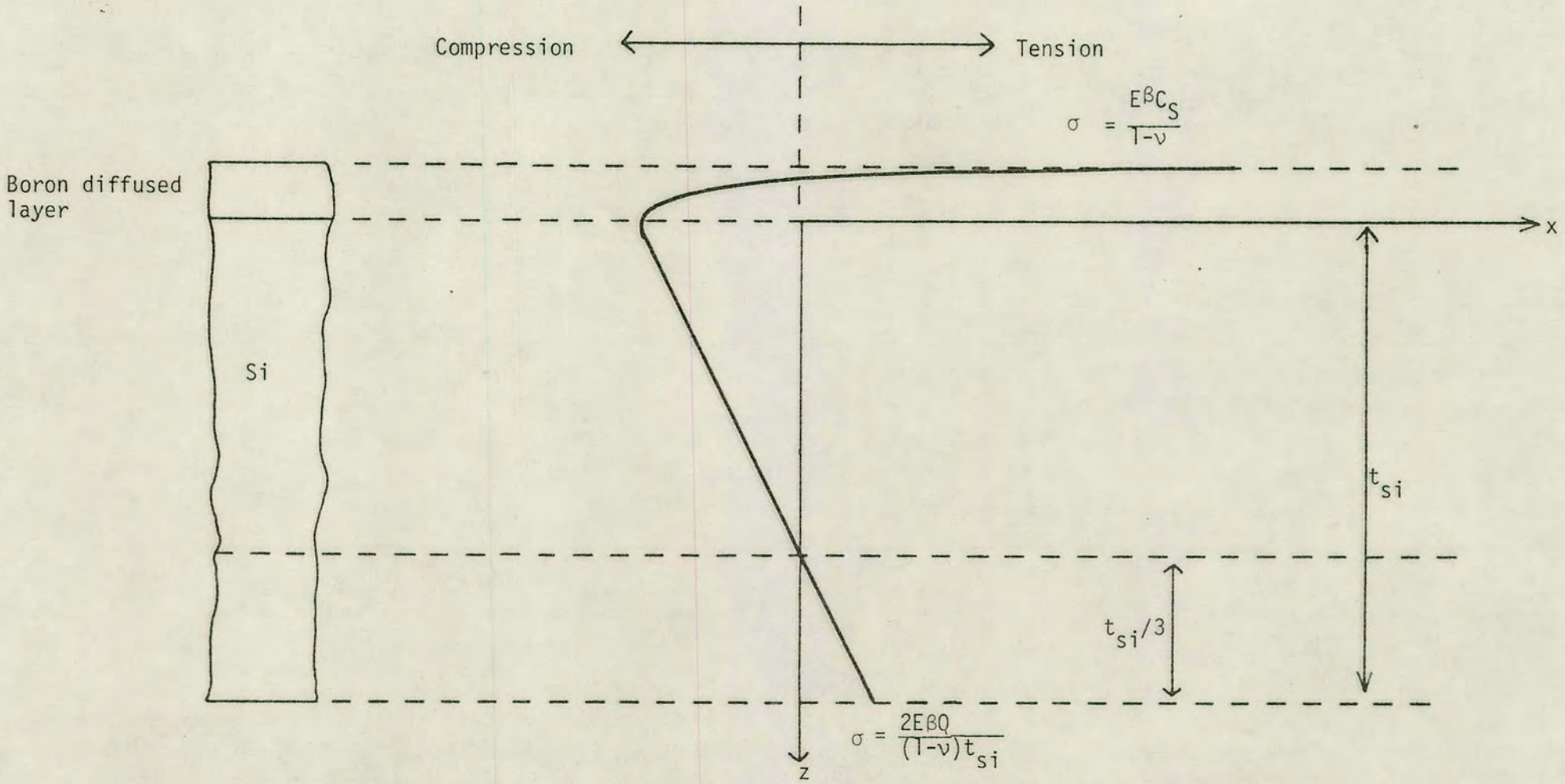

FIGURE 8.2: Schematic illustration of stresses acting at edge of boron diffused region in a silicon slice (c.f. Fig 7.3).

t and surface concentration by the expression (Equation 2.14)

$$Q = 2C_S \sqrt{Dt/\pi} \qquad (8.8)$$

At 950°C, Wolf[2] gives $D = 5.0 \times 10^{-15}$ cm^2/sec. These results are given in Table 8.2.

TABLE 8.2

Inter-ferometer	Diffusion time t (seconds)	$\frac{Q}{2C_S\sqrt{Dt/\pi}}$ (cm^{-2}) (calculated)	Fringe spacing/ disc radius f/r_o	Force acting at edge of diffusion dynes/cm
I3	900	0.96×10^{15}	.383	1.56×10^4
I5	2100	1.46×10^{15}	.354	1.94×10^4
I1	3600	1.91×10^{15}	.243	2.56×10^4
I4	8100	2.87×10^{15}	.221	3.37×10^4

It is interesting to note that in Figs 8.3 and 8.4 a small rotation has been introduced into the lattice by the diffusion. However, it was shown in Chapter 3 that the dilatation and rotation effects are independent of each other and it was also shown how the dilatation may be calculated from the components of moiré fringe spacing in the horizontal direction. Fig 8.6 is interesting in that the characteristic fringe pattern is absent. For this reason the measurements made from this topograph were suspect and were not considered in the ensuing calculations. The characteristic fringe pattern is probably absent due either to the masking oxide being too thin or to some strain centre imposing an overriding dilatational moiré effect.

FIGURE 8.3: Moiré topograph of boron diffused disc.
15 minutes diffusion at 950°C.
(02$\bar{2}$ reflection MoKα radiation)

FIGURE 8.4: Moiré topograph of boron diffused disc. 35 minutes diffusion at 950°C. ($02\bar{2}$ reflection, MoKα radiation)

FIGURE 8.5: Moiré topograph of boron diffused disc.
1 hour diffusion at 950°C
($02\bar{2}$ reflection, MoKα radiation)

FIGURE 8.6: Moiré topograph of boron diffused disc
$2\frac{1}{4}$ hours diffusion at 950°C.
Note absence of predicted fringed pattern
($0\bar{2}2$ reflection, MoKα radiation)

The results of Table 8.2 are presented graphically in Fig 8.7. By using least squares analysis, the gradient of the straight line through these points is calculated to be 1.38×10^{-11}. Hence, from Equation 8.7, β may be calculated to be 6.0×10^{-24} cm^3.

The total impurity diffusion dose was deliberately kept low on account of work by Queisser[7] and Schwuttke and Queisser[8] who showed by both etch and X-ray techniques that dislocations resulted in diffused samples, not as a function of impurity concentration, but as a function of the impurity dose. In the case of boron diffusion, they found that the critical dose was about 3×10^{15} atoms/cm^2. Although no dislocation images are obviously visible in the topograph of Fig 8.6, the resultant fringe pattern may be due to some irregularities taking place in the lattice since the dose is just about the critical value.

Interferometer I6 was subjected to a two hour diffusion at $1100^{o}C$, the diffusion being allowed to take place on the outside of the whole splitter wafer, the rest of the interferometer being covered by masking oxide. The dose corresponding to this diffusion was calculated to be 2.1×10^{16} atoms/cm^2. Fig 8.8 shows how the silicon has dislocated to such an extent that no moiré fringes are visible, only dislocation images. It is interesting to note that these dislocations are arranged in triangular fashion as one would expect with a $\{111\}$ face. Similar dislocation images were also observed in silicon slices diffused with boron for 30 minutes and 15 minutes at $1100^{o}C$. The 15 minute diffusion corresponds to a dose of 7.4×10^{15} atoms/cm^2. It is interesting to note that McQuhae and Brown[17] reported that they did not observe dislocations, even with boron doses as high as 2×10^{16}

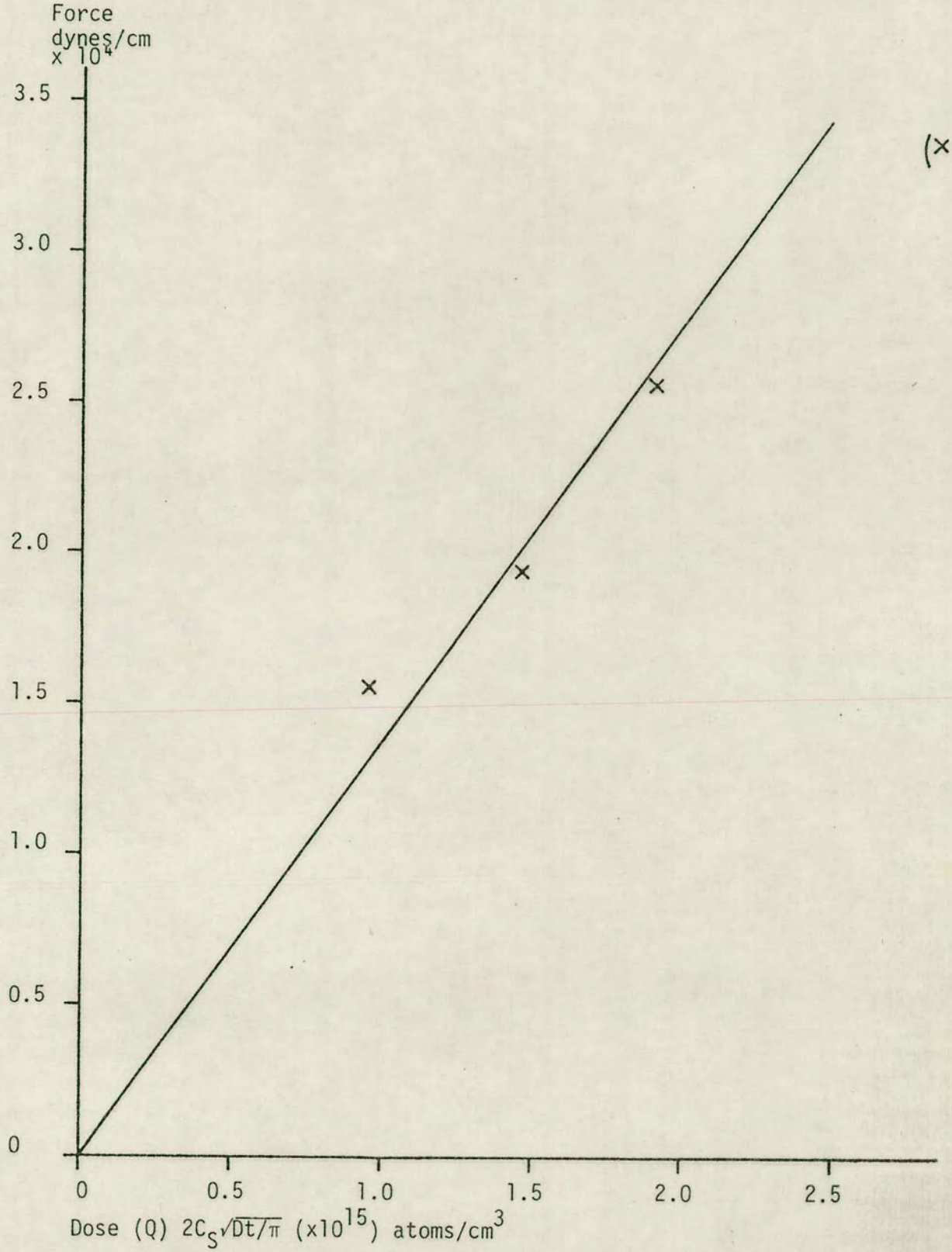

FIGURE 8.7: Force acting into substrate at diffusion edge as a function of dose (assuming an erfc diffusion profile)

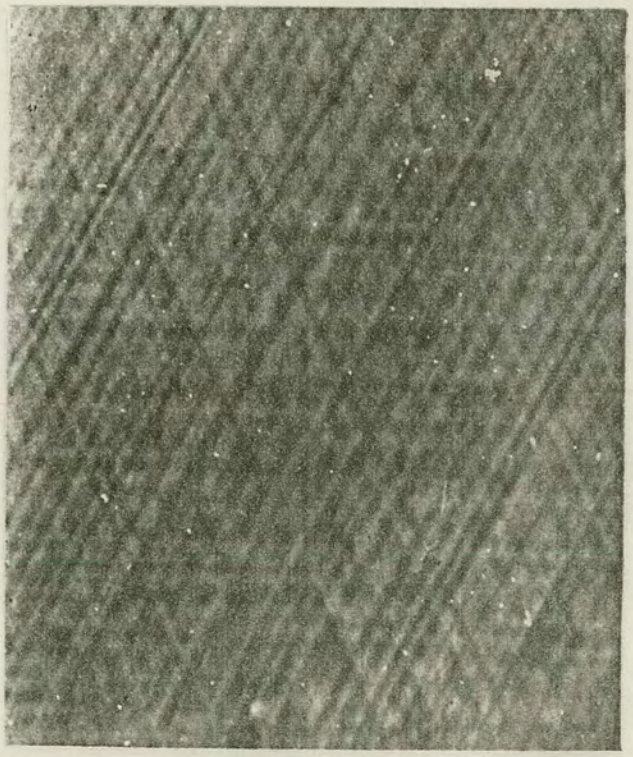

FIGURE 8.8: Dislocations resulting from a 2 hour diffusion at 1100°C. Note that dislocation density is too high for a moiré fringe pattern to form ($02\bar{2}$ reflection, MoKα radiation)

atoms/cm^2.

8.2 MOBILITY MEASUREMENTS

Silicon slices were diffused with boron at the same time as the interferometers. Since silicon becomes p-type after boron diffusion, n-type slices were chosen with resistivity of 50 Ωcm. This was so that after diffusion a depletion region would form causing conductivity to occur only in the surface diffused region (typically within 0.5 μm of the surface). Wolf[2] quotes the equivalent background concentration for 50 Ωcm material as being 2×10^{14} atoms/cm^3. The slices which were available were {100} orientation float-zoned phosphorus diffused samples. The orientation in this application is unimportant since diffusion rates and resistivities are not dependent on orientation. After diffusion, the samples were subjected to a standard four-point probe test, in order to determine their sheet resistance ($R_\square$).

The resistivity is related to carrier mobility by the following relation

$$\rho = \frac{1}{q(n\mu_n + p\mu_p)} \qquad (8.9)$$

where μ_n and μ_p are electron and hole mobilities respectively, and n and p are electron and hole concentrations respectively. q is the electronic charge (= 1.6×10^{-19} coulombs). For heavily doped regions, the minority carriers may be ignored. The mean resistivity in a doped region of varying carrier concentration may therefore be calculated by suitable integration,

$$\frac{1}{\bar{\rho}} = \frac{1}{z_j} \int_0^{z_j} q\mu_p \, C(z)dz \qquad (8.10)$$

where z_j is the junction depth. In this instance, the majority carriers are holes - hence μ_p in the expression.

Carrier mobility is a function of impurity scattering mobility (μ_I) lattice mobility (μ_L) and charge carrier scattering mobility (μ_C)

$$\frac{1}{\bar{\rho}} = \frac{1}{\mu_I} + \frac{1}{\mu_L} + \frac{1}{\mu_C} \qquad (8.11)$$

At low impurity concentrations, the mobility is due to the lattice mobility, but as the concentration increases, the overall mobility decreases. At high concentrations, the silicon becomes degenerate and the mobility is practically constant with impurity concentration. Hence

$$\frac{1}{\bar{\rho}} = \frac{q\mu_p}{z_j} \int_0^{z_j} C(z)dz \qquad (8.12)$$

It will be seen at once that the integral now represents the total impurity dose (Q), or number of carriers within the surface region which give rise to conduction. $(\bar{\rho}/z_j)$ is the effective sheet resistivity, so that under conditions of high impurity concentration the impurity dose (Q) and sheet resistivity may be connected by

$$R_{\square} = \frac{1}{\mu_p q Q} \qquad (8.13)$$

The values of Q were those calculated from the moiré fringe topographs of Figs 8.3 - 8.6 using the value of 6.0×10^{-24} for β as

calculated in Section 8.1. The data is presented in Table 8.3.

TABLE 8.3

Sample	Dose (Q) (Measured)	Sheet Resistance $R_\square$ ($\Omega/\square$)	$1/q\ R_\square$
I3/D3	1.13×10^{15}	47.1	1.33×10^{17}
I5/D5	1.41×10^{15}	34.3	1.82×10^{17}
I1/D1	1.86×10^{15}	27.9	2.24×10^{17}
I4/D4	2.45×10^{15}	23.4	2.67×10^{17}

These results are plotted graphically in Fig 8.9. Least squares analysis yields the gradient to be 122 - this is in fact the mobility ($cm^2/v.sec$). This result gives good agreement with Wolf[2] who quotes the mobility of holes in degenerate p-type silicon as being 115 $cm^2/v.sec$ at room temperature. However, this does not agree well with early measurements of hole mobility in degenerate silicon by Horn[117] who measured values ranging between 46 and 71 $cm^2/v.sec$. This may be due to his samples not being completely dislocation-free.

In order to check the mobility of dislocated samples, samples were diffused with boron for 2 hours and 30 minutes with boron at 1100^oC and both were found to contain dislocations (the result of the 2 hour diffusion is shown in Fig 8.8). The results may be seen in Table 8.4.

TABLE 8.4

Diffusion time at 1100^oC minutes	Dose $\frac{Q}{2C_S\sqrt{Dt/\pi}}$	Sheet resistance $R_\square$ ($\Omega/\square$)	$\mu_p (cm^2/volt\ sec) = 1/qQR_\square$
30	1.05×10^{16}	7.3	82
120	2.10×10^{16}	4.0	74

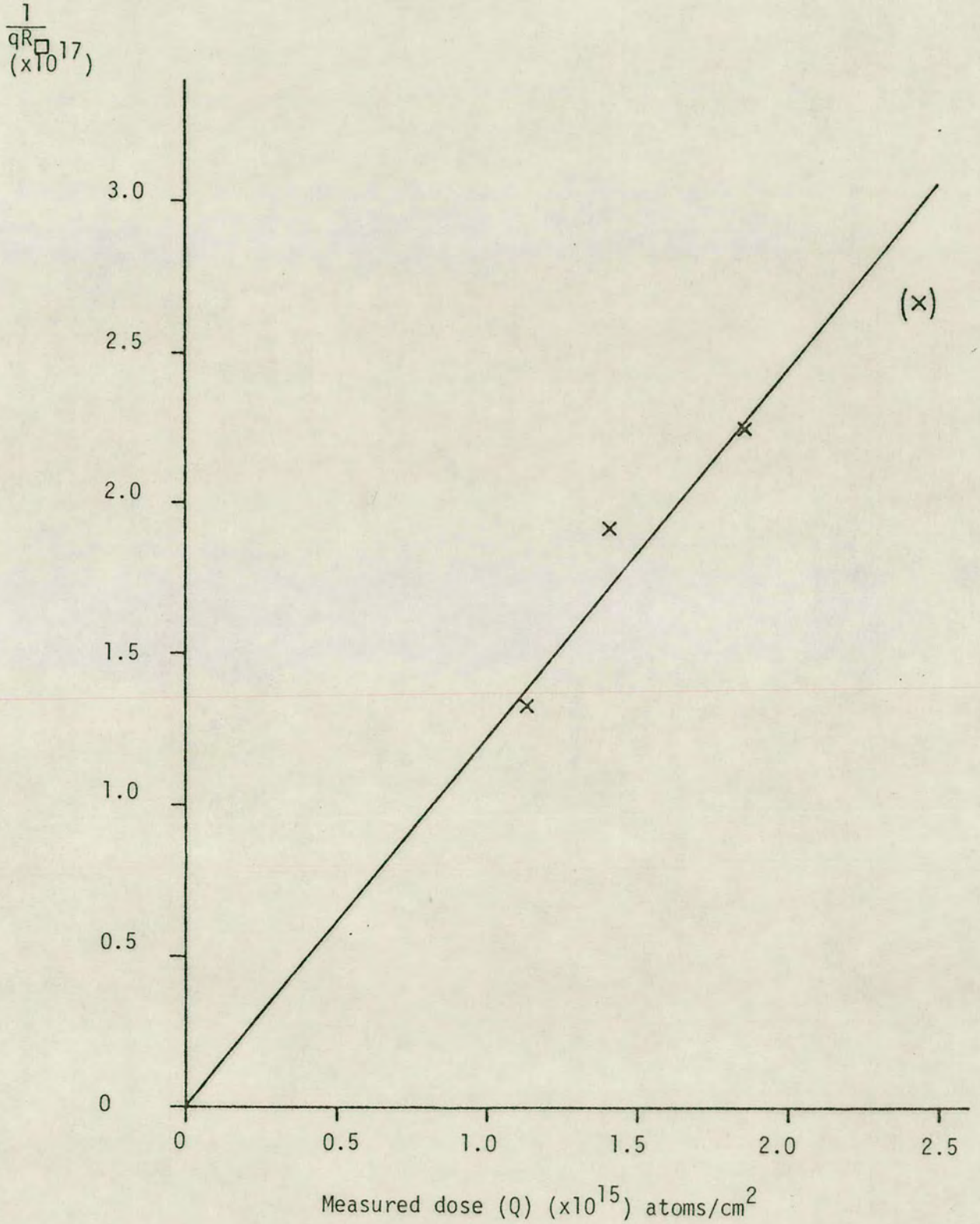

FIGURE 8.9: $\frac{1}{qR_\square}$ as a function of dose calculated from moiré topograph

This would indicate that the presence of dislocations would have the effect of reducing the mobility and would account for the apparent discrepancy in the result.

8.3 DOUBLE CRYSTAL MEASUREMENTS

The measurements made from the moiré topographs yield information about the strain in directions lying within the plane of the silicon slice. It is by using the double crystal spectrometer that information about strain perpendicular to the wafer surface may be readily obtained. Since the silicon is not constrained in this direction, the stress will be zero allowing the atomic spacing to contract due to the smaller atomic radii of the boron atoms. It was from measuring the diffraction peaks simultaneously from the diffused and undiffused regions beneath the surface that Cohen[16] was able to measure the peak separation and hence the lattice contraction coefficient β. A repeat of this experiment was attempted using the control slices diffused with the interferometers.

The extinction coefficient ξ determines the reduction in intensity per atomic plane of an incident beam while undergoing total Bragg reflection. The intensity reduces by a factor of $e^{-2\xi}$. For a 400 reflection $2\xi = 6.06 \times 10^{-5}$ per plane. With a junction depth of ~0.4 μm (assuming an erfc diffusion profile and using graphs in Wolf[2]) for the most heavily diffused sample ($2\frac{1}{4}$ hours at $950^{o}C$) this corresponds to a depth of ~3000 atomic planes. If the impurity concentration is at a constant value over this depth, the ratio of intensities of main and satellite peaks will be 0.17. This is not in fact the case, the concentration following an erfc profile with

depth. The effect is that the satellite peak will broaden out with resultant reduction in intensity. Figs 8.10(a)-(d) show rocking curve measurements made on a reference sample, and samples D5, D1 and D4 respectively where the satellite peak has broadened out to such an extent that it is manifested only as an asymmetry of the rocking curve. Cohen was able to observe separate peaks since he was working with much higher doses of impurities ($\sim 2 \times 10^{16}$ atoms/cm^2) such that the surface regions have much more significant effect. It should be noted, however, that the rocking curve asymmetry of Figs 8.10(a)-(d) increaseswith impurity dose, and therefore junction depth, as would be expected.

The rocking curves were observed through a narrow slit 0.5 mm apart in order to minimise any effects of warpage of the silicon slice and the intensity profiles recorded on paper tape. No significant variation in the rocking curve width at half height could be detected, the average width being 6.0 seconds of arc. This may be compared with the theoretical width at half height of 4.9 seconds.

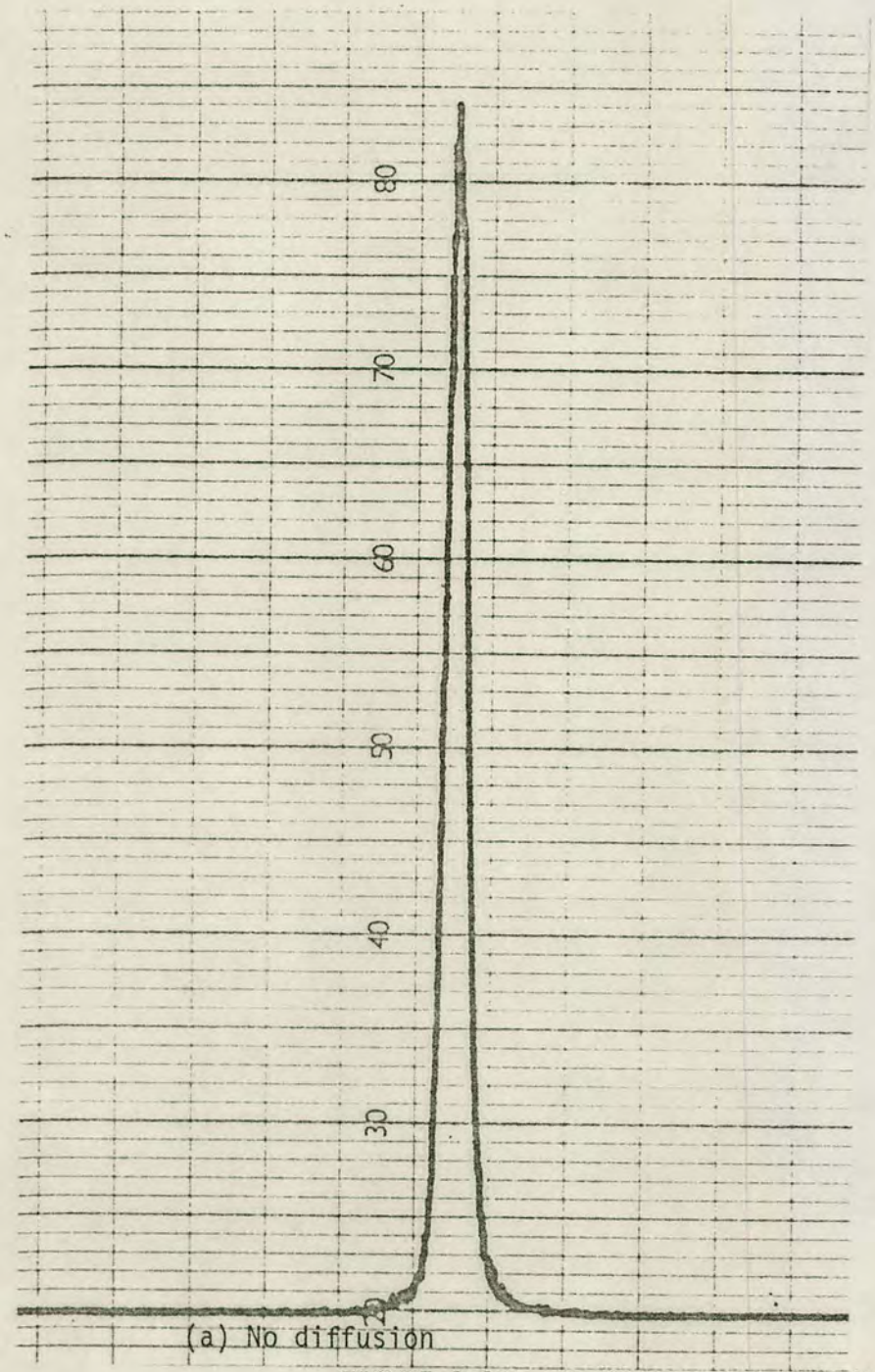

(a) No diffusion

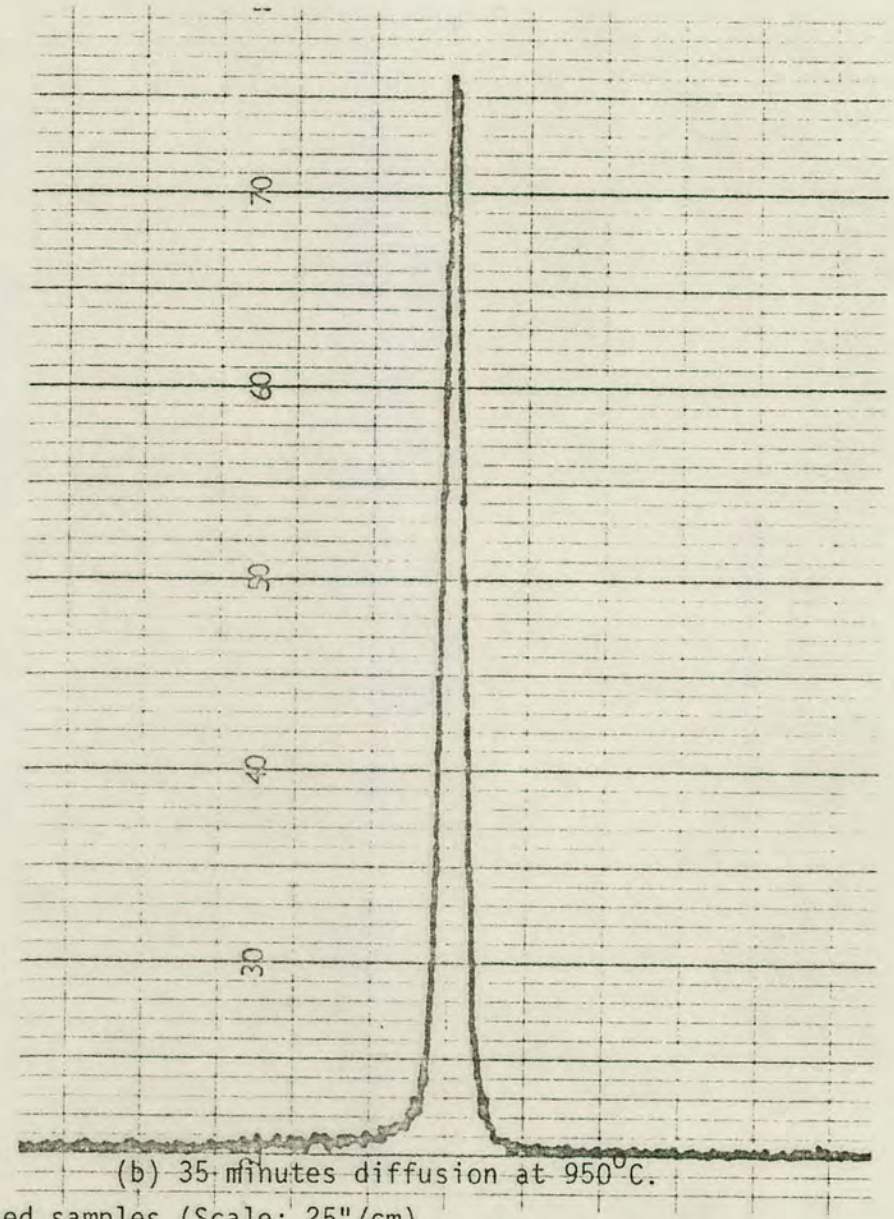

(b) 35 minutes diffusion at 950°C.

FIGURE 8.10: Rocking curves of diffused samples (Scale: 25"/cm)

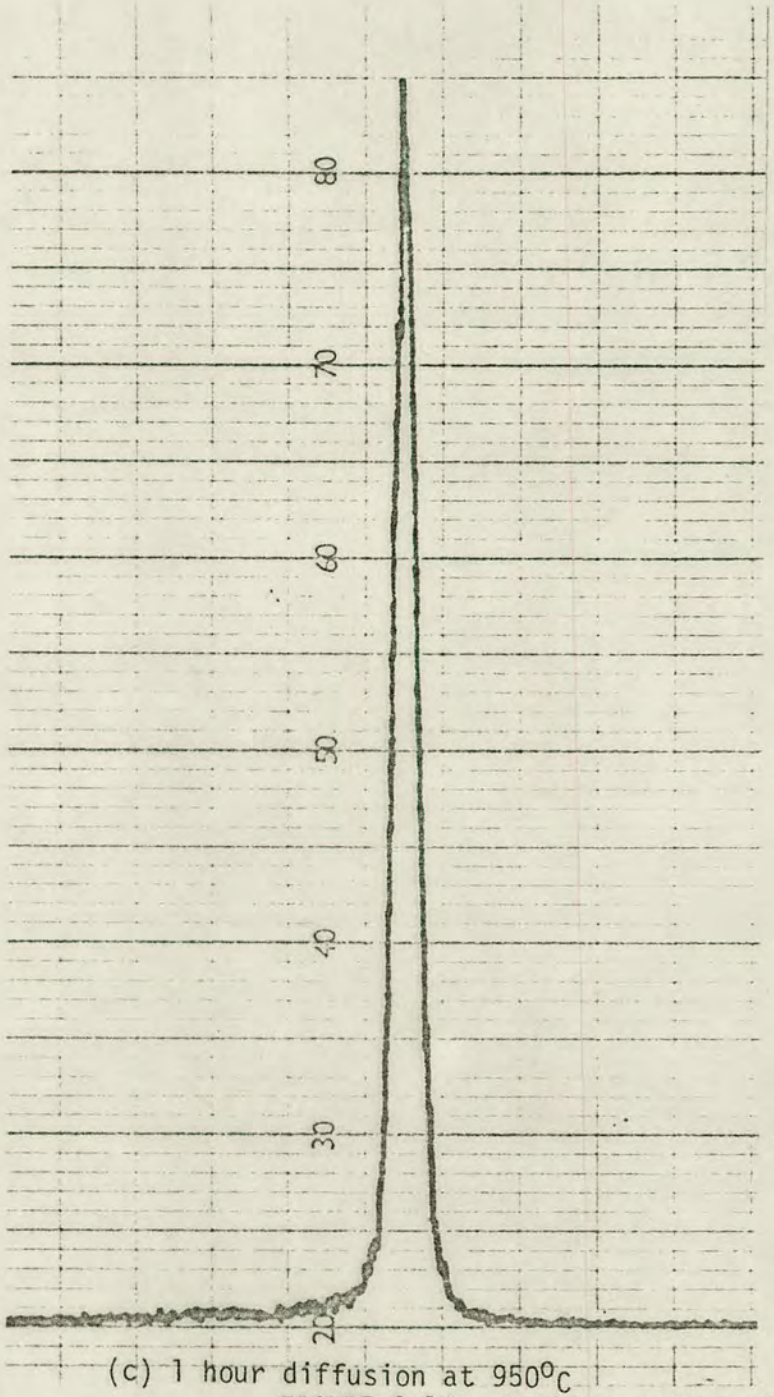

(c) 1 hour diffusion at 950°C

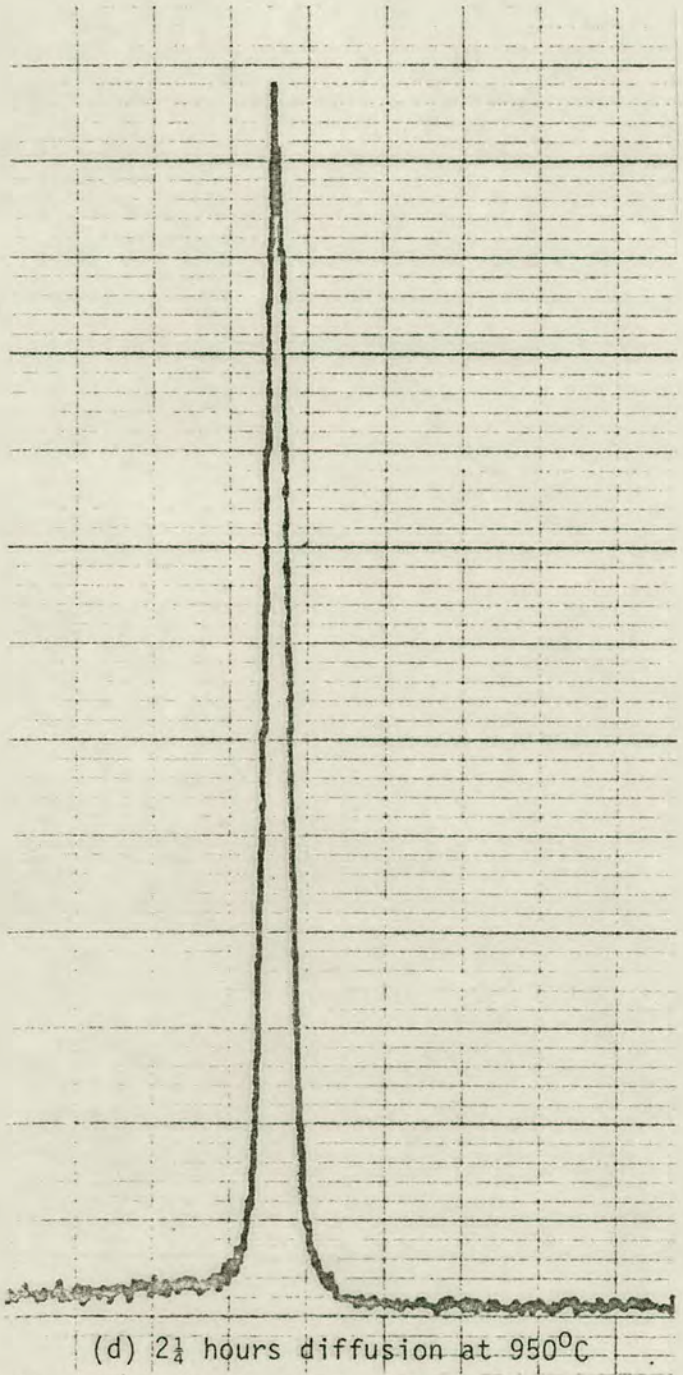

(d) 2¼ hours diffusion at 950°C

FIGURE 8.10: Rocking curves of diffused samples (Scale: 25"/cm)

CHAPTER 9: CONCLUSIONS

It has been the aim of this thesis to use X-ray interferometers to measure the strain induced in silicon by two fundamental processes necessary in the fabrication of integrated circuits, namely oxidation and diffusion. By developing an elasticity model and comparing observed moiré fringe patterns with those predicted by theory, it has been shown that the resultant strain within a silicon slice gives fairly good agreement with theory.

Using X-ray interferometer techniques, it was possible to measure the stress within a thermally grown oxide and the stress which this induced in the silicon substrate. The stress within the oxide was measured to be 1.65×10^9 dynes/cm^2 compared with the value of 2.5×10^9 dynes/cm^2 predicted by considering the relative thermal contractions of SiO_2 and Si. Using double crystal techniques it was possible to measure the radius of curvature of the silicon immediately underneath the oxide. The value of 46 metres for an oxide thickness of 1.18 μm and slice thickness of 378 μm agreed well with the curvature which would be expected from analysis of the moiré fringe pattern. The double crystal technique was also able to show that the mechanical warpage of the wafer was convex on the oxidised side, confirming that the oxide stress was compressive.

The results from the boron diffusion experiments appeared to give better agreement with theory than the oxidation experiments. The lattice contraction coefficient for boron diffusion, β, was measured to be 6.0×10^{-24} compared with the value of 5.0×10^{-24} calculated from consideration of the relative covalent atomic radii sizes of boron and silicon atoms. From four point probe measurements,

it was possible to measure the mobility of holes μ_p in degenerate p-type silicon. μ_p was found to be 122 cm^2/volt sec, giving good agreement with the value of 115 cm^2/volt sec given by Wolf[2]. The values measured by Horn[117] ranging between 46 and 71 cm^2/volt sec are probably due to his samples not being dislocation free.

It was found that there exists a critical impurity dose above which lattice dislocation occurred. This was found to be between 2.9×10^{15} and 7.4×10^{15} atoms/cm^2. This agrees well with the observation by Queisser[7] who determined the critical dose for boron to be 3×10^{15} atoms/cm^2.

An attempt was made to repeat the experiment by Cohen[16] to detect separate diffraction peaks from both the diffused layer and undiffused region underneath using a double crystal spectrometer. However, no distinct peaks were observed since the impurity dosage was deliberately kept low to prevent dislocation of the lattice from occurring.

Several dislocations were observed in one interferometer and their Burger's vectors were analysed. These dislocations arose after two heavy oxidations and much handling. It is interesting to note that despite three further subjections to furnace temperatures they remained immobile.

9.1 APPLICATION TO RESONATORS/MONOCHROMATORS

In Chapter 1, it was proposed that it would be interesting to study the possibility of using oxide or diffusion induced strain to change the silicon lattice parameter by appropriately controlled amounts in order to realise a monolithic resonator or monochromator

which would function at room temperature without needing to be tuned.

The simplest monolithic resonator and monochromator structures are shown in Figs 9.1(a) and (b). The arrangements shown in the figures are Bragg reflecting geometry (i.e. incident and diffracted beams are on the same face of the crystal). Similar arrangements also exist for Laue case geometry (incident and diffracted beam on opposite sides of the crystal) after correction for refractive index, but since this correction is typically only a few parts per million it will be ignored here. The conditions for a resonator or monochromator to work are that diffraction takes place from two sets of atomic planes cut monolithically from the same crystal. If the beam is caused to turn through more than 180^{o}, resonator geometry is realisable, otherwise monochromator geometry. For successive diffractions to occur and if the X-ray beams are to be coplanar, the following conditions apply

$$\begin{aligned} 2d_1 \sin\theta_1 &= 2d_2 \sin\theta_2 = \lambda \\ \theta_2 \mp \theta_1 &= \alpha \end{aligned} \qquad (9.1)$$

where d is spacing of the Bragg planes and θ the Bragg angle. α is the angle between the pair of diffracting planes. These conditions relate the X-ray wavelength λ with the crystal lattice parameter, so that a chosen wavelength immediately determines the lattice parameter for a given pair of diffracting planes.

Hart[64] has calculated possible reflections in germanium and silicon for certain X-ray wavelengths, together with the mismatch between the actual and ideal lattice parameter. His results are given in Table 9.1 for silicon and germanium. For a resonator or

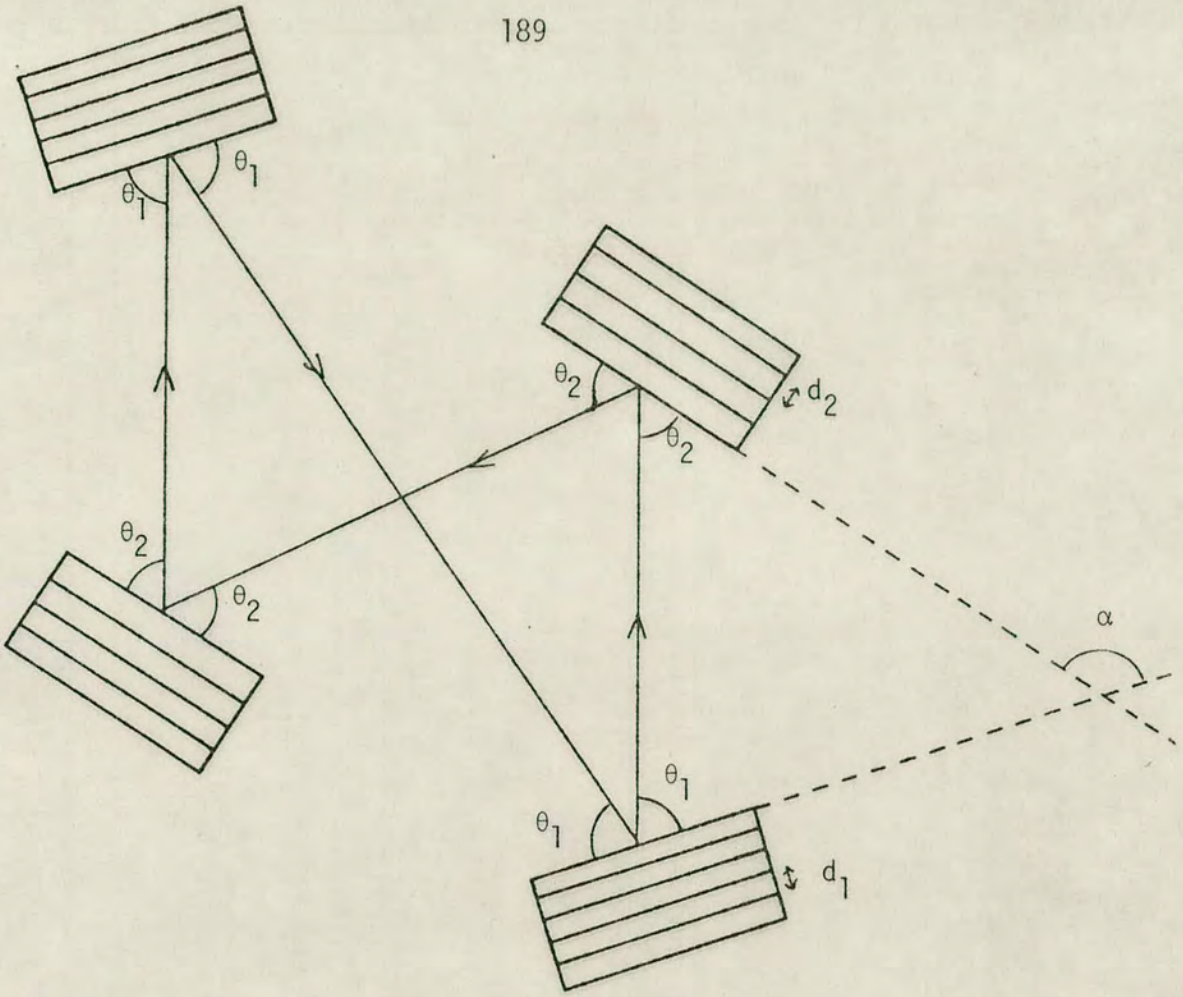

(a)

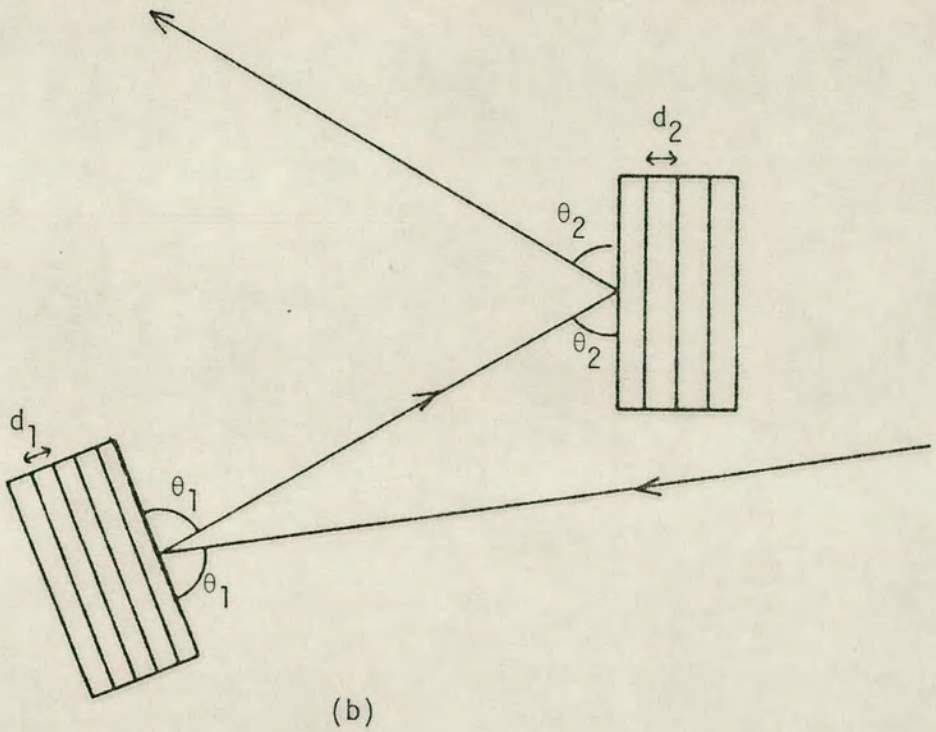

(b)

FIGURE 9.1: (a) Typical resonator geometry
(b) Typical monochromator geometry

TABLE 9.1 (Hart[64])

Radiation		Reflections	α	Mismatch (ppm)
Wavelength(A)	Designation			
Silicon				
0.158 971	Au $K\beta_1$	444, 553	12.27^o	+ 70
0.475 106	Cd $K\beta_1$	624, 462	38.21^o	+ 1
0.475 106	Cd $K\beta_1$	606, 246	40.89^o	∓ 1
0.499 544	Sn $K\alpha_1$	624, 535	40.05^o	∓ 114
0.520 559	Pd $K\beta_1$	555, 511	38.94^o	∓ 75
0.563 855	Ag $K\alpha_2$	715, $1\bar{1}7$	48.76^o	+ 54
0.613 297	Rh $K\alpha_1$	733, $35\bar{1}$	47.04^o	- 130
1.254 210	Ge $K\alpha_1$	606, $\bar{1}\bar{1}1$	90.00^o	- 125
1.254 210	Ge $K\alpha_1$	533, 044	90.00^o	-125
1.312 876	Pt $L\alpha_1$	515, $1\bar{5}5$	119.35^o	+ 123
1.662 860	Ni $K\alpha_2$	404, $0\bar{4}4$	120.00^o	- 670
Germanium				
0.545 610	Rh $K\beta_1$	913, $75\bar{5}$	56.05^o	- 9
0.563 786	Ag $K\alpha_2$	844, $35\bar{1}$	46.36^o	+ 21
0.613 243	Rh $K\alpha_1$	422, $53\bar{1}$	34.09^o	+ 59
1.287 730	Au $L\alpha_2$	511, $\bar{1}37$	97.19^o	- 79
1.312 976	Pt $L\alpha_1$	606, $1\bar{3}3$	130.45^o	+ 46
1.313 007	Pt $L\alpha_1$	202, $\bar{3}35$	149.61^o	+ 24
1.392 284	Cu $K\beta_1$	711, $\bar{5}35$	132.41^o	- 47
1.789 067	Co $K\alpha_1$	202, $40\bar{4}$	90.00^o	- 58
2.289 371	Cr $K\alpha_1$	111, $2\bar{2}4$	118.12^o	- 145
2.289 349	Cr $K\alpha_1$	422, $31\bar{3}$	159.48^o	- 153
2.507 767	V $K\alpha_2$	111, $3\bar{1}3$	97.61^o	- 153
3.771 667	In $L\alpha_1$	111, $0\bar{2}2$	144.73^o	+ 66

monochromator to work therefore, it is necessary to alter the lattice parameter by some means. The easiest way to achieve this is by varying the temperature appropriately, but this could be inconvenient for ordinary laboratory use. The other possible method is by straining the lattice by appropriate oxidation or diffusion.

It has been shown in this thesis that the strain within an oxidised or diffused slice is caused by the resultant bowing of the slice. This bowing obviously rules out Laue geometry devices since the angles between successive diffractions will vary over the width

of the diffracting X-ray beam. The alternative is to use Bragg geometries with oxidation and diffusion taking place on the surfaces of thick blocks of crystal so that bowing does not occur. After oxidation the forces and therefore the greatest strain is directed in the plane of the surface but variation in lattice spacing perpendicular to the surface will arise, however, and may be derived from the strain in directions lying in the surface, by applying Poisson's ratio. However, this amounts to not much more than one part per million and since this can be accounted for by a change in temperature of ~0.4^{o}C, is not worth considering. The only remaining possibility lies in the use of impurity diffusion into the surface of thick blocks of crystal. Cohen[16] has shown that diffraction peaks may be obtained from suitably diffused samples which are angularly displaced from the peak resulting from the host material. However, it was shown in Section 8.1 that if dislocation is not to occur in the host material (the effect of which is a broadening of the reflection curve - the opposite effect from that intended with a resonator or monochromator) the total impurity dose must be kept below a certain limit. In Section 8.3, it was shown that the dose then becomes too small for a significant satellite diffraction peak to occur. For these reasons, it is not feasible to alter the lattice parameter of germanium or silicon by suitable oxidation or diffusion in order to meet the requirements for a working resonator or monochromator.

9.2 FUTURE WORK

It is interesting to note that interferometer measurements agreed with theory much better in the diffusion experiments than in the

oxidation experiments. Since more assumptions had to be made for the former experiments (eg complementary error function diffusion profiles) more weight should be applied to the 'poorer' result of the oxidation experiments than to the 'good'results of the diffusion experiments. Further checks should be made to see if the elasticity model is at fault or if indeed, under the present experimental conditions, a lower stress did exist in the oxide than would be expected. Once this has been established, then greater confidence can be gained for the results from the diffusion experiments.

In the diffusion experiments, the assumption has been made that the diffusion profile has been a complementary error function profile as predicted by theory. It is well known that minor deviations can occur depending on the exact processing conditions. The exact profile may be determined accurately by experimental methods but this involves the use of sophisticated techniques not available here.

A modern processing technique which was not considered is ion implantation. By this technique any chosen diffusion profile may be programmed into a silicon slice. The possibility of its use for suitable lattice parameter alteration in a resonator or monochromator has not been considered here, and until recently would have been inappropriate due to the severe lattice damage which is caused. However, there now exists a technique of laser annealing which is capable of removing this damage. By using ion implantation, problems associated with ordinary diffusion techniques may be avoided. Also, by this technique, the total dose of impurity may be controlled accurately, and so interferometer studies of ion implantation would make interesting comparison with the diffusion results obtained in this thesis.

REFERENCES

1. "Electronics International", McGraw Hill Publications Inc., New York (Jan 1966 - Jan 1978).

2. H.F. WOLF, "Silicon Semiconductor Data", Pergamon Press, (1969).

3. J.M. FAIRFIELD and G.H. SCHWUTTKE, J. Electrochem. Soc., 113, (1966) 1229.

4. A. AUTHIER, D. SIMON, A. SENES, Phys. Stat. Solidi, (a), 10, (1972) 233.

5. M. LEFELD-SOSNOWSKA, E. ZIELINSKA-ROMOZINSKA and J. GRONKOWSKI, Phys. Stat. Solidi, (a), 29, (1975) 535.

6. S. PRUSSIN, J. Appl. Phys., 32, (1961) 1876.

7. H.J. QUEISSER, J. Appl. Phys., 32 (1961) 1776.

8. G.H. SCHWUTTKE and H.J. QUEISSER, J. Appl. Phys., 33, (1962) 1540.

9. J. WASHBURN, G. THOMAS and H.J. QUEISSER, J. Appl. Phys., 35, (1964) 1909.

10. R.J. JACCODINE, Appl. Phys. Lett., 4 (1964) 114.

11. M.L. JOSHI and F. WILHELM, J. Electrochem. Soc., 112, (1965) 185.

12. R.J. JACCODINE and W.A. SCHLEGEL, J. Appl. Phys., 37 (1966) 2429.

13. G.H. SCHWUTTKE and J.K. HOWARD, J. Appl. Phys., 39 (1968) 1581.

14. S.D. BROTHERTON, T.G. READ, D.R. LAMB and A.F.W. WILLOUGHBY, Solid-State Electronics, 16, (1973) 1367.

15. I.A. BLECH and E.S. MEIERAN, J. Appl. Phys., 38, (1967) 2913.

16. B.G. COHEN, Solid State Electronics, 10, (1967) 33.

17. K.G. McQUHAE and A.S. BROWN, Solid-State Electronics, 15 (1972) 259.

18. U. BONSE, M. HART and G.H. SCHWUTTKE, Phys. Stat. Solidi, 33, (1969) 361.

19. N. ITOH, Y. MORIKAWA, T. NAKAN and H. KURODA, Jap. J. Appl. Phys., 14, (1975) 2069.

20. E.S. MEIERAN and I.A. BLECH, J. Appl. Phys., 36,(1965) 3162.

21. I.A. BLECH and E.S. MEIERAN, Appl. Phys. Lett., 9, (1966) 245.

22. L.K. WALFORD and G.J. CARRON, J. Appl. Phys., 39, (1968) 5802.

23. B.G. COHEN and M.W. FOCHT, Solid-State Electronics, 13, (1970) 105.

24. T.I. KAMINS and E.S. MEIERAN, J. Appl. Phys., 44, (1973) 5064.

25. P. PENNING and D. POLDER, Philips Res. Rep., 16, (1960) 419.

26. N. KATO, J. Phys. Soc. Jap., 18, (1963) 1785.

27. N. KATO, J. Phys. Soc. Jap., 19, (1964) 67.

28. U. BONSE, Z. Phys., 177, (1964) 385.

29. M. HART, Appl. Phys. Lett., 7, (1965) 96.

30. M. HART, Z. Phys., 189, (1966) 269.

31. M. KURIYAMA, J. Phys. Soc. Jap., 23, (1967) 1369.

32. M. KURIYAMA, J. Phys. Soc. Jap., 25, (1968) 846.

33. S. TAKAGI, J. Phys. Soc. Jap., 26, (1969) 1239.

34. H. HASHIZUME and K. KOHRA, J. Phys. Soc. Jap., 31, (1971) 204.

35. H. HASHIZUME, J. Phys. Soc. Jap., 31, (1971) 1124.

36. N. KATO and J.R. PATEL, J. Appl. Phys., 44, (1973) 965.

37. J.R. PATEL and N. KATO, J. Appl. Phys., 44, (1973) 971.

38. Y. ANDO, J.R. PATEL and N. KATO, J. Appl. Phys., 44, (1973) 4405.

39. J. KACZER and F. KROUPA, Czech. J. Appl. Phys., 1, (1952) 80.

40. P.S. THEOCARIS, "Moire fringes in strain analysis", Pergamon Press, (1969).

41. U. BONSE and M. HART, Appl. Phys. Lett., 6, (1965) 155.

42. U. BONSE and M. HART, Appl. Phys. Lett., 7, (1965) 99.

43. U. BONSE and M. HART, Z. Physik, 188, (1965) 154.

44. A.R. LANG and V.F. MIUSCOV, Appl. Phys. Lett., 7, (1965) 214.

45. U. BONSE and M. HART, Z. Physik, 194, (1966) 1.

46. U. BONSE and M. HART, Z. Physik, 190, (1966) 455.

47. N. KATO and S. TANEMURA, Phys. Rev. Lett., 19, (1967) 22.

48. U. BONSE, "Present state of X-ray interferometry", Vth International Congress on X-Ray Optics and Microanalysis, TÜbingen, (1968).

49. U. BONSE and M. HART, Acta Cryst., A24, (1968) 240.

50. U. BONSE and E. Te KAAT, Z. Physik, 214, (1968) 16.

51. R.D. DESLATTES, Appl. Phys. Lett., 15, (1968) 386.

52. M. HART, Brit. J. Appl. Phys., 1, (1968) 1405.

53. M. HART, Sci. Prog. Oxford, 56, (1968) 429.

54. U. BONSE and H. HELLKÖTTER, Z. Physik, 223, (1969) 345.

55. M. HART and A.D. MILNE, J. Phys., 2E, (1969) 646.

56. I. CURTIS, I. MORGAN, M. HART and A.D. MILNE, "A New Determination of Avogadro's Number", Precision Measurement and Fundamental Constants. Edited by D.N.Langenburg and B.N. Taylor, National Bureau of Standards, special publication, 343.

57. U. BONSE, E. Te KAAT and P. SPICKER, "Precision Lattice Parameter Measurement by X-Ray Interferometry", Precision Measurement and Fundamental Constants. Edited by D.N. Langenburg and B.N. Taylor, National Burea of Standards, special publication, 343.

58. U. BONSE, "Recent Developments in X-Ray Interferometry", American Crystallographic Association, Summer Meeting, Ottawa, (1970).

59. M. HART, "Absolute Length Standards for X-Ray Analysis", American Crystallographic Association, Summer Meeting, Ottawa, (1970).

60. U. BONSE and M. HART, Physics Today, 23, (1970) 26.

61. M. HART and D.C. CREAGH, Phys. Stat. Solidi, 37, (1970¼ 753.

62. U. BONSE and E. Te KAAT, Z. Physik, 243, (1971) 14.

63. G. CHRISTIANSEN, L. GERWARD and A. LINDEGAARD ANDERSEN, J. Appl. Cryst., 4, (1971) 370.

64. M. HART, Rep. Prog. Phys., 34, (1971) 435.

65. M. KURIYAMA, Acta Cryst., A27, (1971) 273.

66. M. HART, Phil. Mag., 26, (1972) 821.

67. H. HASHIZUME, H. ISHIDA and K. KOHRA, Phys. Stat. Solidi, A12, (1972) 453.

68. U. BONSE and G. MATERLIK, Z. Physik, 253, (1972) 232.

69. P. BESIRGANYAN, F. EIRAMDSHYAN and K. TRUNI, Phys. Stat. Solidi, A20, (1973) 611.

70. U. BONSE, H. RAUCH, W. TREIMER, Phys. Lett., A47, (1974) 369.

71. U. BONSE and P. BECKER, J. Appl. Cryst., 7, (1974) 593.

72. U. BONSE and G. MATERLIK, Acta Cryst., A31, pt 53, (1975) 5232.

73. M. HART, Proc. Roy. Soc., 346, (1975) 1.

74. W. BAUSPIESS, U. BONSE and W. GRAEFF, J. Appl. Cryst., 9, (1976) 68.

75. H. ISHIDA, J. Appl. Cryst., 9, (1976) 240.

76. D. PETRASCHECK and R. FOLK, Phys. Stat. Solidi, A36, (1976) 147.

77. R.B. SOSMAN, Am. Ceramic Soc. Bull., 43, (1964) 213.

78. W.H. ZACHARIASEN, J. Am. Chem. Soc., 54, (1932) 3841.

79. E.A. PORAI-KOSHITS, Glastechn., Berlin, 32, (1959) 450.

80. R.M. BURGER and R.P. DONOVAN, "Fundamentals of Silicon Integrated Device Technology", Vol. 1, Prentice-Hall Inc.

81. GHANDI, "The Theory and Practice of Microelectronics", Wiley and Sons Inc., New York.

82. W.C. DUNLAP, Jr., H.V. BOHM and H.P. MAKON Jr., Phys. Rev., 96, (1954) 822.

83. C.S. FULLER and J.A. DITZENBERGER, J. Appl. Phys., 25, (1956) 1439.

84. J. YAMAGUCHI, S. HORIUCKI, K. MATSUMARA and Y. OGINO, J. Phys. Soc. Jap., 15, (1960) 1541.

85. A.D. KURTZ and R. YEE, J. Appl. Phys., 31, (1960) 303.

86. E.L. WILLIAMS, J. Electrochem. Soc., 108, (1961) 795.

87. R.N. GHOSHTAGORE, Solid-State Electronics, 15, (1972) 1113.

88. G. KELLSTROM, Nova Acta Reg. Soc. Sci. Ups., 8, (1932) 5.

89. C.G. DARWIN, Phil. Mag., 27, (1914) 315,675.

90. P.P. EWALD, Ann. Physik, 49, (1916) 1,117

91. P.P. EWALD, Acta Cryst., 11, (1958) 888.

92. M. Von LAUE, "Rontgenstrahl-Interferenzen", Akademische Verlag, Frankfurt, (1960).

93. W.H. ZACHARIASEN, "Theory of X-Ray Diffraction in Crystals", John Wiley and Sons Inc., New York, (1945).

94. R.W. JAMES, "The Optical Principles of the Diffraction of X-Rays", G. Bell and Sons, London, (1950).

95. P.B. HIRSCH, Acta Cryst., 5, (1952) 176.

96. N. KATO, J. Phys. Soc. Jap., 7, (1952) 397.

97. G. BORRMANN, Z. Physik, 42, (1941) 157.

98. B.W. BATTERMAN and H. COLE, Rev. Mod. Phys., 36, (1964) 681.

99. N. KATO, Acta Cryst., 11, (1958) 885.

100. N. KATO, Acta Cryst., 14, (1961) 627.

101. L. FOUCAULT, Ann. Obs. Paris, 5, (1859) 197.

102. LORD RAYLEIGH, Phil. Mag., 47, (1874) 193.

103. D.W. PASHLEY, J.M. MENTER and G.A. BASSET, Nature, 179, (1957) 752.

104. A.H. COMPTON, Phys. Rev., 10, (1917) 95.

105. W.L. BRAGG, R.W. JAMES and C.H. BOSANQUET, Phil. Mag., 41, (1921) 309.

106. B. DAVIS and W. STEMPEL, Phys. Rev., 17, (1921) 608.

107. B. DAVIS and H. PURKS, Proc. Nat. Acad. Sci., 13, (1927) 419.

108. W. EHRENBERG and H. MARK, Z. Physik, 42, (1927) 807.

109. M. KOHLER, Ann. Physik, 18, (1933) 265.

110. A. AUTHIER, J. Phys. Rad., 23, (1962) 961.

111. M. Von LAUE, Z. Physik, 72, (1931) 472.

112. A.H. COTTRELL, "Theory of Crystal Dislocations", Blackie and Son Ltd., London & Glasgow, (1964).

113. G. STONEY, Proc. Roy. Soc. (London) A82 (1909) 172.

114. "American Institute of Physics Handbook"

115. A.E.H. LOVE, "A Treatise on the Mathematical Theory of Elasticity", Dover Publications, New York (1892).

116. G.L. PEARSON and J. BARDEEN, Phys. Rev. 75 (1949) 865.

117. F.H. HORN, Phys. Rev. 97 (1955) 1521.

118. M. Von LAUE, Acta. Cryst. 5 (1952) 619.

119. M. HART and A.D. MILNE, Phys. Stat. Solidi 26 (1968) 185.

APPENDIX 1: DYNAMICAL THEORY OF X-RAY DIFFRACTION

The classical theory of X-ray diffraction (the kinematical theory) considers incident and diffracted beams within a crystal but does not take into account any interaction between these beams. This theory works well for calculating intensities of diffraction from a powdered crystal or from very imperfect crystals but breaks down when attempts are made to predict phenomena associated with large 'perfect' crystals such as those associated with the semiconductor industry. This is because interaction is now able to take place within the crystal between beams in the incident and diffracted directions and standing wavefields are set up. The dynamical theory is now able to predict accurately phenomena such as the anomalous transmission effect and the so-called Pendellösung interference fringes.

The theoretical work behind the dynamical theory was originally undertaken by Darwin[89], Ewald[90,91] and Von Laue[92] at the beginning of the century and it is interesting to note that only with the recent advent of perfect crystals such as silicon has it been possible to obtain experimental evidence of phenomena originally predicted by them. More recently, Zachariasen[93], James[94] and Hirsch[95] have extended the scope of the theory to highlight specific

crystal lattice, is triply periodic. The wave vectors in the forward and diffracted directions, $\underline{K}_o$ and $\underline{K}_h$ may be related by Bragg's Law,

$$\underline{K}_h = \underline{K}_o + \underline{h} \tag{A.1}$$

It is the coupling of these waves and their magnitudes and relevant phases that the dynamical theory is primarily concerned with.

The electric displacement vector $\underline{D}$ may be written as

$$\underline{D} = \varepsilon\varepsilon_o\underline{E} \tag{A.2}$$

where ε is the dielectric constant, ε_o the permittivity in free space and $\underline{E}$ the electric field.

The polarization $\underline{P}$ may be defined by

$$\underline{D} = \varepsilon_o\underline{E} + \underline{P} \tag{A.3}$$

Hence, the dielectric constant may be written

$$\varepsilon = 1 + \underline{P}/\varepsilon_o\underline{E} = 1 + \chi \tag{A.4}$$

where χ is the susceptibility.

If a sinusoidal electric field of amplitude E_o and frequency ω acts on an electron with a natural frequency of oscillation ω_o, then the amplitude of the induced motion is

$$x = \left(\frac{e}{m}\right) \frac{E_o}{\omega_o^2 - \omega^2} \qquad (A.5)$$

When the radiation is X-radiation, then $\omega >> \omega_o^2$. The polarization amplitude is related to the amplitude of the induced motion by

$$P = \rho e x \qquad (A.6)$$

where ρ is the electron density and e the electronic charge. Hence,

$$\varepsilon(r) = 1 - \left[\left(\frac{e^2}{mc^2}\right) \frac{\lambda^2}{4\pi^2 \varepsilon_o} \rho(\underline{r})\right] \qquad (A.7)$$

Now, for an infinite 'perfect' crystal, the electron density is triply periodic and so may be expressed most conveniently as a Fourier sum.

$$\rho(\underline{r}) = \left(\frac{1}{v}\right) \sum_h F_h \exp\left(-2\pi i \, \underline{h}.\underline{r}\right) \qquad (A.8)$$

where v is the volume of the unit cell, $\underline{h}$ a reciprocal lattice vector and F_h the structure factor, and where the summation is over all h.

The quantity $(e^2/4\pi\varepsilon_o \, mc^2)$ is the classical electron radius r_e. Combining this with Equations A.7 and A.8,

$$\varepsilon(r) = 1 - \frac{r_e \lambda^2}{\pi v} \sum F_h \exp\left(-2\pi i \, \underline{h}.\underline{r}\right) \qquad (A.9)$$

The susceptibility may also be expressed as a Fourier sum in the

same way as the electron density, ie

$$\chi = \sum_{h} \chi_h \exp(-2\pi i \, \underline{h}.\underline{r}) \qquad (A.10)$$

From Equations A.4 and A.9 it will be seen at once that the Fourier component of the susceptibility

$$\chi_h = \frac{-r_e \lambda^2}{\pi v} F_h \qquad (A.11)$$

A.1 SOLUTION OF MAXWELL'S EQUATION

In the ensuing theory it will be assumed, unless otherwise stated, that the incident beam is a plane wave, ie points in space with identical phase and amplitude will be coplanar, the plane so defined being normal to the beam direction.

Since it may be assumed that the electrical conductivity is zero at X-ray frequencies and that the magnetic permeability μ is the same as that for free space, μ_o, then Maxwell's Equation may be written in the form

$$\nabla x \, \underline{E} = -\frac{\partial \underline{B}}{\partial t} = -\mu_o \frac{\partial \underline{H}}{\partial t}$$

$$\nabla x \, \underline{H} = \frac{\partial \underline{D}}{\partial t} = \varepsilon_o \frac{\partial(\varepsilon \underline{E})}{\partial t} \qquad (A.12)$$

The parameters $\underline{E}$, $\underline{D}$, $\underline{H}$ and $\underline{B}$ may all be expressed as Fourier sums over reciprocal space multiplied by the time dependence term $\exp(2\pi i \, \nu t)$.

The incident and diffracted beams are connected by the Bragg condition of Equation A.1. By combining Maxwell's equations (A.12), the Bragg condition (A.1) and the expression for the dielectric constant (A.9) a set of equations describing the total wavefield within the crystal may be obtained. By limiting this to the case when only one diffracted beam is significant, ie when only one reciprocal lattice point is near the Ewald sphere, this set of equations reduces to a pair of equations giving the field amplitudes of the two waves D_o and D_h.

$$\begin{aligned} (k^2(1+\chi_o) - \underline{K}_o.\underline{K}_o)\, D_o + k^2 c\, \chi_{\bar{h}}\, D_h &= 0 \\ k^2 c\, \chi_h\, D_o + (k^2(1+\chi_o) - \underline{K}_h.\underline{K}_h)\, D_h &= 0 \end{aligned} \qquad (A.13)$$

where $k = 1/\lambda$ (in vacuum), $\underline{K}_o$ and $\underline{K}_h$ are the internal wave vectors and c the polarization factor. When the electric field is perpendicular to the plane of incidence (defined by $\underline{K}_o$ and $\underline{K}_h$) the polarization is said to be in the σ state and $c = 1$. When the electric field is parallel to the plane of incidence, π polarization results and $c = |\cos 2\theta|$.

The non-trivial solution to A.13 may be expressed as the determinant (Batterman and Cole[98]),

$$\begin{vmatrix} k^2\,(1+\chi_o) - \underline{K}_o.\underline{K}_o & k^2 c\, \chi_{\bar{h}} \\ k^2 c\, \chi_h & k^2\,(1+\chi_o) - \underline{K}_h.\underline{K}_h \end{vmatrix} = 0 \qquad (A.14)$$

where the wave vectors $\underline{K}_o$ and $\underline{K}_h$ may be taken to be complex

quantities to account for absorption.

Within the crystal, the radius of the Ewald sphere must be corrected for the average index of refraction, n, so that instead of being k (= $1/\lambda$ where λ is the wavelength of incident radiation) it becomes kn. But $n^2 = \varepsilon$ where ε is the dielectric constant, so that in terms of the susceptibility χ, the radius of the Ewald sphere may be approximated by $k\,(1 + \frac{1}{2}\chi_0)$. Equation A.14 defines the wave vectors $\underline{K}_o$ and $\underline{K}_h$ within the crystal which do not lie exactly on their respective Ewald spheres but deviate slightly from them. This deviation may be expressed as the difference in the mangitude of $\underline{K}_o$ or $\underline{K}_h$ and the radius of the Ewald sphere $k\,(1 + \frac{1}{2}\chi_0)$. Thus two new parameters are defined.

$$\alpha_o = (\underline{K}_o.\underline{K}_o)^{\frac{1}{2}} - k(1 + \tfrac{1}{2}\chi_0)$$

$$\alpha_h = (\underline{K}_h.\underline{K}_h)^{\frac{1}{2}} - k(1 + \tfrac{1}{2}\chi_0) \qquad \text{(A.15)}$$

These two equations may be multiplied by $[(\underline{K}_o.\underline{K}_o)^{\frac{1}{2}} + k(1 + \frac{1}{2}\chi_0)]$ and $[(\underline{K}_h.\underline{K}_h)^{\frac{1}{2}} + k(1 + \frac{1}{2}\chi_0)]$ respectively to give

$$\alpha_o\{(\underline{K}_o.\underline{K}_o)^{\frac{1}{2}} + k(1 + \tfrac{1}{2}\chi_0)$$

$$= \{(\underline{K}_o.\underline{K}_o)^{\frac{1}{2}} - k(1 + \tfrac{1}{2}\chi_0)\}\,\{(\underline{K}_o.\underline{K}_o)^{\frac{1}{2}} + k(1 + \tfrac{1}{2}\chi_0)\}$$

(A.16)

$$\alpha_h\,\{(\underline{K}_h.\underline{K}_h)^{\frac{1}{2}} + k(1 + \tfrac{1}{2}\chi_0)\}$$

$$= \{(\underline{K}_h.\underline{K}_h)^{\frac{1}{2}} - k(1 + \tfrac{1}{2}\chi_0)\}\,\{\underline{K}_h.\underline{K}_h + k(1 + \tfrac{1}{2}\chi_0)\}$$

$\{(\underline{K}_o.\underline{K}_o)^{\frac{1}{2}} + k(1 + \frac{1}{2}\chi_o)\} \simeq 2k$ since the refractive index is very close to unity ($\chi_o \simeq 0$). Equation A.16 may therefore be written

$$2k\alpha_o = \underline{K}_o.\underline{K}_o - k^2(1 + \chi_o)$$
$$2k\alpha_h = \underline{K}_h.\underline{K}_h - k^2(1 + \chi_o) \qquad (A.17)$$

Hence Equation A.14 may now be written as a function of these new parameters α_o and α_h to give

$$\alpha_o\alpha_h = \tfrac{1}{4} k^2 c^2 \chi_h \chi_{\bar{h}} \qquad (A.18)$$

A.2 THE DISPERSION SURFACES

Equation A.18 is the fundamental equation describing the dispersion surface by which allowed wave vectors within the crystal may be determined. Fig A.1(a) illustrates the geometrical interpretation of these equations and Fig A.1(b) shows in detail the locus of allowed wave vectors which makes up the dispersion surfaces. Equation A.18 is the equation of a hyperbola which in this case has the spheres about O and H as its asymptotes. Since both states of polarization must be accounted for, Equation A.18 in fact yields two hyperbolae. The refractive index for X-rays in a crystal differs from unity only by a factor of the order of one part in 10^6 so that the spheres about O and H may be approximated to planes in the region of the dispersion surfaces.

The parameters α_o and α_h depend on the product $\chi_h \chi_{\bar{h}}$. For

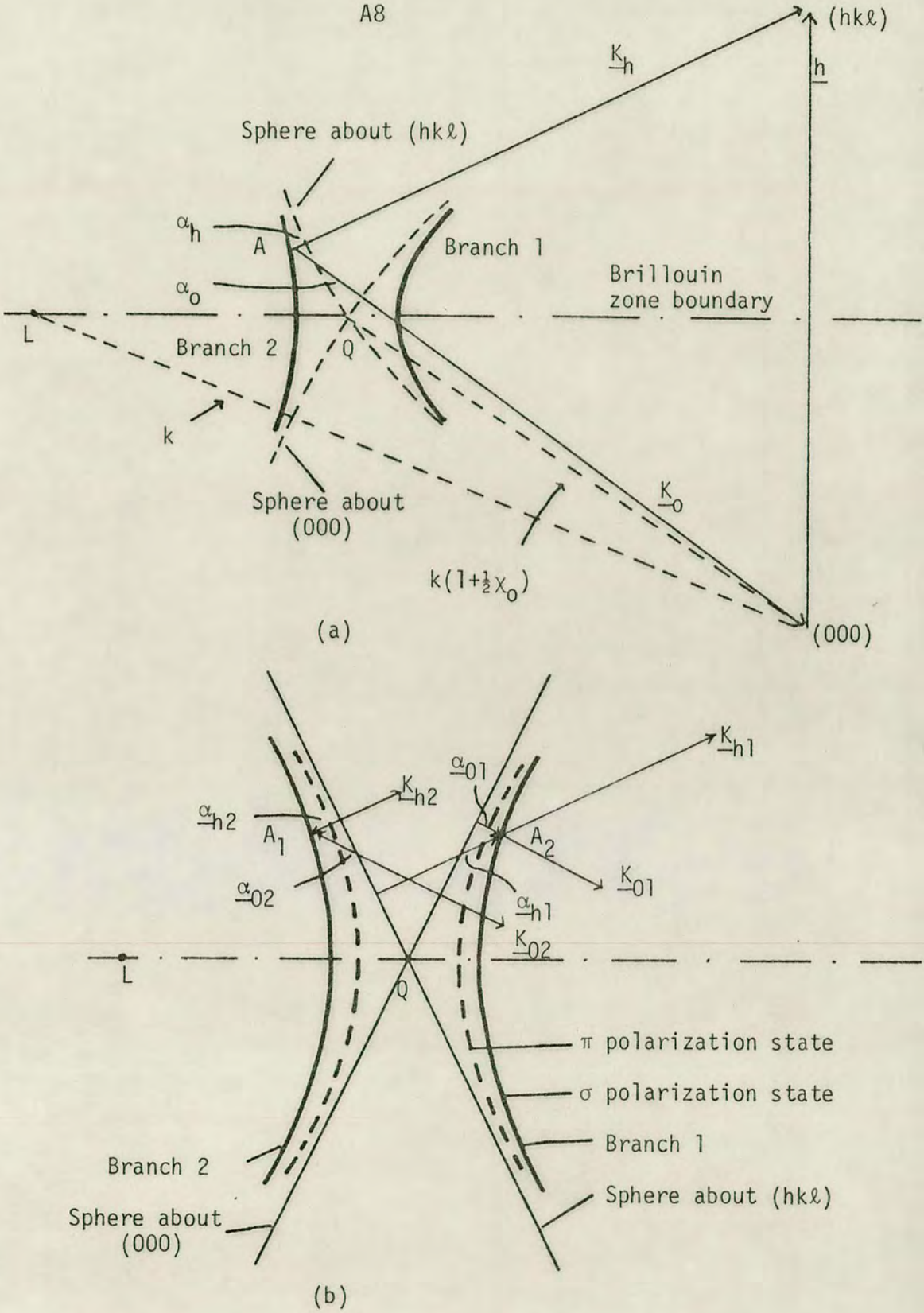

FIGURE A.1: L, Centre of Ewald sphere in vacuum; Q, centre in crystal after correction for average refractive index.
(a): A represents a valid tie point showing typical $\underline{\alpha}_o$ and $\underline{\alpha}_h$.
(b): Close up of (a) showing the dispersion surfaces about Q. The spheres about (000) and (hkℓ) may be approximated to planes, ie straight lines in the diagram

centrosymmetric crystals $\chi_h = \chi_{\bar{h}}$, but χ_h may be a complex quantity with its real and imaginary parts closely associated with the real (directional) and imaginary (absorptive) parts of the wave vector. Hence the parameters α_o and α_h will also be complex.

Having established the allowable waves which may be set up within the crystal, it is from applying the boundary conditions that the actual wave is selected. These solution points on the dispersion surface are known as 'tie points'. The convention is applied such that the branch of the dispersion surface nearest the Laue point (L in Fig A.1(a)) is branch 2, and that furthest away branch 1.

A.3 BOUNDARY CONDITIONS

Since the index of refraction is so close to unity, any reflection from the physical boundary of the crystal may be neglected. Hence the tangential components of the field vectors $\underline{E}$ and $\underline{H}$ will be the same inside the crystal as they will outside. From Maxwell's equations, it can also be shown that the longitudinal components of the field vectors may be neglected. Thus it can be said that for these vectors the physical surface does not exist.

However, the boundary does have an effect on the wave vectors. The components of the wave vectors inside the crystal $\underline{K}_{01}$ and $\underline{K}_{02}$ along the surface must equal the surface component of the wave vector incident on the crystal $\underline{K}^i_o$. Since the incident wave travels in a vacuum there is no absorption and the wave vector (magnitude k) is entirely real. In order to obey the boundary conditions, the imaginary part of the inside wave vectors must therefore lie along the direction

of the surface normal. In other words, planes of constant absorption must be parallel to the physical crystal surface.

The incident wave vector has magnitude k and so, with its tip on O can originate from any point on a sphere centred at O which will have the Laue point on its surface. Thus, in order to maintain these boundary conditions, the tie points of the excited waves (A and B in Fig A.2) and the intersection of the incident wave with the Ewald sphere must all lie in the direction of the surface normal. In this way the tie points may be generated from knowledge of the angle of incidence and the direction of the surface normal. The deviation from the true Bragg angle may be seen from Fig A.2 to be given by LP/k. In the same fashion, boundary conditions may be imposed at the exit surface in order to determine the existing wave vectors $\underline{K}_o^e$ and $\underline{K}_h^e$. In this case, a different exit wave will be produced for each tie point selected unless the entrance and exit surfaces are parallel.

It must be stressed, however, that the properties associated with a wave originating from a selected tie point are invarient and do not in any way depend on the manner in which the tie point was selected.

If a wave is incident upon a parallel sided slab of crystal, then there are two possible faces from which the diffracted beam may exit. If it exits from the same face as the incident face, then this is known as the Bragg diffraction case, but if it exits from the opposite face, then it is known as the Laue case. The appropriate geometries may be seen in Fig A.3. In the Bragg case it will be seen that either only one branch of the dispersion surface will contain the two

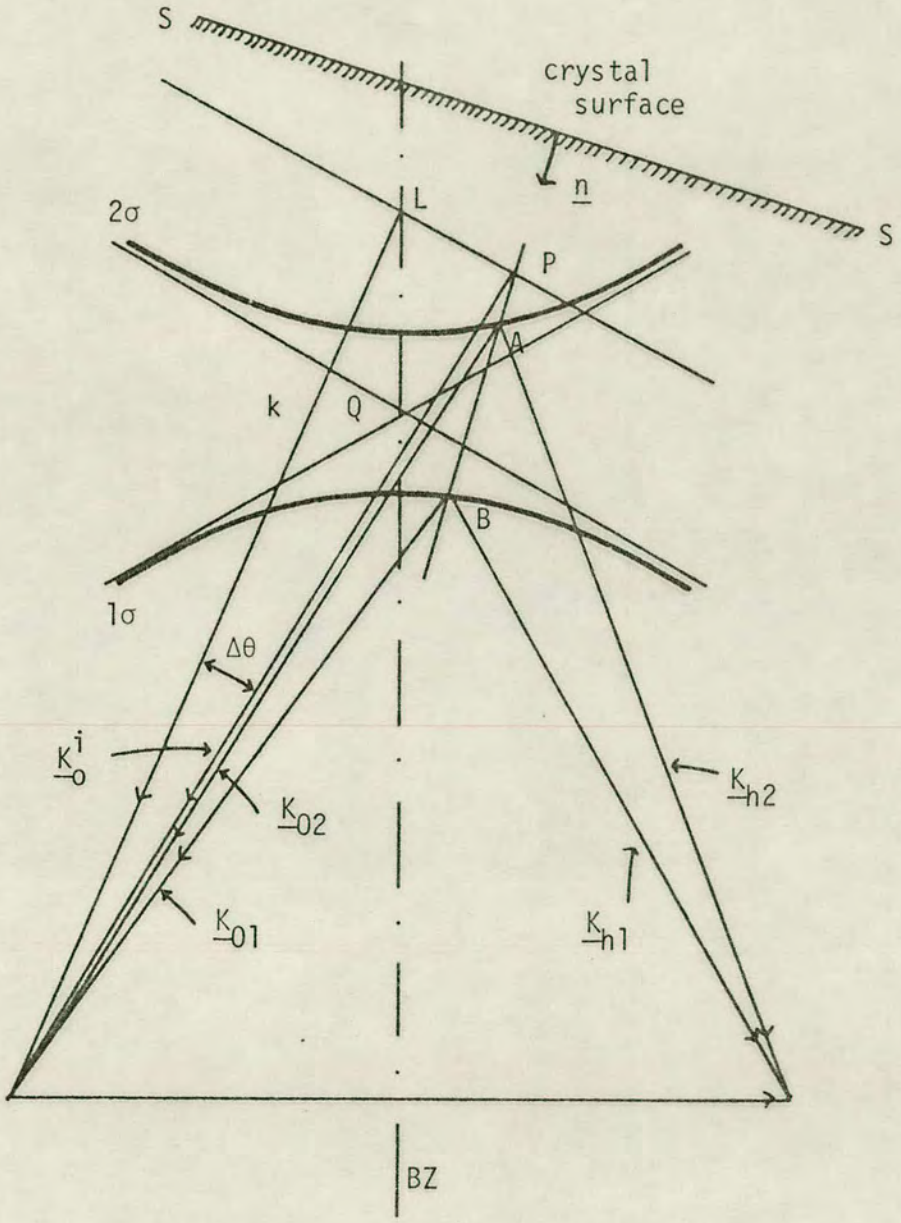

FIGURE A.2: Selection of tie points A,B for boundary conditions defined by deviation from Bragg angle $\Delta\theta(= LP/k)$ and by crystal surface normal $\underline{n}$.

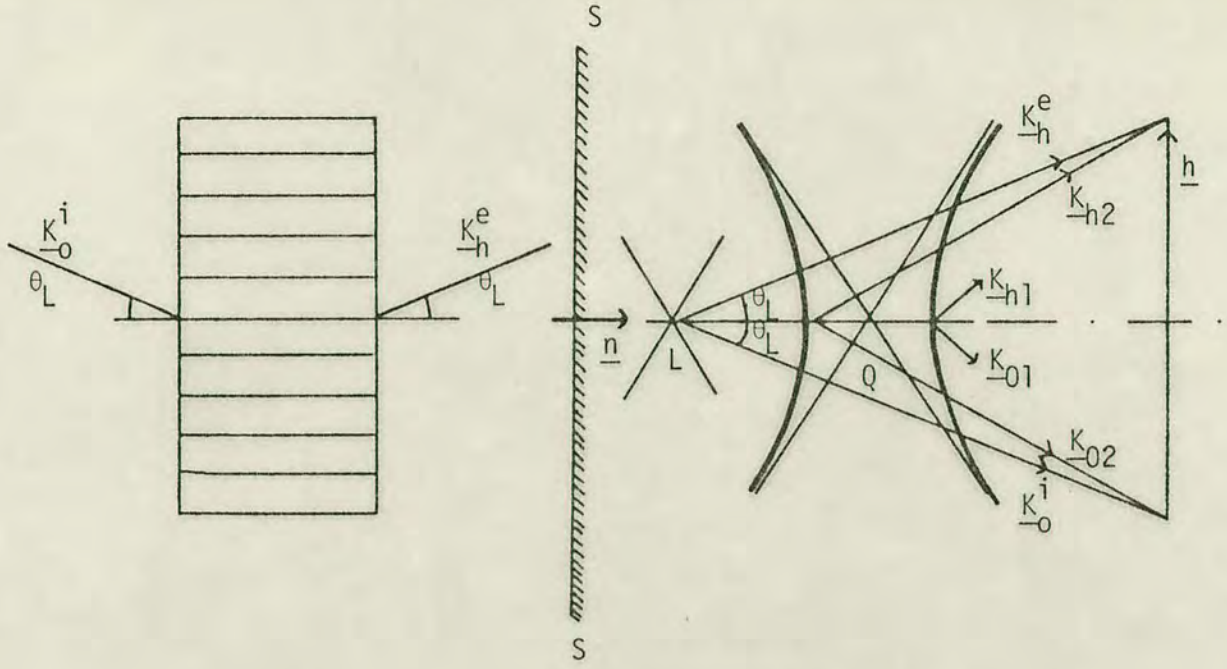

(a)

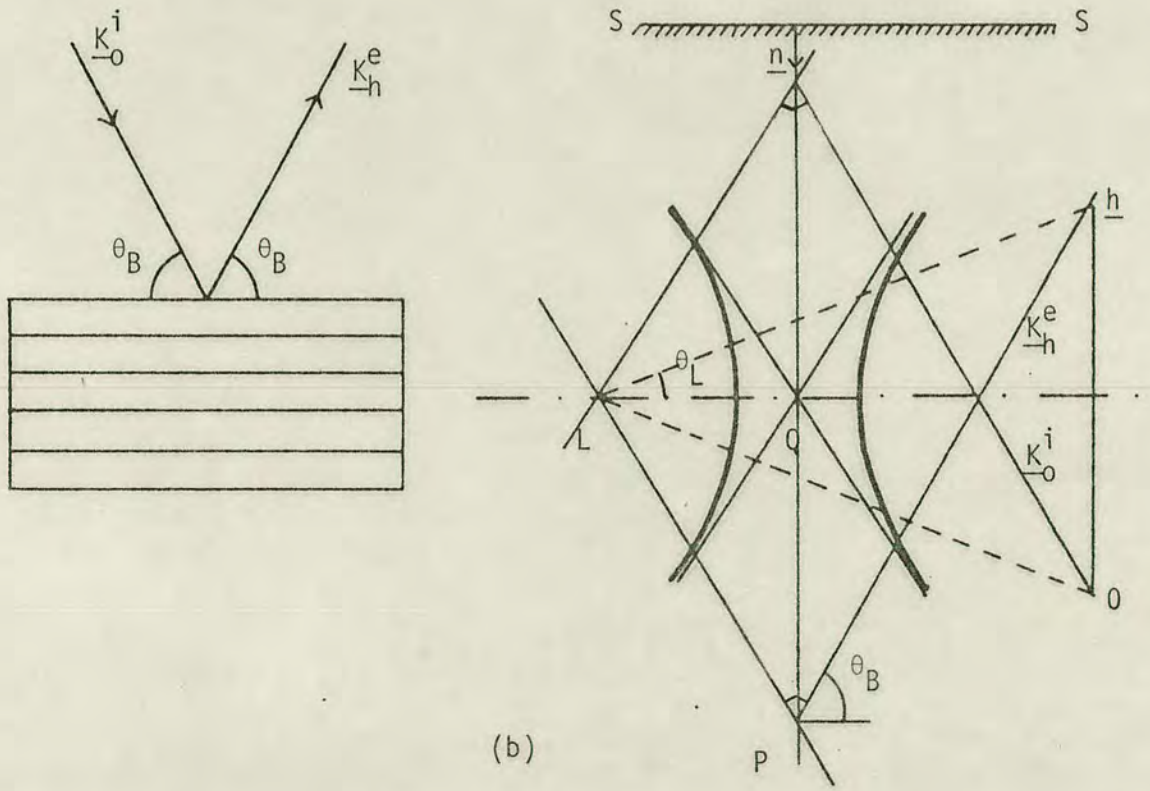

(b)

FIGURE A.3(a): Symmetric Laue case, (b) Symmetric Bragg case. $\underline{K}_h^e$ represents exit beam, making angle θ_L with atomic planes in Laue case and θ_B in Bragg case. The difference between θ_L and θ_B is grossly exaggerated here. In the Bragg case, only one or other branch of the dispersion surface may be excited by an incoming wave. In the case illustrated here, neither branch is excited and total reflection results.

tie points or no tie points at all will be exited over a certain range of incident angles. If neither branch is exited, then there does not exist a propagating solution within the crystal and total reflection results (apart from the absorptive component directed into the crystal). In the Laue case, both sheets of the dispersion surface are available for excitation.

A.4 FIELD AMPLITUDES

By combining Equations A.13 and A.17 an expression relating the ratio of the field amplitudes D_h/D_o to the dispersion surface parameters α_o and α_h will be obtained. It is convenient to define the parameter ξ as this ratio. Hence,

$$\xi = D_h/D_o = \frac{2\alpha_o}{c\,\chi_{\bar{h}}\,k} = \frac{c\chi_h\,k}{2\alpha_h} \qquad (A.19)$$

ie,

$$\xi^2 = \frac{\alpha_o\,\chi_h}{\alpha_h\,\chi_{\bar{h}}} \qquad (A.20)$$

From Equation A.15 it will be seen that for branch 2 of the dispersion surface α_o and α_h are positive. In the zero absorption case, $\chi_{\bar{h}}$ and χ_h are real and negative, so that ξ is always negative on branch 2, and by similar argument always positive on branch 1. Thus there is always a 180^o phase shift between waves generated from tie points on the two surfaces.

Equation A.20 enables the relative amplitude of the diffracted

beam to be deduced as a function of the angle of incidence. In Fig A.4 it will be seen that for tie points A_1 and B_4, $\alpha_o \to 0$ and so $\xi \to \mp 0$. This means that no diffracted beam is generated and only $\underline{D}_o$ propagates through the crystal. At A_4 and B_1 $\alpha_h \to 0$ implying that $\xi \to \pm\infty$. This indicates that if these tie points are excited, a very large diffracted beam would result from the presence of an incident wave. Since this cannot happen from conservation of energy considerations it must be assumed that D_o tends to zero. This implies that the boundary conditions, after selecting the appropriate tie points, distribute the energy between the dispersion surfaces such that energy is conserved. For an incident angle a long way from the true Bragg angle (P4 in Fig A.4) nearly all the energy is diverted into branch 2 of the dispersion surface such that only a wave $\underline{K}_{02}$ propagates through the crystal. As the Bragg angle is reached, so the energy is shared equally between the two dispersion surfaces giving equal intensity waves $\underline{K}_o$ and $\underline{K}_h$. As P1 is approached, so most of the energy becomes diverted into branch 1 of the dispersion surface, and only $\underline{K}_{02}$ is allowed to propagate.

In the symmetric Laue case, the excited tie points lie on the diameter of the dispersion surface and $\xi = 1$ so that incident and diffracted beams have the same amplitudes. In this case the maximum diffraction occurs. Of course, this corresponds to the exact Bragg condition.

The imaginary part of α_o, α_o'', is closely associated with the absorptive part of the wave vector $\underline{K}_o''$ and Batterman and Cole[98] show how the absorption related to each sheet of the dispersion surface deviates at or near the Bragg angle from the absorption coefficient

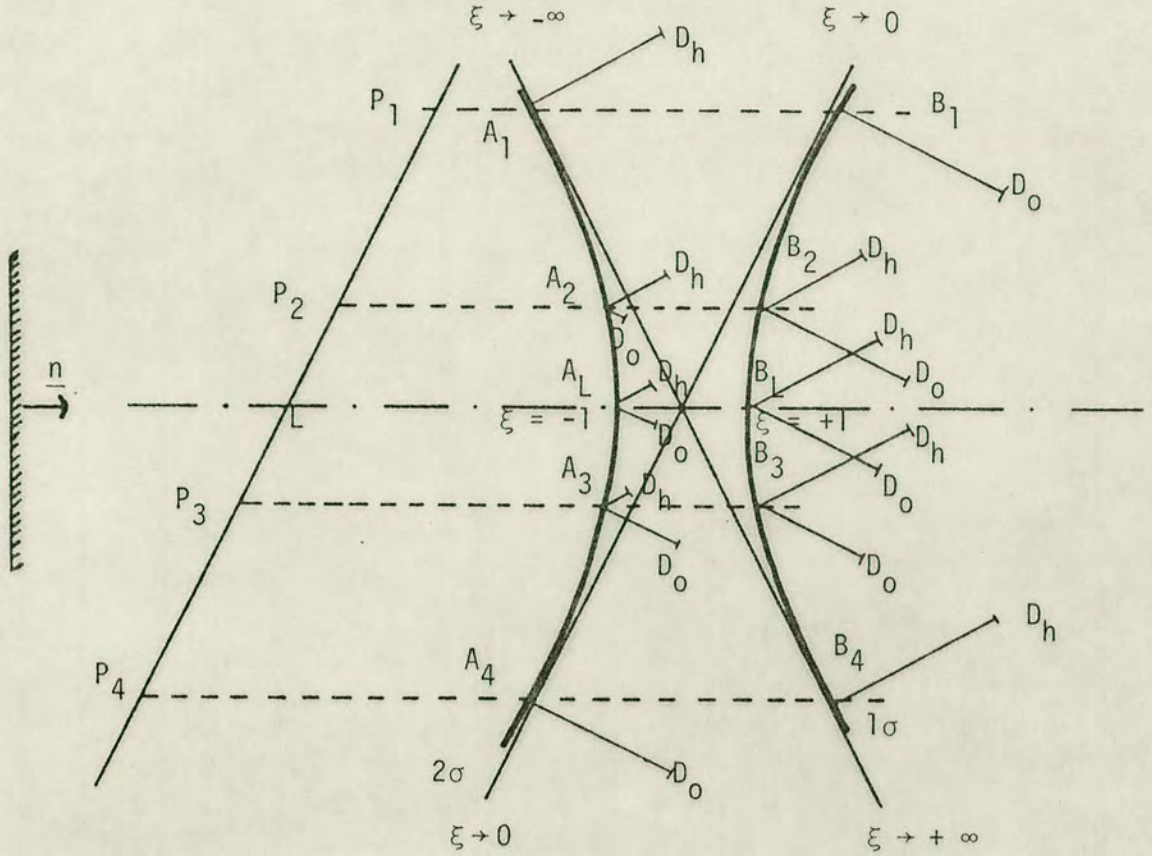

FIGURE A.4: Schematic representation of ratios of field strength D_h/D_o for different tie points under symmetric Laue entrance conditions.

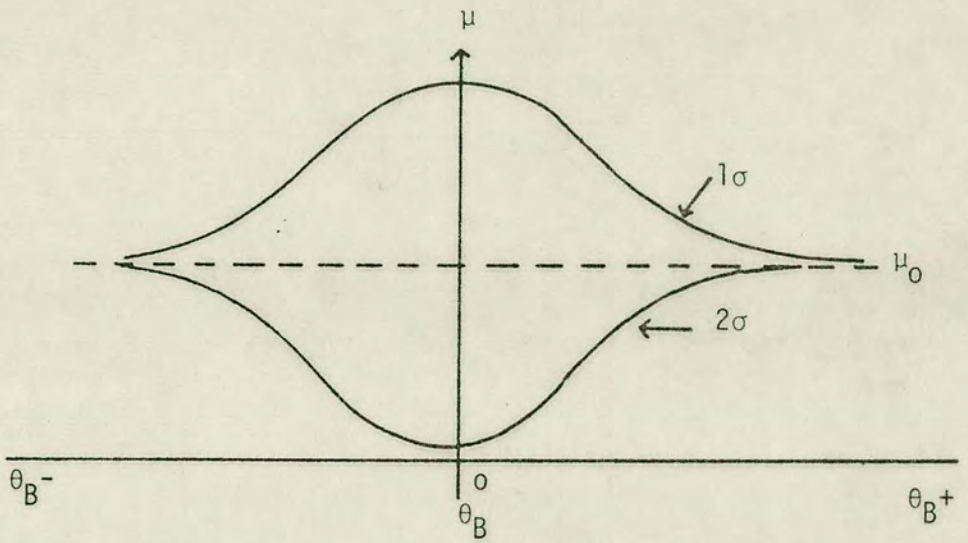

FIGURE A.5: Absorption for each branch of the dispersion surface as a function of deviation from Bragg angle.

in the crystal for a general angle (Fig A.5). The absorption associated with branch 2 decreases as the Bragg angle is approached and at the exact Bragg angle can become very much smaller. Conversely the absorption associated with branch 1 increases until it is almost double that associated with a general direction in the crystal at the Bragg angle.

A.5 ENERGY FLOW AND THE POYNTING VECTOR

If the incident angle is close to the Bragg angle such that transmitted and diffracted waves are generated with amplitudes of the same order of magnitude, then interference will take place between the two beams. Perhaps the best way to understand this coupling between the waves is to consider the ray directions associated with the direction of energy flow in each case. The vector which describes this is known as the Poynting vector. The instantaneous Poynting vector is given by

$$\underline{S} = \frac{c}{4\pi} (\underline{E} \times \underline{H}) \qquad (A.21)$$

This is a complicated function and in this application only the Poynting vector averaged over time and space is required here. This averaging process has been calculated by Von Laue[118] to yield

$$\hat{\underline{S}} = \frac{c}{8\pi} \left(|\underline{E}_o|^2 \hat{\underline{s}}_o + |\underline{E}_h|^2 \hat{\underline{s}}_h \right) \exp\left(4\pi\, Im(\underline{K}_o).r\right) \qquad (A.22)$$

If the electric fields $\underline{E}_o$ and $\underline{E}_h$ are taken to be the sum of the

electric fields associated with each dispersion surface, then $\hat{\underline{S}}$ will be seen to be the sum of three components,

$$\hat{\underline{S}} = \underline{S}_1 + \underline{S}_2 + \underline{S}_{12} \qquad (A.23)$$

where $\underline{S}_1$ is the Poynting vector associated with branch 1, $\underline{S}_2$ branch 2 of the dispersion surface and $\underline{S}_{12}$ represents a coupling term between the two. This coupling term is modulated by the function $\cos 2\pi [(\underline{K}'_{02}-\underline{K}'_{01}).\underline{r}]$ where $\underline{r}$ represents some point in real space, resulting in a periodicity,

$$P = \frac{1}{(\underline{K}'_{02}-\underline{K}'_{01})} \qquad (A.24)$$

Since the boundary conditions demand that $(\underline{K}_{02}-\underline{K}_{01})$ is perpendicular to the entrance surface of the crystal then $\underline{S}_{12}$ is constant in planes parallel to the crystal surface. The interference fringes so formed are known as Pendellösung fringes.

It will be seen from Equation A.22 that the Poynting vector is a function of the field intensities, and in fact it has been shown by Ewald[91], Kato[99] and others that the direction of the Poynting vector is always normal to the dispersion surface. For example, in the case of the incident beam being at the exact Bragg angle, then the Poynting vector will lie perpendicular to the reciprocal lattice vector. The result of this is that the energy flow is directed exactly along the atomic planes responsible for the reflection.

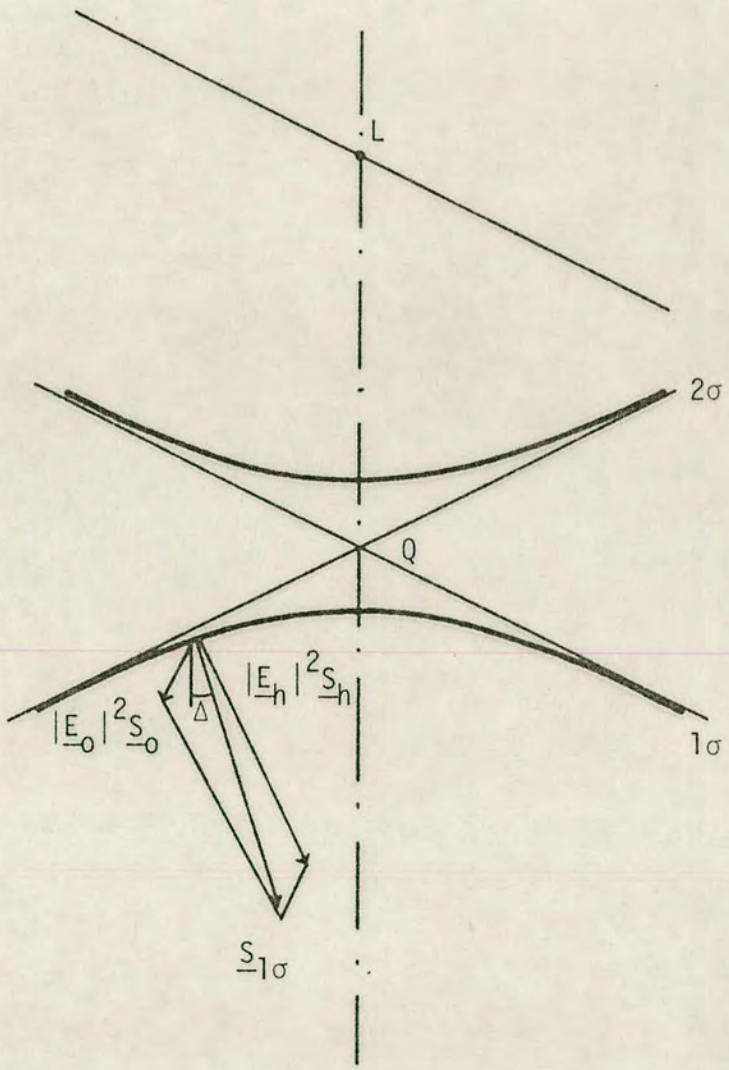

FIGURE A.6: Poynting vector $\underline{S}_{1\sigma}$ as a vector sum of the energy flows in $\underline{S}_h$ and $\underline{S}_o$ directions. Δ represents the angle between the direction flow and the atomic planes. $\underline{S}_{1\sigma}$ is normal to the dispersion surface at the tie point.

A.6 PLANE WAVES - SPHERICAL WAVES

The development of this theory has assumed so far that the incident beam has been a plane wave infinite in extent. However, in practice, any wave originating from a point source must be spherical A valid plane wave approximation can be made, however, if the angular width of a coherent incident wave Ω is much less than ω, the angular width of the reflection. For a typically collimated beam of X-rays, Ω is about 10^{-4} radians and a typical value for ω might be 10^{-5} radians so that a plane wave approximation is invalid. Kato[100] has shown that a spherical wave can be thought of as the superposition of plane waves each with an infinitesimally small angle between them such that the constant phase points lie on the surface of a sphere (ie the waves all originate from the same point source). This implies that the whole dispersion surface becomes illuminated with coherent radiation. Hence the direction of energy flow will cover the 2θ range of angles between $\underline{S}_0$ and $\underline{S}_h$ for only a small angular range of incident beams. This region is known as the 'X-ray fan'.

It is interesting to compare the Pendellösung effect in both the spherical and plane wave cases (Fig A.7). In the spherical wave case, the incident beam width is small compared with the thickness of the crystal. Hence the superposition of plane waves (or wave bundle) which is associated with vectors terminating in a region $d\tau$ of the dispersion surface give rise to energy flows which are physically separated from those resulting from neighbouring regions of the dispersion surface (except near the incident surface). This means that Pendellösung interference cannot take place in the manner described

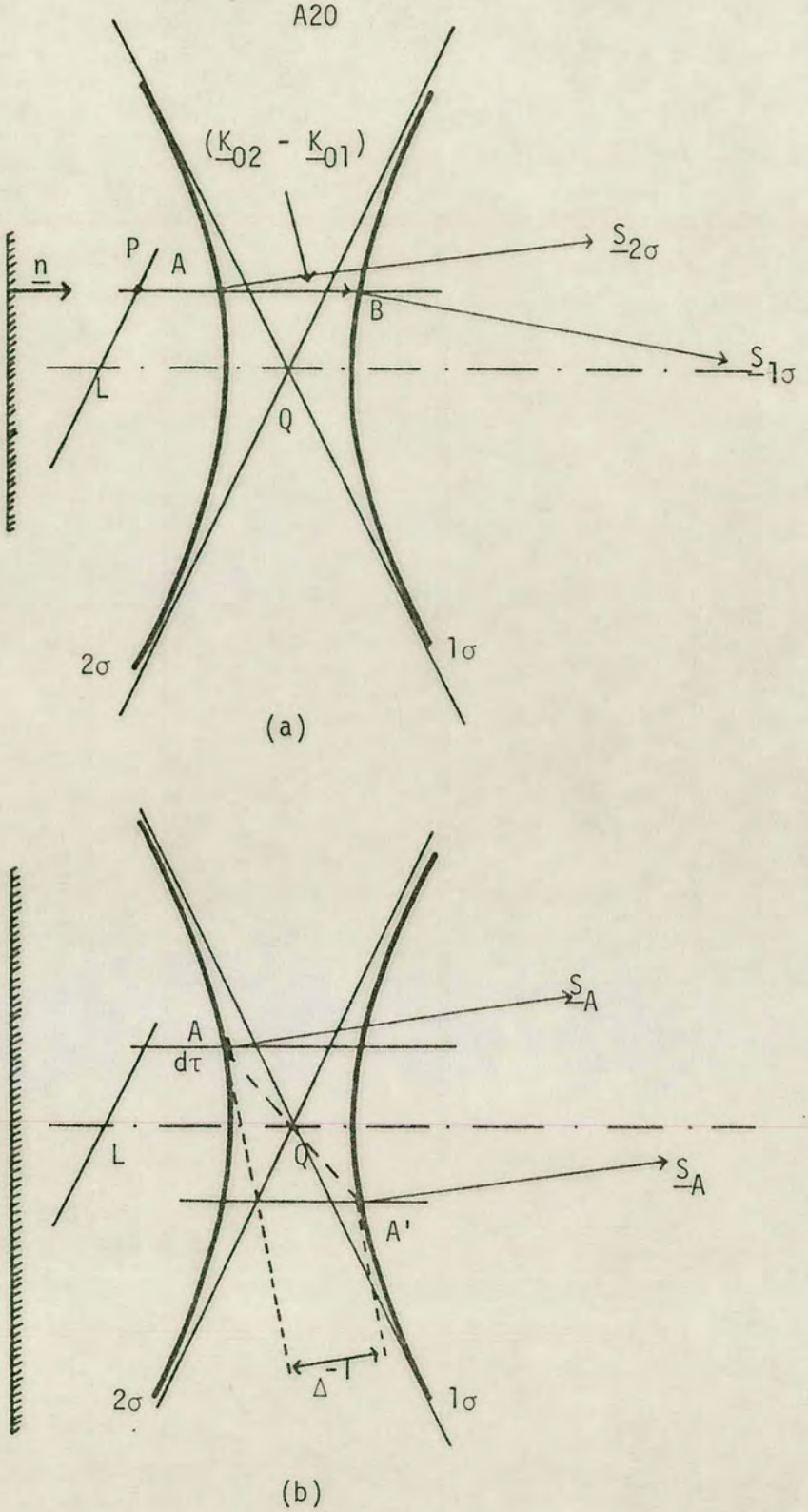

FIGURE A.7: Beams which interfere to give Pendellösung fringes in the plane wave (a) and the spherical wave case (b). In (b) the whole dispersion surface is excited and $\underline{S}_A$ and $\underline{S}_A'$ represent two of the infinite number of beams filling the X-ray fan between $\underline{S}_o$ and $\underline{S}_h$.

for a plane wave infinite in extent. However, interference does take place between waves whose Poynting vectors are in the same direction (A and A' in Fig A.7), and the Pendellösung fringes are a consequence of this interference.

A fundamental difference between Pendellösung fringes arising from the plane wave and spherical wave each may now be illustrated. In the plane wave case, the vector $(\underline{K}_{02}-\underline{K}_{01})$ is a minimum at the Bragg angle and increases with angular deviation from it. Thus the period $P = 1/(\underline{K}_{02}-\underline{K}_{01})$ is a maximum at the Bragg angle and decreasing with angle away from it. However, in the spherical wave case, the normal to the fringe fronts lies in the direction of the interfering beams and so the period is the inverse of the component of $(\underline{K}_{oA}-\underline{K}_{oA'})$ in that direction. This is represented by the inverse distance Δ^{-1} in Fig A.7. For interference in the direction perpendicular to the reciprocal lattice vector (ie the equivalent of the exact Bragg angle in the plane wave case) the period is a minimum and increases with deviation from this angle. Hart and Milne[119] were able to obtain both plane wave and spherical wave Pendellösung fringes simultaneously in the same wedge-shaped crystal.

APPENDIX 2

Appendix 2 contains the fortran computer programme written to calculate the moiré fringe pattern associated with the strain caused by the growth of a disc of thermal oxide on one interferometer wafer. The measured moiré fringe spacing under the oxide disc is entered into the programme and the overall moire fringe pattern is calculated from the model developed in Section 7.1, and the oxide stress required to produce this pattern computed. The fringe pattern is produced as line printer output.

```
      IMPLICIT REAL*8(A-H,O-Z)
      INTEGER CHAR(101,61),SPACE/' '/,STAR/'*'/,ZERO/'0'/
      INTEGER YES/'Y'/
      DIMENSION MF(200),FDISP(200),XXI2(100),RXI2(100)
      DIMENSION ALPHA(151),XX(151)
C READ IN DATA
      WRITE(5,200)
  200 FORMAT(' WAFER THICKNESS (MM) ?')
      READ(5,100)TSI
      TSI=TSI*0.1
      WRITE(5,201)
  201 FORMAT(' OXIDE THICKNESS (MICRONS) ?')
      READ(5,100)TOX
      TOX=TOX*1.0E-04
      WRITE(5,202)
  202 FORMAT(' DISC RADIUS (MM) ?')
      READ(5,100)RO
      RO=RO*0.1
      WRITE(5,203)
  203 FORMAT(' RATIO OF FRINGE SPACING TO DISC RADIUS ?')
      READ(5,100)RAT
      WRITE(5,204)
  204 FORMAT(' DO YOU WANT TO CORRECT FOR IMAGE PROJECTION ?')
      READ(5,400)IANS
  400 FORMAT(A1)
C DISTORTION FACTOR DUE TO IMAGE PROJECTION
      DSTRX=1.0
      DSTRY=1.0
      IF(IANS.NE.YES)GOTO50
      ANGLE=10.65*3.14159/180.0
      DSTRX=DCOS(ANGLE)
      DSTRY=1.11
   50 DSTRN=DSTRY/DSTRX
C CALCULATE STRESS WHICH WILL GIVE
C REQUIRED FRINGE SPACING
      SIGMA=3.476E04*(TSI/TOX)/(RAT*RO)
  100 FORMAT(F10.5)
C CONSTANTS
      SPAC=1.92E-03
      E=16.90E11
      XNU=0.262
C
      XLAMD=E*XNU/((1.0+XNU)*(1.0-2.0*XNU))
      XMU=E/(2.0*(1.0+XNU))
C CORRECTION TO LAMDA FOR PLATE OF FINITE
C THICKNESS - SEE LOVE PAGE 208
      XLAMD=2.0*XLAMD*XMU/(XLAMD+2.0*XMU)
      A=(XLAMD+3.0*XMU)/(2.0*XMU*(XLAMD+2.0*XMU))
      B=A*(XLAMD+XMU)/(XLAMD+3.0*XMU)
```

```
C ITERATE X FROM 0 TO 3.0 * R0
      DO2I=1,151
      XI=I
      X=R0*(XI-1.0)/50.0
C PREPARE CONSTANTS PRIOR TO INTEGRATING
      XR0=X**2+R0**2
      DISPL=0.0
C INTEGRATE WRT PHI FROM 0 TO PI RADIANS
      DO1IANG=2,180,2
      XANG=IANG
      ANG=3.14159*(XANG-1.0)/180.0
      RAD=DSQRT(XR0-2.0*X*R0*DCOS(ANG))
    1 DISPL=DISPL-A*DCOS(ANG)*DLOG(RAD)
     1-B*X*R0*(DSIN(ANG))**2/(RAD**2)
      DPHI=2.0*3.14159/180.0
      FDISP(I)=DISPL*SIGMA*TOX*R0*DPHI*2.0/(SPAC*3.14159*TSI
    2 CONTINUE
C CALCULATE ANGLE VS X
      XX(1)=0.0
      ALPHA(1)=0.0
      DO20I=2,151
      XI=I-1
      XX(I)=XI*R0/5.0
      DALPH=2.063E05*(3.0*SPAC*(FDISP(I)-FDISP(I-1)))/TSI
   20 ALPHA(I)=ALPHA(I-1)+DALPH
C PREPARE CONTOUR MAP
      DO3J=1,61
      YJ=J
      Y=(YJ-1.0)*5.0/(3.0*DSTRN)
      LF=0
      CHAR(1,J)=STAR
      DO3I=2,101
      X=I-1
      XJX=DSQRT(X**2+Y**2)+1.0
      JX=XJX
      XXJX=JX
      XKF=FDISP(JX)+(XJX-XXJX)*(FDISP(JX+1)-FDISP(JX))
      KF=XKF/DSQRT(1.0+(Y/X)**2)
      CHAR(I,J)=SPACE
      IF(KF.GT.LF)CHAR(I,J)=STAR
      IF(KF.LT.LF)CHAR(I-1,J)=STAR
      IF(KF.LT.MF(I).AND.J.NE.1)CHAR(I,J-1)=STAR
      MF(I)=KF
    3 LF=KF
C CALCULATE OXIDE DISC POSITION
      DO13N=1,17
      TN=N
      THETA=(TN-1.0)*0.09817
      IX=50.0*DCOS(THETA)+1.5
      IY=30.0*DSTRN*DSIN(THETA)+1.5
   13 CHAR(IX,IY)=ZERO
```

```
C CALCULATE FRINGE POSITIONS
      IF=FDISP(51)
      L=1
      DO6K=1,IF
      XK=K
      DO7I=L,52
      IF(FDISP(I).GT.XK)GOTO8
    7 CONTINUE
    8 L=I
      XI1=I-1
      XI2=(XK-FDISP(I-1))/(FDISP(I)-FDISP(I-1))+XI1
      XXI2(K)=(XI2-1.0)*DSTRX*R0/5.0
    6 RXI2(K)=(XI2-1.0)/50.0
C PRINT-OUT
      TSI=TSI*10.0
      WRITE(6,301)TSI
      TOX=TOX*1.0E04
      WRITE(6,302)TOX
      R0=R0*10.0
      WRITE(6,303)RC
      SPAC2=SPAC*1.0E08
      WRITE(6,304)SPAC2
      WRITE(6,306)E
      WRITE(6,307)XNU
  301 FORMAT(////,' WAFER THICKNESS =',F5.3,' MM')
  302 FORMAT(' OXIDE THICKNESS =',F5.3,' MICRONS')
  303 FORMAT(' DISC RADIUS =',F5.3,' MM')
  304 FORMAT(' LATTICE SPACING =',F5.3,' ANGSTROM')
  305 FORMAT(/////,' OXIDE STRESS =',E8.3,' CGS')
  306 FORMAT(' YOUNGS MODULUS =',E8.3,' CGS')
  307 FORMAT(' POISSONS RATIO =',F5.3,////)
      DO11J=1,61
      WRITE(6,312)(CHAR(I,62-J),I=1,101)
   11 CONTINUE
  312 FORMAT(101A1)
      DO12J=2,61
      WRITE(6,312)(CHAR(I,J),I=1,101)
   12 CONTINUE
      WRITE(6,305)SIGMA
      WRITE(6,309)
  309 FORMAT(' FRINGE NO.      X(MM)',10X,'X/R0')
      DO9K=1,IF
    9 WRITE(6,310)K,XXI2(K),RXI2(K)
  310 FORMAT(I6,2F15.3)
      WRITE(6,308)FDISP(51)
  308 FORMAT(' FRINGE NUMBER AT EDGE OF DISC =',F6.2,/////)
      WRITE(6,313)
  313 FORMAT(5X,'X(MM)',6X,'ALPHA (SECS)')
```